CARBON MOLECULAR SIEVE MEMBRANES FOR XYLENE ISOMER SEPARATIONS

A Dissertation
Presented to
The Academic Faculty

by

Yao Ma

In Partial Fulfillment
of the Requirements for the Degree
Doctor of Philosophy in the
School of Chemical & Biomolecular Engineering

Georgia Institute of Technology
May 2020

CARBON MOLECULAR SIEVE MEMBRANES FOR XYLENE ISOMER SEPARATIONS

Approved by:

Dr. Ryan P. Lively, Advisor
School of Chemical & Biomolecular Engineering
Georgia Institute of Technology

Dr. William J. Koros
School of Chemical & Biomolecular Engineering
Georgia Institute of Technology

Dr. David S. Sholl
School of Chemical & Biomolecular Engineering
Georgia Institute of Technology

Dr. Krista S. Walton
School of Chemical & Biomolecular Engineering
Georgia Institute of Technology

Dr. M.G. Finn
School of Chemistry &Biochemistry
Georgia Institute of Technology

Date Approved: March 04, 2020

To my supporting and loving family

To my dearest advisor, Dr. Ryan P. Lively

ACKNOWLEDGEMENTS

I wish to express my deepest gratitude to my advisor, Dr. Ryan Lively, who has been a tremendous mentor for me. I would like to thank Dr. Lively for his guidance and support, both academically and emotionally, through the rough road to finish this thesis. Without him, I cannot be who I am today. Besides my advisor, I want to thank the rest of my committee members Dr. William Koros, Dr. David Sholl, Dr. Krista Walton, Dr. M.G. Finn, for their time and insightful suggestions.

I would like to acknowledge the funding source from ExxonMobil Research and Engineering and American Chemical Society Petroleum Research Fund. I also appreciate the helpful discussion with ExxonMobil scientists: Dr. Benjamin McCool, Dr. Dhaval Bhandari, Dr. J.R. Johnson, Dr. Neel Rangnekar, Dr. Daniel Zhou, and Dr. Harry Deckman. Besides, the fellowships and awards from the American Institute of Chemical Engineers (AIChE) Separations Division, ACS I&EC Division, Eastman Chemical Company, The North American Membrane Society and Center for the Science and Technology of Advanced Materials and Interfaces of Georgia Tech are greatly appreciated. I would like to acknowledge the Institute of Electronics and Nanotechnology of Georgia Tech for providing me the characterization equipment.

I am lucky to work in the Lively Group for the past several years. All members deserve thanks. I appreciate the technical and nontechnical guidance from Dr. Melinda Jue, Dr. Brian Pimental, Erkang Zhou, Dr. Simon Pang, Dr. Dong-Yeun Koh, and Dr. Guanghui Zhu. I would like to thank the helpful discussion with Dr. Richelle Lyndon, Dr. Achintya Sujan, Dr. Fengyi Zhang, Stephen DeWitt, Dr. Shaowei Yang, Leo Chiang, Hye Youn Jang, Ronita Mathias, Dr. Yun-Ho Ahn, Matt Rivera and Conrad Roos. I also appreciate the collaborations with Dr. Nicholas Bruno, Dr. Breanne Hamlett and Kirstie Thompson from the Finn group.

Last but not least, I must thank my family for giving me the strength to reach for the stars and chase my dreams. Thank you to my parents, Ms. Yuzhuo Wang and Mr. Wenhai Ma, for their unconditional love. Thanks to my sisters Qiong and Lu for their continuous support. Thanks to my beloved husband Fengyi, who has been my great companion and best friend for sharing the beauty of science and the joys and sorrows of life.

TABLE OF CONTENTS

LIST OF TABLES

LIST OF FIGURES

LIST OF ABBREVIATIONS

BPDA	Biphenyl-tetracarboxylic acid dianhydride
CMS	Carbon molecular sieve
DCM	Dichloromethane
DMF	Dimethylformamide
DVS	Dynamic vapor sorption
FTIR	Fourier-transform infrared spectra
FVV	Fractional free volume
GC	Gas chromatography
GPC	Gel permeation chromatography
HFM	Hollow fiber membranes
IZA	International zeolite association
MS	Maxwell-Stefan
MOF	metal−organic framework
m-xylene	*meta*-Xylene
OSRO	Organic solvent reverse osmosis
o-xylene	*ortho*-xylene
PAN	Polyacrylonitrile
PDI	Polydispersity index
PFA	Polyfurfuryl alcohol
PIM-1	Polymer of intrinsic microporosity−1
PIM-SBF	Spirobifluorene-based polymer of intrinsic microporosity
PVDC-AC	Polyvinylidene chloride-acrylate terpolymer

PVDF	Poly(vinylidene fluoride)
p-xylene	*pare*-Xylene
QENS	Quasielastic neutron scattering
RO	Reverse osmosis
SEM	Scanning electron microscopy
SMB	Simulated moving bed
TFTPN	Tetrafluoroterephthalonitrile
THF	Tetrahydrofuran
TTSBI	5,5’,6,6’-tetrahydroxy-3,3,3’,3’-tetramethyl-1,1’-spirobisindane
WK	Wicke-Kallenbach
XRD	X-ray diffraction
XPS	X-ray photoelectron spectroscopy

SUMMARY

The purification of benzene derivatives, particularly xylene isomers, is one of the most important organic mixture separations practiced in industry. The separation of xylene isomers is especially challenging due to the similarity of their physical properties. Carbon molecular sieve (CMS) membranes are promising materials for such challenging solvent separations due to their stability, ability to be scaled at practical form factors, and the avoidance of expensive supports or complex multi-step fabrication processes, but these materials have not been studied in detail in the case of large organic molecules.

Xylene isomer transport and sorption properties in a CMS membrane derived from a prototypical polymer of intrinsic microporosity (PIM-1) reveal that diffusion selectivity is the dominant factor in contributing to the preferential permeation of *p*-xylene over *o*-xylene. Moreover, the contributions of "enthalpic" and "entropic" selectivity to the diffusion selectivity are studied in detail and reveal that entropic factors dominate the xylene selection mechanism. Another critical challenge is the creation of "mid-range" (e.g., 5-9 Å) microstructures that allow for facile permeation of organic solvents and selection between similarly-sized guest molecules. Here, we create these microstructures via the pyrolysis of the polymer of intrinsic microporosity under low concentrations of hydrogen gas. The introduction of H_2 inhibits the aromatization of the decomposing polymer and ultimately results in the creation of a well-defined bimodal pore network that exhibits an ultramicropore size of 5.1 Å. The H_2-assisted CMS dense membranes show a dramatic increase in *p*-xylene ideal permeability (~15 times), with little loss in *p*-xylene/*o*-xylene selectivity (18.8 vs. 25.0) when compared to CMS membranes pyrolyzed under a pure

argon atmosphere. This approach is successfully extended to hollow fiber membranes operating in organic solvent reverse osmosis mode, highlighting the potential of this approach to be translated from the laboratory to the field.

Moreover, this thesis demonstrates that the gradient of the fractional occupancy of penetrant molecules within the micropores of the membrane is the driving force for permeation without requiring assumptions about pressure within the CMS membrane. Flux equations are derived using both Fickian and Maxwell-Stefan approaches, and different behavior in the permeate flux versus upstream hydraulic pressure relationship is shown to arise as a result of differences in the loading dependence of the single component Maxwell-Stefan diffusivity. Molecular modeling results available in the literature and experimental data obtained from CMS membranes showcase that these loading-dependent changes in the Maxwell-Stefan diffusivity are possible. This loading dependence is separated into three regimes: so-called “weak confinement” diffusion and “strong confinement” diffusion, both of which have been discussed at length in the literature, and a new “hybrid confinement” diffusion, which is introduced here.

Overall, this thesis opens up new opportunities for the membrane-based applications of CMS materials and provides fundamental insight and guidance into the osmotically-moderated sorption-diffusion transport of solvent molecules through CMS membranes.

CHAPTER 1. **INTRODUCTION**

1.1 Organic Solvent Separations

Separation processes convert mixtures (e.g., raw resources, industrial wastes, etc.) into pure value-added chemicals, which plays a critical role in modern industries. According to the Department of Energy, 45% to 55% of energy consumption in US industries is contributed by separation processes [1]. Moreover, at least 80% of the separation process energy consumption is consumed by thermally-driven separation techniques, such as distillation, crystallization, and absorption, among others [2]. Thermally-driven separation techniques differentiate molecules based on their thermal properties (e.g., boiling points, melting points, etc.) and usually involves energy-intensive phase change of the material. As a comparison, non-thermal-driven separation techniques, such as membrane separations requiring little or no phase change, could save 90% energy consumption [3]. For example, the heat of water evaporation during the desalination process is around 640 kWh/m^3, which is significantly higher than the 1 kWh/m^3 Gibbs free energy for salt-water demixing. With the help of heat integration, the modern multi-stage flash process consumes 50 kWh/m^3 energy for desalination, which is still much higher than the theoretical minimum energy requirement. By contrast, commercial membrane-based desalination only consumes 5 kWh/m^3 energy on average, which is approaching the thermodynamic limit [3].

Organic solvent separation processes are widely applied in chemical, petroleum, and pharmaceutical industries. Typical organic solvent separation applications include

product recovery from synthesis solution, crude oil refining, organic solvent purification, chemical waste treatment, among others. In the chemical and pharmaceutical industries, organic solvent separation processes are mostly accomplished by thermal-driven techniques and contribute to 40–70% of the capital cost and operational cost [2]. Replacing the conventional thermal-driven organic solvent separation processes with an energy-efficient separation process is a critical step to achieve sustainable development.

1.2 Xylene Isomer Separations

Xylenes are widely used chemical feedstocks for solvents and the production of synthetic polymers. *para*-Xylene is an important raw material for polymers such as polyester, polyethylene terephthalate, etc. The global production of *para*-xylene is 65 billion pounds per year [4]. *ortho*-Xylene can be converted into phthalic anhydride, an important plasticizer precursor,[5] and *meta*-xylene can be converted into isophthalic acid,[6] a precursor for polyethylene terephthalate.

Xylenes are mostly produced via catalytic reforming, which converts naphthas distillates into octane-rich liquids [7]. The resulting liquid product is also referred to as reformates, which are important resources of aromatic compounds such as benzene, toluene, ethylbenzene, and xylenes. The separation of reformates, especially the separation of xylene isomers, is an important and challenging task. While benzene, ethylbenzene, and toluene can be easily separated, xylene isomer separation is difficult. Xylene isomers have similar atmospheric boiling points: 144 °C for *ortho*-xylene, 139 °C for *meta*-xylene, and 138 °C for *para*-xylene. Such close boiling points make it difficult to separate xylene

isomers via conventional distillation [8]. The number of theoretical plates required for xylene separation to commercial specifications exceeds 360, which is not feasible.

The state-of-the-art separation technique for xylene isomers is fractional crystallization and adsorption. Crystallization separates xylene isomers based on their different freezing points: -25 °C for *ortho*-xylene, -48 °C for *meta*-xylene, and 13 °C for *para*-xylene. While crystallization is a well-developed technique and contributes to around 25% *para*-xylene separation, fractional crystallization of xylene isomers has various drawbacks [9,10]. First, the *para*-xylene recovery rate of crystallization is around 60-70% due to the eutectic point and economic consideration. Second, crystallization is energy-intensive to the cryogenic environment requirement with the high energy required to operate at around -50 °C. In most commercial projects, crystallization is only applied to process *para*-xylene-rich streams (*para*-xylene concentration > 80%) [8].

Compared with crystallization, adsorption separation of xylene isomers is more attractive owing to its higher efficiency and lower energy penalty. Industrial adsorptive separation of xylene isomers is conducted via simulated moving beds (SMBs), which was firstly developed by Universal Oil Products (UOP) in the 1960s. A typical SMB unit operates at around 180 °C with *para*-xylene recovery around 97-99% and *para*-xylene purity of 99.7-99.9%. The performance of SMB processes is determined by the adsorbents and process optimization. In industry, FAU-type zeolites are commonly used to separate xylenes in simulated moving bed chromatography processes. Besides zeolites, researchers are also developing carbon molecular sieves (CMSs), polymers, silica gel, and metal−organic frameworks (MOFs).

1.3 Membrane-based Xylene Isomer Separations

Membrane processes are a promising technique for xylene isomer separation. Compared with crystallization and SMB-based adsorption, membrane-based separation ideally consumes much less energy and requires an easier operation. To date, two membrane separation techniques have been investigated to separate liquid xylene isomer mixtures: pervaporation and organic solvent reverse osmosis.

1.3.1 Pervaporation

Pervaporation is a traditional membrane-based separation process for liquid mixtures [11]. The typical pervaporation scheme is shown in Figure 1.1. A pervaporation membrane is placed in direct contact with the liquid mixture. The membrane serves as a selective transportation media between the liquid phase and the vapor phase. Molecules are transferred from the liquid phase into the vapor phase. Membranes are engineered so that different molecules exhibit different affinities with the membrane or different diffusivity in the membrane, which results in different permeances across the membrane. As a result, the more permeable species are enriched in the permeate (the vapor phase), while the less permeable species are enriched in the retentate side.

Since the transmembrane molecule transfer is driven by the fugacity gradient of different components within the membrane, a low fugacity should be maintained on the permeate side. One strategy is to sweep the permeate side with inert gases, as shown in Figure 1.1a. The other strategy is to maintain low absolute permeate pressure by applying a vacuum (often supplied via a partial condenser), as shown in Figure 1.1b.

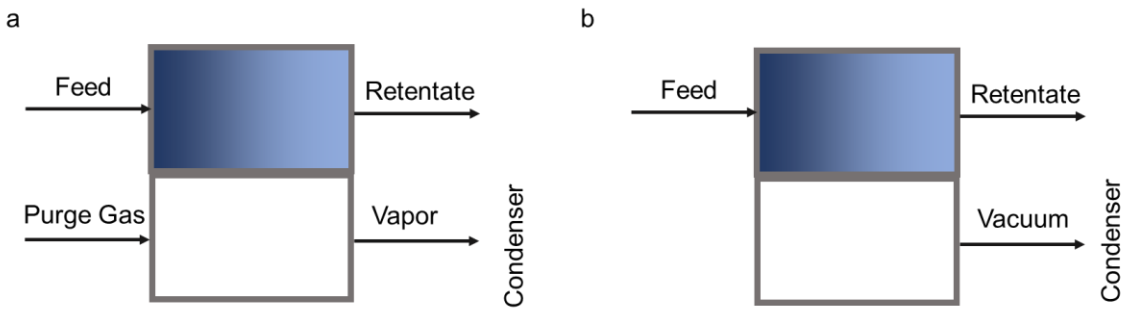

Figure 1.1. Simplified scheme for pervaporation with (a) inert gas purging and (b) vacuum.

Mature pervaporation applications can be sorted into three categories: (1) organic solvent dehydration, (2) dilute organic impurity removal from aqueous solutions, (3) organic mixture separation [12,13]. While pervaporation involves phase changes, it is less energy-intensive compared with traditional thermal-driven separation processes such as distillation when it is designed for selective transportation of the minor components (e.g., < 10 wt.%) in the mixture. For example, state-of-the-art distillation of isopropanol/water (90/10) mixtures can achieve the single plate isopropanol/water separation factor up to 2. As a comparison, the separation factor provided by a pervaporation unit ranges from 2000 to 10000 [14]. However, it is difficult to design the pervaporation membrane to preferentially remove minor components, *ortho*-xylene and *meta*-xylene, from the *para*-xylene-rich stream. Owing to the smaller molecule size, *para*-xylene usually exhibits higher diffusivity than the other xylene isomers. As a result, the high energy penalty for the *para*-xylene phase change cannot be avoided.

While significant research into the pervaporation of xylene isomers has been conducted, existing membranes exhibit low permeance and utilize form factors that likely

cannot be easily commercialized. Generally, pervaporation is a convenient benchmark tool for membrane development. However, it is not attractive to process a large number of xylene isomers via pervaporation.

1.3.2 Organic solvent reverse osmosis

Unlike pervaporation, which involves a phase change across the membrane, organic solvent reverse osmosis (OSRO) directly processes liquid organic solvents without requiring a phase change from the feed to permeate sides of the membrane [15]. OSRO is a fully chemical potential driven process. Successful OSRO relies on the development of stable, scalable, and selective membranes to separate organic solvent molecules with minimal size differences (e.g., xylene isomers). Microporous materials with rigid and tunable pores are viewed as promising materials to differentiate molecules with similar sizes. The confinement of guests within the micropores can significantly influence the diffusion properties of these molecules, which results in different permeation rates [16]. Figure 1.2 illustrates a simplified scheme for OSRO. Without vaporization, the organic solvent mixture is directly pressurized at the feed side of the membrane contactor. The molecules with fast permeance are collected at the other side of the membrane, while the rest of the mixture is collected as the retentate.

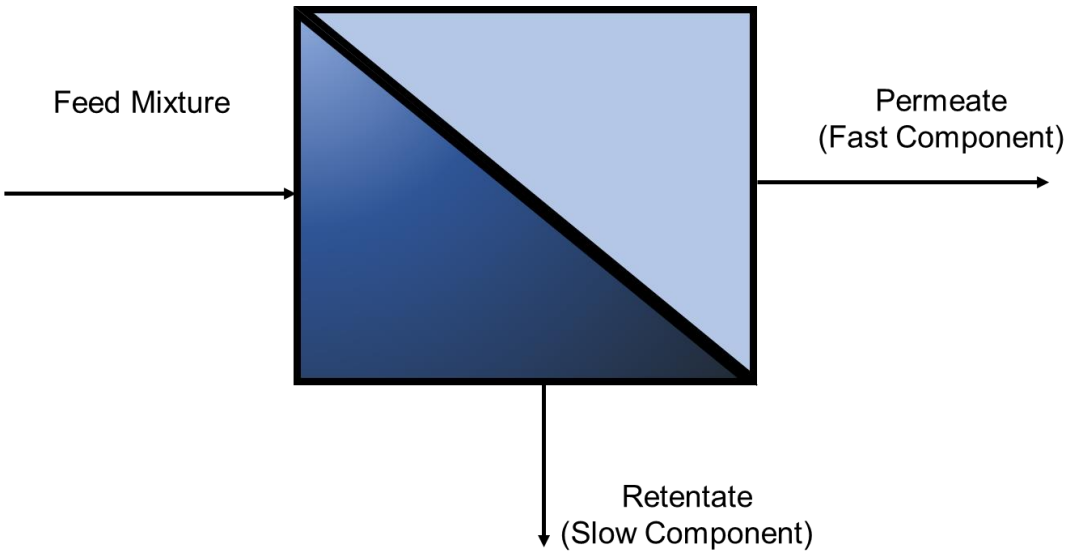

Figure 1.2. Simplified scheme of organic solvent reverse osmosis.

CMS membranes will not swell or plasticize significantly under organic solvents environment, which is a common problem with polymer membranes. This outstanding chemical and thermal stability of CMS membranes suggests that CMS membranes have the potential to enable organic solvent reverse osmosis separations. Previous work has described the successful formation of free-standing CMS membranes with a diffusion selectivity up to 30 for *para*/*ortho*-xylene isomers by pyrolysis of cross-linked porous poly(vinylidene fluoride) (PVDF) hollow fibers [15].

1.4 Research Objectives

While the reported PVDF-derived CMS membranes show promising xylene separation performance, the fundamental mass transfer and separation mechanism was not clear [15]. The overarching goal of this thesis is to provide an in-depth investigation of the

carbon molecular sieve membrane for xylene isomer separation. Three objectives were established to achieve this goal:

1. *Developing advanced carbon molecular sieve membranes*

Energy-efficiency membrane-based xylene separation relies on membranes with high stability, high selectivity, and high permeance. CMS membranes were developed in this thesis as a next-generation organic solvent reverse osmosis platform. Here, polymers of intrinsic microporosity (PIM) were used as a precursor for CMS membrane fabrication. The xylene separation performance of the resulting membranes was evaluated with the Wicke-Kallenbach xylene vapor permeation test and liquid-phase OSRO test.

2. *Manipulating the ultramicropores of carbon molecular sieves*

The CMS pore structures must be carefully manipulated to develop high-performance CMS membranes. An ideal CMS membrane is expected to possess ultramicropores with a diameter of around 5-6 Å to successfully differentiate xylene isomers. Most of the CMS membranes in the literature are developed for gas mixture separation with ultramicropores smaller than 4 Å, which is not suitable for xylene separation. In this thesis, two methods will be used to create well-defined “mid-sized” ultramicropores. First, polymers with intrinsic micropores and rigid polymer backbones were used to hinder the pore collapsing during pyrolysis. Second, a reactive gas, hydrogen, was introduced into the pyrolysis system to inhibit the aromatization of the decomposing polymer and ultimately results in the creation of a well-defined bimodal pore network.

3. Developing mass transfer models for organic solvent reverse osmosis

Predicting the mass transfer across the membrane based on the intrinsic properties (e.g., sorption, diffusion, etc.) is important for the development of advanced membranes and separation process modeling. The development of the correct driving force and flux equations for osmotically-moderated, pressure-induced sorption-diffusion transport for CMS membranes was derived.

1.5 Dissertation Organization

This thesis focusses on carbon molecular sieve membranes for xylene isomer separations. After the introduction in Chapter 1, Chapter 2 will provide background knowledge about membrane materials for xylene isomer separations, including zeolites, metal-organic frameworks and carbon molecular sieves, and the transport theory in carbon molecular sieve membranes. In Chapter 3, the materials and experimental methods used in this thesis are provided in detail. In Chapter 4, PIM-1 films are pyrolyzed into CMS membranes using the conventional fabrication method and used for xylene separation. The xylene molecule transfer across the membrane is evaluated using a sorption-diffusion mechanism. The result shows that the ultramicropores of CMS derived from PIM-1 can successfully differentiate xylene isomers, and the xylene selectivity is dominantly contributed by the entropic diffusion selectivity. In Chapter 5, the influence of reactive pyrolysis atmosphere on the CMS formation is investigated. Under hydrogen-included atmosphere, CMS membranes with well-defined “mid-size” ultramicropores are created. The resulting CMS membranes exhibit significantly improved xylene permeability with a small sacrifice of selectivity. To further improve the performance of the CMS membranes,

Chapter 6 utilizes a spirobifluorene-based polymer of intrinsic microporosity (PIM-SBF) as a polymer precursor, which possesses a more stable polymer backbone and better resistance to pore collapsing during pyrolysis. In Chapter 7, the flux equations for osmotically-moderated sorption-diffusion transport across the CMS membranes are derived and verified. Finally, Chapter 8 summarizes the main results of this work and recommends several directions for future research in the field.

1.6 References

1. D. S. Sholl, R. P. Lively. Seven chemical separations: to change the world: purifying mixtures without using heat would lower global energy use, emissions and pollution--and open up new routes to resources. *Nature* **2016**;532(7600):435-438.

2. P. Marchetti, M. F. Jimenez Solomon, G. Szekely, A. G. Livingston. Molecular separation with organic solvent nanofiltration: a critical review. *Chemical Reviews* **2014**;114(21):10735-10806.

3. W. J. Koros, R. P. Lively. Water and beyond: Expanding the spectrum of large‐scale energy efficient separation processes. *AIChE Journal* **2012**;58(9):2624-2633.

4. M. van der Hoeven, Y. Kobayashi, R. Diercks. Technology roadmap: Energy and GHG reductions in the chemical industry via catalytic processes. *International Energy Agency: Paris* **2013**;56.

5. P. M. Lorz, F. K. Towae, W. Enke, R. Jäckh, N. Bhargava, W. Hillesheim. Phthalic acid and derivatives. *Ullmann's encyclopedia of industrial chemistry* **2000**.

6. A. M. Niziolek, O. Onel, C. A. Floudas. Production of benzene, toluene, and xylenes from natural gas via methanol: Process synthesis and global optimization. *AIChE Journal* **2016**;62(5):1531-1556.

7. G. J. Antos, A. M. Aitani. *Catalytic naphtha reforming, revised and expanded*: CRC Press; **2004**.

8. Y. Yang, P. Bai, X. Guo. Separation of Xylene Isomers: A Review of Recent Advances in Materials. *Industrial & Engineering Chemistry Research* **2017**;56(50):14725-14753.

9. D. Farrusseng. *Metal-organic frameworks: applications from catalysis to gas storage*: John Wiley & Sons; **2011**.

10. A. Torres‐Knoop, R. Krishna, D. Dubbeldam. Separating xylene isomers by commensurate stacking of p‐xylene within channels of MAF‐X8. *Angewandte Chemie International Edition* **2014**;53(30):7774-7778.

11. X. Feng, R. Y. Huang. Liquid separation by membrane pervaporation: a review. *Industrial & Engineering Chemistry Research* **1997**;36(4):1048-1066.

12. P. Shao, R. Huang. Polymeric membrane pervaporation. *Journal of Membrane Science* **2007**;287(2):162-179.

13. B. Smitha, D. Suhanya, S. Sridhar, M. Ramakrishna. Separation of organic–organic mixtures by pervaporation-a review. *Journal of Membrane Science* **2004**;241(1):1-21.

14. P. D. Chapman, T. Oliveira, A. G. Livingston, K. Li. Membranes for the dehydration of solvents by pervaporation. *Journal of Membrane Science* **2008**;318(1-2):5-37.

15. D.-Y. Koh, B. A. McCool, H. W. Deckman, R. P. Lively. Reverse osmosis molecular differentiation of organic liquids using carbon molecular sieve membranes. *Science* **2016**;353(6301):804-807.

16. M. L. Jue, D.-Y. Koh, B. A. McCool, R. P. Lively. Enabling widespread use of microporous materials for challenging organic solvent separations. *Chemistry of Materials* **2017**;29(23):9863-9876.

CHAPTER 2. **BACKGROUND AND THEORY**[*]

2.1 Overview

This chapter provides background and theory to this dissertation. An overview of the membrane materials for xylene isomer separation is included in Section 2.2. Section 2.3 provides the fundamental membrane transport theory, including permeation, sorption, and diffusion. Moreover, the enthalpic and entropic contributions to diffusion selectivity are summarized in Section 2.3.

2.2 Membrane Materials for Xylene Isomer Separations

2.2.1 Zeolites

Zeolites are crystalline hydrated aluminosilicates with a periodic arrangement of nanopores (4-13 Å in diameter). Zeolite frameworks are formed by T atoms (primarily Si and Al) in tetrahedral coordination linked through oxygen atoms that produce a three-dimensional network defined by channels and cavities of molecular dimensions [1]. Based on their Si/Al ratio, zeolites can be classified into three categories: high-silica zeolites (Si/Al>5), intermediate-silica zeolites (2<Si/Al<5) and low-silica zeolites (1≤Si/Al<2). The pore architectures of the zeolites can be tuned by the introduction of organic molecules, which act as pore filling agents. The Swedish chemist Axel Cronstedt was the first researcher to note that the mineral stilbite appeared to boil when heated and thus named

[*] Parts of this chapter has been published on *Sustainable Nanoscale Engineering* as Chapter 3 - Manufacturing Nanoporous Materials for Energy-Efficient Separations: Application and Challenges, **2020**, 33-81.

this kind of materials zeolites or “boiling stones” in 1756 [2]. Currently, there are more than 200 different zeolite framework types that have been synthesized and accepted by the International Zeolite Association (IZA), which are classified according to the channel system (monodirectional, bidirectional, or three-directional) or to the pore size (small-8-MR, medium-10-MR, large-12-MR, or extra large-12-MR). It should be noted that theoretical estimates suggest that that millions of other zeolite structures can be constructed from the primary building blocks, but only a small fraction of these have proven to be accessible using modern synthetic techniques.

The uniform distribution of well-defined nanopores imbues zeolites with the ability to separate molecules with only minor differences in molecule size (i.e., ~0.1Å differences) and shape (i.e., exquisite ethane/ethylene selectivities have been observed in zeolites). Moreover, zeolites possess excellent thermal and chemical stability, as well as the presence of exchangeable ions (“counter-balancing ions”) within the framework, which enables the guest transport and sorption properties to be tuned. All of these features position zeolites as promising materials for the fabrication of molecular sieving membranes and adsorbents [3,4].

Most zeolites contain nanopores with diameters below 2 nm. Pores less than 2 nm are defined by IUPAC as “micropores.” Such micropores are capable of realizing shape selectivity in separation and catalytic modalities involved in various industries (e.g., petrochemistry) [5,6]. Beyond simply microporous zeolites, there is a drive to develop zeolites with larger pores to increase mass transfer rates into and out of the zeolite structure [7]. Indeed, a significant effort has been made to develop zeolites containing mesopores

(by IUPAC definition, pores with a diameter ranging from 2 nm to 50 nm). Mesopores can be introduced within zeolite crystals during synthesis or post-synthesis by introducing gaps between intergrown zeolite nanocrystals. Intracrystalline mesopores are usually created via demetallization, i.e., leaching out silica or aluminum from zeolite networks [8]. Common dealumination methods are high-temperature steaming and acid leaching, which breaks the Si-O-Al bonds and free aluminum from the zeolite networks. Such a dealumination process results in vacancies or amorphous materials, releasing mobile silicon species. Mobile silicon species tend to migrate and condense at other sites resulting in mesopores. Similarly, desilication can be achieved through base leaching [9]. Intercrystalline mesopores can be created via various zeolite nano-particle assembly methods. Another straightforward method is synthesizing zeolites with mesoporous templates, which can be removed afterword. Such templates can either be hard material (e.g., carbon nanotubes, carbon particles, aerogels, etc.) or soft materials (e.g., surfactants) [9]. Besides, assembly of nanoparticles can also be achieved without expensive mesoporous templates via steam-assisted crystallization, [10-12] solid-phase crystallization, [13] nanofusion [14] and repetitive branching [15].

Zeolites (e.g., FAU, MFI, etc.) have been applied and tested for the separation of C8 alkyl aromatic isomers.[16,17] Especially, polycrystalline zeolite MFI-type membranes have been widely studied in the field of xylene isomers separations, typically using pervaporation or vapor permeation separation modalities [18,19]. For instance, Lai and coworkers optimized the microstructure of ZSM-5 zeolite membranes for xylene pervaporation.[19] The resulting oriented ZSM-5 membranes exhibited *para*-xylene/*ortho*-xylene separation factors as high as 400 with para-xylene permeance as high as 3×10^{-7}

mol/m^2 s Pa. However, the MFI framework can undergo structural distortions upon the adsorption of xylene molecules, especially near ambient temperatures and at high xylene loadings. This distortion can induce the phase change of the MFI crystals from an orthorhombic phase (ORTHO) to a second orthorhombic phase (PARA) that renders the structures unable to distinguish between the xylene isomers and reduces the separation efficiency of the membrane.[20,21] This issue, coupled with low xylene permeances at high fractional occupancies of the guest molecule, suggests that MFI-type zeolite membranes will struggle to provide satisfactory xylene isomer separation at industrially-relevant conditions. Moreover, the requirement of expensive supports and the difficulty of scale-up production [22] acts as further deterrents to the practical application of MFI membranes for xylene separations despite their exceptional performance in the lab. As the demand for xylene isomers is expected to maintain a 5-7% yearly growth [23], it is imperative to develop new, scalable membranes that exhibit promising separation performance under practical operating conditions.

2.2.2 Metal-organic frameworks

Metal-organic frameworks (MOFs) refer to crystalline porous materials formed by metal ions and organic ligands that are connected via coordinative bonds.[24] To date, over 20,000 MOFs have been experimentally reported for various applications that are founded on molecular capture and differentiation (i.e., adsorption, membrane, sensing, catalysis, etc.) [25,26].

MOFs have a variety of tailorable structural characteristics that translate into tunable separation properties. For instance, MOF apertures can be varied from a few

angstroms to several nanometers while maintaining uniform pore size distribution. The resulting molecular sieving effect can be applied for size-selective molecule transportation. This feature suggests that MOFs may be useful for separating molecules with similar size [27-30]. Beyond changes in topology, MOF apertures can be further tuned by mixing linkers of different lengths; it is possible to do this while retaining the topology of the MOF comprised of the starting linker [31,32]. Indeed, the immense number of possible metal-ligand combination possibilities provide a rich design space with access to a variety of topologies and customized functionality. MOF functionality can derive from the organic linkers, the metal nodes/clusters, or both [33]. For example, via changing linkers with different functional groups, BET surface areas of UIO-66 derivates can be tuned from 540 m^2/g to 1580 m^2/g. [34] Mixed-linker hybrid zeolitic imidazolate frameworks were also developed with a tunable gate-opening effect for target separation processes [35]. Besides engineering metal nodes of MOFs, organic linkers can also be tuned via either pre-synthesis or post-synthesis modification [29].

Several MOFs such as MIL-47, MIL-53, BIF-20, UIO-66, etc. have also been investigated in laboratories for organic molecules separation [36-44]. Owing to the versatile structures of MOFs, different MOFs are believed to have different hypothesized separation mechanisms. For instance, the separation xylene isomers achieved by MIL-47 is believed to be contributed by the differences in the packing modes of xylene isomers in nanopores while $Zn(bdc)(dabco)_{0.5}$ accomplishes the separation based on the difference in interactions between xylene isomers and the adsorbents [38,44].

Several reports have been published using MOF-based membranes for xylene separations. Kasik and coworkers developed MOF-5 membranes for xylene pervaporation [45]. According to their report, continuous MOF-5 membranes fabricated via a solvothermal method exhibited an ideal separation factor of 2.2 for *para*-xylene over *ortho*-xylene. Although such a low separation factor is not suitable for a real application, this preliminary research provides a good example of MOF-based membrane design for xylene separation. Unfortunately, the crystalline MOF-based membrane materials require expensive supports and are difficult to produce in a defect-free fashion at scales larger than those found in laboratories [45]. Considering the importance of this separation, there is a strong driving force to develop new, scalable membranes that exhibit promising separation performance under practical operating conditions.

2.2.3 Carbon molecular sieves

Carbon molecular sieves (CMSs), a type of nanoporous materials, are produced via the pyrolysis or carbonization of a polymeric, well-defined, and carbonaceous precursor under controlled temperature and atmosphere.[46,47] Often thought of as an inorganic material, CMS structures have excellent thermal and chemical stability in comparison with the starting polymer precursors. Most CMS materials are believed to possess a turbostratic lamellar structure resulting in an amorphous, isotropic, and microporous material. The carbon lamellae contain condensed hexagonal carbon sheets, which exhibit short-range order via the alignment of the sheets parallel to each other but with a random rotational angle. The basic structural units of the CMS are believed to comprise a kinetically trapped array of plates formed from carbonaceous strands created during aromatization and

fragmentation of the precursor backbone, as shown in Figure 2.1 [48]. Over the long-range, these lamellae arrange randomly, bend and twist to form an amorphous structure.

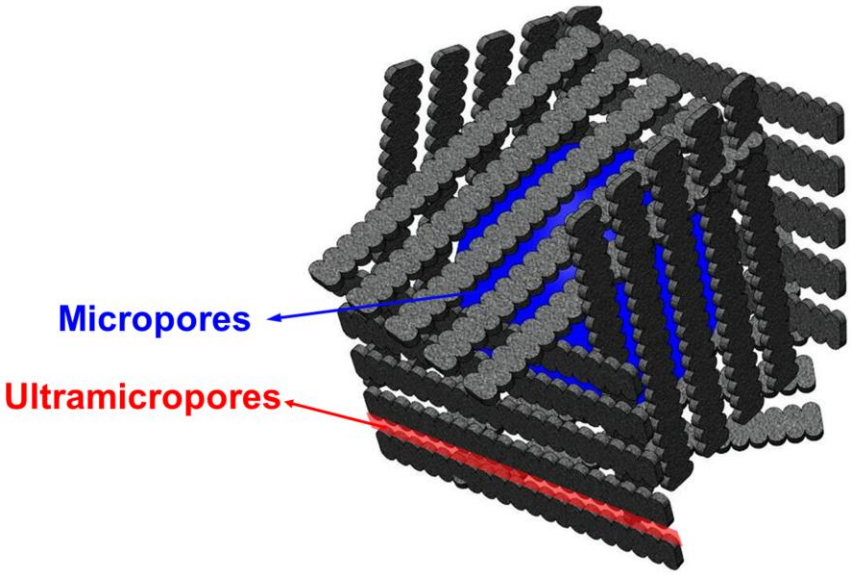

Figure 2.1 Hypothetical short-range turbostratic carbon structure of the CMS membranes.

A simplified, idealized pore structure of CMS materials can be described as a "slit-like" bimodal pore model, as shown in Figure 2.2 [49-51]. CMS is distinct from activated carbon; the former has a well-defined narrow pore size distribution, whereas the latter as a broad pore size distribution ranging from microporous to microporous [52,53]. This bimodal pore size distribution with larger micropores connected by smaller ultramicropores derives from packing imperfections of the carbon sheets. Ultramicropores enable molecular sieving, while micropores provide abundant sorption sites. This combination allows CMS membranes to sustain high permeability and high selectivity at the same time, which is attractive for separations [54].

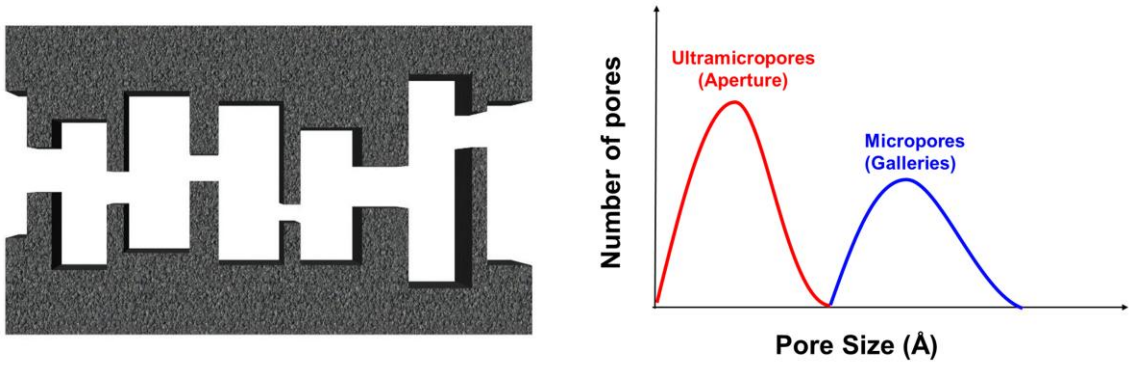

Figure 2.2 Hypothetical bimodal distribution of pores in CMS membranes [55].

CMS membranes are fabricated by the pyrolysis of polymer precursor materials under a controlled environment. The carbonization process is quite complex and intricate, and several reactions may take place at the same time, such as cleavage, dehydrogenation, condensation, isomerization, etc.[56,57] Even though the pyrolysis process by which a polymer precursor is transformed into a CMS material is complex, it results in the reproducible production of carbon materials when pyrolysis conditions are carefully controlled. One proposed mechanism of translation of a polymer coil into rigid carbon molecular sieve membranes under inert atmosphere (non-vacuum) was firstly proposed by Koros and co-workers.[55,58,59] Figure 2.3 illustrated the transformation of PIM-1 to CMS according to this hypothesis.[60] In this theory, CMS materials are believed to be comprised of aromatized strands arranged to form plates, which are further organized into amorphous cellular structures. The narrow slits (typically < 7 Å) between aromatized strands are the ultramicropores, which enable precise angstrom-level discrimination between molecules and are related to the sieving effect of the membrane. The voids (typically between 7 Å to 20 Å) generated from imperfect packing of the carbon plates are

believed to be the micropores that provide abundant sorption sites for penetrant molecules. The transformation from a polymer coil to CMS structure is achieved over the course of three periods: thermal ramp, thermal soak, and cooling. During the thermal ramp process, a highly aromatic strand type structure forms because of the aromatization of the polymer and the evolution of volatiles, as illustrated in Figure 2.3 (i) and (ii). Aromatized strands will then be further aligned into plates driven by entropy to avoid the presence of excluded volume, shown in Figure 2.3 (iii) and (iv). The thermal soak and cooling process collate multiple neighboring cells, resulting in the sharing of ultramicropore "walls" between cells, as illustrated in Figure 2.3 (v).

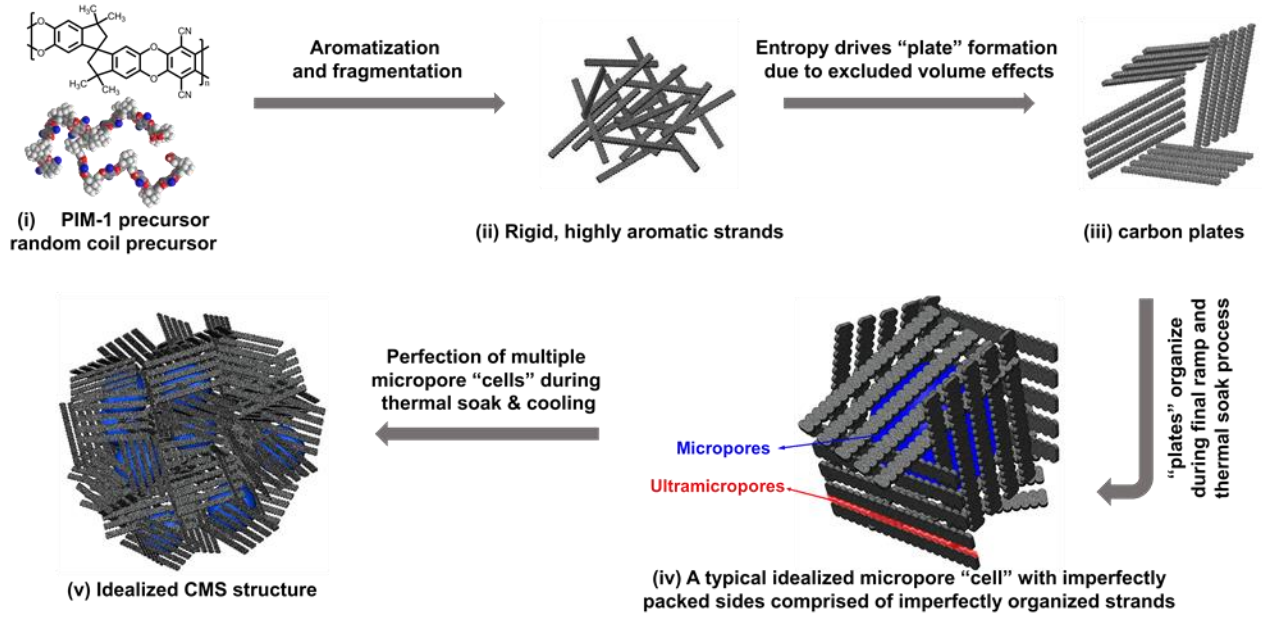

Figure 2.3 Envisioned steps in the transformation from a precursor polymer to organized amorphous CMS material [60].

The performance of CMS membranes is mainly determined by the pore size distribution (i.e., the pore size in the skin layer of the asymmetric membrane). Several parameters play crucial roles in affecting the structural properties and pore sizes of carbon membrane and further enhancing the separation performance of the CMS membrane, such as the starting polymer precursor, pre-treatment conditions, pyrolysis conditions, and post-treatment conditions [55,61,62].

The choice of the polymeric precursor is the first important factor since the pyrolysis of different precursors may bring about different kinds of carbon membranes. Suitable polymer precursors for CMS membranes should firstly not melt or flow before or during pyrolysis conditions [63]. Numerous thermosetting precursors have been used to form carbon membranes, such as polyimide and derivatives, [64,65] polyacrylonitrile (PAN), [66,67] phenolic resin, [68,69] polyfurfuryl alcohol (PFA), [70,71] polyvinylidene chloride-acrylate terpolymer (PVDC-AC), phenol formaldehyde, cellulose derivatives, [63] polymer of intrinsic micropores, [67,72] and others. The intrinsic properties of the starting polymer precursor such as fractional free volume (FVV), chain mobility, chain structure, and glass transition temperature have significant effects on the performance of the resulting CMS membranes [73,74]. The studies by Williams [75] and Park [76] showed that the increase of FVV in the polyimides precursor would lead to a higher permeability in the resulting CMS membranes. The choice of the starting polymer is critical for the fabrication of CMS membranes that will be used to solve specific separation problems.

To ensure the stability of the precursor and preserve its structure to some degree during the pyrolysis process, the polymer precursor is often pre-treated before pyrolysis.

Thermostabilization and pre-oxidation are one of the most commonly used pre-treatment methods. For example, Kusuki et al. found that the hollow fiber precursors based on biphenyl-tetracarboxylic acid dianhydride (BPDA) and aromatic diamines will not soften or collapse during pyrolysis after heated in air at 400 °C for 30 min before pyrolysis [77]. David and Ismail also found that the stability of the PAN hollow fiber precursor would be improved after the pretreatment in air or oxygen at 250 °C for 30 min before pyrolysis. A non-solvent chemical agent is another method for pre-treatment of the polymer precursors [66]. Jue et al. found that the non-solvent pre-treatment will weaken the intermolecular interactions, allow structural rearrangement of carbon chains, lead to smaller pore size and higher selectivity of the CMS membranes [78]. It is worth noting that all the pre-treatment methods need to be optimized for different polymer precursors, which will be further transformed into CMS membranes for specific separation jobs.

Besides using different polymeric precursors, the specific pyrolysis conditions also offer additional tools to tailor the structure of CMS membranes such as final pyrolysis temperature, heating rate, soak time at final pyrolysis temperature, and pyrolysis environment. The final pyrolysis temperature is always chosen based on the decomposition and graphitization temperature of the polymeric precursor. Higher final pyrolysis temperature will lead to smaller ultramicropore and micropores inside the CMS membranes, and lower diffusion coefficient and permeability; however, larger diffusion selectivity and permselectivity are also often observed [79,80]. Koros and coworkers found that the 6FDA/BPDA-DAM-derived CMS membranes produced under vacuum pyrolysis environment showed higher selectivity than those pyrolyzed under inert atmosphere [81,82]. For example, polyimide precursor derived CMS membranes produced using a

vacuum pyrolysis at 550 °C showed higher gas separation selectivities (7.4-9.0 for O_2/N_2 and 64-110 H_2/N_2) than those produced in argon (2.8-6.1 for O_2/N_2 and 6.8-31.2 H_2/N_2) or helium (4.7-6.1 for O_2/N_2 and 15.2-35.7 H_2/N_2) atmospheres at the same temperature [81]. This change of selectivity might be due to the different mechanisms of the carbonization reaction by varying the type pf pyrolysis atmosphere [81]. It has been shown that the activation energy of degradation decreased as the pressure of the inert pyrolysis atmosphere increased [83,84]. That is to say, the polyimide degradation process was "enhanced" when an inert gas was used. By accelerating the carbonization reaction, the inert gas pyrolysis environment appeared to produce a more "open" porous matrix in the CMS membranes resulting in a higher permeability and less selective pore structure [81,82]. Studies by Williams [64] and Kiyono et al. [82] showed that even trace amounts of oxygen in the pyrolysis environment could significantly affect the performance of the CMS membrane. The oxygen in the inert pyrolysis gas will selectively chemisorb in the ultramicroporous regions within the CMS. Intentional O_2 doping of the edges of the ultramicroporous slits has been successfully utilized to fine-tune the diffusion selectivity. The optimum O_2 doping level varies with the separation target and CMS membrane. For example, over doping of oxygen (30 ppm) result in loss of productivity and selectivity [82]. Suda and Haraya found that the smaller heating rate during pyrolysis would lead to smaller pores and lower permeability, but higher selectivity [46]. Finally, soak time at the final pyrolysis temperature promotes pore sintering, thus increasing selectivity and decreasing the permeability of the resulting CMS membranes.

Several post-treatment methods such as post-oxidation, chemical vapor deposition, and coating could be used to further fine-tune the pore size distribution or repair cracks and

defects inside the CMS membrane after pyrolysis. Soffer et al. found that the permeability of cellulose-derived CMS membranes increases significantly after post-treated in the air at 400 °C for 15 min [85]. Hayashi post-treated the BPDA-ODA derived CMS membranes by chemical vapor deposition using a propylene carbon source at 650 °C, which narrowed the pore size and increased the selectivity of the CMS membranes.

2.3 Membrane Transport Theory

2.3.1 Permeation, sorption, and diffusion

The intrinsic transport properties of sorption-diffusion type membranes are described by two main parameters: "permeability", a measurement of intrinsic productivity, and "selectivity", α a measurement of separation efficiency. Permeability ($\mathbb{P}_A$), is equal to the transmembrane fugacity and thickness normalized flux:

$$\mathbb{P}_A = \frac{N_A \ell}{\Delta f_A} \qquad \textbf{Eq. 2.1}$$

Where N_A is the penetrant flux through the membrane of a thickness of ℓ under a transmembrane fugacity difference of Δf_A. For homogeneous dense membranes, the membrane thickness (ℓ) can be measured directly. However, in the case of the asymmetric membrane, the actual membrane thickness is not readily known. Thus, the term of permeance, which is simply the fugacity-normalized flux, is commonly used to describe the productivity as defined below:

$$\frac{\mathbb{P}_A}{\ell} = \frac{N_A}{\Delta f_A} \qquad \textbf{Eq. 2.2}$$

In the sorption-diffusion transport mechanism, guest molecules sorb into the upstream side of the membrane, and diffuse through it due to the presence of a chemical potential gradient, and desorb at the downstream side. The permeability can be expressed as the product of D_A, named the transport diffusion coefficient, and $\mathbb{S}_A$, named the solubility or sorption coefficient.

$$\mathbb{P}_A = D_A \times \mathbb{S}_A \qquad \textbf{Eq. 2.3}$$

Sorption coefficient, $\mathbb{S}_A$, is a thermodynamic factor governed primarily by the condensability of a gas penetrant and the membrane-penetrant interaction. Diffusion coefficient, D_A, is a kinetic property, related to the ability of a guest molecule to jump within the membrane. Figure 2.4 shows a schematic of guest molecules permeation through a membrane to illustrate this process.

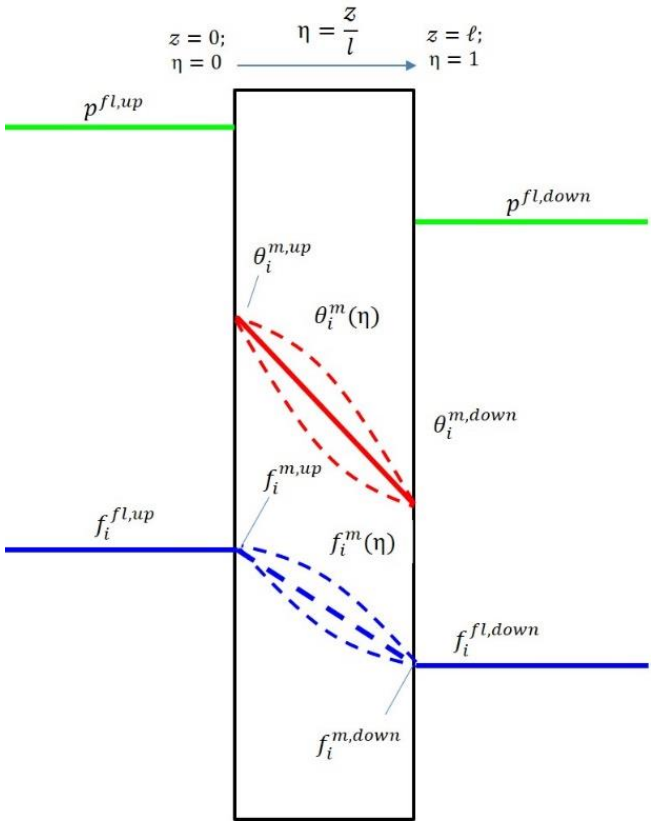

Figure 2.4 Schematic of guest molecules permeation through a membrane.

The ideal permselectivity for guest molecule A vs. B, α_{AB}, reflects the separation efficiency of the membrane and is defined as the ratio of the permeability of the fast component to the slow component. Moreover, the selectivity can be further defined using the sorption-diffusion model as the product of the diffusive selectivity D_A/D_B and sorptive selectivity $\mathbb{S}_A/\mathbb{S}_B$.

$$\alpha_{AB} = \frac{\mathbb{P}_A}{\mathbb{P}_B} = \left(\frac{D_A}{D_B}\right) \times \left(\frac{\mathbb{S}_A}{\mathbb{S}_B}\right) \qquad \textbf{Eq. 2.4}$$

2.3.2 Temperature dependence of permeation, sorption, and diffusion

Permeation and diffusion of guest molecules across microporous membranes are accurately described as activated processes. The activation energies of permeation and diffusion follow Arrhenius relationships, while sorption can be described by a Van't Hoff expression [86,87].

$$\mathbb{P}_A = \mathbb{P}_{0A}\exp\left(\frac{-E_{\mathbb{P},A}}{RT}\right) \quad \textbf{Eq. 2.5}$$

$$D_A = D_{0A}\exp\left(\frac{-E_{D,A}}{RT}\right) \quad \textbf{Eq. 2.6}$$

$$\mathbb{S}_A = \mathbb{S}_{0A}\exp\left(\frac{-\Delta H_{\mathbb{S},A}}{RT}\right) \quad \textbf{Eq. 2.7}$$

R is the universal gas constant, T is the absolute temperature and $\mathbb{P}_{0A}$, $D_{0A}$and $\mathbb{S}_{0A}$ are pre-exponential factors of permeation, diffusion, and sorption, respectively. $E_{\mathbb{P},A}$ is the activation energy for permeation, $E_{D,A}$ is the activation energy for diffusion and $\Delta H_{\mathbb{S},A}$ is the apparent heat of sorption, which is always negative.

Rearrangement of Eq. 2.3 and Eq. 2.5-Eq. 2.7 reveals that activation energy for permeation is the combination of activation energy for diffusion and apparent heat of sorption. Moreover, the pre-exponential factors of permeation are the product of that for diffusion and sorption.

$$\mathbb{P}_{0A} = D_{0A} \times \mathbb{S}_{0A} \quad \textbf{Eq. 2.8}$$

$$E_{\mathbb{P},A} = E_{D,A} + \Delta H_{\mathbb{S},A} \qquad \textbf{Eq. 2.9}$$

2.3.3 Enthalpic ad entropic contributions to diffusion selectivity

The Eyring-Polanyi equation is shown in Eq. 2.10 [88].

$$D_A = \lambda^2 \frac{k_B T}{h} exp\,(\frac{S_{D,A}}{R}) exp\,(\frac{-H_{D,A}}{RT}) \qquad \textbf{Eq. 2.10}$$

where $\frac{k_B T}{h}$ is the universal frequency factor with Boltzmann's constant k_B, absolute temperature T and Planck's constant h. λ is the average diffusive jump length in the membrane, which may be treated equivalent for xylene isomers since the jump length for molecules with similar kinetic diameters to access rigid pores should be the same. $S_{D,A}$ is the activation entropy for diffusion. It is important to note that "S_D" used for entropy here is different from the "$\mathbb{S}_A$" used for the sorption coefficient. By assuming negligible volume change during the diffusion process (when calculating the diffusion selectivity, this assumption is no longer necessary), the activation enthalpy of diffusion $H_{D,A}$ can be expressed as below:

$$H_{D,A} = E_{D,A} + PV \approx E_{D,A} + RT \qquad \textbf{Eq. 2.11}$$

Combining Eq. 2.10 and Eq. 2.11, one can get,

$$D_A = e\lambda^2 \frac{k_B T}{h} exp\,(\frac{S_{D,A}}{R}) exp\,(\frac{-E_{D,A}}{RT}) \qquad \textbf{Eq. 2.12}$$

Similarly, we can write this equation for guest molecule B,

$$D_B = e\lambda^2 \frac{k_B T}{h} exp\,(\frac{S_{D,B}}{R}) exp\,(\frac{-E_{D,B}}{RT}) \qquad \textbf{Eq. 2.13}$$

By combining Eq. 2.12 and Eq. 2.13, one can see that the diffusion selectivity between guest molecule A and B can be expressed in terms of an activation energies for diffusion, but this activation energy clearly originates from the enthalpic contribution to diffusion as shown in Eq. 2.11. Koros and coworkers have utilized transition state theory to decouple the diffusion selectivity into an enthalpic contribution and an entropic contribution [79] as shown in Eq. 2.14.

$$\frac{D_A}{D_B} = exp\,(-\frac{E_{D,A} - E_{D,B}}{RT}) exp\,(\frac{S_{D,A} - S_{D,B}}{R}) \qquad \textbf{Eq. 2.14}$$

where R is the universal gas constant, and T is the absolute temperature. $E_{D,A}$ and $E_{D,B}$ are the diffusion activation energies for guest molecules A and B, respectively. $S_{D,A}$ and $S_{D,B}$ are the diffusion activation entropies for guest molecules A and B, respectively. It is important to note that the "$S_{D,A}$" used for entropy here is different from the "$\mathbb{S}_A$" used for the sorption coefficient. It is worth noting that the activation enthalpy of diffusion $H_{D,A}$ can be expressed as the activation energy for diffusion $E_{D,A} + RT$ assuming negligible volume change during the diffusion process, while the RT terms for both A & B end up as an "e" multiplier, which can be essentially canceled out when taking the ratio of the two diffusivities. Moreover, considering that the diffusion Arrhenius relationship contains $E_{D,A}$ rather than $H_{D,A}$, it will be easier to use $E_{D,A}$ for the final enthalpic diffusion selectivity calculation.

On the one hand, the "enthalpic diffusion selectivity" generally captures the part of the relative difficulty of diffusive "displacements" associated with differences in activation energies or enthalpies. On the other hand, the entropic diffusion selectivity describes the relative difficulty of diffusion displacements associated with differences in diffusion activation entropies of the two penetrants. Such entropic activation differences arise in the rigid pore structure of the carbon membrane, which provides constraints on the degrees of freedom for molecules in the "activated" diffusion state (i.e., in the ultramicropores) [79]. The entropic diffusion selectivity tends to be dependent on the shape, rather than only the molecular volume. Such an entropic feature provides the ability to separate isomers by affecting the relative difference in the frequency of successful displacements [79]. It is worth noting that, due to the larger thermal fluctuations in polymer backbones (relative to thermal fluctuations of a highly rigid CMS), polymeric membrane materials do not effectively discriminate based on configurational differences of diffusing molecules [89]. The significance of entropic diffusion selectivity for rigid membranes in the area of gas separations such as CO_2/CH_4, O_2/N_2, or N_2/CH_4 has been previously discussed in the literature [90-93], and these studies have concluded that entropic diffusion selectivity is the critical enabler for challenging separations where sub-Angstrom differences in the molecular pair exist. In the current work, we conduct an experimental campaign to develop a fundamental understanding of xylene isomer transport in CMS membranes and to determine whether entropic diffusion selectivity can be realized for large organic molecules permeating through CMS materials.

2.4 References

1. D. Breck. Zeolite Molecular Sieves Wiley, New York. *Google Scholar* **1974**.

2. A. Cronstedt. Observation and description of an unknown kind of rock to be named zeolites. *Kongl Vetenskaps Acad Handl Stockh* **1756**;17:120-123.

3. N. Kosinov, J. Gascon, F. Kapteijn, E. J. Hensen. Recent developments in zeolite membranes for gas separation. *Journal of Membrane Science* **2016**;499:65-79.

4. M. A. Snyder, M. Tsapatsis. Hierarchical Nanomanufacturing: From Shaped Zeolite Nanoparticles to High‐Performance Separation Membranes. *Angewandte Chemie International Edition* **2007**;46(40):7560-7573.

5. A. Corma. Inorganic solid acids and their use in acid-catalyzed hydrocarbon reactions. *Chemical Reviews* **1995**;95(3):559-614.

6. J. Weitkamp. Zeolites and catalysis. *Solid State Ionics* **2000**;131(1-2):175-188.

7. D. Zhao, J. Feng, Q. Huo, N. Melosh, G. H. Fredrickson, B. F. Chmelka, G. D. Stucky. Triblock copolymer syntheses of mesoporous silica with periodic 50 to 300 angstrom pores. *science* **1998**;279(5350):548-552.

8. S. Van Donk, A. H. Janssen, J. H. Bitter, K. P. de Jong. Generation, characterization, and impact of mesopores in zeolite catalysts. *Catalysis Reviews* **2003**;45(2):297-319.

9. Y. Wei, T. E. Parmentier, K. P. de Jong, J. Zečević. Tailoring and visualizing the pore architecture of hierarchical zeolites. *Chemical Society Reviews* **2015**;44(20):7234-7261.

10. K. Möller, B. Yilmaz, R. M. Jacubinas, U. Müller, T. Bein. One-step synthesis of hierarchical zeolite beta via network formation of uniform nanocrystals. *Journal of the American Chemical Society* **2011**;133(14):5284-5295.

11. C. Li, Y. Wang, B. Shi, J. Ren, X. Liu, Y. Wang, Y. Guo, Y. Guo, G. Lu. Synthesis of hierarchical MFI zeolite microspheres with stacking nanocrystals. *Microporous and Mesoporous Materials* **2009**;117(1-2):104-110.

12. G. Majano, S. Mintova, O. Ovsitser, B. Mihailova, T. Bein. Zeolite Beta nanosized assemblies. *Microporous and Mesoporous Materials* **2005**;80(1-3):227-235.

13. L. H. Chen, X. Y. Li, G. Tian, Y. Li, J. C. Rooke, G. S. Zhu, S. L. Qiu, X. Y. Yang, B. L. Su. Highly Stable and Reusable Multimodal Zeolite TS‐1 Based Catalysts with Hierarchically Interconnected Three‐Level Micro–Meso–Macroporous Structure. *Angewandte Chemie International Edition* **2011**;50(47):11156-11161.

14. K. Möller, B. Yilmaz, U. Müller, T. Bein. Nanofusion: mesoporous zeolites made easy. *Chemistry–A European Journal* **2012**;18(25):7671-7674.

15. X. Zhang, D. Liu, D. Xu, S. Asahina, K. A. Cychosz, K. V. Agrawal, Y. Al Wahedi, A. Bhan, S. Al Hashimi, O. Terasaki. Synthesis of self-pillared zeolite nanosheets by repetitive branching. *Science* **2012**;336(6089):1684-1687.

16. M. Guisnet, J.-P. Gilson. *Zeolites for cleaner technologies.* Vol 3: Imperial College Press London; **2002**.

17. G.-Q. Guo, H. Chen, Y.-C. Long. Separation of p-xylene from C8 aromatics on binder-free hydrophobic adsorbent of MFI zeolite. I. Studies on static equilibrium. *Microporous and Mesoporous Materials* **2000**;39(1-2):149-161.

18. D. Kim, M. Y. Jeon, B. L. Stottrup, M. Tsapatsis. para ‐ Xylene Ultra ‐ selective Zeolite MFI Membranes Fabricated from Nanosheet Monolayers at the Air–Water Interface. *Angewandte Chemie International Edition* **2018**;57(2):480-485.

19. Z. Lai, G. Bonilla, I. Diaz, J. G. Nery, K. Sujaoti, M. A. Amat, E. Kokkoli, O. Terasaki, R. W. Thompson, M. Tsapatsis. Microstructural optimization of a zeolite membrane for organic vapor separation. *Science* **2003**;300(5618):456-460.

20. M. Daramola, A. Burger, M. Pera-Titus, A. Giroir-Fendler, L. Lorenzen, J.-A. Dalmon. Xylene vapor mixture separation in nanocomposite MFI-alumina tubular membranes: Influence of operating variables. *Separation Science and Technology* **2009**;45(1):21-27.

21. G. Xomeritakis, S. Nair, M. Tsapatsis. Transport properties of alumina-supported MFI membranes made by secondary (seeded) growth. *Microporous and Mesoporous Materials* **2000**;38(1):61-73.

22. J. Gascon, F. Kapteijn, B. Zornoza, V. Sebastian, C. Casado, J. Coronas. Practical approach to zeolitic membranes and coatings: state of the art, opportunities, barriers, and future perspectives. *Chemistry of Materials* **2012**;24(15):2829-2844.

23. Y. Khabzina, C. Laroche, J. Perez-Pellitero, D. Farrusseng. Xylene separation on a diverse library of exchanged faujasite zeolites. *Microporous and Mesoporous Materials* **2017**;247:52-59.

24. A. U. Czaja, N. Trukhan, U. Müller. Industrial applications of metal–organic frameworks. *Chemical Society Reviews* **2009**;38(5):1284-1293.

25. H. Furukawa, K. E. Cordova, M. O'Keeffe, O. M. Yaghi. The chemistry and applications of metal-organic frameworks. *Science* **2013**;341(6149):1230444.

26. L. E. Kreno, K. Leong, O. K. Farha, M. Allendorf, R. P. Van Duyne, J. T. Hupp. Metal–organic framework materials as chemical sensors. *Chemical Reviews* **2011**;112(2):1105-1125.

27. X. Zhao, Y. Wang, D. S. Li, X. Bu, P. Feng. Metal–Organic Frameworks for Separation. *Advanced Materials* **2018**;30(37):1705189.

28. J.-R. Li, J. Sculley, H.-C. Zhou. Metal–organic frameworks for separations. *Chemical Reviews* **2011**;112(2):869-932.

29. S. Kitagawa. Metal–organic frameworks (MOFs). *Chemical Society Reviews* **2014**;43(16):5415-5418.

30. S. Qiu, M. Xue, G. Zhu. Metal–organic framework membranes: from synthesis to separation application. *Chemical Society Reviews* **2014**;43(16):6116-6140.

31. W. Kleist, F. Jutz, M. Maciejewski, A. Baiker. Mixed‐Linker Metal‐Organic Frameworks as Catalysts for the Synthesis of Propylene Carbonate from Propylene Oxide and CO2. *European Journal of Inorganic Chemistry* **2009**;2009(24):3552-3561.

32. H. Deng, C. J. Doonan, H. Furukawa, R. B. Ferreira, J. Towne, C. B. Knobler, B. Wang, O. M. Yaghi. Multiple functional groups of varying ratios in metal-organic frameworks. *Science* **2010**;327(5967):846-850.

33. P. Deria, J. E. Mondloch, O. Karagiaridi, W. Bury, J. T. Hupp, O. K. Farha. Beyond post-synthesis modification: evolution of metal–organic frameworks via building block replacement. *Chemical Society Reviews* **2014**;43(16):5896-5912.

34. M. J. Katz, Z. J. Brown, Y. J. Colón, P. W. Siu, K. A. Scheidt, R. Q. Snurr, J. T. Hupp, O. K. Farha. A facile synthesis of UiO-66, UiO-67 and their derivatives. *Chemical Communications* **2013**;49(82):9449-9451.

35. J. A. Thompson, C. R. Blad, N. A. Brunelli, M. E. Lydon, R. P. Lively, C. W. Jones, S. Nair. Hybrid zeolitic imidazolate frameworks: controlling framework porosity and functionality by mixed-linker synthesis. *Chemistry of Materials* **2012**;24(10):1930-1936.

36. V. Finsy, C. E. Kirschhock, G. Vedts, M. Maes, L. Alaerts, D. E. De Vos, G. V. Baron, J. F. Denayer. Framework Breathing in the Vapour‐Phase Adsorption and Separation of Xylene Isomers with the Metal‐Organic Framework MIL‐53. *Chemistry-A European Journal* **2009**;15(31):7724-7731.

37. R. Lyndon, J. Bacsa, M. L. Jue, R. P. Lively. Direct Structural Evidence of Molecular Packing Effects of Xylene Isomers Adsorbed in BIF-20. *Crystal Growth & Design* **2018**.

38. V. Finsy, H. Verelst, L. Alaerts, D. De Vos, P. A. Jacobs, G. V. Baron, J. F. Denayer. Pore-Filling-Dependent Selectivity Effects in the Vapor-Phase Separation of Xylene Isomers on the Metal− Organic Framework MIL-47. *Journal of the American Chemical Society* **2008**;130(22):7110-7118.

39. C. Serre, F. Millange, C. Thouvenot, M. Nogues, G. Marsolier, D. Louër, G. Férey. Very Large Breathing Effect in the First Nanoporous Chromium (III)-Based Solids: MIL-53 or Cr^{III} (OH)·{$O_2C-C_6H_4-CO_2$}·{$HO_2C-C_6H_4-CO_2H$}$_x$·H_2O_y. *Journal of the American Chemical Society* **2002**;124(45):13519-13526.

40. M. A. Moreira, J. o. C. Santos, A. F. Ferreira, J. M. Loureiro, F. Ragon, P. Horcajada, K.-E. Shim, Y.-K. Hwang, U.-H. Lee, J.-S. Chang. Reverse shape selectivity in the liquid-phase adsorption of xylene isomers in zirconium terephthalate MOF UiO-66. *Langmuir* **2012**;28(13):5715-5723.

41. H. Li, M. Eddaoudi, M. O'Keeffe, O. M. Yaghi. Design and synthesis of an exceptionally stable and highly porous metal-organic framework. *nature* **1999**;402(6759):276.

42. Z. Y. Gu, X. P. Yan. Metal‐Organic Framework MIL‐101 for High‐Resolution Gas‐Chromatographic Separation of Xylene Isomers and Ethylbenzene. *Angewandte Chemie International Edition* **2010**;49(8):1477-1480.

43. M. Edgar, R. Mitchell, A. M. Slawin, P. Lightfoot, P. A. Wright. Solid‐State Transformations of Zinc 1, 4‐Benzenedicarboxylates Mediated by Hydrogen‐Bond‐Forming Molecules. *Chemistry-a European Journal* **2001**;7(23):5168-5175.

44. Z.-Y. Gu, D.-Q. Jiang, H.-F. Wang, X.-Y. Cui, X.-P. Yan. Adsorption and separation of xylene isomers and ethylbenzene on two Zn− terephthalate metal− organic frameworks. *The Journal of Physical Chemistry C* **2009**;114(1):311-316.

45. A. Kasik, Y. Lin. Organic solvent pervaporation properties of MOF-5 membranes. *Separation and Purification Technology* **2014**;121:38-45.

46. H. Suda, K. Haraya. Gas permeation through micropores of carbon molecular sieve membranes derived from Kapton polyimide. *The Journal of Physical Chemistry B* **1997**;101(20):3988-3994.

47. B. Rand, A. Hosty, S. West, H. Marsh. Introduction to carbon science. *Butterworths, London* **1989**:75-92.

48. H. O. Pierson. Handbook of Carbon, Graphite, Diamond, and Fullerenes, Processing, Properties and Applications: Noyes publications New York:; **1993**.

49. K. M. Steel, W. J. Koros. Investigation of porosity of carbon materials and related effects on gas separation properties. *Carbon* **2003**;41(2):253-266.

50. L. Shao, T.-S. Chung, G. Wensley, S. H. Goh, K. P. Pramoda. Casting solvent effects on morphologies, gas transport properties of a novel 6FDA/PMDA–TMMDA copolyimide membrane and its derived carbon membranes. *Journal of Membrane Science* **2004**;244(1):77-87.

51. D.-Y. Koh, B. A. McCool, H. W. Deckman, R. P. Lively. Reverse osmosis molecular differentiation of organic liquids using carbon molecular sieve membranes. *Science* **2016**;353(6301):804-807.

52. A. Samanta, A. Zhao, G. K. Shimizu, P. Sarkar, R. Gupta. Post-combustion CO2 capture using solid sorbents: a review. *Industrial & Engineering Chemistry Research* **2011**;51(4):1438-1463.

53. W. J. Koros, C. Zhang. Materials for next-generation molecularly selective synthetic membranes. *Nature materials* **2017**;16(3):289.

54. M. Das, J. D. Perry, W. J. Koros. Gas-Transport-Property Performance of Hybrid Carbon Molecular Sieve− Polymer Materials. *Industrial & Engineering Chemistry Research* **2010**;49(19):9310-9321.

55. M. Rungta, G. B. Wenz, C. Zhang, L. Xu, W. Qiu, J. S. Adams, W. J. Koros. Carbon molecular sieve structure development and membrane performance relationships. *Carbon* **2017**;115:237-248.

56. H. Hatori, Y. Yamada, M. Shiraishi, M. Yoshihara, T. Kimura. The mechanism of polyimide pyrolysis in the early stage. *Carbon* **1996**;34(2):201-208.

57. G. Ehlers, K. Fisch, W. Powell. Thermal degradation of polymers with phenylene units in the chain. IV. Aromatic polyamides and polyimides. *Journal of Polymer Science Part A: Polymer Chemistry* **1970**;8(12):3511-3527.

58. O. Sanyal, C. Zhang, G. B. Wenz, S. Fu, N. Bhuwania, L. Xu, M. Rungta, W. J. Koros. Next generation membranes—using tailored carbon. *Carbon* **2018**;127:688-698.

59. H. O. Pierson. *Handbook of carbon, graphite, diamonds and fullerenes: processing, properties and applications*: William Andrew; **2012**.

60. Y. Ma, M. L. Jue, F. Zhang, R. Mathias, H. Y. Jang, R. P. Lively. Creation of well‐defined "mid‐sized" micropores in carbon molecular sieve membranes. *Angewandte Chemie* **2019**;131(38):13393-13399.

61. C. Zhang, W. J. Koros. Ultraselective carbon molecular sieve membranes with tailored synergistic sorption selective properties. *Advanced Materials* **2017**;29(33).

62. S. Fu, G. B. Wenz, E. S. Sanders, S. S. Kulkarni, W. Qiu, C. Ma, W. J. Koros. Effects of pyrolysis conditions on gas separation properties of 6FDA/DETDA: DABA (3: 2) derived carbon molecular sieve membranes. *Journal of Membrane Science* **2016**;520:699-711.

63. J. E. Koresh, A. Sofer. Molecular sieve carbon permselective membrane. Part I. Presentation of a new device for gas mixture separation. *Separation Science and Technology* **1983**;18(8):723-734.

64. P. J. Williams, W. J. Koros. Gas separation by carbon membranes. *Advanced membrane technology and applications* **2008**:599-631.

65. C. W. Jones, W. J. Koros. Carbon molecular sieve gas separation membranes-I. Preparation and characterization based on polyimide precursors. *Carbon* **1994**;32(8):1419-1425.

66. L. David, A. Ismail. Influence of the thermastabilization process and soak time during pyrolysis process on the polyacrylonitrile carbon membranes for O2/N2 separation. *Journal of Membrane Science* **2003**;213(1-2):285-291.

67. Y. Ma, F. Zhang, S. Yang, R. P. Lively. Evidence for entropic diffusion selection of xylene isomers in carbon molecular sieve membranes. *Journal of Membrane Science* **2018**.

68. A. B. Fuertes, I. Menendez. Separation of hydrocarbon gas mixtures using phenolic resin-based carbon membranes. *Separation and Purification Technology* **2002**;28(1):29-41.

69. W. Wei, H. Hu, L. You, G. Chen. Preparation of carbon molecular sieve membrane from phenol–formaldehyde Novolac resin. *Carbon* **2002**;40(3):465-467.

70. M. Acharya, H. C. Foley. Spray-coating of nanoporous carbon membranes for air separation. *Journal of Membrane Science* **1999**;161(1-2):1-5.

71. M. Acharya, B. A. Raich, H. C. Foley, M. P. Harold, J. J. Lerou. Metal-supported carbogenic molecular sieve membranes: synthesis and applications. *Industrial & Engineering Chemistry Research* **1997**;36(8):2924-2930.

72. H. J. Kim, D.-G. Kim, K. Lee, Y. Baek, Y. Yoo, Y. S. Kim, B. G. Kim, J.-C. Lee. A carbonaceous membrane based on a polymer of intrinsic microporosity (PIM-1) for water treatment. *Scientific reports* **2016**;6:36078.

73. Y. K. Kim, H. B. Park, Y. M. Lee. Gas separation properties of carbon molecular sieve membranes derived from polyimide/polyvinylpyrrolidone blends: effect of the molecular weight of polyvinylpyrrolidone. *Journal of Membrane Science* **2005**;251(1-2):159-167.

74. Y. K. Kim, H. B. Park, Y. M. Lee. Preparation and characterization of carbon molecular sieve membranes derived from BTDA–ODA polyimide and their gas separation properties. *Journal of Membrane Science* **2005**;255(1-2):265-273.

75. P. J. Williams. *Analysis of factors influencing the performance of CMS membranes for gas separation*, Georgia Institute of Technology; 2006.

76. H. B. Park, Y. K. Kim, J. M. Lee, S. Y. Lee, Y. M. Lee. Relationship between chemical structure of aromatic polyimides and gas permeation properties of their

carbon molecular sieve membranes. *Journal of Membrane Science* **2004**;229(1-2):117-127.

77. Y. Kusuki, H. Shimazaki, N. Tanihara, S. Nakanishi, T. Yoshinaga. Gas permeation properties and characterization of asymmetric carbon membranes prepared by pyrolyzing asymmetric polyimide hollow fiber membrane. *Journal of Membrane Science* **1997**;134(2):245-253.

78. M. L. Jue, Y. Ma, R. P. Lively. Streamlined Fabrication of Asymmetric Carbon Molecular Sieve Hollow Fiber Membranes. *ACS Applied Polymer Materials* **2019**;1(8):1960-1964.

79. A. Singh, W. Koros. Significance of entropic selectivity for advanced gas separation membranes. *Industrial & Engineering Chemistry Research* **1996**;35(4):1231-1234.

80. A. Singh-Ghosal, W. Koros. Energetic and entropic contributions to mobility selectivity in glassy polymers for gas separation membranes. *Industrial & Engineering Chemistry Research* **1999**;38(10):3647-3654.

81. V. C. Geiszler, W. J. Koros. Effects of polyimide pyrolysis conditions on carbon molecular sieve membrane properties. *Industrial & Engineering Chemistry Research* **1996**;35(9):2999-3003.

82. M. Kiyono, P. J. Williams, W. J. Koros. Effect of pyrolysis atmosphere on separation performance of carbon molecular sieve membranes. *Journal of Membrane Science* **2010**;359(1-2):2-10.

83. B. Dickens. Thermally degrading polyethylene studied by means of factor - jump thermogravimetry. *Journal of Polymer Science: Polymer Chemistry Edition* **1982**;20(4):1065-1087.

84. B. Dickens. Thermal degradation study of isotactic polypropylene using factor - jump thermogravimetry. *Journal of Polymer Science: Polymer Chemistry Edition* **1982**;20(5):1169-1183.

85. J. E. Koresh, A. Soffer. The carbon molecular sieve membranes. General properties and the permeability of CH4/H2 mixture. *Separation Science and Technology* **1987**;22(2-3):973-982.

86. G. J. Van Amerongen. The permeability of different rubbers to gases and its relation to diffusivity and solubility. *Journal of Applied Physics* **1946**;17(11):972-985.

87. W.J.Koros. Barrier polymers and structures. *Americal Chmical Society, Washington DC, **1990***

88. S. Glasstone, K. J. Laidler, H. Eyring. *The theory of rate processes; the kinetics of chemical reactions, viscosity, diffusion and electrochemical phenomena*: McGraw-Hill Book Company;1941.

89. P. S. Rallabandi, D. M. Ford. Entropic and energetic selectivity in air separation with microporous materials. *AIChE Journal* **2000**;46(1):99-109.

90. S. Fu, E. S. Sanders, S. S. Kulkarni, G. B. Wenz, W. J. Koros. Temperature dependence of gas transport and sorption in carbon molecular sieve membranes derived from four 6FDA based polyimides: Entropic selectivity evaluation. *Carbon* **2015**;95:995-1006.

91. J. Adams, N. Bighane, W. J. Koros. Pore morphology and temperature dependence of gas transport properties of silica membranes derived from oxidative thermolysis of polydimethylsiloxane. *Journal of Membrane Science* **2017**;524:585-595.

92. J. B. James, J. Wang, L. Meng, Y. Lin. ZIF-8 Membrane Ethylene/Ethane Transport Characteristics in Single and Binary Gas Mixtures. *Industrial & Engineering Chemistry Research* **2017**;56(26):7567-7575.

93. X. Ning, W. J. Koros. Carbon molecular sieve membranes derived from Matrimid® polyimide for nitrogen/methane separation. *Carbon* **2014**;66:511-522.

CHAPTER 3. **MATERIALS AND EXPERIMENTAL METHODS**

3.1 Overview

This chapter describes the materials and experimental methods used in this work. Section 3.2 discusses the materials used to synthesize membranes and conduct separation testing. The polymer synthesis methods are provided in Section 3.3. Section 3.4 and 3.5 discuss the preparation of dense polymeric membranes and hollow fiber membranes. Section 3.6 outlines the various characterization techniques. Section 3.7 summarizes the organic vapor sorption measurements for the sorption and diffusion study. Finally, section 3.8 and 3.9 present the Wicke-Kallenbach permeation tests and organic solvent reverse osmosis measurements used to characterize the membrane separation performance.

3.2 Materials

Tetrafluoroterephthalonitrile (TFTPN) (Sung-Young Chemical Limited, Shanghai, China) was recrystallized via vacuum sublimation at 140 °C before use. 5,5',6,6'-tetrahydroxy-3,3,3',3'-tetramethyl-1,1'-spirobisindane (TTSBI) (Alfa Aesar) was purified by reprecipitation from hot methanol with dichloromethane. Methanol (CH_3OH, 99%), potassium carbonate (K_2CO_3, anhydrous, 99%), chloroform ($CHCl_3$, >99.8%), dichloromethane (DCM, >99.5%), dimethylformamide (DMF, >99.8%), tetrahydrofuran (THF, >99.5%), *p*-xylene (99%) and *o*-xylene (99%) were of analytic grade from Alfa Aesar and used as received. Nitrogen (UHP 5.0 Grade), argon (UHP 5.0 Grade), 4 vol% hydrogen balanced with argon, and liquid nitrogen were purchased from Airgas.

3.3 Synthesis of PIM-1

PIM-1 was synthesized using the low-temperature polycondensation method reported by Budd et al., as shown in Figure 3.1 [1]. The two purified monomers, TFTPN and TTSBI, were added to anhydrous DMF at an equimolar ratio in a round-bottom flask. After the monomers were completely dissolved, anhydrous highly crushed K_2CO_3 (2.5 mol eq. times with respect to TFTPN) was added to the solution, and the polymerization reaction was continuously stirred under a nitrogen atmosphere at 65 °C for 72 hrs. After the reaction, upon cooling, deionized water was used to quench the reaction and precipitate the PIM-1 polymer. The crude product was then collected by filtration and washed with additional deionized water to remove salts and residual solvent. Repeated reprecipitation from chloroform further purified the polymer. Finally, the fluorescent yellow PIM-1 polymer was dried at 70 °C under vacuum for 12 hrs before use. The molecular weight as determined by gel permeation chromatography (GPC) in THF was Mn = 46,500 with a polydispersity index (PDI) = 1.5 when compared against polystyrene standards.

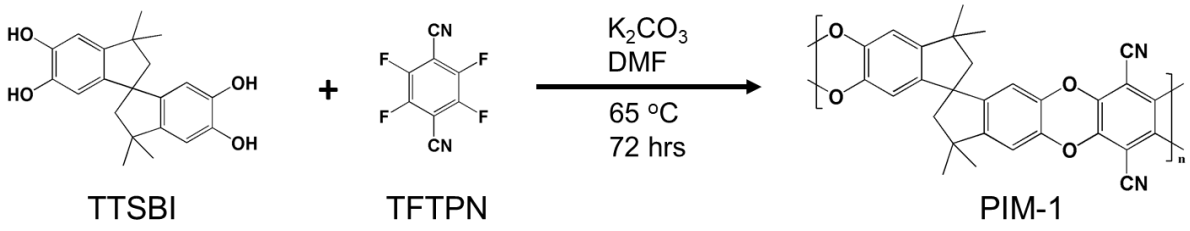

Figure 3.1 Reaction scheme for the low temperature synthesis of PIM-1.

3.4 Dense Polymeric Film Preparation

The dried polymer was dissolved in THF or Chloroform to form a 10 wt% polymer solution and placed on a roller at room temperature for 6 hrs to form a homogeneous solution. The resulting polymer solution was then used to prepare polymeric films by a solution casting method inside a glove bag (Glas-Col) placed in a fume hood at room temperature. The polymer solution, a glass plate, a doctor blade, and a beaker containing excess THF or Chloroform were placed inside the glove bag prior to film casting. The glove bag was then sealed, purged with nitrogen three times, and allowed to saturate with THF or Chloroform for 5 hrs. Afterwards, the solution was transferred from the vial to the glass plate and cast into a uniform film, as shown in Figure 3.2 [2]. Subsequently, the film solidified as the solvents slowly evaporated in the glove bag for 3 days, followed by vacuum drying for another 24 hrs before use.

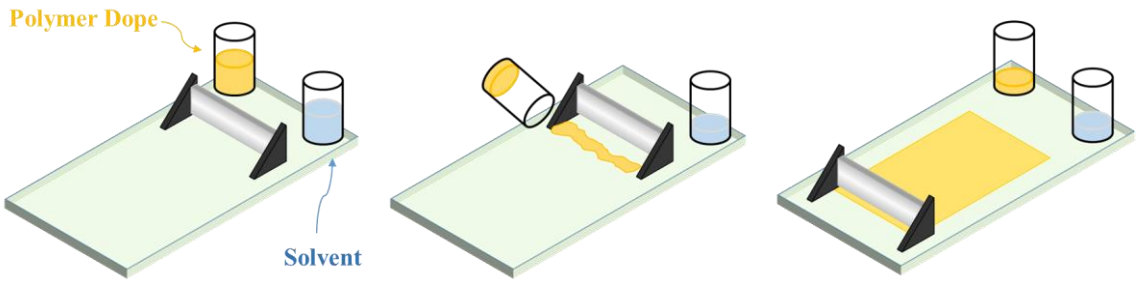

Figure 3.2 A schematic of the fabrication of polymeric films.

3.5 Hollow Fiber Membrane Fabrication

Asymmetric PIM-1 hollow fiber membranes (HFMs) were spun using a simulated dual-bath method, as shown in Figure 3.3 [3,4]. A multicomponent PIM-1 solution was extruded through the middle channel of a coaxial spinneret, and a neutral fluid (a solvent mixture that won't extract or precipitate the polymer) was extruded through the inner channel. A third fluid layer, consisting of 1-butanol and THF was supplied to the outermost layer surrounding the polymer solution filament to slow down THF evaporation. The solvent exchange between the polymer solution and the outermost layer (the first bath) forms the selective skin layer and the solvent exchange in the water quench bath (the second bath) completes the phase inversion for the entire hollow fiber membranes.

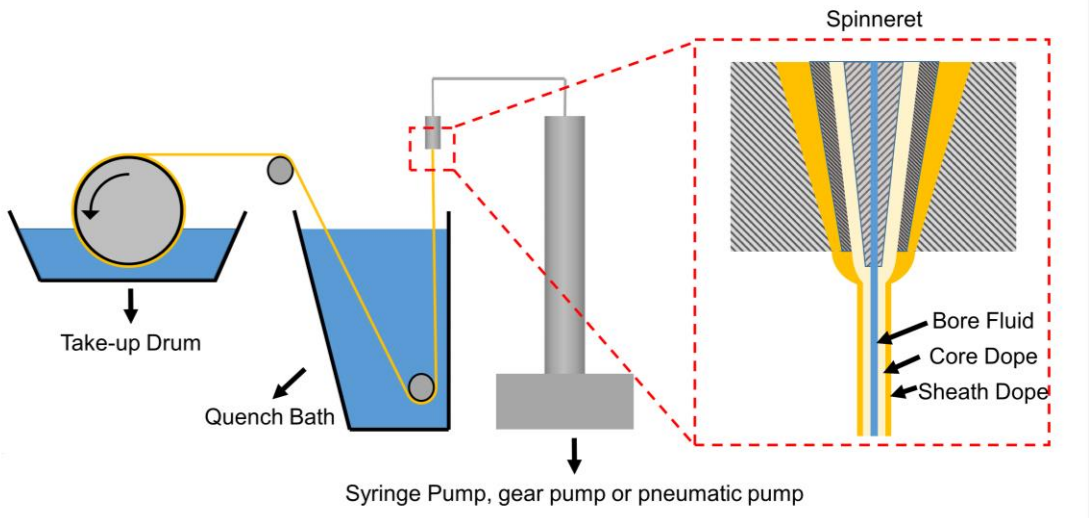

Figure 3.3 A schematic of a dry-wet spinning setup.

3.6 Material Characterization

3.6.1 Nitrogen Physisorption Experiments

Nitrogen physisorption experiments were performed on a Belsorp MAX (MicrotracBEL, Japan) at 77 K. Pore size distributions were obtained from the N_2 isotherms using 2D-NLDFT (two-dimensional non-local density functional theory) developed for carbon materials with infinite slit pores (Micro Active software package, Micromeritics) [5]. Only pores accessible for the probe molecules (N_2) can be detected in this porosity characterization, which means the micropores surrounded by ultramicropores with a width smaller than or similar to the size of N_2 molecules can not be detected. This method cannot differentiate from "dead-end" microporous networks and microporous networks that percolate throughout the membrane. The total pore volume was calculated based on the total amount of N_2 adsorbed at p/p^0 of 0.95. The samples were degassed under vacuum on a Belsorp-Vac II below 10-2 kPa for 12 hrs at 110 °C. The free space measurement was performed after each analysis.

3.6.2 X-ray Photoelectron Spectroscopy

X-ray photoelectron spectroscopy (XPS) was performed using a K-Alpha XPS (Thermo Fisher Scientific, West Palm Beach, FL), which is equipped with a monochromatic Al-Kα X-ray source. The silver oxide was used as the internal standard to calibrate the spectra. The XPS analysis chamber was evacuated to a pressure of 2×10^{-8} mbar or lower before collecting XPS spectra.

3.6.3 X-ray Diffraction Analyses

X-ray diffraction (XRD) analyses were performed on an X'Pert PRO Alpha-1X-ray diffractometer (PANalytical) with X' celerator detector and Cu Kα radiation (λ = 1.5406 Å) at a voltage of 45 kV and current of 40 mA using the scanning angle 2θ, at a step size of 0.016° and scan time of 20 s/step.

3.6.4 Fourier-Transform Infrared Spectra

Fourier-transform infrared spectra (FTIR) were recorded under transmittance mode on a Nicolet iS50 FT-IR spectrometer (Thermo Scientific, West Palm Beach, FL). Samples were ground with potassium bromide (KBr) in a mass ratio of 1:100 and pressed into a wafer. The range was measured with 64 scans and a resolution of 8 cm^{-1}.

3.6.5 Scanning Electron Microscopy

Scanning electron microscopy (SEM) micrographs were obtained on a Hitachi SU8230 FE-SEM microscope with a cold field emission gun at 10 kV accelerating potential and 5 µA emission current. Before imaging, the dried samples were coated by a Hummer 6 Gold sputterer to make them conductive. ImageJ® software was used to post process the images and determine the thickness of the membranes.

3.6.6 Mass Spectrometry

Gases evolving from the pyrolysis process were measured with an Omnistar quadrupolar mass spectrometer (GSD 320 O_2, Pfeiffer Vacuum GmbH, Germany).

To accurately measure the amount of evolved gases during the pyrolysis process of CMS membranes, the precursors were dried in a vacuum oven under 120 °C for 12 hrs to remove any moisture inside the materials. The total amount of evolved CO_2 and H_2O were measured by the integral area of the corresponding MS curves along the pyrolysis time. The total percentage weight loss of the sample was calculated using Eq. 3.1:

$$\%\ weight\ loss = \frac{weight_{before\ pyrolysis} - weight_{after\ pyrolysis}}{weight_{before\ pyrolysis}} \times 100 \quad \textbf{Eq. 3.1}$$

3.7 Organic vapor sorption measurements

3.7.1 VTI-SA+ automated vapor sorption analyzer method

The gravimetric vapor sorption of pure xylene components in PIM-1-derived CMS was measured with a VTI-SA+ automated vapor sorption analyzer (TA Instruments, New Castle, DE) at a relative pressure ranging from 0.000 to 0.400 at 55 °C. Before each test, the carbon sample was first crushed into smaller particles (average particle size obtained from SEM) to enable sufficient sample loading and then dried in situ at 120 °C for 720 min under flowing nitrogen. ImageJ® software was used to analyze the particle size distribution of the powder samples. The equilibrium criteria for each step was set for mass changes less than 0.0005 wt% over a 60 min period.

The average equivalent spherical radius of the carbon particles, $\overline{R}$ was calculated using:

$$\overline{R} = \frac{\sum_i V_i R_i}{\sum_i V_i} = \sum_i X_i R_i \qquad \textbf{Eq. 3.2}$$

where R_i and V_i are the equivalent spherical radius and volume of each individual particle, respectively, and X_i is the volume-weighted fraction of particles with a radius of R_i.

The Fickian transport diffusion coefficient of the xylene isomers in the CMS can be determined by analyzing the gravimetric sorption data. It should be noted that the vapor concentration within the sample chamber does not change instantaneously, and an exponential boundary condition needs to be taken into account when applying Fickian solutions to the uptake data [6].

The obtained weight change data from the kinetic sorption curves is first normalized by using Eq. 3.3 [7].

$$\frac{M_t}{M_\infty} = \frac{M(t) - M(0)}{M(t = \infty) - M(0)} \qquad \textbf{Eq. 3.3}$$

where $M(t)$ is the total weight of CMS and the adsorbed organic molecules at time point *t* and $M(t = \infty)$ is the theoretical total weight after infinite time ∞; M_t is the amount of organic sorption into the CMS at time point *t* and M_∞ is the theoretical sorption amount after infinite time ∞.

The mathematical infinite series solution for the Fickian uptake for spherical particles of diameter *Ri* with an exponential boundary condition is given by Eq. 3.4 as proposed by Crank [7],

$$\left.\frac{M_t}{M_\infty}\right|_{R_i} = 1 - \frac{3D}{\beta R_i^2}\exp(-\beta t)\left\{1 - \left(\frac{\beta R_i^2}{D}\right)^{\frac{1}{2}} cot\left(\left(\frac{\beta R_i^2}{D}\right)^{\frac{1}{2}}\right)\right\} + \frac{6\beta R_i^2}{D\pi^2}\sum_{n=1}^{\infty}\frac{exp\left[-\frac{Dn^2\pi^2 t}{R_i^2}\right]}{n^2\left(n^2\pi^2 - \frac{\beta R_i^2}{D}\right)} \quad \textbf{Eq. 3.4}$$

where β is the inverse characteristic time constant of the exponential boundary.

Therefore, the apparent Fickian uptake considering both particle size distribution and the exponential boundary condition can be approximated as the superposition of the solutions for each particle within the population [8]:

$$\left.\frac{M_t}{M_\infty}\right|_{PSD} \approx \sum_i X_i \left.\frac{M_t}{M_\infty}\right|_{R_i} \quad \textbf{Eq. 3.5}$$

3.7.2 Dynamic vapor sorption analyzer method

Dynamic Vapor Sorption Analyzer (DVS Vacuum, Surface Measurement Systems, Allentown, PA, USA) was also utilized to measure the xylene sorption in CMS at a relative pressure lower than 0.005 or higher than 0.500 at 55 °C. The crushed CMS particles (average particle size obtained from SEM) were used to enable sufficient sample loading and then dried in situ at 120 °C for 720 min under a high vacuum (< 1×10^{-3} Pa). The

equilibrium criteria for each step was set for mass changes less than 0.0005 wt% over a 60 min period.

During the experiment, DVS was operating at the dynamic mode: pure xylene vapor continuously flows through the sample chamber, the pressure of which is controlled at a target value. Xylene vapor flowrate is tuned via PID control to minimize the time required to change the sample chamber pressure below 3 seconds.

Compared with VTI, DVS has the capability to achieve a lower xylene pressure (e.g., 0.005), which makes DVS more suitable to measure the kinetic uptake at the low partial pressure. Moreover, DVS is equipped with a microbalance with a 0.0001 mg resolution (VTI has a 0.001 mg resolution). Since the uptake amount is low when changing the partial pressure value from a relatively high value to another higher value (e.g., 0.45~0.50). DVS with a higher resolution is more suitable for the high partial pressure measurement.

It should be noticed that there is no exponential boundary condition for DVS measurement. Different from Eq. 3.4, for a spherical particle subject to a step-change in adsorbate concentration at its external surface at time zero, the mathematical infinite series solution for the Fickian uptake is given by Eq. 3.6 proposed by Crank [7]. Eq. 3.2, Eq. 3.3 and Eq. 3.5 are still applicative to DVS measurement.

$$\left.\frac{M_t}{M_\infty}\right|_{R_i} = 1 - \frac{6}{\pi^2}\sum_{n=1}^{\infty}\frac{1}{n^2}exp\left[-\frac{Dn^2\pi^2 t}{{R_i}^2}\right] \qquad \textbf{Eq. 3.6}$$

3.7.3 Uptake measurements at unit activity

All uptake amounts at unit activity (a condensed liquid phase in this work) were measured at least three times manually. In each test, the CMS membrane was dried under vacuum at 110 °C for 12 hours to remove moisture and was weighed to obtain the initial mass value. After that, the membrane (around 10 μm) was soaked in pure liquid *p*-xylene or *o*-xylene in a 20 mL vial and then placed in an oven at 35, 45, or 55 °C for one month, which was estimated to be sufficient to achieve equilibrium. All the samples have been weighed at 25 days and 31 days, and the sample weight was found to be identical in each case, thus we conclude the sample was at equilibrium. The weight of the saturated membrane was used to obtain the uptake amount at the unit activity point.

3.8 Wicke-Kallenbach Permeation Measurements

For the Wicke-Kallenbach permeation measurements, the free-standing dense CMS membranes were fixed between rings of aluminum tape (0.003 inches thick, McMaster-Carr) with an outer diameter of 1 inch and the inner diameter of 3/8 inch and sealed by a chemically-resistant epoxy (MarineWeld 8272, JB Weld). The CMS HFM modules were assembled in 316 stainless steel tubes using J-B weld MarineWeld 8272 epoxy.

The Wicke-Kallenbach permeation experiments for xylene vapors were conducted in a custom-built apparatus, as shown in Figure 3.4 [2]. For all Wicke-Kallenbach permeation tests, the permeate activity was maintained at essentially 0, which was achieved by utilizing pure nitrogen sweeping the permeate to a gas chromatograph continuously. For the pure component Wicke-Kallenbach permeation tests, the “pure” xylene upstream (*p*-xylene or *o*-xylene) with unit activity was generated by bubbling nitrogen through a

corresponding pure xylene liquid reservoir at 55 °C continuously. For the mixed-xylene Wicke-Kallenbach permeation tests, an equimolar, saturated, *p*-xylene/*o*-xylene vapor upstream was generated by bubbling nitrogen through a *p*-xylene/*o*-xylene liquid mixture with a molar ratio of 4:5 (as at 55 °C, *p*-xylene sat/*o*-xylene sat ≈ 5/4) continuously. An equimolar *p*-xylene/*o*-xylene vapor upstream with 0.05 activity was generated by mixing a pure nitrogen flow with an equimolar *p*-xylene/*o*-xylene vapor flow (generated by nitrogen bubbling through the *p*-xylene/*o*-xylene liquid mixture with a molar ratio of 4:5) with a flow rate ratio of 1:19.

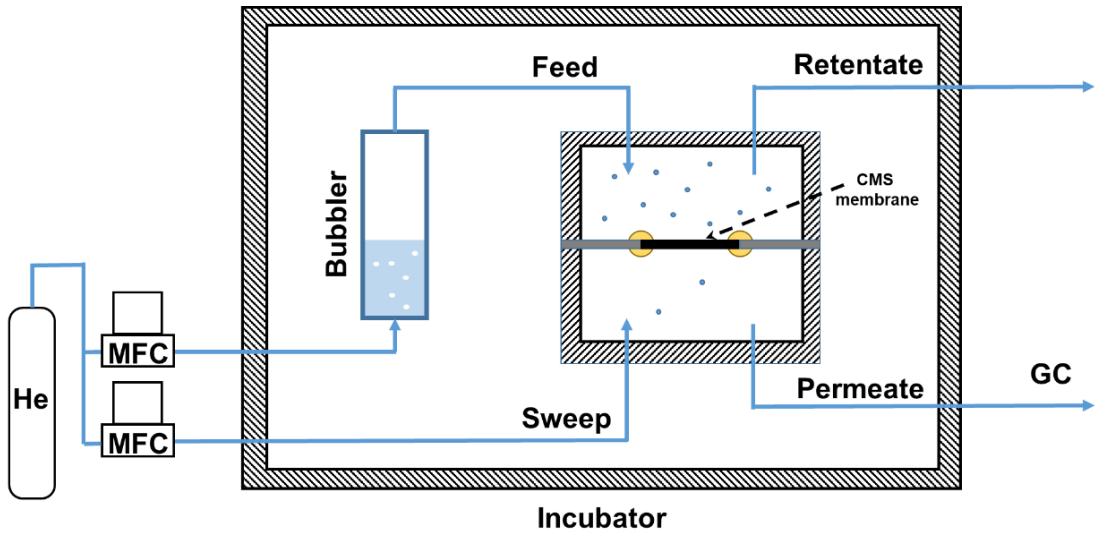

Figure 3.4 Wicke-Kallenbach permeation apparatus.

Continuous sampling of the permeate was used to determine the steady state composition and was usually achieved after 24 hrs. The permeability of *p*-xylene or *o*-xylene measured via Wicke-Kallenbach permeation can be calculated using Eq. 3.7.

$$\mathbb{P}_A = \frac{\dot{n}_A \times \ell}{A \times \left[p_{A,upstream} - p_{A,downstream}\right]} \qquad \textbf{Eq. 3.7}$$

$\dot{n}_A$ is the molar flow rate of *p*-xylene or *o*-xylene and can be obtained from the gas chromatograph and mass flow controller information. Here, $p_{A,upstream}$ is the vapor pressure of *p*-xylene or *o*-xylene and $p_{A,downstream}$ is set as 0. ℓ is the thickness of the CMS membrane as measured by SEM. A is the permeation area of the CMS membrane and was obtained using ImageJ® software.

The permeaslectivity can be calculated by using the measured permeability of *p*-xylene and *o*-xylene:

$$\alpha_{A/B} = \frac{\mathbb{P}_A}{\mathbb{P}_B} \qquad \textbf{Eq. 3.8}$$

3.9 Organic Solvent Reverse Osmosis (OSRO) Measurements

As shown in Figure 3.5, liquid xylene mixture separation of CMS hollow fiber membranes was conducted in a custom crossflow system using two high-pressure syringe pumps (500D, Teledyne Isco) connected by a dual-pump continuous flow system (500E, Teledyne Isco) at room temperature [9-11]. A 90:10 (mol/mol) liquid mixture of *p*-xylene/*o*-xylene was used as the feed mixture and was supplied to the shell-side of the membrane module while the retentate was recycled back to the feed vessel. Prior to exposure to the liquids, the module was slowly exposed to the xylene isomer vapors to condition the module for use. The liquid feed mixture was then circulated on the shell side to remove the trapped air in the system before pressurization to the testing pressure. The

permeate sample was collected from the bore side of the membrane module after ten times of the downstream volume had permeated through the system to ensure steady-state performance. The permeate flow rate was measured by the weight of the permeate fluid at each time interval, while the permeate composition was analyzed by GC (7890B, Agilent) using an FID detector.

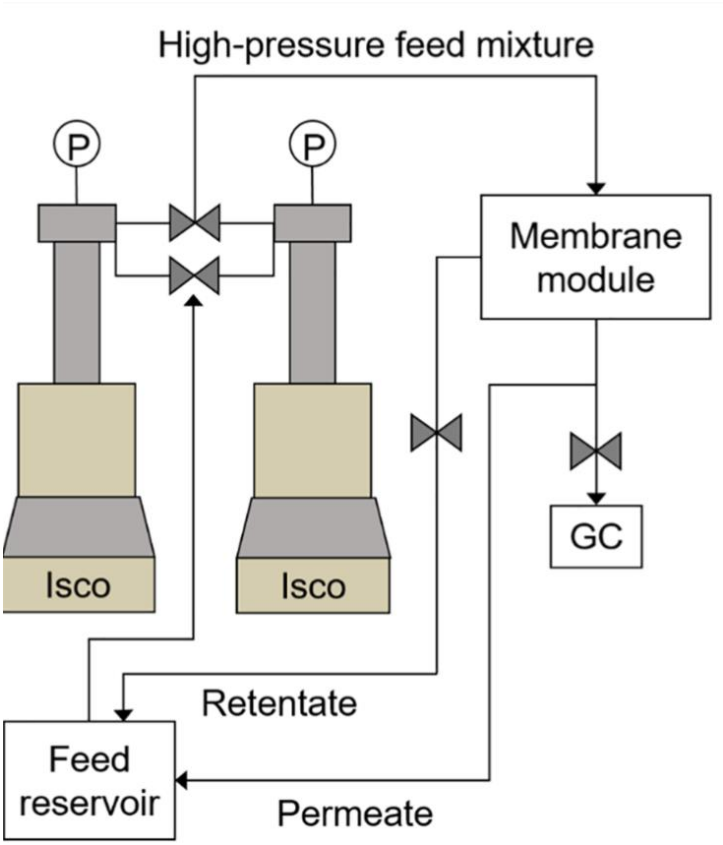

Figure 3.5 A dual-pump crossflow system for high-pressure mixture separation [10].

The measured permeate composition can be used to calculate the separation factor (an engineering parameter, the ratio of permeate composition over the feed composition):

$$\text{Separation Factor} = \beta_{A/B} = \frac{x_A^{permeate}/x_B^{permeate}}{x_A^{feed}/x_B^{feed}} \qquad \textbf{Eq. 3.9}$$

The flux of *p*-xylene and *o*-xylene can be obtained from the measured permeate flow rate:

$$\text{OSRO Flux} = \frac{\dot{n}_A}{A} \qquad \textbf{Eq. 3.10}$$

$\dot{n}_A$ is the molar flow rate of *p*-xylene or *o*-xylene and can be obtained from the permeate flow rate and composition. *A* is the permeation area of the CMS membrane and was obtained using the hollow fiber outer diameter and module active length.

The measured permeate flow rate can be used to calculate the hydraulic permeance of both *p*-xylene and *o*-xylene, which is normalized by the transmembrane pressure:

$$\text{OSRO Hydraulic permeance} = \frac{\mathbb{P}_{A,hydraulic}}{\ell} = \frac{Flux}{\text{Transmembrane pressure}} = \frac{\frac{\dot{n}_A}{A}}{p^{feed} - p^{permeate}} \qquad \textbf{Eq. 3.11}$$

The measured permeate flow rate and composition can be used to calculate the intrinsic permeance of both *p*-xylene and *o*-xylene by considering the intrinsic driving force; here we approximate the intrinsic driving force for *p*-xylene as the "uncoupled" transmembrane fugacity for a Langmuir-type isotherm [12]:

$$\frac{\mathbb{P}_{A,intrinsic}}{\ell} = \frac{\frac{\dot{n}_A}{A}}{\frac{\mathrm{RT}}{\hat{V}_A}\ln\left(\frac{1+b_A f_A^{feed}}{1+b_A f_A^{permeate}}\right)} \qquad \textbf{Eq. 3.12}$$

R is the gas constant (83.1 cm^3-bar/mol-K), T is the measurement temperature, $\hat{V}_A$ is the specific molar volume of component A. b_A is the Langmuir affinity constant for component A, which can be obtained from the sorption isotherm measurements. f_A^{feed} and $f_A^{permeate}$ are the fugacity of component A in the feed or permeate side and can be calculated using the following equation:

$$f_A = x_A \gamma_A p_A^{sat} \exp\left[\frac{\hat{V}_A}{\mathrm{RT}}(p - p_A^{sat})\right] \qquad \textbf{Eq. 3.13}$$

γ_A are the activity coefficient of component A in the feed or permeate side and calculated using the Peng-Robinson equation of state. p_A^{sat} is the saturation vapor pressure of the xylene isomer under the operating temperature and can be obtained from the appropriate Antoine equation.

3.10 References

1. P. M. Budd, E. S. Elabas, B. S. Ghanem, S. Makhseed, N. B. McKeown, K. J. Msayib, C. E. Tattershall, D. Wang. Solution‐processed, organophilic membrane derived from a polymer of intrinsic microporosity. *Advanced Materials* **2004**;16(5):456-459.

2. Y. Ma, F. Zhang, S. Yang, R. P. Lively. Evidence for entropic diffusion selection of xylene isomers in carbon molecular sieve membranes. *Journal of Membrane Science* **2018**;564:404-414.

3. M. L. Jue, V. Breedveld, R. P. Lively. Defect-free PIM-1 hollow fiber membranes. *Journal of Membrane Science* **2017**;530:33-41.

4. M. L. Jue, Y. Ma, R. P. Lively. Streamlined Fabrication of Asymmetric Carbon Molecular Sieve Hollow Fiber Membranes. *ACS Applied Polymer Materials* **2019**;1(8):1960-1964.

5. A. V. Neimark, P. I. Ravikovitch, M. Grün, F. Schüth, K. K. Unger. Pore size analysis of MCM-41 type adsorbents by means of nitrogen and argon adsorption. *Journal of Colloid and Interface Science* **1998**;207(1):159-169.

6. S. Burgess, R. Kriegel, W. Koros. Diffusion coefficient modeling in polyester barrier materials: applications of infinite series solutions. *Soc. Plast. E.-ANTEC* **2014**:830-835.

7. J. Crank. *The mathematics of diffusion*: Oxford university press; **1979**.

8. C. Zhang, R. P. Lively, K. Zhang, J. R. Johnson, O. Karvan, W. J. Koros. Unexpected molecular sieving properties of zeolitic imidazolate framework-8. *The journal of physical chemistry letters* **2012**;3(16):2130-2134.

9. D.-Y. Koh, B. A. McCool, H. W. Deckman, R. P. Lively. Reverse osmosis molecular differentiation of organic liquids using carbon molecular sieve membranes. *Science* **2016**;353(6301):804-807.

10. H. Y. Jang, J. Johnson, Y. Ma, R. Mathias, D. A. Bhandari, R. P. Lively. Torlon® hollow fiber membranes for organic solvent reverse osmosis separation of complex aromatic hydrocarbon mixtures. *AIChE Journal* **2019**;65(12).

11. Y. Ma, M. L. Jue, F. Zhang, R. Mathias, H. Y. Jang, R. P. Lively. Creation of well‐defined “mid‐sized” micropores in carbon molecular sieve membranes. *Angewandte Chemie* **2019**;131(38):13393-13399.

12. F. Kapteijn, J. Moulijn, R. Krishna. The generalized Maxwell–Stefan model for diffusion in zeolites:: sorbate molecules with different saturation loadings. *Chemical Engineering Science* **2000**;55(15):2923-2930.

CHAPTER 4. FORMATION OF PIM-1 DERIVED CMS MEMBRANES AND THEIR SEPARATION MECHANISM[†]

4.1 Introduction

Carbon molecular sieves are a class of microporous carbonaceous materials derived from the pyrolytic decomposition of polymeric precursors. These turbostratic carbon materials have the ability to withstand high transmembrane pressure when fabricated in the form of asymmetric hollow fibers and exhibit chemical and thermal stability [1,2]. The transport of guest molecules through these microporous materials can be tuned via the selection of polymer precursor, pyrolysis protocol, and pyrolysis atmosphere, and as a result of this eminent tunability, these materials have risen to prominence within the area of gas, vapor and organic solvent separations [3-9]. A potentially interesting class of polymeric precursors for CMS materials are polymers of intrinsic microporosity (PIMs), which are characterized by a highly rigid backbone with a site of contortion that enables high free volume and permanent microporosity. Among these novel materials, PIM-1, a prototypical PIM, has attracted the most attention due to its relative ease in synthesizing a high molecular weight polymer [10-13] and has been converted into CMS materials for gas separations [14-16], and water treatment applications [17]. The CMS materials in these previous works displayed promising performance in those applications; we hypothesize that the thermal stability and high free volume of PIM-1 will result in CMS microstructures that effectively transport and separate xylene isomers. The free volume elements in PIM-1

[†] This chapter has been published on *Journal of Membrane Science* as Evidence for entropic diffusion selection of xylene isomers in carbon molecular sieve membranes, 564, **2018**, 404-414.

have been estimated to be approximately 3-7 Å in size (note that the kinetic diameters of *p*-xylene and *o*-xylene are 5.8 Å and 6.8 Å, respectively) [18]. Importantly, the glass transition temperature (~442 °C) exceeds the pyrolytic decomposition temperature (~400 °C) [19], which suggests that PIM-1 should be resistant to morphological collapse during thermal treatments. These two factors combined indicate that PIM-1 may be a useful starting material for the production of high performance CMS membranes for xylene isomers separations [20].

CMS hollow fiber membranes derived from cross-linked poly(vinylidene fluoride) (PVDF) have also been applied in a separation modality known as "organic solvent reverse osmosis" (OSRO) for xylene isomer separations. Unlike low pressure vapor separations, OSRO handles liquid feeds and permeates at conditions relevant to industrial separations, which suggests that these types of membranes will produce industrially-meaningful fluxes. However, OSRO is in the early stages of development, and fundamental sorption-diffusion properties of organic molecules in CMS membranes are needed to better guide OSRO research and engineering [4]. In this chapter, fundamental sorption and diffusion measurements were conducted at temperatures of 35 °C, 45 °C, and 55 °C via gravimetric sorption of xylene vapors into the CMS materials. The testing temperatures were chosen based on potential operating temperatures for OSRO separations. The contributions of "enthalpic" and "entropic" selectivity to the diffusion selectivity were estimated to obtain a fundamental understanding of entropic factors as effective tools to enhance the separation performance of carbon membranes. The permeabilities estimated from the sorption-diffusion model and the generalized Maxwell-Stefan model (based on experimental

measurements of the sorption and diffusion coefficients) were validated using Wicke-Kallenbach permeation experiments of xylene vapor mixtures.

4.2 Fabrication of CMS Membranes

Carbon molecular sieve dense membranes were produced by pyrolyzing the PIM-1 dense films at 550 °C under an oxygen-free argon atmosphere in a pyrolysis set-up as shown in Figure 4.1. Dried circular PIM-1 polymeric films were first placed on a stainless steel mesh plate and then placed into a quartz tube (MTI Corporation) before being loaded into a three-zone furnace (OTF-1200X-III-S-UL, MTI Corporation). The quartz tube was sealed with a pair of SS 304 vacuum flanges with double high-temperature silicone o-rings. An inert atmosphere was achieved by purging the tube with argon for at least 12 hours, and the typical oxygen concentration was below 0.5 ppm as measured by an oxygen analyzer (R1100-ZF Rapidox 1100ZF, CEA Instruments, Inc.). A digital flow meter (Bubble-O-Meter) was used to monitor the argon flow rate, which is critical to remove pyrolysis by-products.

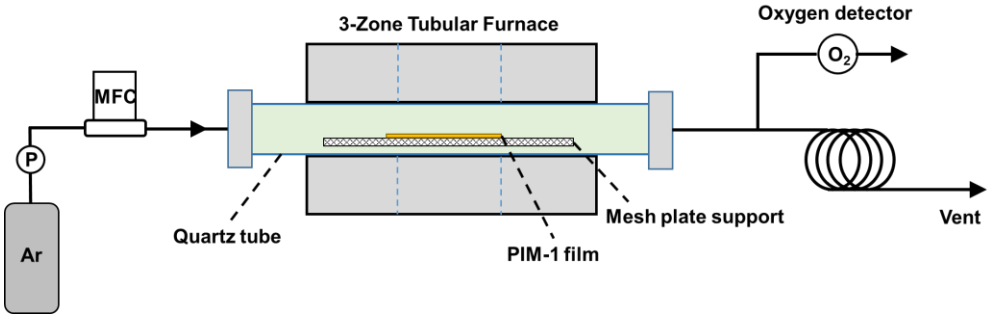

Figure 4.1 Schematic diagram of the pyrolysis set-up used for CMS membranes fabrication under a pure argon environment.

The optimized heating protocol used to reach a final temperature of 550 °C is shown in Table 4.1 [21,22]. The heating rate is 13.3 °C/min initially when the heating temperature (25-250 °C) is far from the final soaking temperature and decreased to be 3.85 °C/min when the heating temperature (250-535 °C) is close to the final soaking temperature. From 535 °C to 550 °C, the heating rate is reduced to be 0.25 °C/min to prevent the overshoot of the temperature. After the heating cycle was complete, the furnace was allowed to cool down naturally, while remaining UHP Argon gas flow, to below 50 °C before venting the furnace and unloading the samples.

Table 4.1 The heating protocol used to fabricate PIM-1-derived CMS in a pure Ar environment.

Step	protocol
1	25-250 °C at a ramp rate of 10 °C /min
2	250-535 °C at a ramp rate of 3 °C /min
3	535-550 °C at a ramp rate of 0.25 °C /min
4	Soak for 2 hours at 550 °C
5	Naturally cooling back to 25 °C under UHP Argon

4.3 Characterization Results of PIM-1 and CMS Membranes

XRD patterns were used to reveal the structural properties of the CMS derived from PIM-1 and also the PIM-1 precursor. As shown in Figure 4.2, three apparent characteristic broad reflections at 13.6 °, 18.2 °, and 22.6 ° were found for the PIM-1 precursor, which correspond to d-spacings of 6.5 Å, 4.9 Å, and 3.8 Å, respectively. The broad reflection at 13.6 ° corresponds to the inefficiently packed polymer chains that originate from the contortion sites inside the PIM-1 structure [23,24]. The broad reflections located at 18.2 ° derive from the micropores between space efficiently packed polymer chains, and the one located at 22.6 ° is a typical reflection for the stacking of aromatic systems [25,26]. Moreover, the XRD data provides a detailed method to investigate the d-spacing of the CMS membranes, which is typically manifested as a broad reflection representing the average center-to-center inter-planar distance between carbon sheets. As the slit-like micropores in CMS are formed by inefficient packing of adjacent carbon sheets, the center-to-center inter-layer distance can be used to qualitatively assess changes to the diffusional passageways for guest molecules, although it is difficult to extract quantitative pore size information from this technique. The broad reflections of the PIM-1-derived CMS membrane are observed at 23.2 ° and 10.9 °. This corresponds to an average d-spacing of around 3.83 Å and 8.12 Å, although it is again important to note that these d-spacings are not the sizes of the ultramicropores and the micropores. The picture that emerges from the XRD experiments is a reduction in the inter-planar distance as the pyrolysis temperature increases corroborating changes in the gas transport rates in CMS membranes derived from PIM-1 [27]. A reflection around 44 ° was observed for the CMS samples. This reflection, which reveals a d-spacing value of 2.1 Å, is the traditional location of the carbon-carbon

spacing of the graphitic planes (the (100) plane in ideal graphite), and reveals the formation of partially ordered carbon structures in the CMS samples [27-29]. Such face-to-face packing of the carbon sheets prevents xylene transport through those graphitic domains.

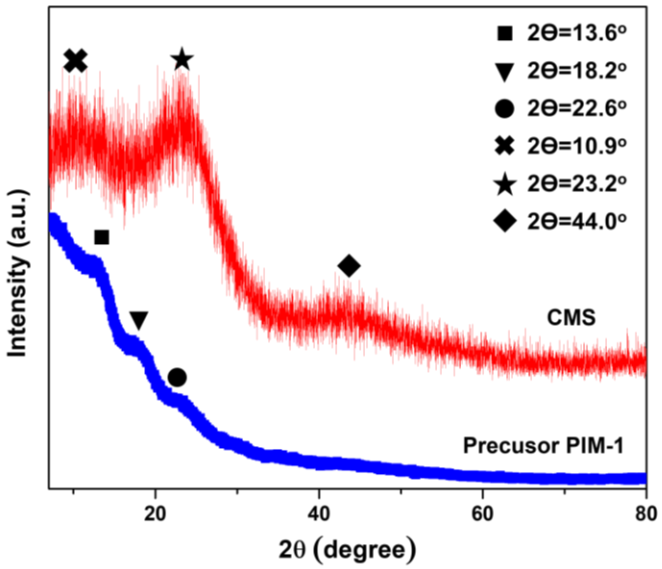

Figure 4.2 XRD patterns for precursor PIM-1 and.CMS derived from PIM-1 pyrolyzed under 550 °C and a pure argon environment.

FTIR spectra (recorded under transmittance mode) in Figure 4.3 shows the chemical bond information for the PIM-1 precursor and the corresponding CMS. The spectra of PIM-1 shows characteristic absorbance bands at 2238 cm^{-1} (C≡N), 1607 cm^{-1} (aromatic C=C bending), 1470-1430 cm^{-1} (-C-H bending within $-CH_2-$ and $-C-CH_3$ groups) and 1300-1000 cm^{-1} (-C-O- stretching). These FTIR results were in accordance with the representative spectrum of pristine PIM-1 [30]. The peak intensities of several bands

reduced significantly compared to the PIM-1 precursor (i.e., most of the functional groups in PIM-1 disappeared after pyrolysis). We do not observe graphitic features in the IR spectra of the CMS, which is expected as graphite structures are only weakly excited by IR beams [31].

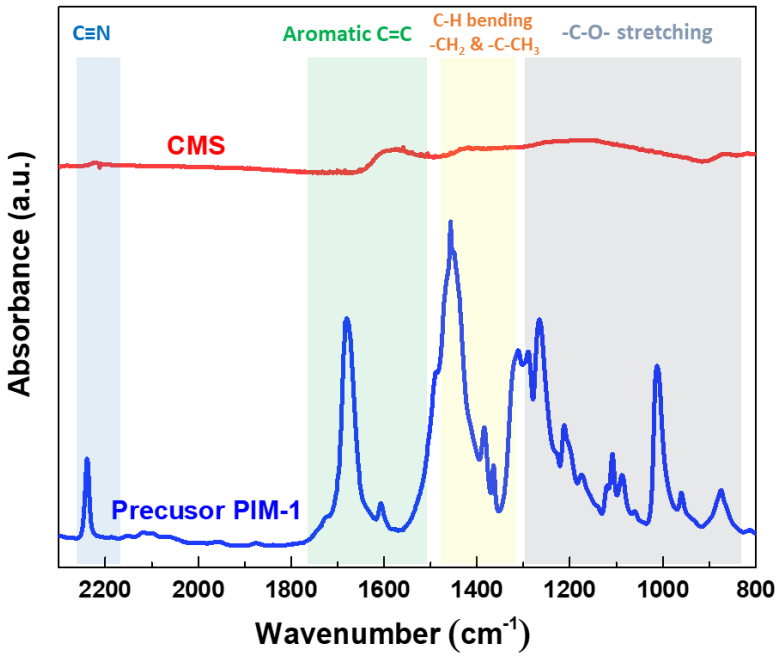

Figure 4.3 FTIR spectra of precursor PIM-1 and CMS derived from PIM-1 pyrolyzed under 550 °C and a pure argon environment.

4.4 Temperature Dependence of Sorption Coefficients

The temperature dependence of the sorption coefficients of *p*-xylene and *o*-xylene isomers in PIM-1-derived CMS membranes was investigated from 35 to 55 °C. As shown in Figure 4.4, *p*-xylene and *o*-xylene sorption isotherms of PIM-1-derived CMS were

collected at 35, 45, and 55 °C, respectively. As illustrated in the full sorption isotherms, the uptake for *p*-xylene and *o*-xylene at each relative pressure exhibited only small differences (within 5 wt%) relative to each other due to their similar chemical nature. Due to the sharp Langmuir-type isotherms, the pure component sorption coefficients for each of the two xylene isomers (𝕊 p-xylene, 𝕊 o-xylene) are calculated according to Eq. 4.1. These sorption coefficient estimates are for a membrane with a xylene activity gradient of 1.0 (upstream) to 0.0 (downstream), which is representative of a pure component permeation case with a saturated vapor upstream and a vacuum downstream [32,33].

$$\mathbb{S}_A \equiv \frac{\rho_{CMS}\times q_A^{sat}}{p_A{}^{up} - p_A{}^{down}} \ln\left(\frac{1-\theta_A^{m,down}}{1-\theta_A^{m,up}}\right) = \frac{\rho_{CMS}\times q_A^{sat}}{p_A^{sat}-0} \ln\left(\frac{1-0}{1-\theta_A^{m,up}}\right) = \frac{\rho_{CMS}\times q_A^{sat}}{p_A^{sat}} \ln\left(\frac{1}{1-\theta_A^{m,up}}\right) \quad \textbf{Eq. 4.1}$$

Here, q_A^{sat} is the Langmuir saturation loading of xylene in the CMS membrane at the corresponding temperature; ρ_{CMS} is the density of the carbon membrane and can be treated as 2.0 g/cm3 and p_A^{sat} is the saturation vapor pressure of xylene isomer under the operating temperature and can be obtained from the Antoine equation. $\theta_A^{m,up}$ and $\theta_A^{m,down}$ are the fractional occupancy of the adsorption sites in the membrane surface contacted with the upstream and downstream, and these can be calculated as q_A/q_A^{sat}. The sorption coefficients of *p*-xylene and *o*-xylene in the CMS membrane as a function of inverse absolute temperature are shown in Figure 4.5. As expected, the temperature dependence of the sorption coefficients follows a Van't Hoff relationship as described by Eq. 2.7:

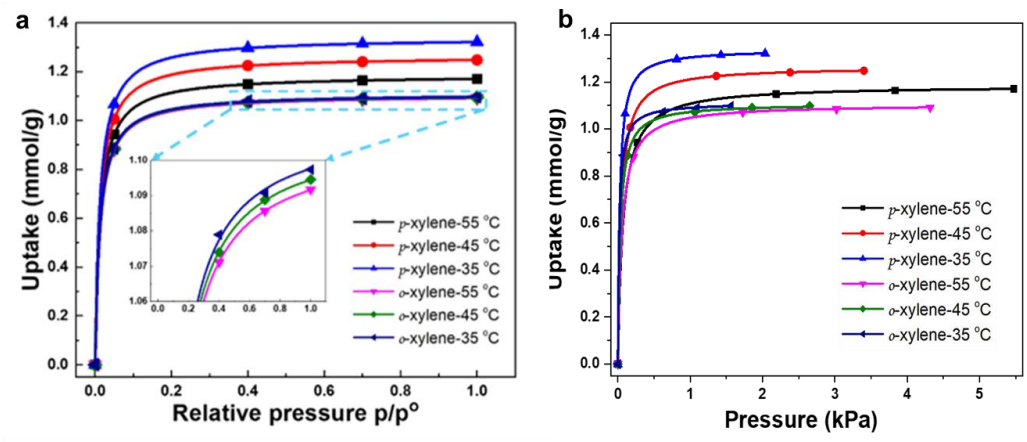

Figure 4.4 (a) Sorption isotherms for *p*-xylene and *o*-xylene in PIM-1-derived CMS membrane as a function of (a) relative pressure and (b) pressure.

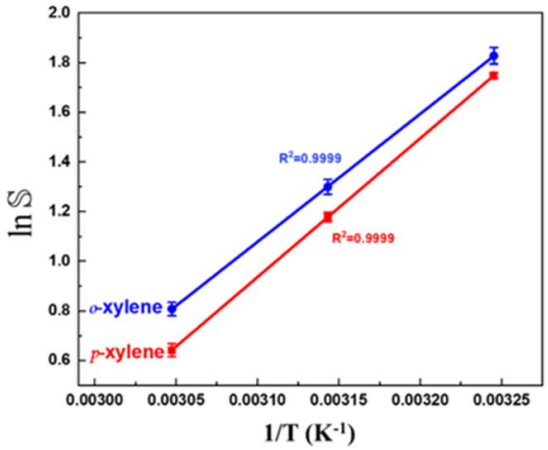

Figure 4.5 Temperature dependence of the sorption coefficients over an activity gradient of 1.0 (upstream) to 0.0 (downstream) for xylene isomers in PIM-1-derived CMS membranes from 35 to 55 °C (sorption coefficients, $\mathbb{S}$ are in the units of mol/(m^3×Pa); error bars represent the standard deviation of at least three measurements, each on different membranes).

The apparent heats of sorption $\Delta\widehat{H}_{\mathbb{S}}$ and the corresponding sorption pre-exponential factors $\mathbb{S}_0$ for *p*-xylene and *o*-xylene were obtained from least squares fitting using Eq. 2.7 and are tabulated in Table 4.2. PIM-1-derived CMS exhibits a lower absolute value for the heat of sorption compared to MFI-type zeolites (-60 to -85 kJ/mol) [34,35]. This result indicates that the adsorption sites provided by the PIM-1-derived CMS have weaker interactions with the xylenes than the MFI-type zeolites. The significant uptake of xylene molecules suggests that there are large micropores within the structure of the PIM-1 CMS. Large micropores would exhibit weaker sorption confinement effects relative to the somewhat narrow 5-6 Å pores in the MFI-type zeolites, suggesting that the lower heats of sorption in the PIM-1 CMS relative to MFI-type zeolites are reasonable. As might be expected, the sorption properties for p-xylene and *o*-xylene are quite similar in the PIM-1derived CMS membranes. Moreover, the sorption selectivity favors the more condensable molecule, which is typically the larger molecule with a higher critical temperature in the absence of any non-van der Waals sorbent-sorbate interaction [36-38]. The apparent heat of sorption of *o*-xylene is somewhat less negative than that of *p*-xylene for PIM-1-derived CMS. This difference is likely due to the inability of the *o*-xylene to pack into the CMS micropore space as efficiently as the slender and more symmetric *p*-xylene molecule. The sorption selectivity between *p*-xylene and *o*-xylene is nearly 1, confirming that the membrane does not separate these two molecules based on any sorption-selective mechanism.

Table 4.2 Sorption properties of xylene isomers for PIM-1-derived CMS compared with MFI-type zeolites.

		PIM-1derived CMS		MFI-type zeolite
		p-xylene	*o*-xylene	*p*-xylene
$\Delta\widehat{H}_{\mathbb{S}}\ \frac{kJ}{mol}$		- 46.5 ± 0.1	- 42.9 ± 0.1	- 65 ~ - 85a
$\mathbb{S}_0\ 10^{-8}\frac{mol}{m^3 \times Pa}$		7.6 ± 0.0	0.3 ± 0.1	-
$\mathbb{S}^b$ $\frac{mol}{m^3 \times Pa}$	55 °C	1.9 ± 0.0	2.2 ± 0.1	2.4
	45 °C	3.2 ± 0.1	3.7 ± 0.1	4.1
	35 °C	5.7 ± 0.1	6.2 ± 0.2	7.5
$\frac{\mathbb{S}\ p-\text{xylene}}{\mathbb{S}\ o-\text{xylene}}$	55 °C	0.85 ± 0.06		-
	45 °C	0.89 ± 0.10		-
	35 °C	0.92 ± 0.19		-

a Adsorption enthalpy of *p*-xylene in MFI-type zeolites is obtained from Thamm et al. and Grahn et al. [34,35]. b Sorption coefficients of *p*-xylene in MFI-type zeolites are estimated based on data from Talu et al. [39] at 50, 40, and 30 °C respectively.

4.5 Temperature Dependence of Diffusion Coefficients

4.5.1 Transport diffusion coefficients

The transient uptake profiles (Figure 4.6a) of the gravimetric sorption experiments can be utilized to estimate the transport (or Fickian) diffusion coefficients of *p*-xylene and *o*-xylene in the CMS material [40-42]. The temperature dependence of the transport diffusion coefficients for *p*-xylene and *o*-xylene in PIM-1-derived CMS membranes is shown in Figure 4.6b. The transport diffusion coefficients of both xylene isomers increase with temperature, following an Arrhenius-type temperature dependence (as shown in Eq. 2.6) with a positive diffusion activation energy.

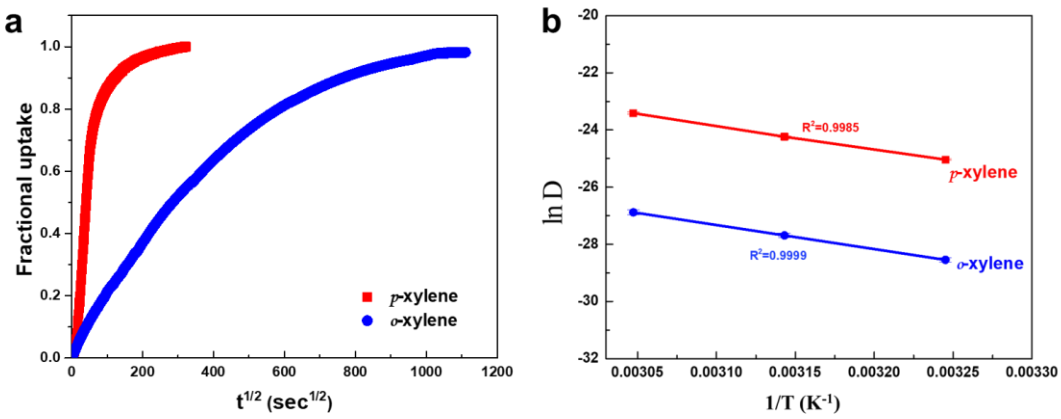

Figure 4.6 (a) Representative kinetic uptake curves for *p*-xylene and *o*-xylene in PIM-1-derived CMS at 35 °C. (b) Temperature dependence of the transport diffusion coefficients for xylene isomers in CMS from 35 to 55 °C (transport diffusion coefficient, *D* are in the units of cm^2/s, error bars represent the standard deviation of at least three runs, each on the same CMS sample).

This diffusion activation energy $E_{D,A}$ describes the energy required for a diffusive molecular displacement from one sorption location to another through an ultramicropore in the rigid, porous carbon membrane. Table 4.3 shows the numerical values of the activation energy for diffusion E_D and the respective diffusion pre-exponential factors D_0 for *p*-xylene and *o*-xylene. From Table 4.3, the diffusion activation energy is seen to increase with penetrant kinetic diameter where *p*-xylene < *o*-xylene, implying a higher diffusion energy barrier for *o*-xylene to enable passage compared with the smaller molecule, *p*-xylene. Moreover, high diffusion selectivities (~30) at relatively high fractional occupancies (~0.8) were observed. These high diffusive selectivities are fundamentally attributable to the rigid ultramicropores in the carbon material. PIM-1-derived CMS exhibits a higher diffusion activation energy than MFI-type zeolites (53-58 kJ/mol) [43], which is consistent with our hypothesis regarding the narrowness of the ultramicropores in the CMS based on cryogenic N_2 sorption measurements. As the CMS possesses very narrow slit-type channels, it requires higher energy for a single xylene molecule to successfully pass through an ultramicropore. Nevertheless, the micropores inside the CMS provide little resistance to the diffusion of guest molecules. Owing to the unique bimodal pore size distribution, the PIM-1-derived CMS with ultramicropores and micropores connected in series exhibits comparable diffusivity for *p*-xylene with that in MFI zeolites (~10^{-11} cm^2/s at 20 °C) [44]. Compared with PVDF-derived CMS (*p*-xylene/*o*-xylene diffusion selectivities range from 10 to 25 with *p*-xylene diffusion coefficient around 2×10^{-10} cm^2/s at 25 °C) [4], PIM-1-derived CMS exhibits higher selectivity and lower diffusivity, which indicates a trade-off between diffusion selectivity and diffusivity for CMS-type materials.

Table 4.3 Transport diffusion properties of xylene isomers for PIM-1-derived CMS compared with MFI-type zeolites.

		PIM-1derived CMS		MFI-type zeolite	
		p-xylene	*o*-xylene	*p*-xylene	*o*-xylene
$E_D \ \frac{kJ}{mol}$		67.8 ± 1.8	70.0 ± 0.1	53 ~ 58[a]	-
$D_0 \ \frac{cm^2}{s}$		4.1 ± 0.3	0.3 ± 0.0	-	-
D $10^{-12} \frac{cm^2}{s}$	55 °C	68.0 ± 2.6	2.1 ± 0.2		
	45 °C	29.8 ± 0.9	0.9 ± 0.1	9.9[b], 400 [c]	2.2[b], 20 [c]
	35 °C	13.4 ± 0.3	0.4 ± 0.0		
$\frac{D\,p-\text{xylene}}{D\,o-\text{xylene}}$	55 °C	32.1 ±1.2			
	45 °C	31.6 ±0.9		4.5[b], 20[c]	
	35 °C	33.4 ±0.8			

[a] Obtained from Masuda et al. [43]. [b] Data collected at 20 °C using gravimetric methods by Wu et al. [44]. [c] Data collected at 298K using the zero length column method by Ruthven et al. [45].

4.5.2 Maxwell-Stefan diffusion coefficients

Although widely used in characterizing the performance of carbon membranes [46-49], it is possible for transport diffusion coefficients to be highly dependent on concentration [50]. A thermodynamic correction can be applied to the transport diffusion coefficient, which in the single component transport case is also known as the Maxwell-Stefan diffusion coefficient. The Fickian transport diffusion coefficient, D, determined from fits to the Fickian diffusion model can be corrected using a thermodynamic factor that results from the non-linear relationship between activity and sorbed concentration to yield a Maxwell-Stefan diffusion coefficient Đ as shown in Eq. 4.2 [51].

$$Đ = D\frac{dlnq}{dlnp} \qquad \textbf{Eq. 4.2}$$

where p is the gas-phase equilibrium pressure and q is the loading, that is, guest concentration q in equilibrium with the surrounding pressure p. Only for systems that are thermodynamically ideal ($p \propto q$) does $dlnq/dlnp \rightarrow 1.0$; non-linear sorption like that observed in PIM-1-derived CMS results in $dlnq/dlnp \equiv (dq/dp)/(q/p) > 1$. Xylene isomer sorption in carbon membranes can be described by Langmuir isotherm, as shown below:

$$\theta = \frac{q}{q^{sat}} = \frac{bp}{1+bp} \qquad \textbf{Eq. 4.3}$$

where θ is the fractional occupancy of the adsorption sites, q^{sat} is the Langmuir saturation loading of gust species, and b is the Langmuir affinity constant. By rearranging

Eq. 4.2 and Eq. 4.3, one can easily obtain Eq. 4.4, which can be used to calculate Maxwell-Stefan diffusion coefficients in this work.

$$Đ = D(1-\theta) \qquad \textbf{Eq. 4.4}$$

The temperature dependence of Maxwell-Stefan diffusion coefficients for both *p*-xylene and *o*-xylene in carbon membrane with least squares fitting, were presented in Figure 4.7. One can see that the results and conclusions derived from observations of the Fickian transport diffusion coefficient also apply to the Maxwell-Stefan diffusion coefficient. Table 4.4 tabulates the Maxwell-Stefan diffusion activation energy $E_{Đ}$ and the respective Maxwell-Stefan diffusion pre-exponential factors $Đ_0$ for both xylene isomers. Similar to the case of the transport diffusivity, *p*-xylene exhibited a lower diffusion activation energy compared with o-xylene when the Maxwell-Stefan diffusivity was utilized.

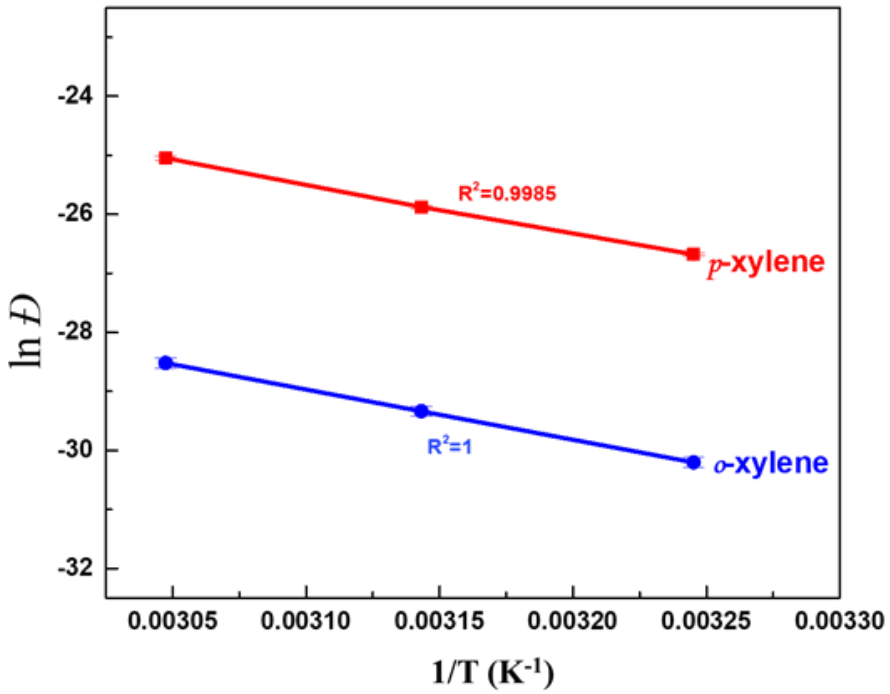

Figure 4.7 Temperature dependence of Maxwell-Stefan diffusion coefficients for xylene isomers in carbon membranes over the temperature range 35 to 55 °C (Maxwell-Stefan diffusion coefficient, Đ are in the units of cm^2/s, all data points are shown with error bars, some of them are too small to be seen).

Table 4.4 Maxwell-Stefan diffusion properties of xylene isomers for CMS membranes over temperatures ranging from 35-55 °C.

		p-xylene	*o*-xylene
$E_Đ \frac{kJ}{mol}$		68.1 ± 1.8	70.7 ± 0.2
$Đ_0 \frac{cm^2}{s}$		0.9 ± 0.1	0.1 ± 0.0(1)
$Đ\ 10^{-12} \frac{cm^2}{s}$	55 °C	13.2 ± 0.5	0.4 ± 0.0(3)
	45 °C	5.78 ± 0.2	0.2 ± 0.0(1)
	35 °C	2.59 ± 0.1	0.1 ± 0.0(1)
$\frac{Đ\ p-\text{xylene}}{Đ\ o-\text{xylene}}$	55 °C	32.2 ± 1.2	
	45 °C	31.9 ± 0.9	
	35 °C	33.8 ± 0.8	

4.6 Temperature Dependence of Permeabilities

4.6.1 Prediction of pure component permeability based on the sorption-diffusion model

The sorption isotherms of xylene isomers in PIM-1 derived CMS membrane at 35, 45 or 55 °C were fit using the Langmuir model:

$$\theta_A = q_A/q_A^{sat} = \frac{b_A p_A}{1 + b_A p_A} \qquad \textbf{Eq. 4.5}$$

Where θ_A is the fractional occupancy of the adsorption sites, q_A is the loading of component *A* (*p*-xylene or *o*-xylene) in the CMS membrane and p_A is the gas-phase equilibrium partial pressure of that component, that is, guest concentration q_A in equilibrium with the surrounding partial pressure p_A. q_A^{sat} is the Langmuir saturation loading of guest species *A* and b_A is the Langmuir affinity constant for that species.

From Eq. 4.5, we can obtain the loading for upstream (the activity of upstream is 1.0) and downstream, respectively,

$$\theta_A^{m,up} = \frac{b_A p_A^{sat}}{1 + b_A p_A^{sat}} \qquad \textbf{Eq. 4.6}$$

$$\theta_A^{m,down} = \frac{b_A p_A^{sat} a_{A,downstream}}{1 + b_A p_A^{sat} a_{A,downstream}} \qquad \textbf{Eq. 4.7}$$

Moreover, for an ideal vapor, the pressure for upstream and downstream conditions can be easily related to the activity,

$$p_{A,upstream} = p_{a_A=1} = p_A^{sat} \qquad \textbf{Eq. 4.8}$$

$$p_{A,downstream} = p_A^{sat} a_{A,downstream} \qquad \textbf{Eq. 4.9}$$

Assuming the transport diffusivity is a constant (obtained in Table 4.3) for different downstream activity conditions, the pure component permeability under different downstream activities with an upstream activity of 1.0 (corresponding to a pure component pervaporation experiment) can be calculated using the sorption-diffusion model. The sorption coefficient in these ideal conditions can be obtained by using the following equation [32,33].

$$\mathbb{S}_A = \frac{\rho_{CMS} \times q_A^{sat}}{p_A\,(upstream) - p_A\,(downstream)} \ln\left(\frac{1-\theta_A^{m,down}}{1-\theta_A^{m,up}}\right) \qquad \textbf{Eq. 4.10}$$

By putting Eq. 4.6 to Eq. 4.9 into Eq. 4.10, one can easily obtain Eq. 4.11, which can be used to calculate the pure component sorption coefficient under different downstream activities with an upstream activity of 1.0, viz.,

$$\mathbb{S}_A = \frac{\rho_{CMS} \times q_A^{sat}}{p_A^{sat}(1 - a_{A,downstream})} \ln\left(\frac{1-\frac{b_A p_A^{sat} a_{A,downstream}}{1+b_A p_A^{sat} a_{A,downstream}}}{1-\frac{b_A p_A^{sat}}{1+b_A p_A^{sat}}}\right) \qquad \textbf{Eq. 4.11}$$

The corresponding Langmuir model parameters and saturation pressure values for *p*-xylene and *o*-xylene are listed in Table 4.5. Transport diffusivities are shown in Table 4.3 and ρ_{CMS} , the density of the carbon membrane can be treated as 2.0 g/cm^3.

Table 4.5 Langmuir model parameters and saturation pressure values for *p*-xylene and *o*-xylene in PIM-1 derived CMS pyrolyzed in a pure argon environment.

	q^{sat} 10^{-4} mol/g			b kPa^{-1}			p^{sat} kPa		
	55 °C	45 °C	35 °C	55 °C	45 °C	35 °C	55 °C	45 °C	35 °C
p-xylene	11.9	12.6	13.4	14.2	22.9	38.4	5.5	3.4	2.0
o-xylene	11.1	11.1	11.1	18.0	29.7	50.9	4.3	2.7	1.6

Finally, the sorption-diffusion model, along with the diffusivities data, can be used to predict the pure component permeabilities.

4.6.2 Prediction of equimolar p-xylene/o-xylene permeation based on the Maxwell-Stefan model

4.6.2.1 Case A: No frictional coupling effects.

In the case that the downstream activities for both *p*-xylene and *o*-xylene are 0, the generalized Maxwell-Stefan model without frictional coupling effects between xylene isomers can be used to predict the mixture permeation of *p*-xylene (component A) and *o*-xylene (component B); the model can be reduced to the following equations in this case [52,53]:

$$\mathbb{P}_A$$

$$= \frac{\rho_{CMS} q_A^{sat} Đ_A}{p_A^{up} - p_A^{down}} \left(\theta_A^{up} - \theta_A^{down} + \theta_A^{down}\theta_B^{up} - \theta_A^{up}\theta_B^{down}\right) \frac{\ln\left(\frac{1-\theta_A^{down}-\theta_B^{down}}{1-\theta_A^{up}-\theta_B^{up}}\right)}{\left(1-\theta_A^{down}-\theta_B^{down}\right)-\left(1-\theta_A^{up}-\theta_B^{up}\right)} \quad \textbf{Eq. 4.12}$$

$$= \frac{\rho_{CMS} q_A^{sat} Đ_A}{p_A^{up}} \theta_A^{up} \frac{\ln\left(\frac{1}{1-\theta_A^{up}-\theta_B^{up}}\right)}{\theta_A^{up}+\theta_B^{up}}$$

$$\mathbb{P}_B$$

$$= \frac{\rho_{CMS} q_B^{sat} Đ_B}{p_B^{up} - p_B^{down}} \left(\theta_B^{up} - \theta_B^{down} + \theta_A^{up}\theta_B^{down} - \theta_A^{down}\theta_B^{up}\right) \frac{\ln\left(\frac{1-\theta_A^{down}-\theta_B^{down}}{1-\theta_A^{up}-\theta_B^{up}}\right)}{\left(1-\theta_A^{down}-\theta_B^{down}\right)-\left(1-\theta_A^{up}-\theta_B^{up}\right)} \quad \textbf{Eq. 4.13}$$

$$= \frac{\rho_{CMS} q_B^{sat} Đ_B}{p_B^{up}} \theta_B^{up} \frac{\ln\left(\frac{1}{1-\theta_A^{up}-\theta_B^{up}}\right)}{\theta_A^{up}+\theta_B^{up}}$$

where ρ_{CMS}, q_A^{sat}, $Đ_A$, p_A^{up} and q_B^{sat}, $Đ_B$, p_B^{up} have been discussed already in the previous section.

In the case of binary mixture permeation, the xylene fractional occupancies can be calculated by using the following equations:

$$\theta_{\mathrm{A}}^{\mathrm{up}} = \frac{b_A p_{\mathrm{A}}^{\mathrm{up}}}{1 + b_A p_{\mathrm{A}}^{\mathrm{up}} + b_B p_{\mathrm{B}}^{\mathrm{up}}} \qquad \textbf{Eq. 4.14}$$

$$\theta_{\mathrm{B}}^{\mathrm{up}} = \frac{b_B p_{\mathrm{B}}^{\mathrm{up}}}{1 + b_A p_{\mathrm{A}}^{\mathrm{up}} + b_B p_{\mathrm{B}}^{\mathrm{up}}} \qquad \textbf{Eq. 4.15}$$

4.6.2.2 Case B: Frictional coupling effects considered.

The generalized Maxwell-Stefan model with frictional coupling effects between xylene isomers can be used to predict the mixture permeation of *p*-xylene (component A) and *o*-xylene (component B); the model can be used to generate the following equations[33,52,53]:

$$(N) = \frac{\rho_{CMS}}{\ell} \frac{\ln\left(\frac{1-\theta_{\mathrm{A}}^{\mathrm{down}}-\theta_{\mathrm{B}}^{\mathrm{down}}}{1-\theta_{\mathrm{A}}^{\mathrm{up}}-\theta_{\mathrm{B}}^{\mathrm{up}}}\right)}{\frac{1}{1-\theta_{\mathrm{A}}^{\mathrm{up}}-\theta_{\mathrm{B}}^{\mathrm{up}}} - \frac{1}{1-\theta_{\mathrm{A}}^{\mathrm{down}}-\theta_{\mathrm{B}}^{\mathrm{down}}}} [q^{sat}]\left[B_{up}(0)\right]^{-1}\left(\pi_{up} - \pi_{down}\right) \qquad \textbf{Eq. 4.16}$$

Where $\theta_{\mathrm{A}}^{\mathrm{down}}$ and $\theta_{\mathrm{B}}^{\mathrm{down}}$ are 0 when the downstream activities for both *p*-xylene and *o*-xylene are 0. ρ_{CMS}, $\theta_{\mathrm{A}}^{\mathrm{up}}$ and $\theta_{\mathrm{B}}^{\mathrm{up}}$ are shown in Eq. 4.14-Eq. 4.15. $[q^{sat}]$ is a diagonal matrix of saturation capacities, as shown in Eq. 4.17. $\left[B_{up}(0)\right]$ is a square matrix of inverse Maxwell-Stefan coefficients at zero loading and the membrane upstream as defined in Eq. 4.18 and Eq. 4.19. (N) and $\left(\pi_{up} - \pi_{down}\right)$ are component vectors as shown in Eq. 4.20 and Eq. 4.21 respectively.

$$[q^{sat}] = \begin{bmatrix} q_A^{sat} & o \\ o & q_B^{sat} \end{bmatrix} \quad \textbf{Eq. 4.17}$$

$$\left[B_{up}(0)\right] = \begin{bmatrix} \frac{1}{Đ_A} + \frac{\theta_B^{up}}{Đ_{AB}} & -\frac{\theta_A^{up}}{Đ_{AB}} \\ -\frac{\theta_B^{up}}{Đ_{BA}} & \frac{1}{Đ_B} + \frac{\theta_A^{up}}{Đ_{BA}} \end{bmatrix} \quad \textbf{Eq. 4.18}$$

$$Đ_{AB} = Đ_{BA} = Đ_A^{\frac{\theta_A^{up}}{\theta_A^{up}+\theta_B^{up}}} \times Đ_B^{\frac{\theta_B^{up}}{\theta_A^{up}+\theta_B^{up}}} \quad \textbf{Eq. 4.19}$$

$$\left(\pi_{up} - \pi_{down}\right) = \begin{pmatrix} b_A p_A^{up} - b_A p_A^{down} \\ b_B p_B^{up} - b_B p_B^{down} \end{pmatrix} = \begin{pmatrix} b_A p_A^{up} \\ b_B p_B^{up} \end{pmatrix} \quad \textbf{Eq. 4.20}$$

$$(N) = \begin{pmatrix} N_A \\ N_B \end{pmatrix} \quad \textbf{Eq. 4.21}$$

Eq. 4.16 - Eq. 4.21 allows us to calculate the individual xylene isomer fluxes, which permits calculations of the permeability for xylene isomers via the following equations:

$$\mathbb{P}_A = \frac{N_A \ell}{p_A^{up} - p_A^{down}} \quad \textbf{Eq. 4.22}$$

$$\mathbb{P}_B = \frac{N_B \ell}{p_B^{up} - p_B^{down}} \quad \textbf{Eq. 4.23}$$

4.6.3 Model predicted permeability compared with experimental results

The sorption-diffusion model was utilized to calculate the pure component permeabilities of *p*-xylene and *o*-xylene through the PIM-1-derived CMS membrane under different downstream activity conditions; these are shown in Figure 4.8 (utilizing an activity of upstream 1.0). In this simple calculation, the activity difference between upstream and downstream can be visualized as supplying varying degrees of vacuum to the downstream or by increasing the pressure on the upstream (as in an organic solvent reverse osmosis modality). The relatively flat nature of the sorption isotherm at high activities results in a strong reduction in the sorption coefficient as the activity gradient across the membrane goes towards 0, thus resulting in significant reductions in the permeability coefficient. This simple analysis assumes a constant transport diffusivity as a function of penetrant loading; additional experiments measuring transport diffusivities under different relative pressures (i.e., different penetrant loadings) are needed to probe the validity of this assumption, although it is unlikely that the transport diffusion coefficient will increase with increasing penetrant loading in the membrane. Although the focus of this chapter is on fundamental transport measurements of xylene isomers in CMS derived from PIM-1, we experimentally investigated the permeability of p-xylene and o-xylene through these membranes to validate our sorption-diffusion measurements and permeability calculations derived from those measurements. The permeabilities of *p*-xylene and *o*-xylene through PIM-1-derived CMS membranes over an activity gradient of 1.0 (upstream) to 0.0 (downstream) at 55 °C were measured via Wicke-Kallenbach permeation. As illustrated in Figure 4.8, the permeabilities ($(5.75 \pm 0.05) \times 10^{-15} \frac{mol \times m}{m^2 \times s \times Pa}$ for *p*-xylene, ($2.24 \pm$

$0.39) \times 10^{-16} \frac{mol \times m}{m^2 \times s \times Pa}$ for *o*-xylene) determined from the Wicke-Kallenbach permeation measurements are within a factor of two of the values calculated via the sorption-diffusion model, and the selectivity (25.7 ± 4.5) is very close to the values calculated via the sorption-diffusion model.

We can compare these permeabilities to other membranes that have shown promise for this challenging separation. State-of-art ultra-thin MFI membranes are designed for high temperature pervaporation and reported *p*-xylene permeabilities ranges from 10^{-14} to $10^{-13} \frac{mol \times m}{m^2 \times s \times Pa}$ in the temperature range from 100 °C to 400 °C [54,55]. Although *p*-xylene permeabilities in PIM-1-derived CMS in this work are one order of magnitude lower than the reported values for MFI zeolites, they can be further increased via increasing the operating temperature owing to the positive permeation activation energy for PIM-1-derived CMS. For example, assuming that heat of sorption and activation energy for diffusion are not strongly affected by temperature, the *p*-xylene permeability of PIM-1-derived CMS would be $3 \times 10^{-14} \frac{mol \times m}{m^2 \times s \times Pa}$ at 200 °C, which is comparable to MFI membranes.

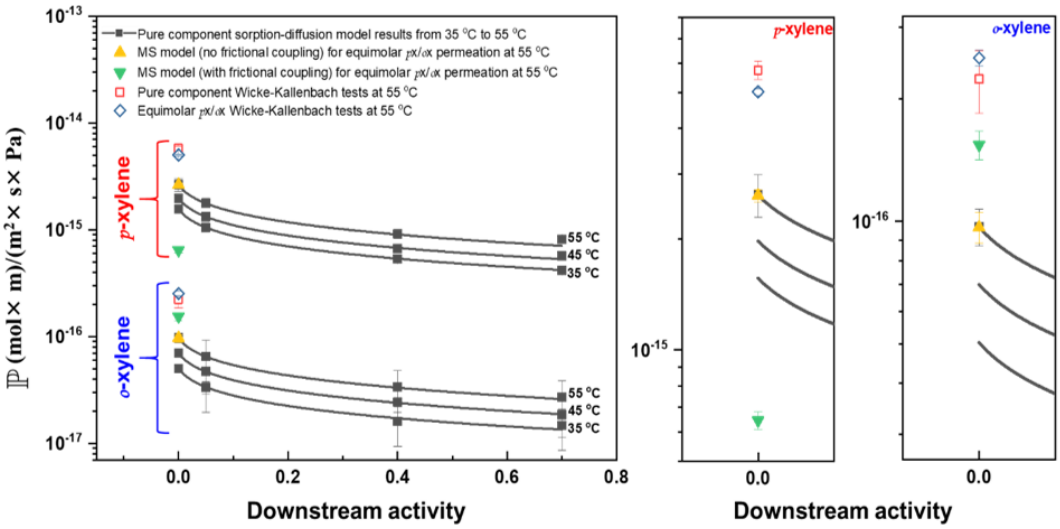

Figure 4.8 Left: Permeability of *p*-xylene and *o*-xylene through PIM-1-derived CMS membranes as a function of downstream activity; an upstream activity of 1.0 is utilized for all pure component data, and an upstream pressure of 2.42 kPa for both *p*-xylene and *o*-xylene is utilized for all mixture permeation data. Right: Comparisons of pure and mixed vapor permeation experiments as well as the sorption-diffusion and Maxwell-Stefan (MS) models with and without frictional coupling effects. —■— : permeabilities calculated via the sorption-diffusion model using pure component data; error bars represent the standard deviation propagated from the measurements of $\mathbb{S}$ and *D*. □: experimental permeabilities from pure component Wicke-Kallenbach measurements performed at 55 °C; error bars represent the standard derivation of at least three runs, each on a different CMS membrane. ▲: permeabilities calculated via the MS model using pure component sorption/diffusion data without considering the frictional coupling effects between xylene isomers; error bars represent the standard deviation propagated from the *D* measurements. ▼: permeabilities calculated via the MS model using pure component sorption/diffusion data considering the frictional coupling effects between xylene isomers; error bars represent the standard deviation propagated from the *D* measurements. ◇: experimental permeability from the equimolar Wicke-Kallenbach experiment performed at 55 °C; error bars are the standard derivation propagated from three GC runs on the same sample.

Wicke-Kallenbach permeation measurements of equimolar *p*-xylene and *o*-xylene (2.42 kPa p-xylene and 2.42 kPa o-xylene vapor upstream, helium sweep downstream) at 55 °C were conducted to further investigate the separation performance of PIM-1-derived CMS membranes and its ability to be described by the sorption-diffusion modeling approach. We utilized our single component sorption and diffusion data as inputs into the generalized Maxwell-Stefan (MS) equations, and we assessed the model's ability to predict the mixture permeabilities with and without frictional coupling effects; the frictional coupling effects were estimated using a Vignes-type correlation [52,56]. As shown in Figure 4.8, the experimental xylene permeabilities for both pure components and the mixture are higher (2.2-2.3x higher in pure component case, 1.9-2.6x higher in MS mixture case without frictional coupling effect, 1.6-7.8x higher in MS mixture case with frictional coupling effect) than the model-predicted values. Since the experimental pure component selectivities are somewhat lower (~6 %) than the selectivities predicted from pure component sorption-diffusion data (Figure 4.9), it is reasonable to conclude that small, nonselective leak pathways are contributing to the experimental permeabilities.

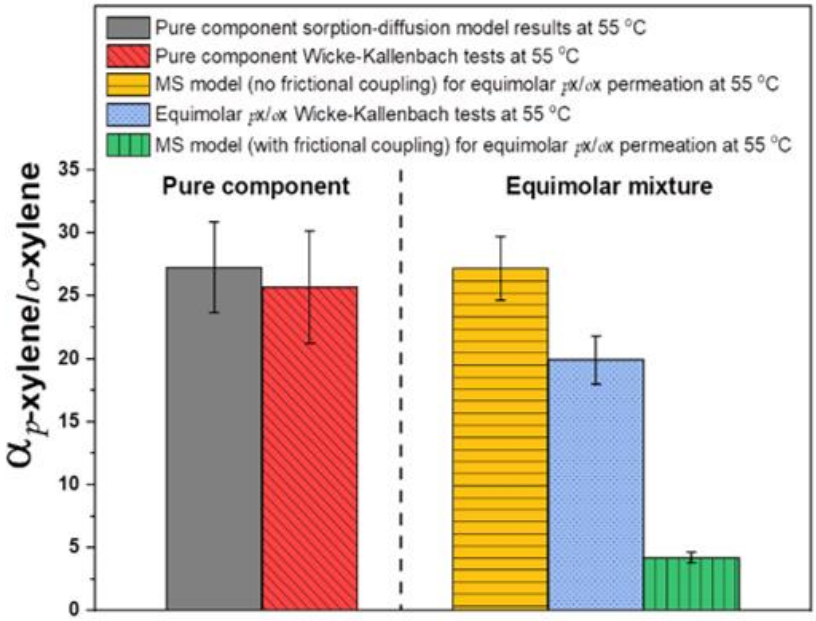

Figure 4.9 Permselectivity of *p*-xylene over *o*-xylene in PIM-1-derived CMS membrane at 55 °C; error bars are standard deviation propagated from the corresponding permeabilities.

The permeability of *p*-xylene in the mixture was observed to be ~12% lower than the corresponding pure component case, while the *o*-xylene was found to be ~13% higher than its corresponding pure component case. This is expected within the generalized Maxwell-Stefan framework (and indeed, the model also captures these trends correctly), where the frictional coupling effects between rapidly and slowly transporting components are known to reduce the transport rates of the former and increase the transport rates of the latter. It is interesting to note that the selectivity losses in the membrane were not as severe as predicted by the Maxwell-Stefan equations with frictional effects considered. This suggests that the Vignes-type correlation is not accurately capturing the extent of the frictional coupling, or, the severity of the coupling effect follows a loading gradient in the

membrane (i.e., total xylene loadings near 100% are found on the upstream side of the membrane, and strong coupling effects are exhibited, while loadings of approximately 0% are found on the downstream side of the membrane and exhibit negligible coupling effects).

Figure 4.10 highlights the least squares fitting of the permeability for the two xylene isomers studied here as a function of inverse absolute temperature. As indicated by Eq. 2.5, the temperature dependence of xylene isomer permeability follows an Arrhenius relationship. As shown in Eq. 2.9, the activation energy for sorption-diffusion permeation is the addition of the activation energy for diffusion and the apparent heat of sorption [57]. It is important to note that the activation energy for diffusion is always positive (i.e., faster diffusion at a higher temperature) while the heat of sorption is always negative (i.e., less sorption at a higher temperature); the activation energy of permeation can, therefore, be positive or negative.

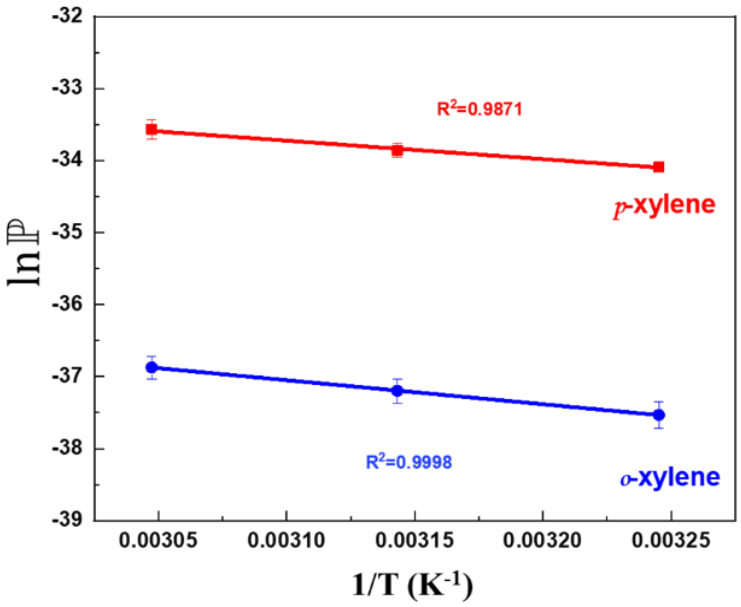

Figure 4.10 Temperature dependence of calculated permeabilities for xylene isomers in CMS (permeability ℙ, in the unit of (mol×m)/(m²×s×Pa), is calculated based on the pure component sorption-diffusion model); error bars represent the standard deviation propagated from the measurements of 𝕊 and *D*.

As shown in Table 4.2 and Table 4.3, despite the large heats of sorption for the xylene isomers in the CMS, the activation energy for diffusion is sufficiently high that the activation energy for permeation is positive; i.e., the permeability will increase with increasing temperature. The positive value of activation energy for permeation indicates that permeation is dominated by the diffusion process. Aside from the temperature dependence of permeation and selectivity (which is based on a particular CMS microstructure), the CMS performance can be further tuned via a careful choice of pyrolysis protocol, pyrolysis atmosphere, and polymer precursor functionality [18,27,58]. Unlike the PIM-1-derived CMS in this work, MFI-type zeolites exhibit negative activation

energies for xylene permeation, which results in the decrease of permeabilities for both xylenes with increasing temperature [55]. However, the selectivity of MFI membranes as a function of temperature depends on the orientation of the zeolite's pores within the membrane itself: the selectivities for *p*-xylene over *o*-xylene of the resulting membrane decrease with increasing temperature for c-oriented structures and increase with increasing temperature for a- and b-oriented structures [55]. The permeation activation energy $E_{\mathbb{P}}$ and the respective pre-exponential factors of permeation $\mathbb{P}_0$ were calculated using Eq. 2.5 and are listed in Table 4.6. *o*-Xylene has a slightly larger activation energy for permeation than *p*-xylene, which suggests that the selectivity for *p*-xylene over *o*-xylene in the CMS membrane will decrease with increasing temperature. The permeation pre-exponential factors represent the permeability at an idealized infinite temperature. The critical point to improve the separation performance of carbon membranes lies in enhancing the diffusive selectivity and increasing the diffusion coefficient.

Table 4.6 Permeation properties of xylene isomers for PIM-1-derived CMS from 35-55 °C.

			p-xylene	*o*-xylene
	$E_{\mathbb{P}}$ $(\frac{kJ}{mol})$		21.3 ± 1.7	27.8 ± 0.3
	$\mathbb{P}_0$ $(10^{-11}\ \frac{mol \cdot m}{m^2 \cdot s \cdot Pa})$		0.6 ± 0.2	0.3 ± 0.0
α *p*-xylene/*o*-xylene	Sorption-diffusion model for pure component [a]	55 °C	27.3 ± 3.6	
		45 °C	28.2 ± 2.7	
		35 °C	31.2 ± 2.0	
	WK pure component experiments [b]	55 °C	25.7 ± 4.5	
	WK mixture experiments [c]	55 °C	19.9 ± 1.9	
	MS prediction without frictional coupling effect [d]	55 °C	24.2 ± 2.5	
	MS prediction with frictional coupling effect [d]	55 °C	4.2 ± 0.4	

[a] Model based on unit activity vapor upstream and zero activity vapor downstream.

[b] Determined from Wicke-Kallenbach pure component permeation measurements (unit activity vapor upstream, helium sweep downstream) at 55 °C.

[c] Determined from Wicke-Kallenbach equimolar mixture permeation of *p*-xylene and *o*-xylene (2.42 kPa *p*-xylene and 2.42 kPa *o*-xylene vapor upstream, helium sweep downstream) at 55 °C.

[d] Model based on 2.42 kPa *p*-xylene and 2.42 kPa *o*-xylene vapor upstream and zero activity vapor downstream.

4.7 Entropic and Enthalpic Diffusion Selectivities of Xylene Isomers

The enthalpic, entropic, and the overall diffusive selectivity of xylene isomers at temperatures ranging from 35 to 55 °C are listed in Table 4.7. The enthalpic selectivity was obtained by comparing the diffusion activation energy values for the two xylene isomers, while the entropic diffusion selectivity was calculated according to Eq. 2.14. As shown in Table 4.7, based on the transport diffusion coefficients, the enthalpic diffusion selectivity is approximately 2.3, while the entropic diffusion selectivity is as large as 14.3. Also, as expected, the enthalpic (2.7) and entropic (12.3) diffusion selectivities calculated based on the Maxwell-Stefan diffusivity show consistent trends in Table 4.7 with those obtained from transport diffusivity-based calculations. These experiments provide strong evidence that the ultramicropores within PIM-1-derived CMS are capable of differentiating large organic molecules based on differences in available conformations in the activated state, and this study is one of the first to suggest that the entropic diffusion selectivity concept can be extended beyond relatively simple gas molecules with fewer vibrational and rotational modes. Moreover, the diffusion selectivity reported here is also higher than that of MFI-type zeolites at similar temperatures (e.g., selectivities of 4.5-20 are observed in MFI at 20-25 $^{\circ}$C) [44,45].

Table 4.7 Contributions to the diffusive selectivity of *p*-xylene /*o*-xylene in pure argon pyrolyzed PIM-1-derived CMS.

	Transport Diffusivity	Maxwell-Stefan Diffusivity
Enthalpic Diffusion Selectivity	2.3 ± 0.0 (2.2 ± 0.0)	2.7 ± 0.0 (2.6 ± 0.0)
Entropic Diffusion Selectivity	14.3 ± 0.7 (14.6 ± 1.4)	12.3 ± 0.6 (12.5 ± 1.2)
Diffusive Selectivity	32.4 ± 1.7 (32.1 ± 3.0)	32.6 ± 1.7 (32.2 ± 3.0)

[a] Non-parentheses values are the average selectivity in the temperature ranging from 35 to 55 °C, while the numbers inside the parentheses are selectivity at 55 °C.

4.8 Summary and Conclusions

In summary, this chapter suggests that pure argon pyrolyzed PIM-1-derived carbon molecular sieve membranes have the potential to be used in the separation of *p*-xylene and *o*-xylene. The effect of temperature on permeation, sorption and diffusion was studied not only for practical purposes (i.e., many industrial streams are at temperatures well above ambient laboratory temperatures), but also to obtain a fundamental understanding of the factors dominating the separation of xylene isomers. The dominating effect in permeation for both isomers was found to be diffusion such that the permeability of the membrane increased with increasing temperature, although the selectivity decreases as a result. The selectivity derives almost entirely from differences in molecular motion (i.e., diffusivity) of the isomers within the CMS material. Significant entropic diffusion selectivity was

observed in favor of *p*-xylene over *o*-xylene, and this is attributed to the relatively tight "slit-shaped" micropore structure in the carbon membrane, which effectively limits more conformational states of the less symmetric *o*-xylene during its diffusive jump through an ultramicropores when compared to the more symmetric *p*-xylene. Mixture permeation experiments at high upstream loadings and relatively low temperatures (55 $^{\circ}$C) also reveal promising *p*-xylene/*o*-xylene selectivities (~20). Although frictional coupling effects played a role in reducing the selectivity somewhat relative to the pure component permselectivity, the extent of this factor was not as severe as predicted by the Maxwell-Stefan model. For the first time, this study provides solid evidence for the significance of entropic diffusion selectivity of non-gaseous molecules in carbon membranes. More importantly, this understanding can significantly impact membrane design and lead to further improvement of the separation performance by tuning the entropic diffusion selectivity.

4.9 References

1. D. R. Paul. Creating new types of carbon-based membranes. *Science* **2012**;335(6067):413-414.

2. N. Bhuwania, Y. Labreche, C. S. Achoundong, J. Baltazar, S. K. Burgess, S. Karwa, L. Xu, C. L. Henderson, P. J. Williams, W. J. Koros. Engineering substructure morphology of asymmetric carbon molecular sieve hollow fiber membranes. *Carbon* **2014**;76:417-434.

3. C. Zhang, W. J. Koros. Ultraselective carbon molecular sieve membranes with tailored synergistic sorption selective properties. *Advanced Materials* **2017**;29(33).

4. D.-Y. Koh, B. A. McCool, H. W. Deckman, R. P. Lively. Reverse osmosis molecular differentiation of organic liquids using carbon molecular sieve membranes. *Science* **2016**;353(6301):804-807.

5. H. Richter, H. Voss, N. Kaltenborn, S. Kämnitz, A. Feldhoff, J. Caro, S. Roitsch, I. Voigt, A. Wollbrink. High‐flux carbon molecular sieve membranes for gas separation. *Angewandte Chemie* **2017**.

6. R. Lively. Carbon molecular sieve membranes aim to cut energy use in hydrocarbon separations. *Membrane Technology* **2017**;2017(1):9-10.

7. O. Sanyal, C. Zhang, G. B. Wenz, S. Fu, N. Bhuwania, L. Xu, M. Rungta, W. J. Koros. Next generation membranes—using tailored carbon. *Carbon* **2018**;127:688-698.

8. W. J. Koros, C. Zhang. Materials for next-generation molecularly selective synthetic membranes. *Nature materials* **2017**;16(3):289-297.

9. Y. Song, D. K. Wang, G. Birkett, W. Martens, M. C. Duke, S. Smart, J. C. D. da Costa. Mixed matrix carbon molecular sieve and alumina (CMS-Al2O3) membranes. *Scientific reports* **2016**;6:30703.

10. N. B. McKeown, P. M. Budd. Polymers of intrinsic microporosity (PIMs): organic materials for membrane separations, heterogeneous catalysis and hydrogen storage. *Chemical Society Reviews* **2006**;35(8):675-683.

11. E. K. McGuinness, F. Zhang, Y. Ma, R. P. Lively, M. D. Losego. Vapor phase infiltration of metal oxides into nanoporous polymers for organic solvent separation membranes. *Chemistry of Materials* **2019**;31(15):5509-5518.

12. F. Zhang, Y. Ma, Y. Kondo, V. Breedveld, R. P. Lively. A guide to solution‐based additive manufacturing of polymeric structures: Ink design, porosity manipulation, and printing strategy. *Journal of Advanced Manufacturing and Processing* **2020**;2(1):e10026.

13. F. Zhang, Y. Ma, J. Liao, V. Breedveld, R. P. Lively. Solution‐Based 3D Printing of Polymers of Intrinsic Microporosity. *Macromolecular Rapid Communications* **2018**;39(13):1800274.

14. K.-S. Liao, S. Japip, J.-Y. Lai, T.-S. Chung. Boron-embedded hydrolyzed PIM-1 carbon membranes for synergistic ethylene/ethane purification. *Journal of Membrane Science* **2017**;534:92-99.

15. J. Liu, Y. Xiao, T.-S. Chung. Flexible thermally treated 3D PIM-CD molecular sieve membranes exceeding the upper bound line for propylene/propane separation. *Journal of Materials Chemistry A* **2017**;5(9):4583-4595.

16. O. Salinas, X. Ma, E. Litwiller, I. Pinnau. High-performance carbon molecular sieve membranes for ethylene/ethane separation derived from an intrinsically microporous polyimide. *Journal of Membrane Science* **2016**;500:115-123.

17. H. J. Kim, D.-G. Kim, K. Lee, Y. Baek, Y. Yoo, Y. S. Kim, B. G. Kim, J.-C. Lee. A Carbonaceous Membrane based on a Polymer of Intrinsic Microporosity (PIM-1) for Water Treatment. *Scientific reports* **2016**;6:36078.

18. R. Swaidan, B. S. Ghanem, E. Litwiller, I. Pinnau. Pure-and mixed-gas CO 2/CH 4 separation properties of PIM-1 and an amidoxime-functionalized PIM-1. *Journal of Membrane Science* **2014**;457:95-102.

19. H. Yin, Y. Z. Chua, B. Yang, C. Schick, W. J. Harrison, P. M. Budd, M. Böhning, A. Schönhals. First Clear-Cut Experimental Evidence of a Glass Transition in a Polymer with Intrinsic Microporosity: PIM-1. *The journal of physical chemistry letters* **2018**;9(8):2003-2008.

20. P. M. Budd, B. S. Ghanem, S. Makhseed, N. B. McKeown, K. J. Msayib, C. E. Tattershall. Polymers of intrinsic microporosity (PIMs): robust, solution-processable, organic nanoporous materials. *Chemical Communications* **2004**(2):230-231.

21. M. Rungta, L. Xu, W. J. Koros. Carbon molecular sieve dense film membranes derived from Matrimid® for ethylene/ethane separation. *Carbon* **2012**;50(4):1488-1502.

22. D. Q. Vu, W. J. Koros, S. J. Miller. High pressure CO2/CH4 separation using carbon molecular sieve hollow fiber membranes. *Industrial & Engineering Chemistry Research* **2002**;41(3):367-380.

23. N. Du, G. P. Robertson, J. Song, I. Pinnau, S. Thomas, M. D. Guiver. Polymers of intrinsic microporosity containing trifluoromethyl and phenylsulfone groups as materials for membrane gas separation. *Macromolecules* **2008**;41(24):9656-9662.

24. Z. Tian, S. Wang, Y. Wang, X. Ma, K. Cao, D. Peng, X. Wu, H. Wu, Z. Jiang. Enhanced gas separation performance of mixed matrix membranes from graphitic

carbon nitride nanosheets and polymers of intrinsic microporosity. *Journal of Membrane Science* **2016**;514:15-24.

25. J. Weber, Q. Su, M. Antonietti, A. Thomas. Exploring polymers of intrinsic microporosity – microporous, soluble polyamide and polyimide. *Macromolecular Rapid Communications* **2007**;28(18 - 19):1871-1876.

26. U. H. Bunz, V. Enkelmann, L. Kloppenburg, D. Jones, K. D. Shimizu, J. B. Claridge, H.-C. zur Loye, G. Lieser. Solid-state structures of phenyleneethynylenes: comparison of monomers and polymers. *Chemistry of Materials* **1999**;11(6):1416-1424.

27. O. Salinas, X. Ma, E. Litwiller, I. Pinnau. Ethylene/ethane permeation, diffusion and gas sorption properties of carbon molecular sieve membranes derived from the prototype ladder polymer of intrinsic microporosity (PIM-1). *Journal of Membrane Science* **2016**;504:133-140.

28. G. Jenkins, K. Kawamura. *Polymeric carbons- carbon fibre, glass and char***1976**.

29. B. Zhang, T. Wang, S. Zhang, J. Qiu, X. Jian. Preparation and characterization of carbon membranes made from poly (phthalazinone ether sulfone ketone). *Carbon* **2006**;44(13):2764-2769.

30. L. Hao, K.-S. Liao, T.-S. Chung. Photo-oxidative PIM-1 based mixed matrix membranes with superior gas separation performance. *Journal of Materials Chemistry A* **2015**;3(33):17273-17281.

31. S. A. El-Khodary, G. M. El-Enany, M. El-Okr, M. Ibrahim. Preparation and characterization of microwave reduced graphite oxide for high-performance supercapacitors. *Electrochimica Acta* **2014**;150:269-278.

32. K. Eum, C. Ma, D. Y. Koh, F. Rashidi, Z. Li, C. W. Jones, R. P. Lively, S. Nair. Zeolitic Imidazolate Framework Membranes Supported on Macroporous Carbon Hollow Fibers by Fluidic Processing Techniques. *Advanced Materials Interfaces* **2017**;4(12).

33. F. Kapteijn, J. Moulijn, R. Krishna. The generalized Maxwell–Stefan model for diffusion in zeolites:: sorbate molecules with different saturation loadings. *Chemical Engineering Science* **2000**;55(15):2923-2930.

34. H. Thamm. Calorimetric study on the state of aromatic molecules sorbed on silicalite. *Journal of Physical Chemistry* **1987**;91(1):8-11.

35. M. Grahn, A. Holmgren, J. Hedlund. Adsorption of n-hexane and p-xylene in thin silicalite-1 films studied by FTIR/ATR spectroscopy. *The Journal of Physical Chemistry C* **2008**;112(20):7717-7724.

36. W. Koros, G. Fleming. Membrane-based gas separation. *Journal of Membrane Science* **1993**;83(1):1-80.

37. L. Costello, W. Koros. Thermally stable polyimide isomers for membrane‐based gas separations at elevated temperatures. *Journal of Polymer Science Part B: Polymer Physics* **1995**;33(1):135-146.

38. L. M. Costello, W. J. Koros. Effect of structure on the temperature dependence of gas transport and sorption in a series of polycarbonates. *Journal of Polymer Science Part B: Polymer Physics* **1994**;32(4):701-713.

39. O. Talu, C. J. Guo, D. T. Hayhurst. Heterogeneous adsorption equilibria with comparable molecule and pore sizes. *The Journal of Physical Chemistry* **1989**;93(21):7294-7298.

40. C. Zhang, R. P. Lively, K. Zhang, J. R. Johnson, O. Karvan, W. J. Koros. Unexpected molecular sieving properties of zeolitic imidazolate framework-8. *The journal of physical chemistry letters* **2012**;3(16):2130-2134.

41. J. Crank. *The mathematics of diffusion*: Oxford university press; **1979**.

42. S. Burgess, R. Kriegel, W. Koros. Diffusion coefficient modeling in polyester barrier materials: applications of infinite series solutions. *Soc. Plast. E.-ANTEC* **2014**:830-835.

43. T. Masuda, Y. Fujikata, T. Nishida, K. Hashimoto. The influence of acid sites on intracrystalline diffusivities within MFI-type zeolites. *Microporous and Mesoporous Materials* **1998**;23(3-4):157-167.

44. P. Wu, A. Debebe, Y. H. Ma. Adsorption and diffusion of C6 and C8 hydrocarbons in silicalite. *Zeolites* **1983**;3(2):118-122.

45. D. M. Ruthven, M. Eic, E. Richard. Diffusion of C8 aromatic hydrocarbons in silicalite. *Zeolites* **1991**;11(7):647-653.

46. J. Su, A. C. Lua. Experimental and theoretical studies on gas permeation through carbon molecular sieve membranes. *Separation and Purification Technology* **2009**;69(2):161-167.

47. S. Lagorsse, F. Magalhaes, A. Mendes. Carbon molecular sieve membranes: sorption, kinetic and structural characterization. *Journal of Membrane Science* **2004**;241(2):275-287.

48. J. Adams, N. Bighane, W. J. Koros. Pore morphology and temperature dependence of gas transport properties of silica membranes derived from oxidative thermolysis of polydimethylsiloxane. *Journal of Membrane Science* **2017**;524:585-595.

49. X. Ning, W. J. Koros. Carbon molecular sieve membranes derived from Matrimid® polyimide for nitrogen/methane separation. *Carbon* **2014**;66:511-522.

50. A. I. Skoulidas, D. S. Sholl, R. Krishna. Correlation effects in diffusion of CH4/CF4 mixtures in MFI zeolite. A study linking MD simulations with the Maxwell− Stefan formulation. *Langmuir* **2003**;19(19):7977-7988.

51. J. Kärger, D. M. Ruthven, D. N. Theodorou. *Diffusion in nanoporous materials*: John Wiley & Sons; **2012**.

52. R. Krishna, R. Baur. Analytic solution of the Maxwell–Stefan equations for multicomponent permeation across a zeolite membrane. *Chemical Engineering Journal* **2004**;97(1):37-45.

53. R. Krishna, R. Baur. Modelling issues in zeolite based separation processes. *Separation and Purification Technology* **2003**;33(3):213-254.

54. J. Hedlund, J. Sterte, M. Anthonis, A.-J. Bons, B. Carstensen, N. Corcoran, D. Cox, H. Deckman, W. De Gijnst, P.-P. de Moor. High-flux MFI membranes. *Microporous and Mesoporous Materials* **2002**;52(3):179-189.

55. Z. Lai, G. Bonilla, I. Diaz, J. G. Nery, K. Sujaoti, M. A. Amat, E. Kokkoli, O. Terasaki, R. W. Thompson, M. Tsapatsis. Microstructural optimization of a zeolite membrane for organic vapor separation. *Science* **2003**;300(5618):456-460.

56. R. Krishna, J. Wesselingh. The Maxwell-Stefan approach to mass transfer. *Chemical Engineering Science* **1997**;52(6):861-911.

57. S. Fu, E. S. Sanders, S. S. Kulkarni, G. B. Wenz, W. J. Koros. Temperature dependence of gas transport and sorption in carbon molecular sieve membranes derived from four 6FDA based polyimides: Entropic selectivity evaluation. *Carbon* **2015**;95:995-1006.

58. R. J. Swaidan, X. Ma, I. Pinnau. Spirobisindane-based polyimide as efficient precursor of thermally-rearranged and carbon molecular sieve membranes for enhanced propylene/propane separation. *Journal of Membrane Science* **2016**;520:983-989.

CHAPTER 5. CREATION OF WELL-DEFINED "MID-SIZED" MICROPORES IN PIM-1 DERIVED CMS MEMBRANES[‡]

5.1 Introduction

The previous chapter on "dense" CMS films prepared from PIM-1 precursors has shown that these materials have competitive xylene permeabilities and entropy-dominated selectivities for the *para*-/*ortho*- isomer pair [1]. Importantly, these performance parameters were achieved under conditions of high guest molecule fractional occupancy in the membrane. However, the size of the ultramicropores inside this kind of CMS material is quite similar to N_2 (3.64 Å), which severely limits the transport rate of *p*-xylene [1]. Various templating and block copolymer techniques are able to create well-defined carbonaceous pores in the range of 1-2 nm [2-4] and pyrolysis of high free volume polyimides is capable of creating CMS materials with pores less than 0.5 nm [5,6]. However, the creation of well-defined micropores in the range of 0.5-1 nm is difficult, and existing techniques require complex precursor pretreatments or extensive chemical post-treatments on the as-made CMS membranes. Kim et al. fabricated carbonaceous membranes for water treatment by heating PIM-1 in an N_2/H_2 gas (95/5 vol%) environment (1100-1300 °C at 5 °C min^{-1}); however, these authors observed a carbon pore structure with a wide distribution of pores [7]. Inspired by this work and the teachings from the pyrolysis of high free volume polyimides, we create "mid-range" micropores in CMS membranes via incorporation of H_2 in our pyrolysis environment, but utilize a heating

[‡] This chapter has been published on *Angewandte Chemie International Edition* as Creation of Well-Defined "Mid-Sized" Micropores in Carbon Molecular Sieve Membranes, 58 (38), **2019**, 13259-13265.

protocol designed for the fabrication of well-defined CMS structures. Moreover, we show that this approach can be easily applied to create hollow fiber membranes capable of separating xylene isomers.

5.2 Fabrication of CMS Membrane with the Help of H_2

CMS membranes were fabricated from the polymeric precursor in a pyrolysis set-up located inside a fume hood, as shown in Figure 5.1. Dried circular polymeric films or hollow fiber membranes were first placed on a stainless steel mesh plate, placed into a quartz tube, and loaded into a three-zone tube furnace (OTF-1200X-III-S-UL, MTI Corporation). Each zone is independently temperature controlled and thus, the temperature distribution inside the quartz tube was assumed to be uniform. Sealing of the quartz tube was insured by a pair of SS 304 vacuum flanges with double high-temperature silicone o-rings. An oxygen-free atmosphere was achieved by purging the tube with the desired gas mixture for at least 12 hrs. Two digital flow meters (Bubble-O-Meter) were used to monitor the flow rates of hydrogen/argon mixed gas and pure argon lines, which can precisely control the hydrogen concentration in the inert environment. A surface-mounted hydrogen detector is triggered if the hydrogen concentration exceeds 8000 ppm inside the fume hood. The typical oxygen concentration in the tube furnace before pyrolysis was below 0.5 ppm as measured by an inline oxygen analyzer (R1100-ZF Rapidox 1100ZF, CEA Instruments, Inc.).

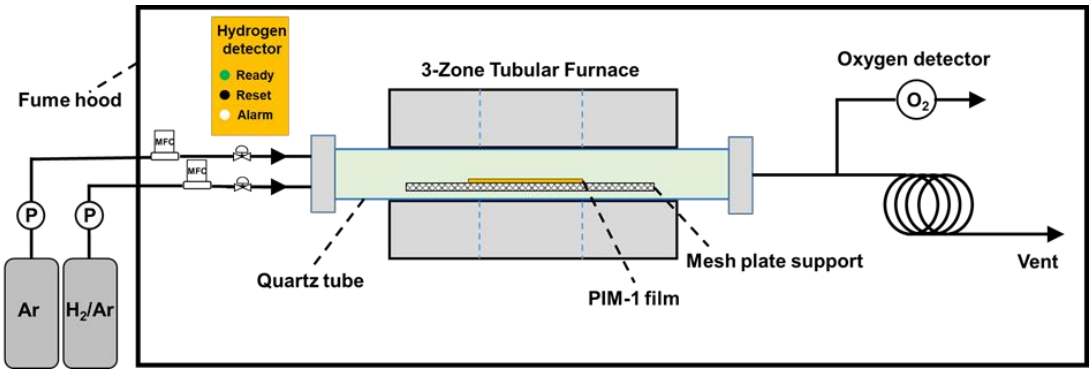

Figure 5.1 Diagram of the pyrolysis setup with H_2 in the pyrolysis environment.

The H_2 concentration (4, 2, 1, or 0 vol%) was tuned by combining a premixed 4 vol% H_2/Ar and a UHP Ar stream at the appropriate flow rate ratios. It is important to note that 4 vol% is the lower explosive limit of hydrogen in air at ambient temperature and pressure;[8] we elected to use vendor-mixed tanks of H_2/Ar to stay below this limit and then further dilute this tank with pure argon to tune the hydrogen concentration. The resulting dense membrane samples were named with the final pyrolysis temperature and H_2 concentration. For example, "CMS_500 °C_4% H_2" indicates a dense PIM-1 derived CMS membrane fabricated at 500 °C in a 4 vol% H_2 atmosphere. The CMS hollow fiber membranes were fabricated only at 500 °C and are named according to their H_2 concentration such as "CMS_HFM_4% H_2". The optimized heating protocols used are illustrated in Table 5.1 [9,10]:

Table 5.1 Heating protocols used to fabricate CMS with well-defined "mid-sized" micropores.

Protocol phase	Step	Heating rate (°C/min)	Final pyrolysis temperature		
			500 °C	800 °C	1100 °C
Ramp	1	10	25-200 °C	25-500 °C	25-800 °C
	2	3	200-485 °C	500-785 °C	800-1085 °C
	3	0.25	485-500 °C	785-800 °C	1085-1100 °C
Soak	4	0	Soak for 2 hrs at 500 °C	Soak for 2 hrs at 800 °C	Soak for 2 hrs at 1100 °C
Cool	5	-	Natural cooling back to 25 °C under pyrolysis environment		

As shown in Figure 5.2, the free-standing dense CMS membranes were fixed between rings of aluminum tape (0.003 inches thick, McMaster-Carr) with an outer diameter of 1 inch and the inner diameter of 3/8 inch and sealed by a chemically-resistant epoxy (MarineWeld 8272, JB Weld) for the permeation tests. The CMS hollow fiber membrane (HFM, Figure 5.3) modules were assembled in 316 stainless steel tubes using J-B weld MarineWeld 8272 epoxy.

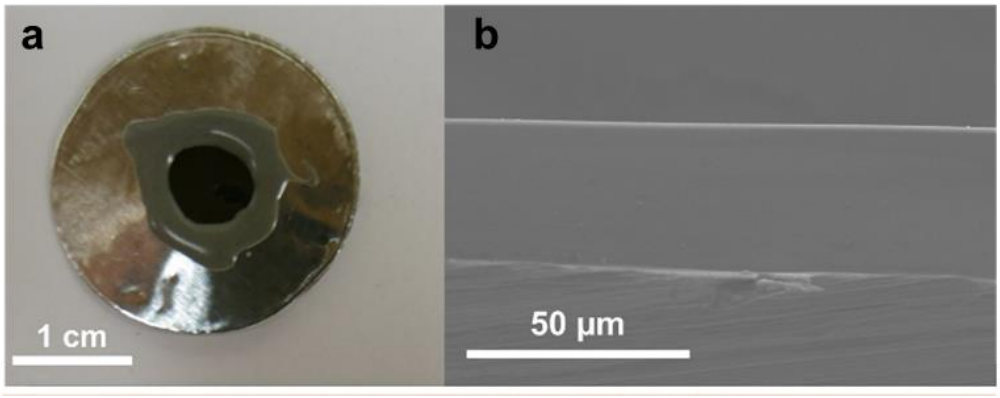

Figure 5.2 a) Digital photograph of a PIM-1-derived CMS dense membrane sealed with epoxy and aluminum tape for permeation testing. b) The SEM cross-sectional image of a CMS dense membrane.

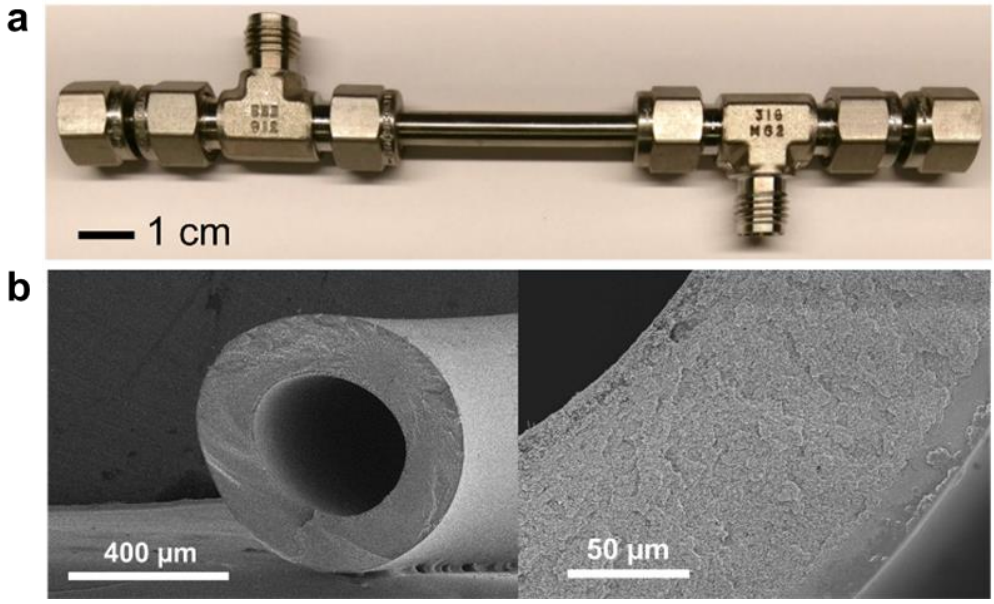

Figure 5.3 a) Digital photograph of a CMS HFM module. b) SEM cross-sectional images of a CMS HFM.

5.3 Membrane Characterization

5.3.1 N_2 physisorption experiments

The tuning effect of H_2 on the pore structure of CMS is demonstrated by N_2 physisorption experiments performed at 77 K (Figure 5.4 and Figure 5.5). Pore volume and surface obtained from the N_2 physisorption experiments were summarized in Table 5.2.

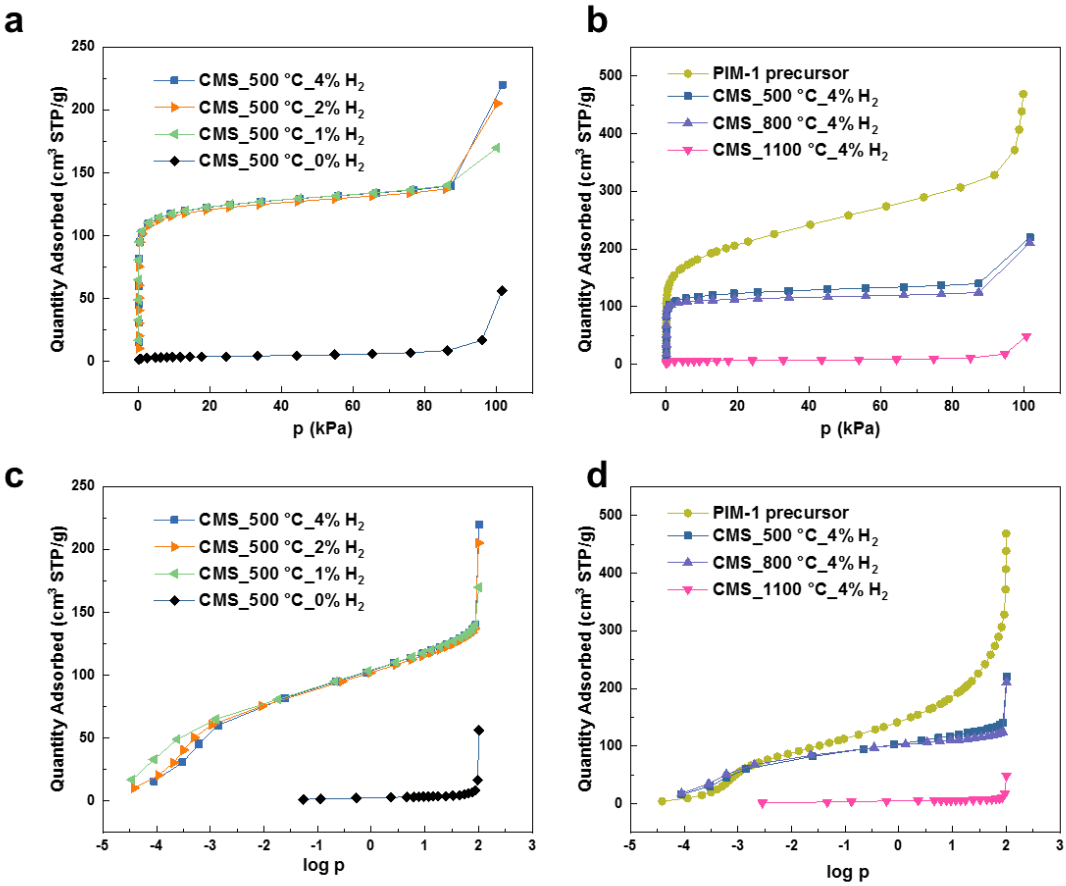

Figure 5.4 Nitrogen physisorption at 77 K for PIM-1 and PIM-1-derived CMS pyrolyzed under different H_2 concentrations (a, c) and different final pyrolysis temperature (b, d) as a function of p (a, b) and log p (c, d) used for the derivation of pore size distribution.

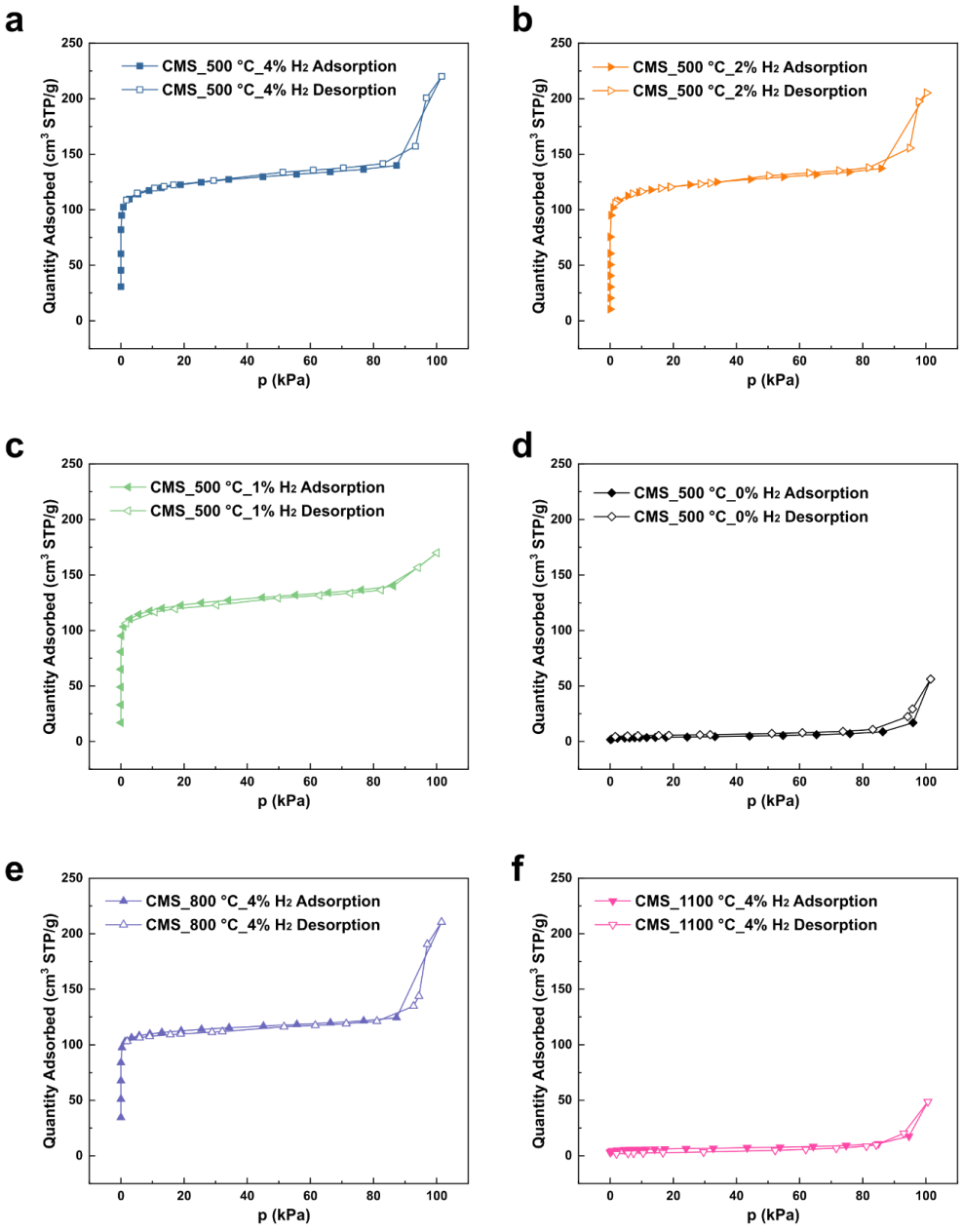

Figure 5.5 Nitrogen adsorption/desorption isotherms at 77 K for PIM-1-derived CMS pyrolyzed under different fabrication conditions.

Table 5.2 Pore volume and surface area from N_2 physisorption experiments for PIM-1 precursor and CMS formed under different conditions.

Sample	Pore volume (cm^3/g)	Surface area (m^2/g)
PIM-1 precursor	0.725	723
CMS_500 °C_0% H_2	0.007	23
CMS_500 °C _1% H_2	0.153	450
CMS_500 °C _2% H_2	0.158	461
CMS_500 °C _4% H_2	0.161	471
CMS_800 °C _4% H_2	0.156	447
CMS_1100 °C _4% H_2	0.004	14

As illustrated in Figure 5.6, three hydrogen volume fractions and a control experiment (i.e., 4, 2, 1, and 0 vol% H_2), were investigated using a final pyrolysis temperature of 500 °C. It is worth noting that reasonable nitrogen physisorption isotherms at 77 K for CMS pyrolyzed under a 0% H_2 atmosphere cannot be obtained, which indicates that the size of ultramicropores within this CMS is quite similar to N_2 (3.64 Å) thus resulting in extremely slow N_2 diffusion (it is important to note that these materials can still adsorb and permeate xylene isomers at 55°C) [1]. In contrast, the CMS pyrolyzed under H_2-containing atmospheres revealed ultramicropores ranging from 5 to 7 Å, which are significantly larger than those in the CMS pyrolyzed without H_2. Moreover, the distributions of ultramicropores are narrower as the hydrogen content decreases from 4% to 1% (full width at half maximum decreases from 2.8 Å to 1.1 Å). Interestingly, the pore size distribution of the resulting CMS is similar to that of the PIM-1 precursor. It can be

observed that the distributions of micropores do not change appreciably at the varying levels of hydrogen in the pyrolysis atmosphere. The micropores in CMS_500°C_0% H_2 are not detectable by N_2 physisorption experiments due to the extremely narrow ultramicropores existing in the sample. By comparing the pore size distribution of CMS samples pyrolyzed under 500 and 800 °C, one can see that higher pyrolysis temperature will narrow both the micropores and ultramicropores. As expected, under very high pyrolysis temperature (1100 °C), a severe tightening of the CMS matrix still occurs even in the presence of H_2.

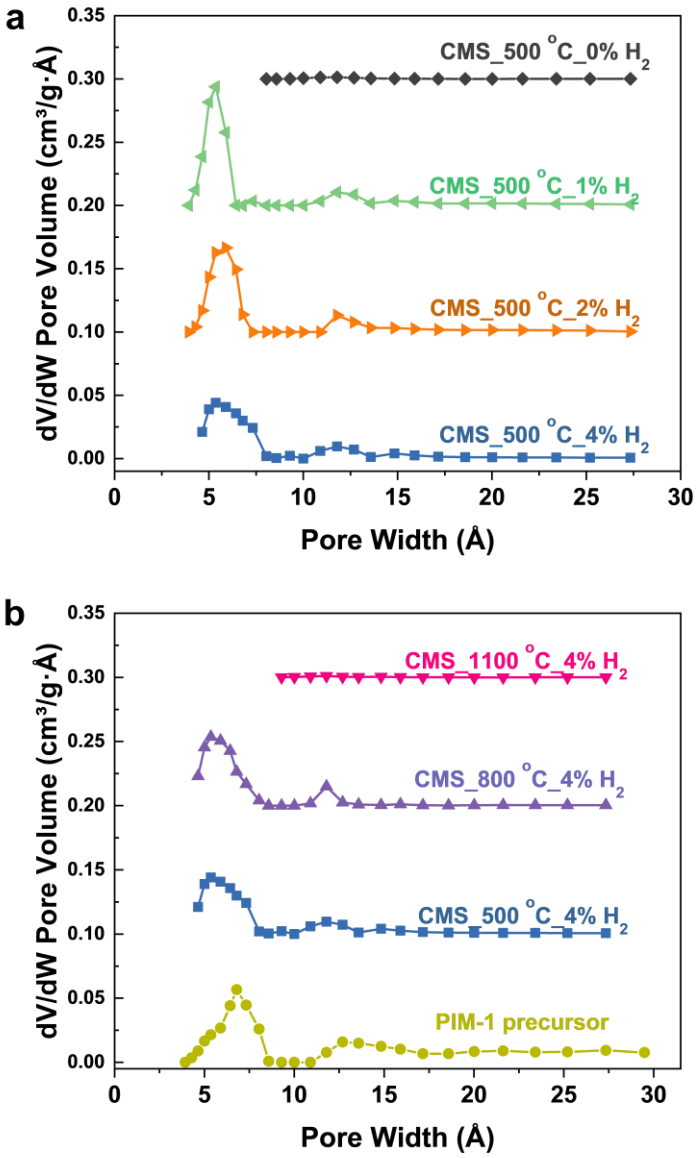

Figure 5.6 Pore size distributions measured by N_2 physisorption at 77 K for CMS pyrolyzed under a) different H_2 concentrations and b) different final pyrolysis temperatures.

It is worth noting that the pore size distribution probed by nitrogen physisorption does not include the pores with a size smaller than the nitrogen kinetic diameter (i.e., 3.64

Å) due to the diffusion limitation. The lack of nitrogen uptake data at low pressure range makes the direct calculation of pores smaller than 5 Å difficult. However, as investigated in Chapter 4, the ultramicropores smaller than 5 Å may play essential roles in the selective transportation of xylene isomers. In order to fully understand the pore structures of PIM-derived CMS membranes, the sub-5-Å ultramicropore volumes were estimated by subtracting the pore volumes for pores larger than 5 Å from the total pore volumes. The total pore volume was calculated from the total nitrogen uptake at 99 % partial pressure, which is expected to completely occupy the pores due to the condensation. The pore volumes under different size range for CMS_ PIM-1 _500 °C_4% H_2 are summarized in Table 5.3. Combined with the highly selective sub-5-Å ultramicropores resulted from the tight carbon strand packing, the trimodal pore size distribution contributes to the highly tunable xylene transportation performance.

Table 5.3 Pore volume values for CMS_ PIM-1 _500 °C_4% H_2

CMS_ PIM-1 _500 °C_4% H_2	Pore volume (cm^3/g)
Total pore volume	0.161
Pore volume (>20 Å)	0.011
Pore volume (10-20 Å)	0.034
Pore volume (5-10 Å)	0.113
Estimated pore volume (<5 Å)	0.003

The above analysis indicates that both final pyrolysis temperature and H_2 concentration in the pyrolysis atmosphere play vital roles in the pore structure of CMS. Moreover, the development of these "mid-range" micropores is related to the polymer precursor structure. As a control experiment, we pyrolyzed Matrimid® (a high free volume polyimide, but not a PIM material) in the presence of H_2 and were unable to detect microporosity via N_2 physisorption techniques (Figure 5.7).

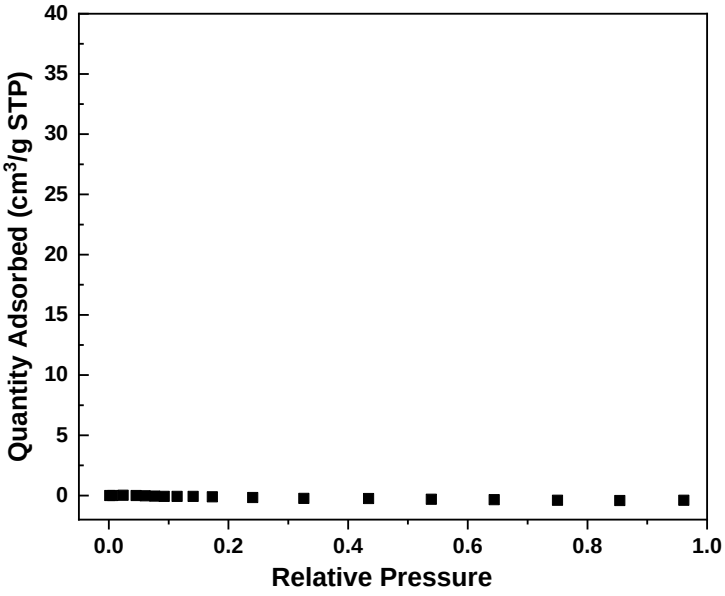

Figure 5.7 Adsorption isotherm of N_2 at 77 K for Matrimid®-derived CMS pyrolyzed at 500 °C in a 4 vol% H_2/Ar gas environment.

5.3.2 XPS

In order to investigate the carbon bonding nature inside the samples, each C1s spectrum from X-ray photoelectron spectroscopy (Figure 5.8) for the different CMS samples is deconvoluted to three Gaussian peaks. For all the investigated samples, good

fits were obtained as indicated by a square root of reduced χ^2 less than 3 and a coefficient of determination R^2 greater than 0.99. The two strongest signals with a relative binding energy distance of around 1 eV between their maxima are associated with different hybridization states. The lower binding energy signal corresponds to the sp^2-hybridized carbon, and the signal with an energy shift of around 1 eV higher is attributed to the sp^3 hybridized carbon [11-13]. Moreover, a third signal observed around 289 eV is evidence of the existence of a C-O carbon state [14]. On the one hand, we hypothesize that sp^3 hybridized carbon, a three-dimensional structure, disrupts the plate packing and is useful for imparting high guest molecule flux. On the other hand, we hypothesize that sp^2 hybridized carbons, a two-dimensional graphite layered structure, enable plate packing and thus lead to more compact microstructures with smaller ultramicroporous gaps in the plates. Therefore, a higher ratio of sp^3/sp^2 carbons should result in more permeable, yet less selective structures. The sp^2 and sp^3 hybridized carbon content in each CMS sample can be estimated by their peak area ratios from the XPS spectra.

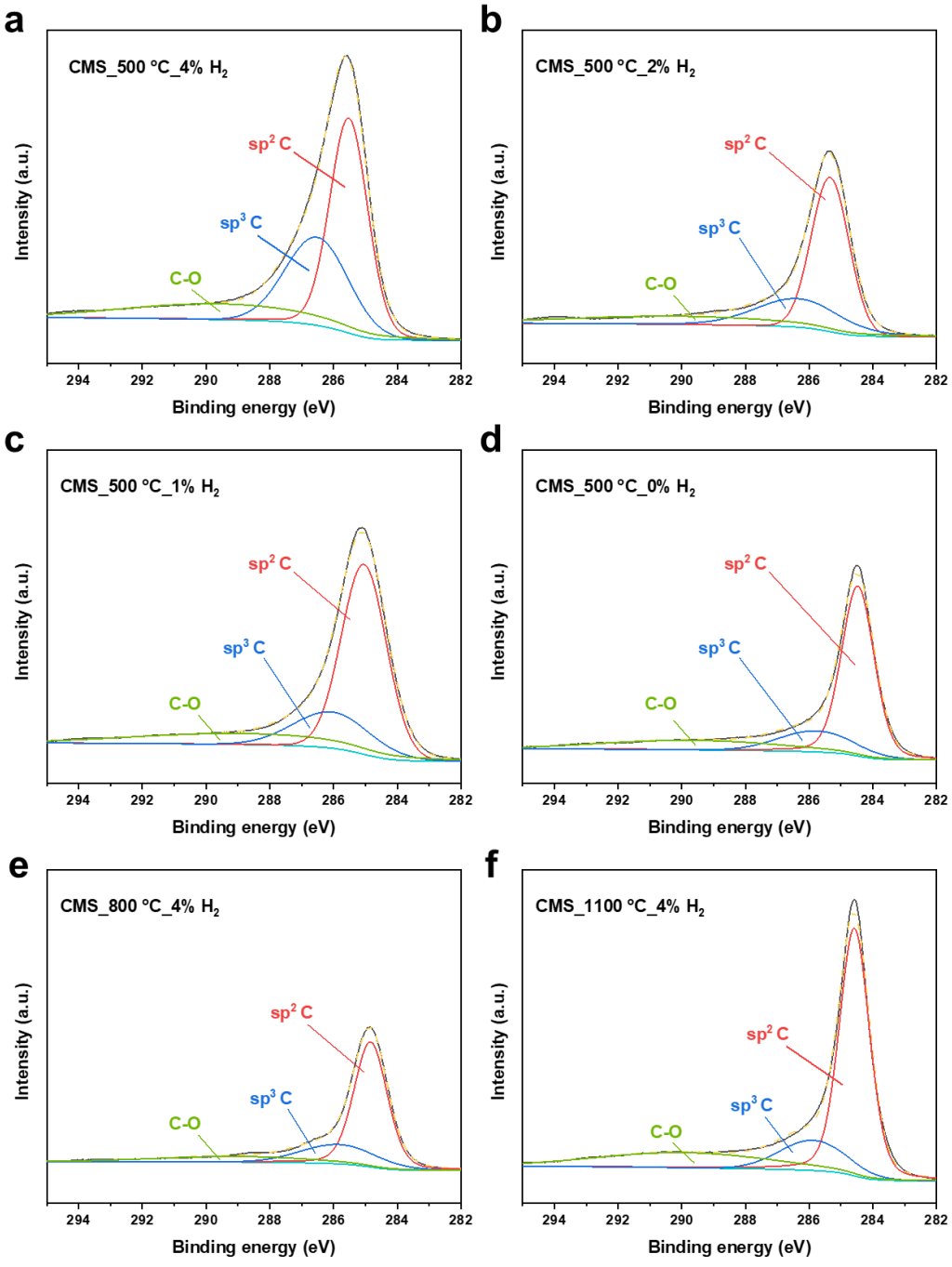

Figure 5.8 Deconvolution of C 1s spectra for CMS powder samples fabricated under different conditions.

As shown in Figure 5.9, the sp^3/sp^2 carbon ratio in the CMS increased monotonically with a decrease in pyrolysis temperature or an increase in hydrogen concentration. The increased sp^3/sp^2 carbon ratio also implies a higher free volume, which is generally consistent with the N_2 physisorption results (Table 5.2).

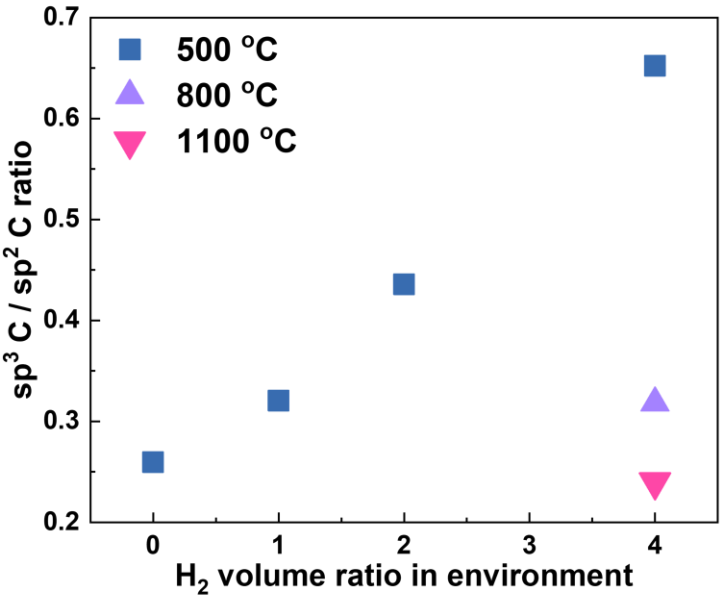

Figure 5.9 sp^3/sp^2 carbon ratio as a function of H_2 concentration determined from XPS spectra.

5.3.3 XRD

XRD data (Figure 5.10) provides detailed information to investigate the d-spacing of the CMS materials, which is manifested as a broad reflection representing the average inter-planar distance between the carbon sheets [15]. As the slit-like micropores in the CMS are formed by inefficient packing of adjacent carbon sheets, the inter-layer distance

can be used to qualitatively assess the diffusional passageways for guest molecules. The detected broad reflections of the CMS membrane moved gradually from 22.7° to 23.8° with the increase in pyrolysis temperature. The movement of the center position of the reflections shown in XRD revealed that the interlayer spacing between adjacent planes reduced with increasing pyrolysis temperature. The average d-spacing decreased from 3.91 Å to 3.74 Å, and this average spacing is mainly determined by the difference in the conditions of atomic organization and degree of carbonization for different pyrolysis temperatures [16]. The decreased d-spacing values for the CMS materials qualitatively suggest a lower free volume within the membrane samples. In addition, the reflections observed around 44.0° were more pronounced at higher pyrolysis temperatures. This reflection, which reveals a d-spacing value of 2.06 Å, is the signal of the carbon-carbon spacing of the graphitic planes ((100) plane in ideal graphite), and reveals the formation of well packed and more ordered carbon structures in CMS [16]. To some extent, this phenomenon demonstrates that the structure of the CMS membranes became more like that of ideal graphite at higher pyrolysis temperatures. The XRD results presented here, which support the hypothesis of temperature-induced loss of porosity in CMS materials, agrees well with the results from CMS analogs derived from cross-linked PIM-1 developed by Pinnau et al. [17]. The effect of pyrolysis hydrogen concentration on the XRD patterns was also studied, as shown in Figure 5.10b. The broad reflections moved gradually from 23.2° to 22.7° as the H_2 concentration increase from 0% to 4%, which means that average d-spacing increased from 3.83 Å to 3.91 Å. This also provides evidence that the presence of H_2 frustrates plate packing during the pyrolysis process.

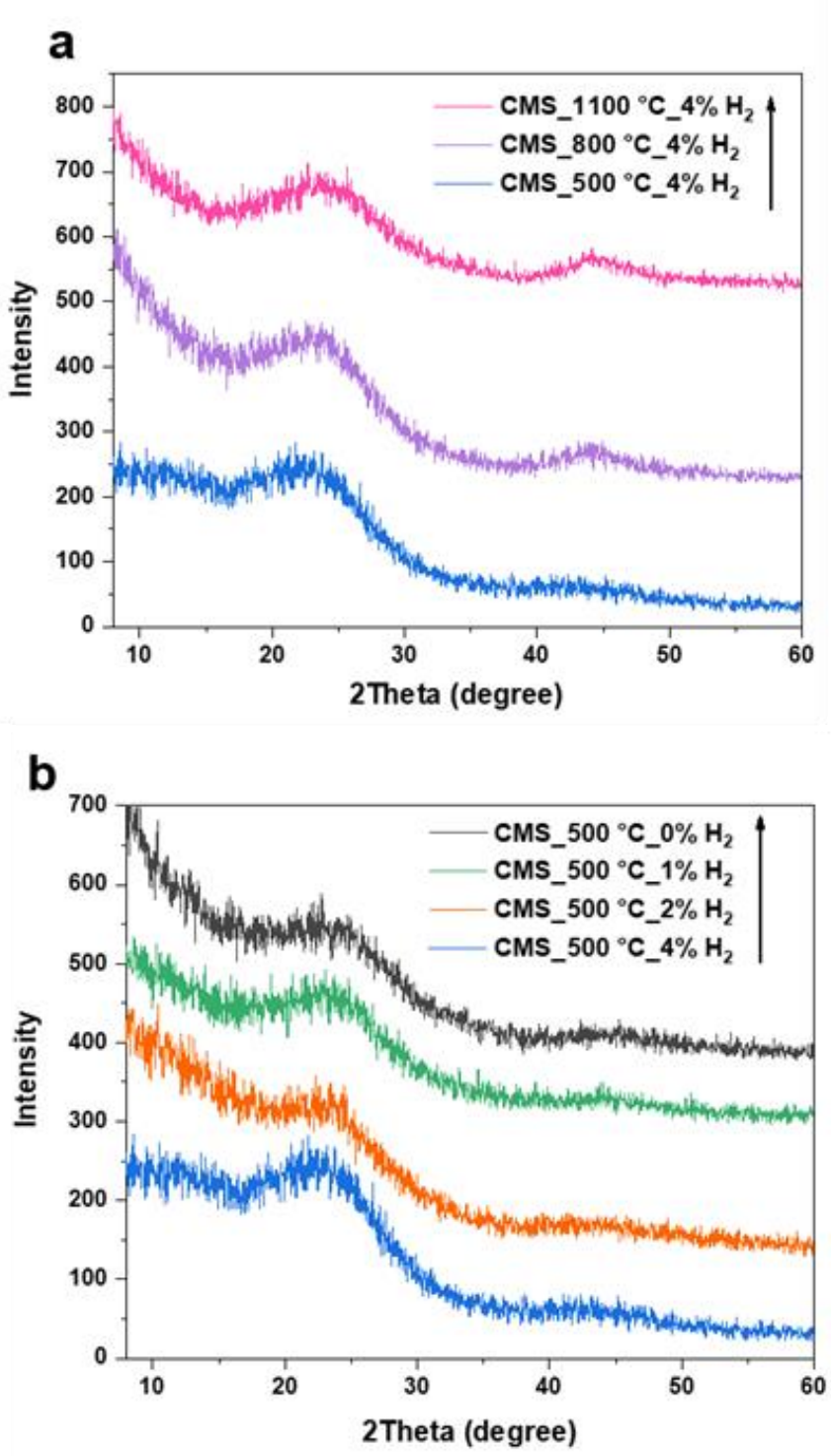

Figure 5.10 XRD spectra for CMS samples fabricated under different conditions.

5.3.4 FTIR

FTIR spectra (Figure 5.11) show the chemical evolution of the carbonized PIM-1 as a function of pyrolysis temperature and H_2 concentration. The PIM-1 spectrum shows characteristic absorbance bands at 2238 cm^{-1} (C≡N), 1607 cm^{-1} (aromatic C=C bending), 1470-1430 cm^{-1} (-C-H bending within -CH_2- and -C-CH_3 groups) and 1300-1000 cm^{-1} (-C-O- stretching) [18]. As shown in Figure 5.11, for CMS pyrolyzed at 500 °C, even though the peak intensities of several bands reduce significantly compared to the PIM-1 precursor, there are still obvious absorbance bands, which means CMS samples pyrolyzed at relatively low temperatures retain some degree of polymeric characteristics to some degree. However, the absorbance bands disappear as the pyrolysis temperature further increased to 800 °C or 1100 °C. XRD results show that CMS formed at higher pyrolysis temperatures are more graphite-like. It is worth noting that there are no functional groups presenting in the FTIR spectrum for ideal graphite [19]. In addition, the peak intensities of the characteristic bands increase obviously as the H_2 concentration in the pyrolysis environment increases. This phenomenon suggests that the CMS samples pyrolyzed under higher H_2 amount condition, to some degree, are more polymer-like, which is also supported by experiments measuring the total sample weight loss after pyrolysis (discussed in section 5.4).

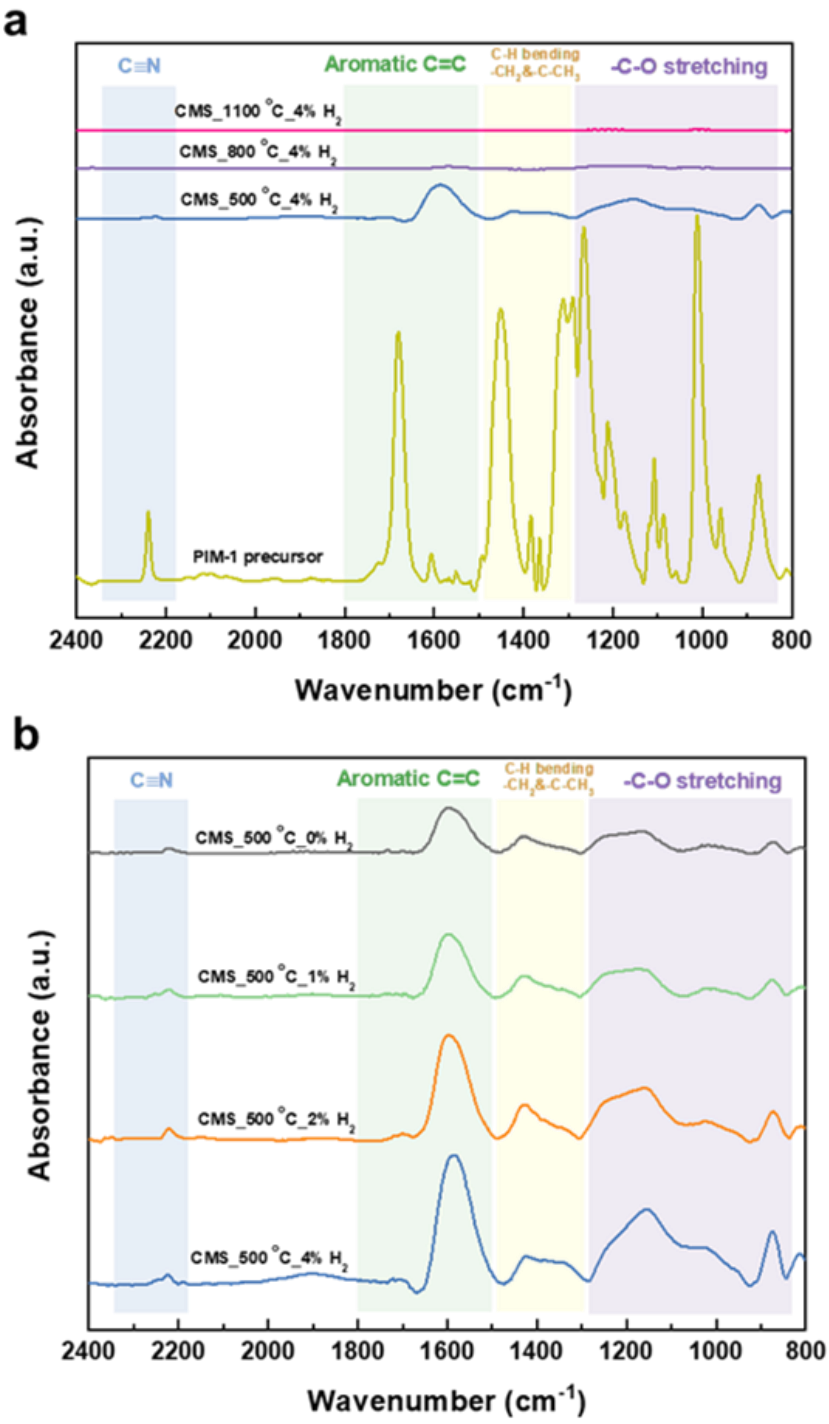

Figure 5.11 FTIR spectra of CMS samples fabricated under different conditions.

5.4 Evaluation of CMS Microstructure Formation

The evolution of the CMS microstructure during the pyrolysis of polyimides has been investigated in detail by Rungta et al. [20,21]. Although CMS materials formed from various polymer precursors are likely to be different in final structure and performance, the general evolution of the CMS structure should be qualitatively similar for all precursors of a similar class (e.g., high free volume, linear, glassy polymers). In a typical pyrolysis protocol for CMS membranes (as represented in Table 5.1 with three distinct periods: ramp, soak, and cool), PIM-1 will evolve from a random polymer coil to an amorphous, isotropic, and microporous CMS material as illustrated in Figure 2.3 [20].

The organization process of rigid strands into packed plates and the formation of microporous "cells" from these packable plates is a complex process, but can be understood at a high level by using Boltzmann's expression [22-24],

$$S = k_B ln\Omega \qquad \textbf{Eq. 5.1}$$

where S is the entropy of the system, k_B is the Boltzmann constant, and Ω is the total number of states (microstates) that is accessible to the system.

The conventional understanding of Ω in this equation is a measurement for the "disorder" in the studied system. The larger the "disorder", the larger the entropy of the system will be. In CMS systems, "order" and "disorder" are understood in the following way: packed plates are more "ordered" than the random rigid strands. At first glance, this seems counterintuitive that the entropy of the system can increase by organizing the disordered random rigid strands to orientationally-ordered plates. However, one should

notice that the "order" of a system is not only contributed by the orientational ordering, but also by the translational ordering. For the organization process of rigid strands into packed plates, the loss of orientational entropy in the system is more than offset by the increase of translational entropy of the system, which results in the increase of the system entropy. It can also be understood in the following way that the available space for any one strand increases as the strands become more aligned in the form of plates. The rigid strands optimize their local packing into plates for the system to maximize entropy and minimize its Helmholtz free energy A, $A = U - TS$ where U is the internal energy of the system, and T is the temperature. We thus believe that the microporous cells formed by the plate packing are kinetically trapped structures created at high temperatures. Kinetic restrictions hinder organization within the plates themselves and cause long range stacking defects between plates during "ramp" and "soak" periods where mobility is highest; based on observations of CMS aging processes [25], we believe that the plate mobility is dramatically reduced at room temperature to the point that the microstructures can be considered to be essentially stable. Moreover, within this "packing problem" framework, higher pyrolysis temperatures suggest that the system will continue to minimize its total free energy, which is to "relax out" the microporous cells. Our experimental results that investigate the effects of pyrolysis temperature on microporosity support this interpretation.

The enlargement of ultramicropores due to the introduction of H_2 is illustrated in Figure 5.12 and can be explained by investigating the transition of the PIM-1 coils to CMS.

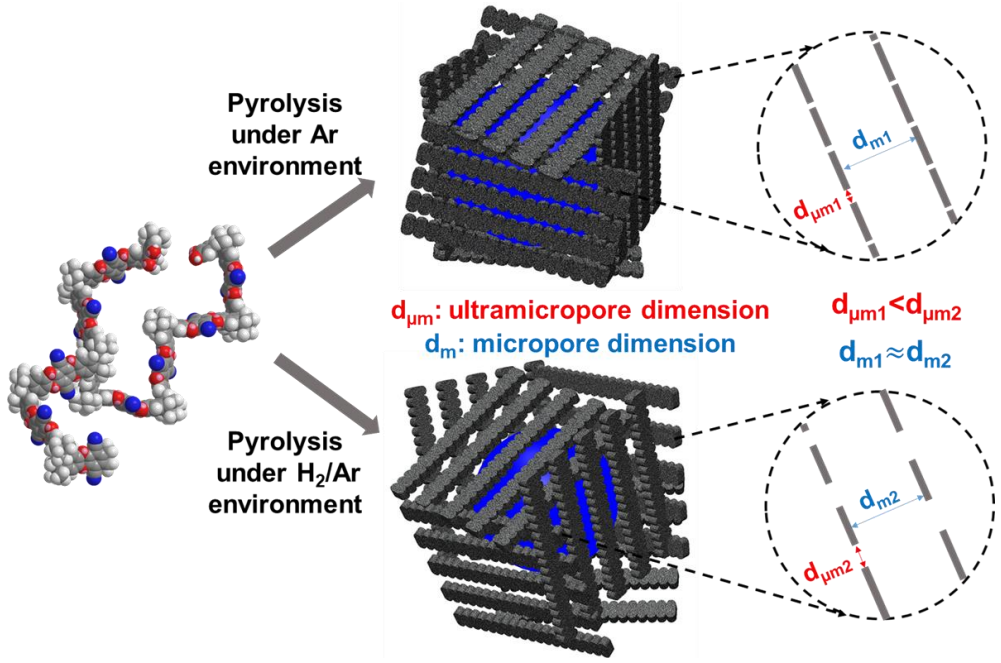

Figure 5.12 Illustration that the introduction of H_2 to the pyrolysis environment results in an enlargement of the ultramicropores with only minor changes in the size of the micropore.

Initially, in the thermal ramp process, the entangled semi-flexible PIM-1 precursor (Figure 2.3(i)) undergoing aromatization and fragmentation will tend to experience sufficient localized stresses such that periodic scissions along the polymer backbone occur. Such backbone scissions generate CO_2 and H_2O that remove most of the oxygen atoms in PIM-1, resulting in potentially rigid, highly aromatic strands (Figure 2.3(ii)). Based on the amount of evolved CO_2 and H_2O during pyrolysis as measured by off-gas mass spectrometry (Figure 5.13) and sp^3/sp^2 carbon ratio measured by X-ray photoelectron spectroscopy (Figure 5.9), hypothetical reaction pathways for this process are proposed (Figure 5.14). The generated reaction products will then connect with each other to form the rigid strands. The existence of H_2 in the pyrolysis environment will inhibit the loss of oxygen in the form of CO_2 (as shown in idealized pyrolysis reaction 1) and promote the removal of oxygen atoms in the form of H_2O (as shown in idealized pyrolysis reactions 2

and 3). As compared to the inert pyrolysis case, the evolved gases from the H_2-included pyrolysis show a substantial reduction in the evolution of CO_2 and a significant increase in the production of H_2O (Figure 5.13b). As a result, the strands formed in the H_2-included pyrolysis environment will be more kinked compared to those formed in pure Ar, since the conversion of PIM-1 units to relatively twisted units (products of idealized pyrolysis reaction 2 and 3) is favored while the conversion to relatively linear units (products of idealized pyrolysis reaction 1) is inhibited (the hypothetical structure of the strands formed in the pure Ar or H_2-included pyrolysis environment is shown in Figure 5.15). The 3D geometries of these hypothetical strands are obtained by minimizing the total steric energy using the MM2 force fields built in Chem3D (CambridgeSoft). The steric energy refers to the energy associated with bond stretching, bending, torsion, and non-bond interaction. After minimization, the hypothetical strand produced in 4% H_2/Ar (Figure 5.15b) exhibits a more twisted structure than the hypothetical strand produced in pure Ar (Figure 5.15a). According to the optimization result, the lowest steric energy for strands produced in pure Ar is 145.33 kcal/mol while the value for strands produced in 4% H_2/Ar is 450.01 kcal/mol. The difference in total steric energy may be mainly due to the bulky sp^3 carbon sections in the strand produced in 4% H_2/Ar environment, which generates a more significant steric effect and inhibits the alignment of strands during the evolution of CMS. The carbonized strands are shorter and more mobile than the entangled precursor polymer, but must first "solve" a packing problem to maximize the entropy of the system. The rigid strands will organize into more easily packable plates (Figure 2.3(iii)) to have an overall higher entropy value and reduce the excluded volume present within a random phase packing of strands. The kinked structure generated in the presence of H_2 inhibits strand alignment (i.e., the

"packing problem" will be more difficult to solve), which increases the imperfections within the plates of strands. This ultimately increases the sizes of the ultramicropores.

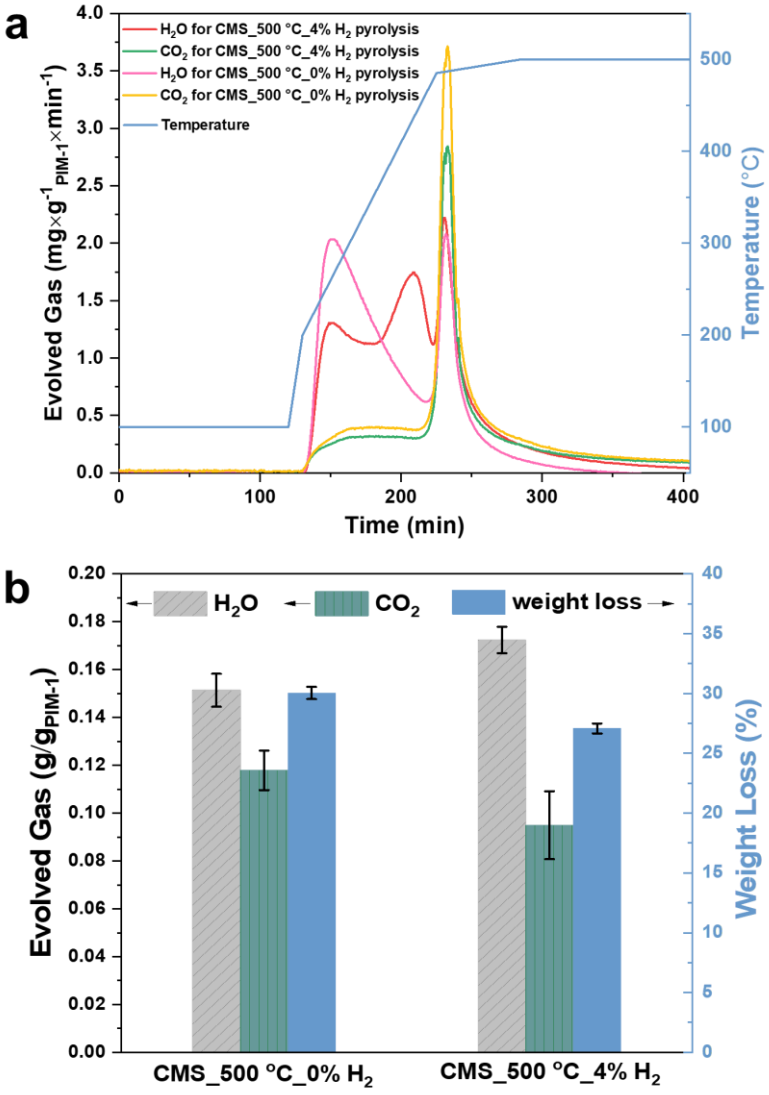

Figure 5.13 a) Quantitative measurements of the evolved CO_2 and H_2O from the pyrolysis of CMS_500 °C_0% H_2 and CMS_500 °C_4% H_2 as measured by mass spectrometry. b) Quantitative results of the CO_2 and H_2O evolved from the pyrolysis processes measured by mass spectrometry along with the total sample weight loss after pyrolysis.

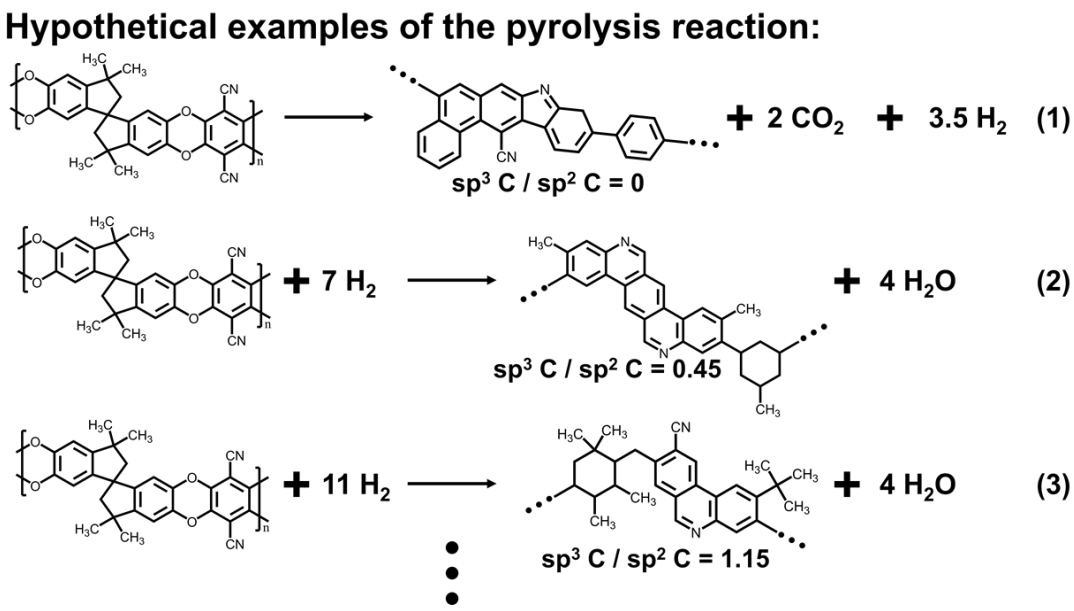

Figure 5.14 Hypothetical example reaction pathways generating CO_2 and H_2O during pyrolysis; note that many pyrolytic reactions can be envisioned.

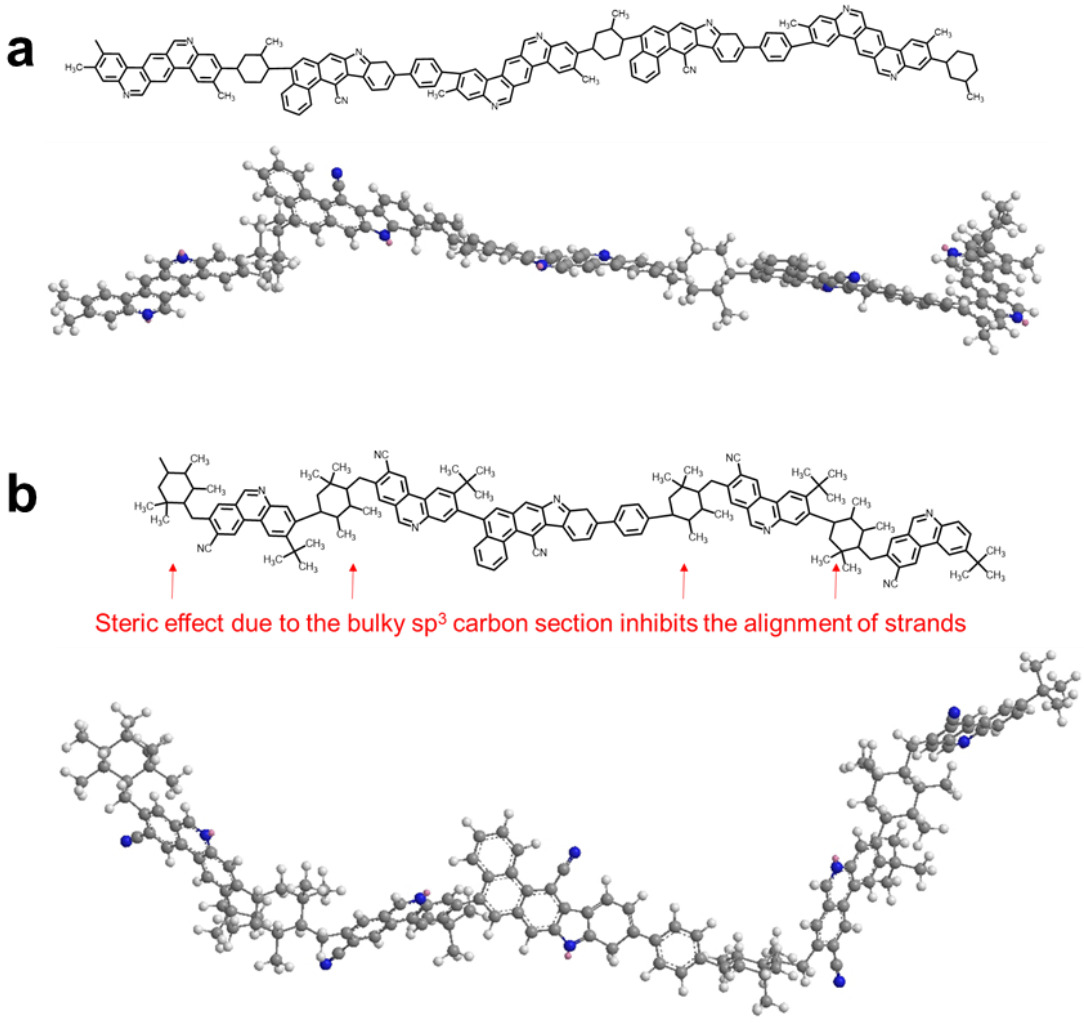

Figure 5.15 Example hypothetical chemical structure and optimal 3D geometry of the carbon strands formed in the a) pure Ar or b) 4 vol% H_2/Ar pyrolysis environment.

It should be noted that lateral linkages between strands may occur due to inter-strand reactions, which can only evolve molecular H_2 in the process [20]. However, the reaction between lateral stands will be suppressed by H_2 molecules present in the pyrolysis atmosphere, thus resulting in reduced inter-strand crosslinking and larger gaps between the strands on average (Figure 5.16). Kinetic restrictions (i.e., limited time for the final ramp

and soak periods at high temperature) lead to the imperfect organization of strands within the plates themselves and long-range plate-stacking defects. A typical idealized micropore "cell" with imperfectly packed plates comprising imperfectly organized strands is illustrated in Figure 2.3(iv). In CMS materials, the slits between strands are the ultramicropores that enable molecular sieving while the voids between the imperfectly-stacked plates are the micropores that provide abundant sorption sites and allow for guest molecules to realize many of their conformational degrees of freedom. During the soak and cooling phases, ongoing formation and coalescence (i.e., sharing ultramicroporous "walls" between cells) of multiple neighboring cells will generate an idealized CMS structure (Figure 2.3(v)) with a bimodal distribution of pores.

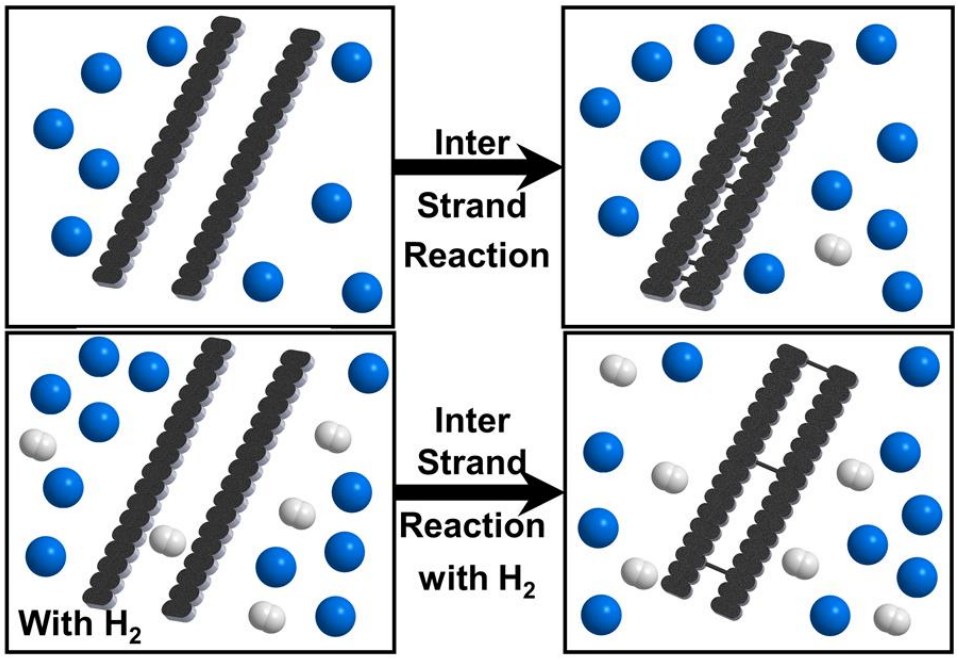

Figure 5.16 Illustration of the effect of H_2 on the lateral linkages between strands. grey=H_2, blue=Ar.

5.5 Sorption and Diffusion Property of PIM-1-derived CMS

5.5.1 Sorption property

The sorption isotherms of *p*-xylene and *o*-xylene collected at 55 °C for both CMS_500 °C_4% H_2 and CMS_500 °C_0% H_2 (Figure 5.17) display a sharp increase in adsorption capacity in the low saturation region and then plateau at higher saturation values. As might be expected, the uptake for *p*-xylene and *o*-xylene at each relative pressure exhibited only minor differences (within 1 wt%) relative to each other due to their similar chemical nature, revealing an absence of a sorption-selective separation mechanism. It is worth noting that both isomers have nearly identical sorption isotherms with the ones obtained for CMS_500 °C_4% H_2 and CMS_500 °C_0% H_2, indicating little change in the sorption properties of the CMS materials after the introduction of H_2 to the pyrolysis environment. Combined with the N_2 physisorption results, this suggests that the larger micropore volume in the CMS is relatively unaffected by the presence of the reactive H_2 pyrolysis gas, which indicates that the primary effect of the H_2 is to interfere with the formation of the plates.

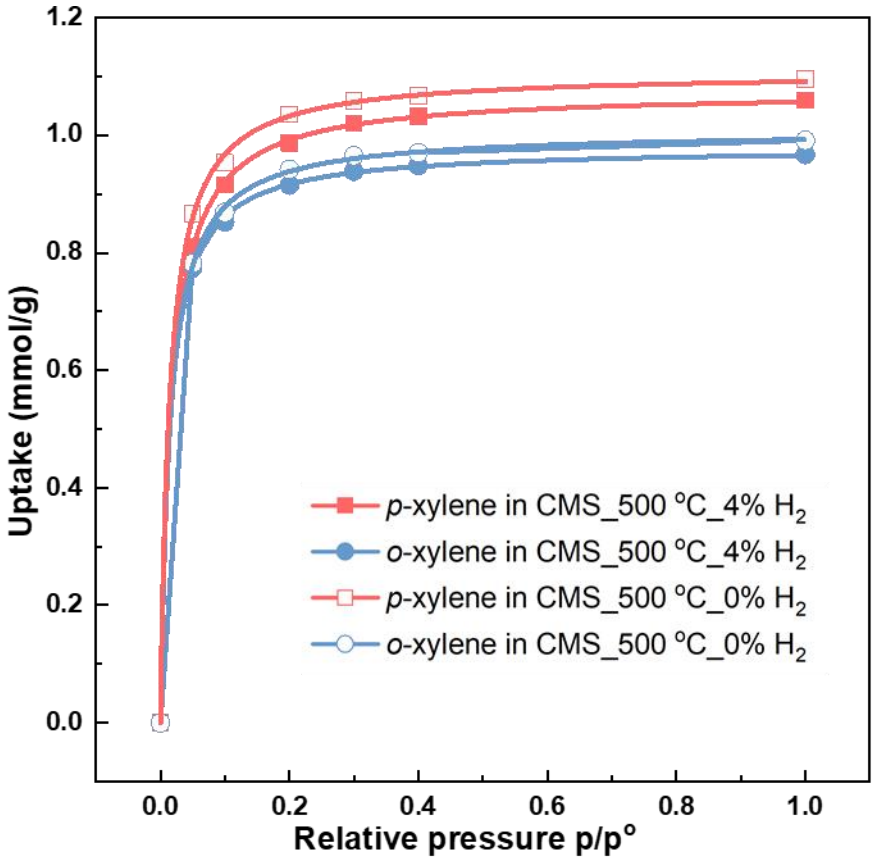

Figure 5.17 Single component sorption isotherms of *p*-xylene and *o*-xylene in CMS_500 °C_4% H_2 and CMS_500 °C_0% H_2 measured at 55 °C.

5.5.2 Diffusivity estimation

The ultramicropores inside the rigid CMS enable molecular sieving and allow for more rapid activated diffusion of the smaller *p*-xylene molecules relative to the larger *o*-xylene molecules. Single component diffusion studies revealed significant differences in the kinetic uptakes (Figure 5.18) of *p*-xylene and *o*-xylene, with slower *o*-xylene diffusion observed, and these experiments were utilized to estimate the transport diffusivities, D.

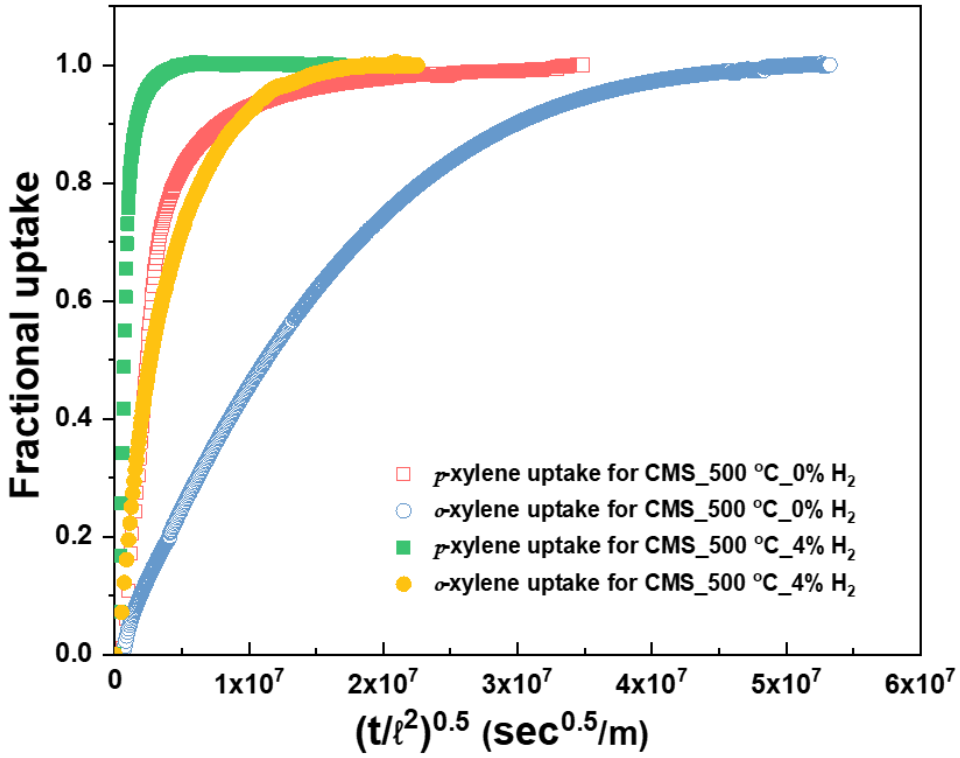

Figure 5.18 The kinetic uptake curves of *p*-xylene and *o*-xylene in CMS_500 °C_0% H_2 and CMS_500 °C_4% H_2 performed at 55 °C with a 0.00 - 0.05 change in relative pressure.

As shown in Figure 5.19, the transport diffusivities for both isomers in the H_2-pyrolyzed CMS samples increase significantly relative to the control case without H_2 in the pyrolysis environment (1.0×10^{-9} vs. 7.2×10^{-11} cm^2/s for *p*-xylene, 4.0×10^{-11} vs. 2.3×10^{-12} cm^2/s for *o*-xylene). Consistent with our observations of the ultramicropore size, the H_2-assisted CMS exhibits a slightly lower diffusion selectivity (25 vs. 31), which indicates that a trade-off between diffusion selectivity and diffusivity for CMS-type materials may exist.

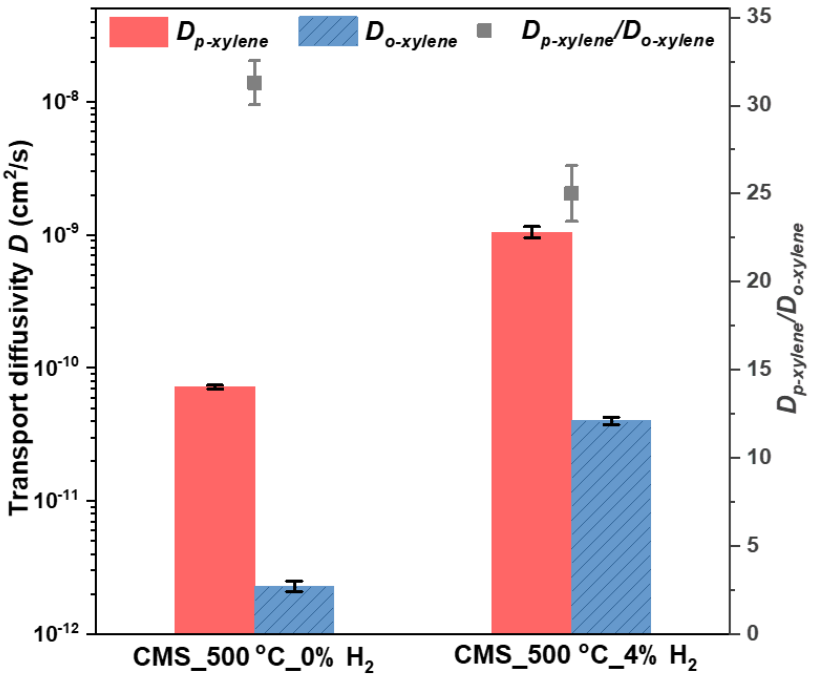

Figure 5.19 Transport diffusion coefficients for xylene isomers in CMS_500 °C_4% H_2 and CMS_500 °C_0% H_2 at 55 °C.

5.6 Permeation Performance of PIM-1-derived CMS Membranes

5.6.1 Dense CMS membranes

The separation performance of the CMS membranes was tested using a Wicke-Kallenbach permeation setup, where the total pressure difference across the membrane is maintained at zero. The feed, either pure xylene or a xylene mixture vapor carried by nitrogen, flushes the upstream while a nitrogen sweep carries the permeate to a gas chromatograph to determine the xylene flux across the membrane (details in Section 3.8). As illustrated in Figure 5.20, lower pyrolysis temperatures or higher H_2 concentration in the pyrolysis environment will result in a higher *p*-xylene permeability and a lower *p*-xylene/*o*-xylene permselectivity.

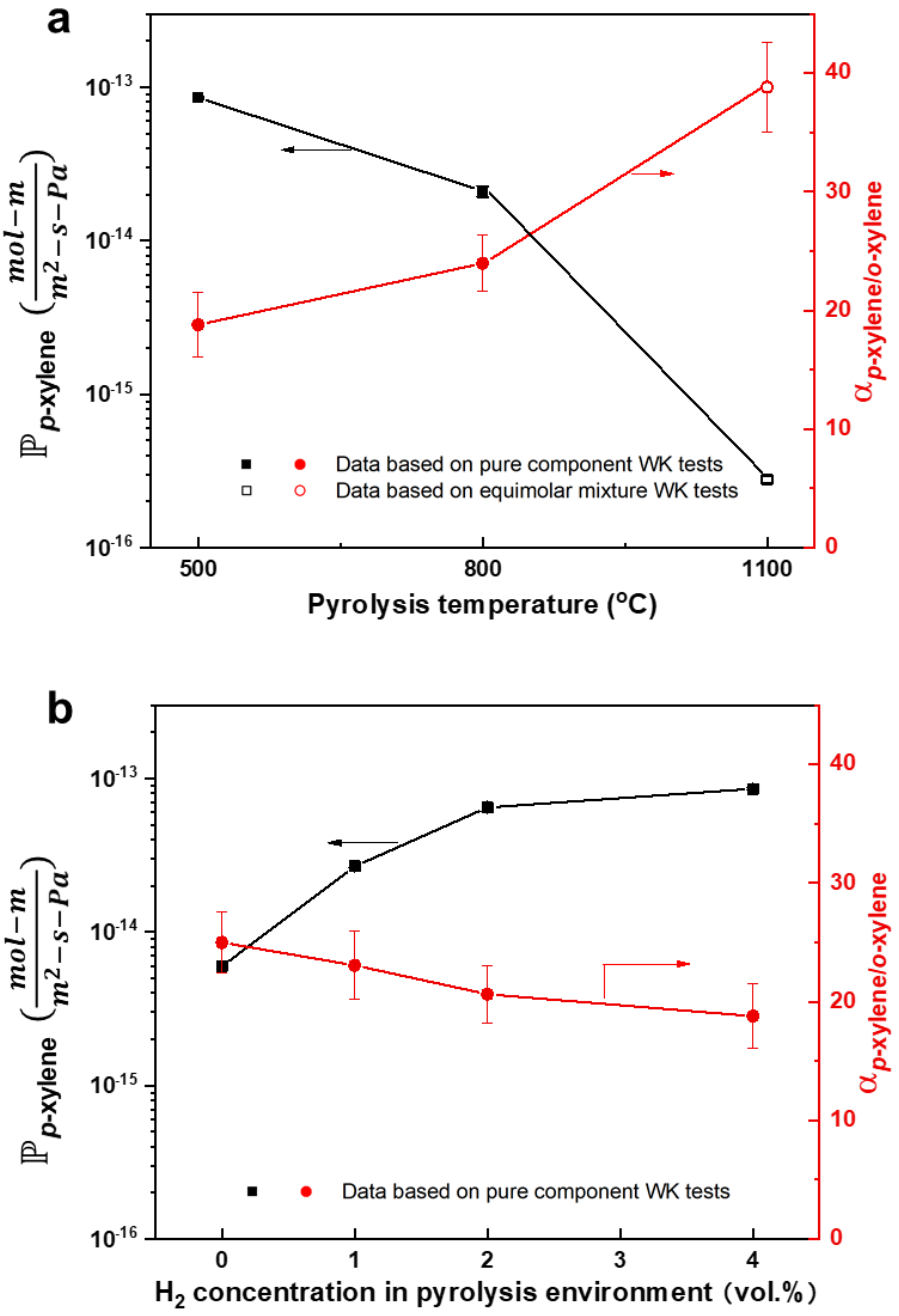

Figure 5.20 Permeation performance of dense CMS membranes at 55 °C. Permeability of *p*-xylene and permselectivity of *p*-xylene/*o*-xylene as a function of a) pyrolysis temperature, b) H_2 concentration in the pyrolysis environment.

It has been shown above that both the H_2 concentration and pyrolysis temperature effectively manipulate the pore size distribution and sp^3/sp^2 hybridized carbon ratio inside the CMS. As discussed previously, sp^3-hybridized carbon has a 3D structure that we hypothesize contributes to the molecular flux, while sp^2-hybridized carbon is comprised of a planar structure. As noted earlier, we hypothesize that there might be a positive correlation between the sp^3/sp^2 hybridized carbon ratio of the CMS and the permeability of guest molecules. As shown in Figure 5.21, as the sp^3/sp^2 hybridized carbon ratio increases from 0.24 to 0.65, the permeability of *p*-xylene through the CMS membranes improves significantly from 2.8×10^{-16} to 8.5×10^{-14} $mol\ m/m^2\ s\ Pa$ (>300x, 30,257% increase) while the permselectivity decreases only slightly from 38.9 to 18.8 (52% decrease). To the best of our knowledge, this is the first study that has considered the correlation between the sp^3/sp^2 hybridized carbon ratio and the permeation properties of CMS membranes. This observation—if generalizable beyond the polymer and conditions investigated here—provides a fundamental basis for understanding and improving the separation performance of CMS membranes for various applications.

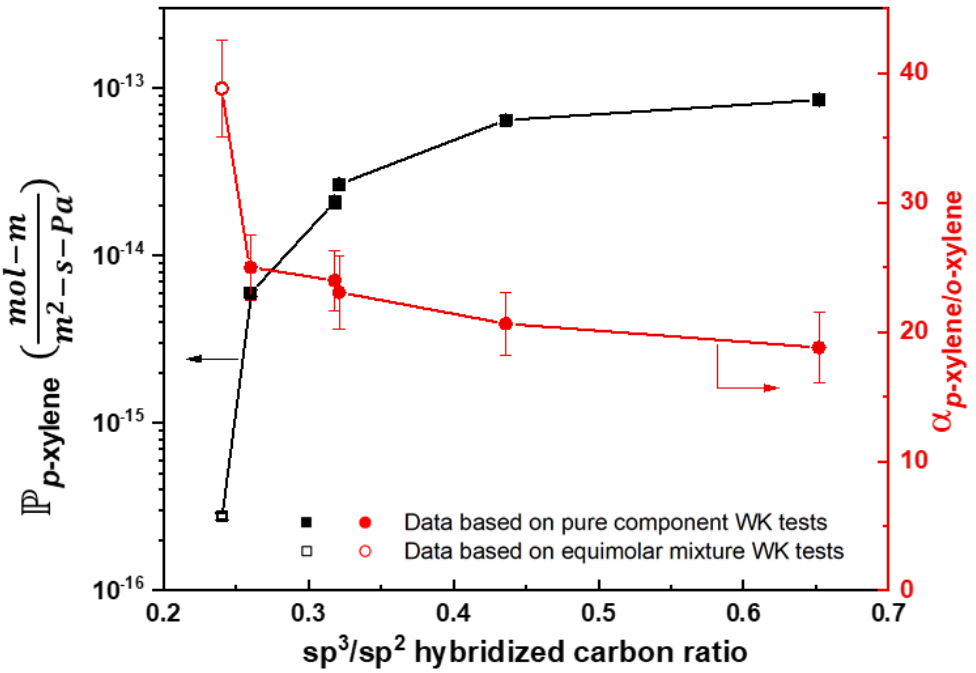

Figure 5.21 Permeation performance of dense CMS membranes at 55 °C. Permeability of *p*-xylene and permselectivity of *p*-xylene/*o*-xylene as a function of sp^3/sp^2 hybridized carbon ratio.

The effect of H_2 on the permeation performance of CMS membranes for the separation of xylene isomers is further illustrated in Figure 5.22 by the use of mixed xylene isomers feeds. An equimolar *p*-xylene/*o*-xylene vapor mixture permeation through dense membranes was also tested at 55 °C. Figure 5.22 shows that the tightening of the ultramicropores (via decreasing H_2 concentration or via increasing final pyrolysis temperature) improves the discrimination between xylene isomers at the cost of membrane permeability.

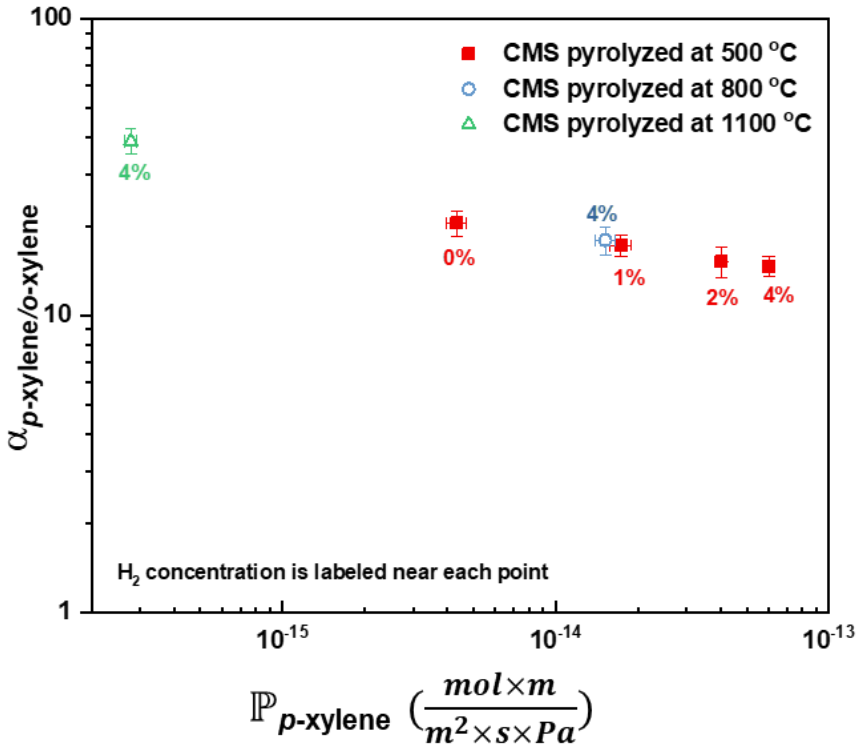

Figure 5.22 The effect of hydrogen concentration and final pyrolysis temperature on the *p*-xylene/*o*-xylene separation performance of CMS membranes based on the Wicke-Kallenbach experiments using an equimolar feed.

As shown in Figure 5.23, the membranes prepared at 4 vol% H_2/Ar gain at least 14 times more *p*-xylene permeability than the membrane prepared without H_2, as shown by estimates from the sorption-diffusion model and the experimental permeability from the Wicke-Kallenbach measurements. This is consistent with our characterization results that the larger ultramicropores generated with the help of H_2 provide less resistance to diffusion of guest molecules compared to the extremely narrow ultramicropores resulting from the pure Ar pyrolysis. Unlike the permeability, the permselectivity exhibits much smaller

changes. This is likely owing to the fact that the permselectivity is mainly dominated by the ultramicropores inside the CMS membrane and the size of the H_2 enlarged ultramicropores is around 5-7 Å (note that the xylene isomers used, *p*-xylene and *o*-xylene, have kinetic diameters of 5.8 Å and 6.8 Å, respectively). As a result, the H_2-assisted CMS can still effectively distinguish between *p*-xylene and *o*-xylene via a kinetic effect provided by the rigid ultramicropores with the appropriate size. For the pure component Wicke-Kallenbach tests, the *p*-xylene permeability is higher, and the permselectivity is lower than those predicted by the sorption-diffusion model (8.5×10^{-14} vs. $4.1\times10^{-14} mol\ m/m^2\ s\ Pa$ and 18.8 vs. 24.6, respectively). This difference could be the result of some small, nonselective leak pathways inside or around the CMS membranes. The *p*-xylene permeability in the equimolar mixture test is smaller than the value obtained from the pure component test (6.0×10^{-14} vs. $8.5\times10^{-14}\ mol\ m/m^2\ s\ Pa$) while the permselectivity decreases in the mixture case (14.7 vs. 18.8), which is a well-known " fingerprint" of the frictional coupling effects between rapidly and slowly transporting xylene molecules.

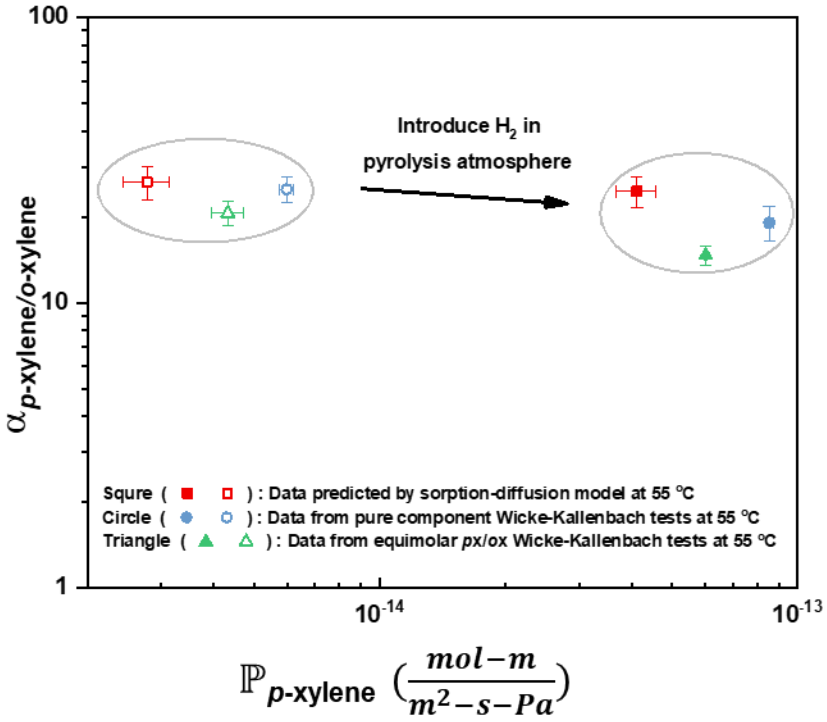

Figure 5.23 *p*-Xylene/*o*-xylene separation performance of 4% H_2-assisted dense CMS membranes (solid markers) compared to Ar pyrolyzed membranes (hollow markers). Square:sorption-diffusion model predicted value, Circle: experimental data from pure component Wicke-Kallenbach tests, Triangle: experimental data from equimolar xylene vapor mixture Wicke-Kallenbach tests.

5.6.2 CMS hollow fiber membranes

To demonstrate the ability of this concept to translate to the fabrication of membrane devices, we elected to pyrolyze defect-free PIM-1 hollow fiber membranes in the presence of 4 % H_2 and at 500 °C. PIM-1 fiber pyrolyzed without H_2 is utilized as a control case and its best performance is shown in Table 5.4 [26]. In these experiments, both membranes are exposed to a fully saturated equimolar *p*-xylene and *o*-xylene vapor

mixture, which simulates high activity liquid-phase organic solvent reverse osmosis conditions. As shown in Table 5.4, the permeation rate enhancements observed in the dense films are also observed for the fiber case. Specifically, CMS HFMs fabricated in an H_2-included pyrolysis environment exhibit increases of both permeance (~38x) and permselectivity (~6x; the anomalously low selectivity of the control case is not a result of defects and has been discussed elsewhere) [26]. For a more direct comparison with state-of-the-art MFI-type zeolite membranes, the CMS HFMs fabricated in the H_2-included environment were also tested under a relatively low feed activity value (0.05), which is similar to the typical testing protocol for zeolitic membranes [27,28]. We observe that permeance increases significantly (~4.2x, to $2.2\times10^{-9}\ mol/m^2\ s\ Pa$) and permselctivity is improved to 11.8.

Table 5.4 Separation results for PIM-1-derived CMS hollow fiber membranes.

Sample		CMS_HFM_0%[a]	CMS_HFM_4%[b]		
Test mode		WK[c]	WK[c]	WK[c]	OSRO[d]
Separation factor *p*X/*o*X		1.4 ± 0.1	8.9 ± 0.2	11.8 ± 0.5	3.7
pX activity feed/permeate		0.5/0	0.5/0	0.025/0	1.22/0.98[g]
Relative saturation of feed/permeate		100%/~0%	100%/~0%	5%/~0%	100%/100%
Permeance ($10^{-11}\frac{mol}{m^2 \cdot s \cdot Pa}$)	*p*X	1.36 ± 0.04	52.3 ± 0.7	222 ± 14	25.5[e] 36.0[f]
	oX	0.98 ± 0.06	5.87 ± 0.04	18.8 ± 0.5	0.78[e] 0.21[f]

[a] CMS pyrolyzed at 575 °C from previous work [29]. [b] CMS pyrolyzed at 500 °C. [c] Wicke-Kallenbach tests were conducted at 55 °C with a nitrogen sweep on the permeate side with an equimolar *p*-xylene and *o*-xylene feed. [d] Organic solvent reverse osmosis tests were conducted at 22 °C under 60 bar with a 90:10 (mol/mol) mixture of *p*-xylene and *o*-xylene liquid feed and a stage cut of < 1%. The permeate composition was found to be 97.1 mol% *p*-xylene at steady state. [e] Hydraulic permeance based on the transmembrane pressure difference. [f] Intrinsic permeance based on fugacity driving force. [g] The detailed calculation of the feed and permeate activity is available in Table 5.5; the thermodynamic reference state is the pure liquid at 22 °C and 1 atm.

Table 5.5 Example OSRO measurement of a PIM-1-derived CMS hollow fiber membrane fabricated at 500 °C and 4 vol% H_2/Ar.

Feed mixture	90:10 (mol/mol) liquid mixture of *p*-xylene/*o*-xylene
Testing temperature	295 K
Gas constant	83.1 cm^3-bar/mol-K
Module active length	8 cm
Hollow fiber outer diameter	0.06 cm
Membrane permeance area *A*	$\pi \times 0.06$ cm $\times 8$ cm $= 1.51$ cm^2
Total permeate flow rate	0.1057 mL/hr
p-xylene permeate composition	0.9711 mol/mol
o-xylene permeate composition	0.0289 mol/mol
Specific molar volume of *p*-xylene	123.3 cm^3/mol
Specific molar volume of *o*-xylene	120.6 cm^3/mol
Feed side pressure	60 bar, g+1 bar=61 bar, abs
Permeate side pressure	1 bar, abs
Saturation pressure of *p*-xylene	$p_{p-xylene}^{sat}\,(295K) = 0.979\ kPa \approx 0.010\ bar$
Saturation pressure of *o*-xylene	$p_{0-xylene}^{sat}\,(295K) = 0.746\ kPa \approx 0.007\ bar$

Separation factor

$$\beta_{p-xylene/o-xylene} = \frac{x_{p-xylene}^{permeate}/x_{o-xylene}^{permeate}}{x_{p-xylene}^{feed}/x_{o-xylene}^{feed}} = \frac{0.9711/0.0289}{0.9/0.1} = 3.73$$

Flux of *p*-xylene

$$\frac{\dot{n}_{p-xylene}}{A} = \frac{1}{1.51\ \mathrm{cm}^2} \cdot \frac{10^4 \mathrm{cm}^2}{\mathrm{m}^2} \cdot \frac{0.1057\ \frac{ml}{hr} \cdot 0.9711}{123.3\ \frac{\mathrm{cm}^3}{\mathrm{mol}}} \cdot \frac{hr}{3600s}$$

$$= 1.53 \times 10^{-3}\ \frac{mol}{\mathrm{m}^2 \cdot s}$$

Flux of *o*-xylene

$$\frac{\dot{n}_{o-xylene}}{A} = \frac{1}{1.51\ \mathrm{cm}^2} \cdot \frac{10^4 \mathrm{cm}^2}{\mathrm{m}^2} \cdot \frac{0.1057 \frac{ml}{hr} \cdot 0.0289}{120.6 \frac{\mathrm{cm}^3}{\mathrm{mol}}} \cdot \frac{hr}{3600s}$$

$$= 4.66 \times 10^{-5}\ \frac{mol}{\mathrm{m}^2 \cdot s}$$

Hydraulic permeance of *p*-xylene

$$\frac{\mathbb{P}_{p-xylene,hydraulic}}{\ell} = \frac{\frac{\dot{n}_{p-xylene}}{A}}{p^{feed} - p^{permeate}} = \frac{1.53 \times 10^{-3} \frac{mol}{\mathrm{m}^2 \cdot s}}{61\ bar - 1\ bar} = 2.55 \times$$

$$10^{-5}\ \frac{mol}{\mathrm{m}^2 \cdot s \cdot bar} = 2.55 \times 10^{-10}\ \frac{mol}{\mathrm{m}^2 \cdot s \cdot Pa}$$

Hydraulic permeance of *o*-xylene

$$\frac{\mathbb{P}_{o-xylene,hydraulic}}{\ell} = \frac{\frac{\dot{n}_{o-xylene}}{A}}{p^{feed} - p^{permeate}} = \frac{4.66 \times 10^{-5} \frac{mol}{\mathrm{m}^2 \cdot s}}{61\ bar - 1\ bar} = 7.77 \times$$

$$10^{-7}\ \frac{mol}{\mathrm{m}^2 \cdot s \cdot bar} = 7.77 \times 10^{-12}\ \frac{mol}{\mathrm{m}^2 \cdot s \cdot Pa}$$

Feed side activity of *p*-xylene

$$x_{p-xylene}^{feed} \gamma_{p-xylene}^{feed} \exp\left[\frac{\bar{V}_{p-xylene}}{\mathrm{RT}}\left(p^{feed} - p_{p-xylene}^{sat}\right)\right] = 0.9 \cdot$$

$$1.0001 \cdot \exp\left[\frac{123.3 \frac{\mathrm{cm}^3}{\mathrm{mol}}}{\frac{83.1\ \mathrm{cm}^3 \cdot \mathrm{bar}}{\mathrm{mol} \cdot \mathrm{K}} \cdot 295\ \mathrm{K}} (61 - 0.010) bar\right] = 1.22$$

Feed side activity of *o*-xylene

$$x_{o-xylene}^{feed} \gamma_{o-xylene}^{feed} \exp\left[\frac{\bar{V}_{o-xylene}}{RT}\left(p^{feed} - p_{o-xylene}^{sat}\right)\right] = 0.1 \cdot$$

$$1.0086 \cdot \exp\left[\frac{120.6 \frac{\mathrm{cm}^3}{\mathrm{mol}}}{\frac{83.1\ \mathrm{cm}^3 \cdot \mathrm{bar}}{\mathrm{mol} \cdot \mathrm{K}} \cdot 295\ \mathrm{K}} (61 - 0.007) bar\right] = 0.14$$

Permeate side activity of *p*-xylene	$x_{p-xylene}^{permeate}\gamma_{p-xylene}^{permeate}\exp\left[\frac{\hat{V}_{p-xylene}}{\mathrm{RT}}\left(p^{permeate}-p_{p-xylene}^{sat}\right)\right]=$ $0.9711\cdot 1\cdot\exp\left[\frac{123.3\frac{\mathrm{cm}^3}{\mathrm{mol}}}{\frac{83.1\ \mathrm{cm}^3\cdot\mathrm{bar}}{\mathrm{mol}\cdot\mathrm{K}}\cdot 295\ \mathrm{K}}(1-0.010)bar\right]=0.98$
Permeate side activity of *o*-xylene	$x_{o-xylene}^{permeate}\gamma_{o-xylene}^{permeate}\exp\left[\frac{\hat{V}_{o-xylene}}{\mathrm{RT}}\left(p^{permeate}-p_{o-xylene}^{sat}\right)\right]=$ $0.0289\cdot 1.0101\cdot\exp\left[\frac{120.6\frac{\mathrm{cm}^3}{\mathrm{mol}}}{\frac{83.1\ \mathrm{cm}^3\cdot\mathrm{bar}}{\mathrm{mol}\cdot\mathrm{K}}\cdot 295\ \mathrm{K}}(1-0.007)bar\right]=0.03$
Intrinsic permeance of *p*-xylene	$\frac{\mathbb{P}_{p-xylene,intrinsic}}{\ell}=\frac{\frac{\dot{n}_{p-xylene}}{A}}{\frac{\mathrm{RT}}{\hat{V}_{p-xylene}}\ln\left(\frac{1+b_{p-xylene}f_{p-xylene}^{feed}}{1+b_{p-xylene}f_{p-xylene}^{permeate}}\right)}=$ $\frac{1.53\times10^{-3}\frac{mol}{\mathrm{m}^2\cdot s}}{\frac{83.1\ \mathrm{cm}^3\cdot\mathrm{bar}}{\mathrm{mol}\cdot\mathrm{K}}\cdot\frac{295\ \mathrm{K}}{123.3\frac{\mathrm{cm}^3}{\mathrm{mol}}}\cdot\ln\left[\frac{1+38.4\ kPa^{-1}\cdot(1.22\cdot0.979\ kPa)}{1+38.4\ kP^{-1}\cdot(0.98\cdot0.979\ kPa)}\right]}=3.60\times$ $10^{-5}\frac{mol}{m^2\cdot s\cdot bar}=3.60\times10^{-10}\frac{mol}{m^2\cdot s\cdot Pa}$
Intrinsic permeance of *o*-xylene	$\frac{\mathbb{P}_{o-xylene,intrinsic}}{\ell}=\frac{\frac{\dot{n}_{o-xylene}}{A}}{\frac{\mathrm{RT}}{\hat{V}_{o-xylene}}\ln\left(\frac{1+b_{o-xylene}f_{o-xylene}^{feed}}{1+b_{o-xylene}f_{o-xylene}^{permeate}}\right)}=$ $\frac{4.66\times10^{-5}\frac{mol}{\mathrm{m}^2\cdot s}}{\frac{83.1\ \mathrm{cm}^3\cdot\mathrm{bar}}{\mathrm{mol}\cdot\mathrm{K}}\cdot\frac{295\ \mathrm{K}}{120.6\frac{\mathrm{cm}^3}{\mathrm{mol}}}\cdot\ln\left[\frac{1+50.8\ kPa^{-1}\cdot(.014\cdot0.764\ kPa)}{1+50.8\ kPa^{-1}\cdot(0.03\cdot0.764\ kPa)}\right]}=2.10\times$ $10^{-7}\frac{mol}{m^2\cdot s\cdot bar}=2.10\times10^{-12}\frac{mol}{m^2\cdot s\cdot Pa}$

5.6.3 Performance comparison with MFI-type zeolite membranes

The separation performance comparison of PIM-1 derived CMS membranes with MFI-type Zeolite Membranes is shown in Figure 5.24, Figure 5.25 and Figure 5.26.

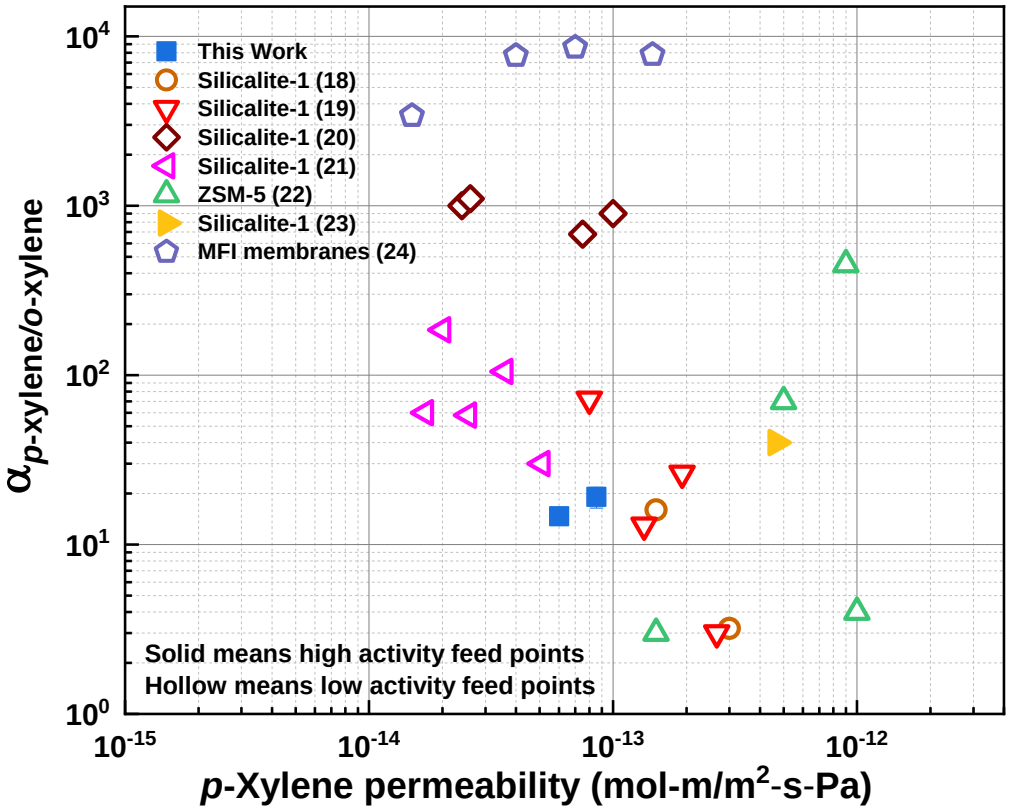

Figure 5.24 *p*-Xylene/*o*-xylene permselectivities of different advanced membranes as a function of permeability (mol-m/m^2-s-Pa). PIM-1-derived dense CMS membranes fabricated at 500 °C and 4 vol% H_2/Ar (solid blue square) at 55 °C and 2.4-5.5 kPa of *p*-xylene. Silicalite-1 membranes (orange circle) at 100 to 390 °C and 0.27 kPa of *p*-xylene [30]. c-Oriented MFI membranes (red down-triangle) at 50 to 200°C and 0.45-0.9 kPa of *p*-xylene [31]. a- and b-Oriented silicalite-1 membranes (brown diamond) at 200 °C and 0.32 kPa of *p*-xylene [32]. b-Out-of-plane-oriented silicalite-1 membranes (pink left-triangle) at 150 °C and 0.5 kPa of *p*-xylene [33]. b-, c- and a/b mixed-oriented ZSM-5 membranes (green triangle) at 100 to 200 °C and 0.45 kPa of *p*-xylene [27]. Silicalite-1 membranes prepared by a template-free secondary growth method (solid yellow right-triangle) at 50 °C and 2.3 kPa of *p*-xylene [34]. MFI membranes prepared by a gel-free secondary growth method (purple pentagon) at 100 to 250 °C and 0.5 kPa of *p*-xylene [28].

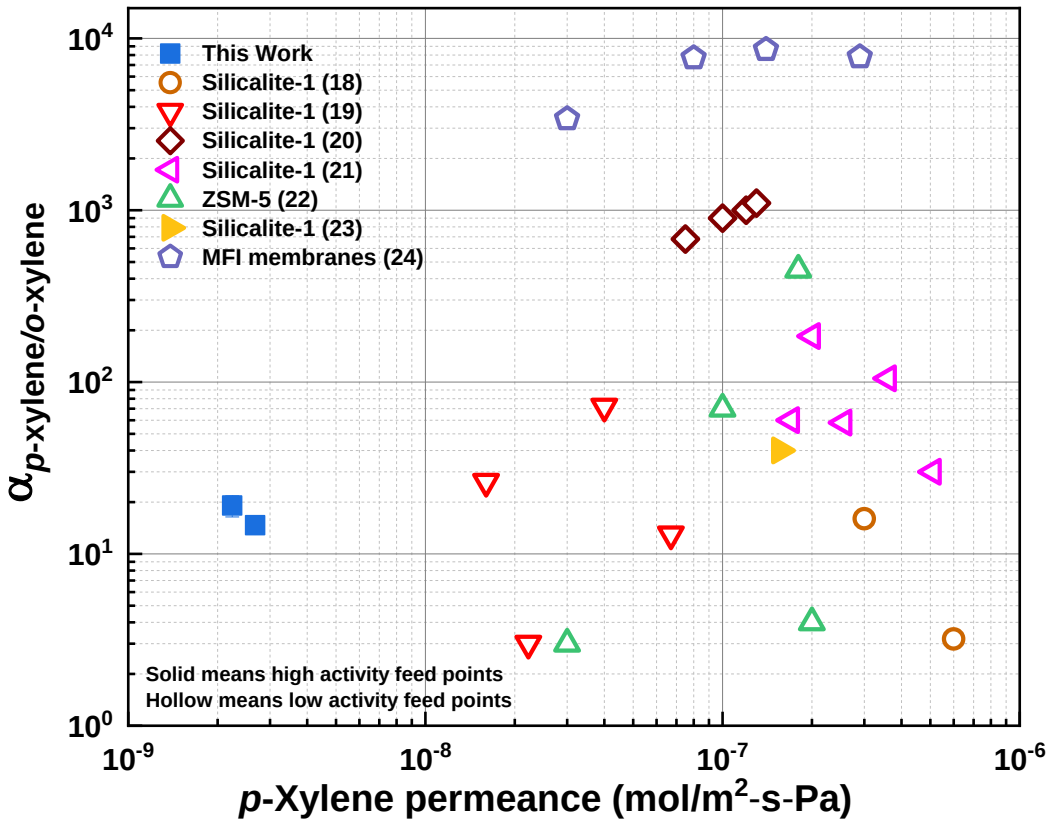

Figure 5.25 *p*-Xylene/*o*-xylene permselectivities of different advanced membranes as a function of permeance (mol/m^2-s-Pa). PIM-1-derived dense CMS membranes fabricated at 500 °C and 4 vol% H_2/Ar (solid blue square) at 55 °C and 2.4-5.5 kPa of *p*-xylene. Silicalite-1 membranes (orange circle) at 100 to 390 °C and 0.27 kPa of *p*-xylene [30]. c-Oriented MFI membranes (red down-triangle) at 50 to 200°C and 0.45-0.9 kPa of *p*-xylene [31]. a- and b-Oriented silicalite-1 membranes (brown diamond) at 200 °C and 0.32 kPa of *p*-xylene [32]. b-Out-of-plane-oriented silicalite-1 membranes (pink left-triangle) at 150 °C and 0.5 kPa of *p*-xylene [33]. b-, c- and a/b mixed-oriented ZSM-5 membranes (green triangle) at 100 to 200 °C and 0.45 kPa of *p*-xylene [27]. Silicalite-1 membranes prepared by a template-free secondary growth method (solid yellow right-triangle) at 50 °C and 2.3 kPa of *p*-xylene [34]. MFI membranes prepared by a gel-free secondary growth method (purple pentagon) at 100 to 250 °C and 0.5 kPa of *p*-xylene [28].

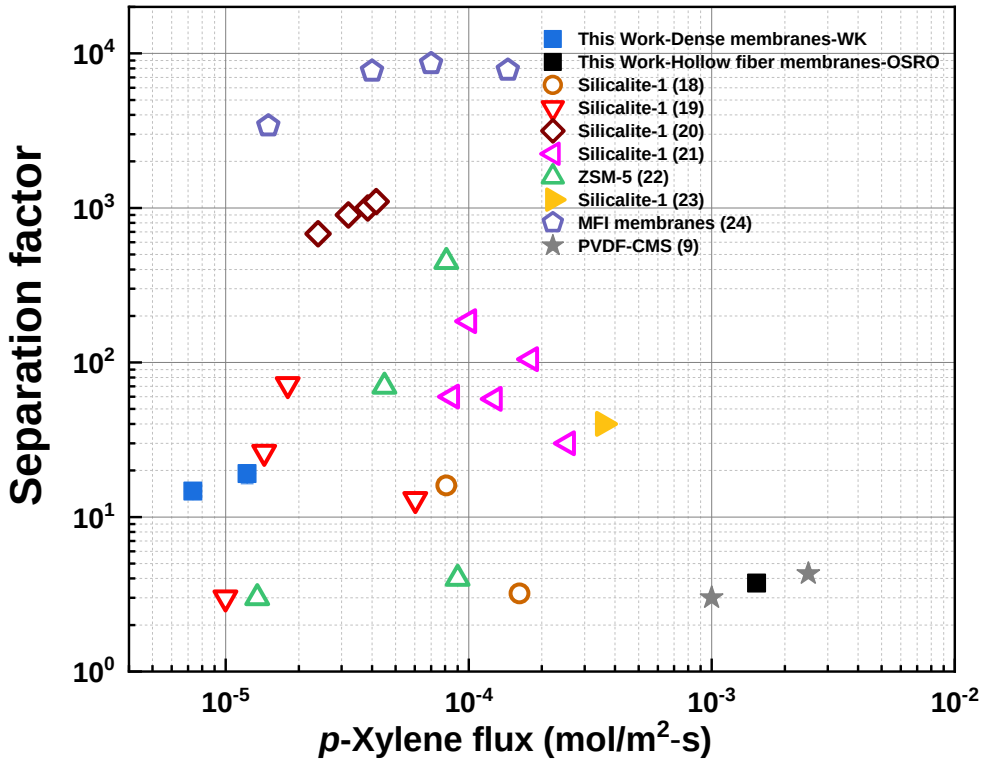

Figure 5.26 *p*-Xylene/*o*-xylene permselectivities of different advanced membranes as a function of flux (mol/m^2-s). PIM-1-derived dense CMS membranes fabricated at 500 °C and 4 vol% H_2/Ar (solid blue square) at 55 °C and 2.4-5.5 kPa of *p*-xylene measured by WK. PIM-1-derived hollow fiber CMS membranes fabricated at 500 °C and 4 vol% H_2/Ar (solid black square) at 25 °C and 5400 kPa of *p*-xylene measured by OSRO. Silicalite-1 membranes (orange circle) at 100 to 390 °C and 0.27 kPa of *p*-xylene [30]. c-Oriented MFI membranes (red down-triangle) at 50 to 200°C and 0.45-0.9 kPa of *p*-xylene [31]. a- and b-Oriented silicalite-1 membranes (brown diamond) at 200 °C and 0.32 kPa of *p*-xylene [32]. b-Out-of-plane-oriented silicalite-1 membranes (pink left-triangle) at 150°C and 0.5 kPa of *p*-xylene [33]. b-, c- and a/b mixed-oriented ZSM-5 membranes (green triangle) at 100 to 200 °C and 0.45 kPa of *p*-xylene [27]. Silicalite-1 membranes prepared by a template-free secondary growth method (solid yellow right-triangle) at 50 °C and 2.3 kPa of *p*-xylene [34]. MFI membranes prepared by a gel-free secondary growth method (purple pentagon) at 100 to 250 °C and 0.5 kPa of *p*-xylene [28]. PVDF derived CMS (solid grey star) at 22 °C and 3000-11300 kPa of *p*-xylene measured by OSRO [35].

Continued refinements of the pyrolysis atmosphere, protocol, and polymer precursors have the potential to make CMS membranes perform comparably with MFI for high activity solvent vapor separations [27,30]. Moreover, the hollow fiber CMS materials enable energy-efficient liquid phase osmotically-moderated separations that generally have much higher product fluxes and lower separation factors than MFI and CMS membranes operating in vapor separation modalities. Our experimental OSRO results reveal that the separation performance of the PIM-1-derived CMS HFM was comparable to the cross-linked polyvinylidene fluoride (PVDF) derived CMS HFM described in earlier work [35]. Importantly, the PIM-1 CMS HFM has a dramatically simplified fabrication scheme due to the avoidance of complex and cumbersome precursor pretreatments, which makes PIM-1-derived CMS more attractive for scale-up and practical applications.

5.7 Separation Mechanism of PIM-1-derived CMS Membranes

An effective diffusion-based separation requires a medium with pores small enough to discriminate between different solvent molecules. Koros and coworkers have investigated the source of the diffusion selectivity in sorption-diffusion membranes via application of an Eyring-Polanyi transition state theory approach (Eq. 2.14) [36].

The temperature dependence of the diffusion coefficient was assessed at low loadings (i.e., p/p^0 stepped from 0 to 0.05) where the Transport and Maxwell-Stefan diffusion coefficients are alike. Transient kinetic uptake curves (Figure 5.27) of *p*-xylene and *o*-xylene taken at different temperatures (35, 45 and 55°C) in both CMS_500 °C_0% H_2 and CMS_500 °C_4% H_2 samples were used to evaluate the temperature dependence

of the transport diffusivities and assess the separation mechanism of xylenes in these two rigid bimodally microporous membranes [37].

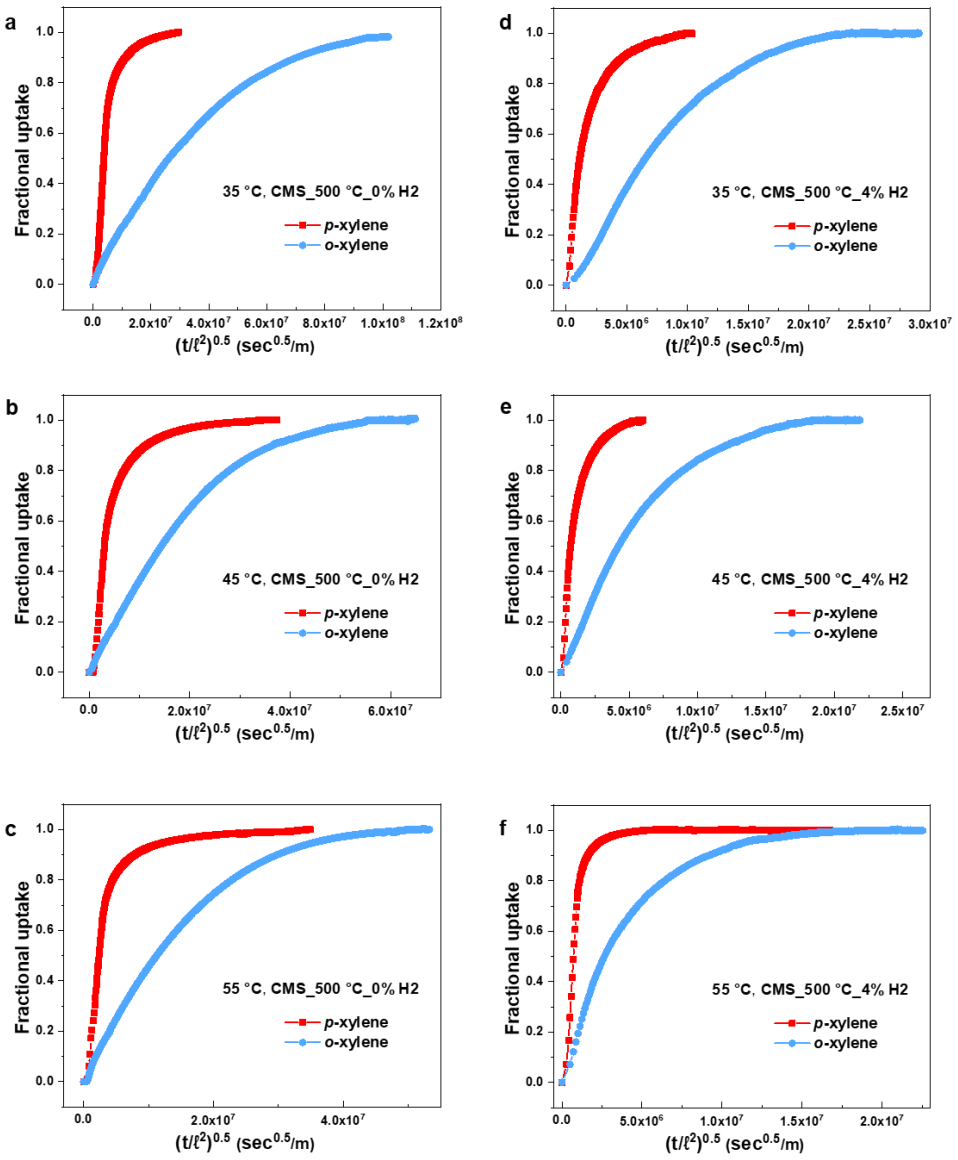

Figure 5.27 The kinetic uptake curves of *p*-xylene and *o*-xylene performed at 35 °C (a, d), 45 °C (b, e) and 55 °C (c, f) in CMS_500 °C_0% H_2 (a, b and c) and CMS_500 °C_4% H_2 (d, e and f) with a 0.00-0.05 change in relative pressure.

As shown in Figure 5.28, transport diffusivities of both *p*-xylene and *o*-xylene increase with temperature, following an Arrhenius-type temperature dependence relationship ($D_i = D_{0i} exp\ (\frac{-E_{D,i}}{RT})$) with a positive diffusion activation energy.

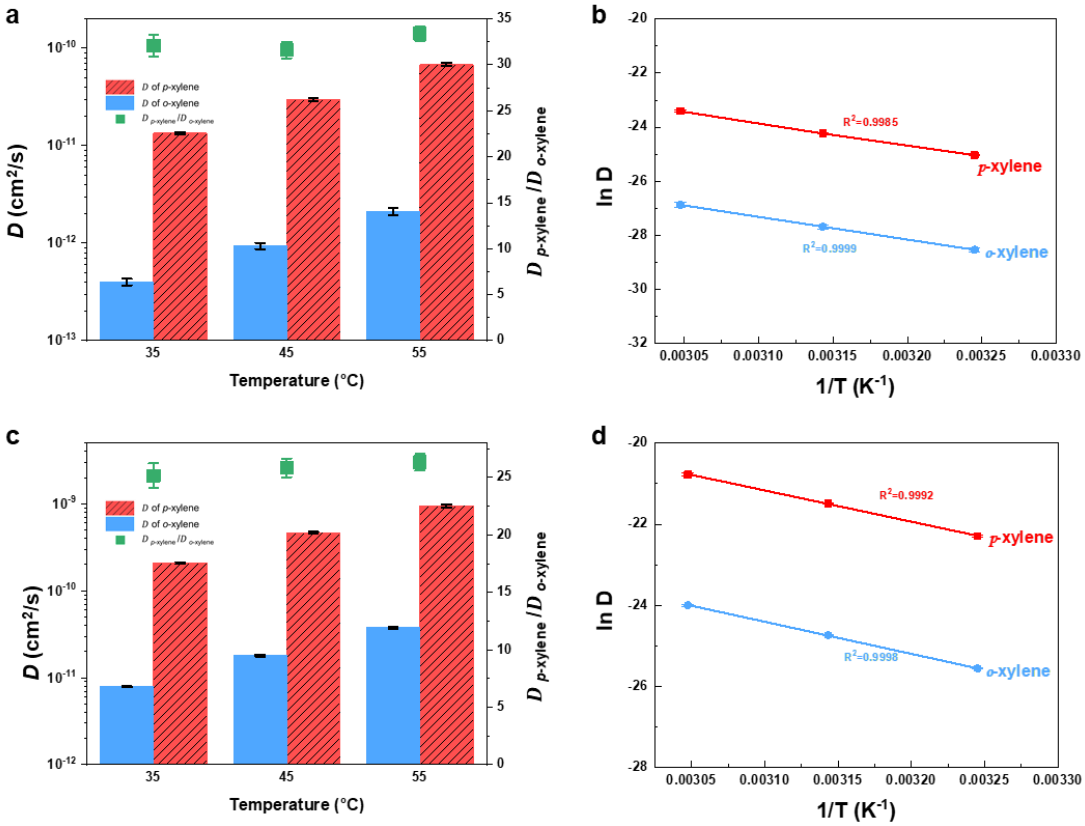

Figure 5.28 Transport diffusion coefficients for xylene isomers and diffusion selectivity between *p*-xylene and *o*-xylene in (a) CMS_500 °C_0% H_2 and (c) CMS_500 °C_4% H_2 from 35 to 55 °C. Temperature dependence of the transport diffusion coefficients for xylene isomers in (b) CMS_500 °C_0% H_2 and (d) CMS_500 °C_4% H_2 from 35 to 55 °C (transport diffusion coefficient, *D* are in the units of cm^2/s, error bars represent the standard deviation of at least three runs, each on the different CMS samples).

The diffusion activation energies $E_{D,i}$ and the pre-exponential factors of diffusion D_{0i} for both *p*-xylene and *o*-xylene in CMS_500 °C_0% H_2 and CMS_500 °C_4% H_2 are summarized in Table 5.6. As shown in Table 5.6, the diffusion activation energies for *o*-xylene is always larger than that for the smaller molecule, *p*-xylene, indicating a higher diffusion energy barrier for *o*-xylene to enable a diffusive molecular displacement. The enthalpic, entropic, and the overall diffusive selectivity of xylene isomers for CMS_500 °C_0% H_2 and CMS_500 °C_4% H_2 are also listed in Table 5.6. The enthalpic diffusion selectivity was obtained by comparing the diffusion activation energy values for the two xylene isomers, while the entropic diffusion selectivity was calculated according to Eq. 2.14. As shown in Table 5.6, the transport diffusion selectivity between *p*-xylene/*o*-xylene is higher for CMS_500 °C_0% H_2 sample than that for CMS_500 °C_4% H_2 sample (32.4 vs. 25.8), which is attributed to the narrow ultramicropores inside CMS_500 °C_0% H_2 sample.

Table 5.6 Transport diffusion properties of xylene isomers for PIM-1-derived CMS membranes fabricated under different conditions.

Sample	CMS_500 °C_0% H_2		CMS_500 °C_4% H_2	
	p-xylene	*o*-xylene	*p*-xylene	*o*-xylene
E_D $(\frac{kJ}{mol})$	67.8 ± 1.8	70.0 ± 0.1	64.1 ± 1.1	66.0 ± 0.2
D_0 $(\frac{cm^2}{s})$	4.1 ± 0.3	0.3 ± 0.0	15.2 ± 0.7	3.2 ± 0.3
Transport diffusion selectivity	32.4 ± 1.7		25.8 ± 0.5	
*p*x/*o*x	(32.1 ± 3.0)		(25.2 ± 1.1)	
Enthalpic diffusion selectivity	2.3 ± 0.0		2.0 ± 0.0	
*p*x/*o*x	(2.2 ± 0.0)		(2.0 ± 0.0)	
Entropic diffusion selectivity	14.3 ± 0.7		12.8 ± 0.3	
*p*x/*o*x	(14.6± 1.4)		(12.7 ± 0.5)	

[a] Non-parentheses values are the average selectivity in the temperature ranging from 35 to 55 °C, while the numbers inside the parentheses are selectivity at 55 °C.

Based on these experimental measurements, it is clear that both CMS membranes are separating the xylene isomers based on differences in the conformational availability of the isomer in the activated state of diffusion. However, to our knowledge, the observation of such "entropic diffusion selectivity" in cases where the Maxwell-Stefan

diffusion coefficients are not strongly dependent on loading has not previously been observed in liquids. We attempt to provide one possible explanation for this behavior.

The ultramicropores inside the rigid bimodal microporous CMS membranes enable the observed separation. As a result, the ultramicropore size distributions for both CMS_500 °C_0% H_2 and CMS_500 °C_4% H_2 were studied to illustrate the separation mechanism of rigid bimodally microporous membranes. As indicated by nitrogen physisorption experiments, nitrogen molecules at 77 K cannot easily access the ultramicropores of the CMS derived from PIM-1 under pure argon condition (CMS_500 °C_0% H_2) [1]. We believe that the ultramicropores of the CMS_500 °C_0% H_2 are thus similar to but somewhat larger than the kinetic diameter of nitrogen (3.64 Å; the ultramicropores must be larger than this as we observe sorption and diffusion of xylene isomers at higher temperatures) [1]. With this in mind, a hypothetical ultramicropore size distribution of CMS_500 °C_0% H_2 is drawn in Figure 5.29, where we hypothesize that most of the ultramicropores of CMS_500 °C_0% H_2 are expected to fall in the range from 2 Å to 5 Å. On the other hand, the CMS derived from PIM-1 under a 4 vol% hydrogen/argon environment (CMS_500 °C_4% H_2) possesses a large number of ultramicropores that can be probed by nitrogen physisorption (Figure 5.29) [38]. The majority of ultramicropores of CMS_500 °C_4% H_2 are thus known to fall in the range of 4 Å to 7 Å and are shown on the plot [38].

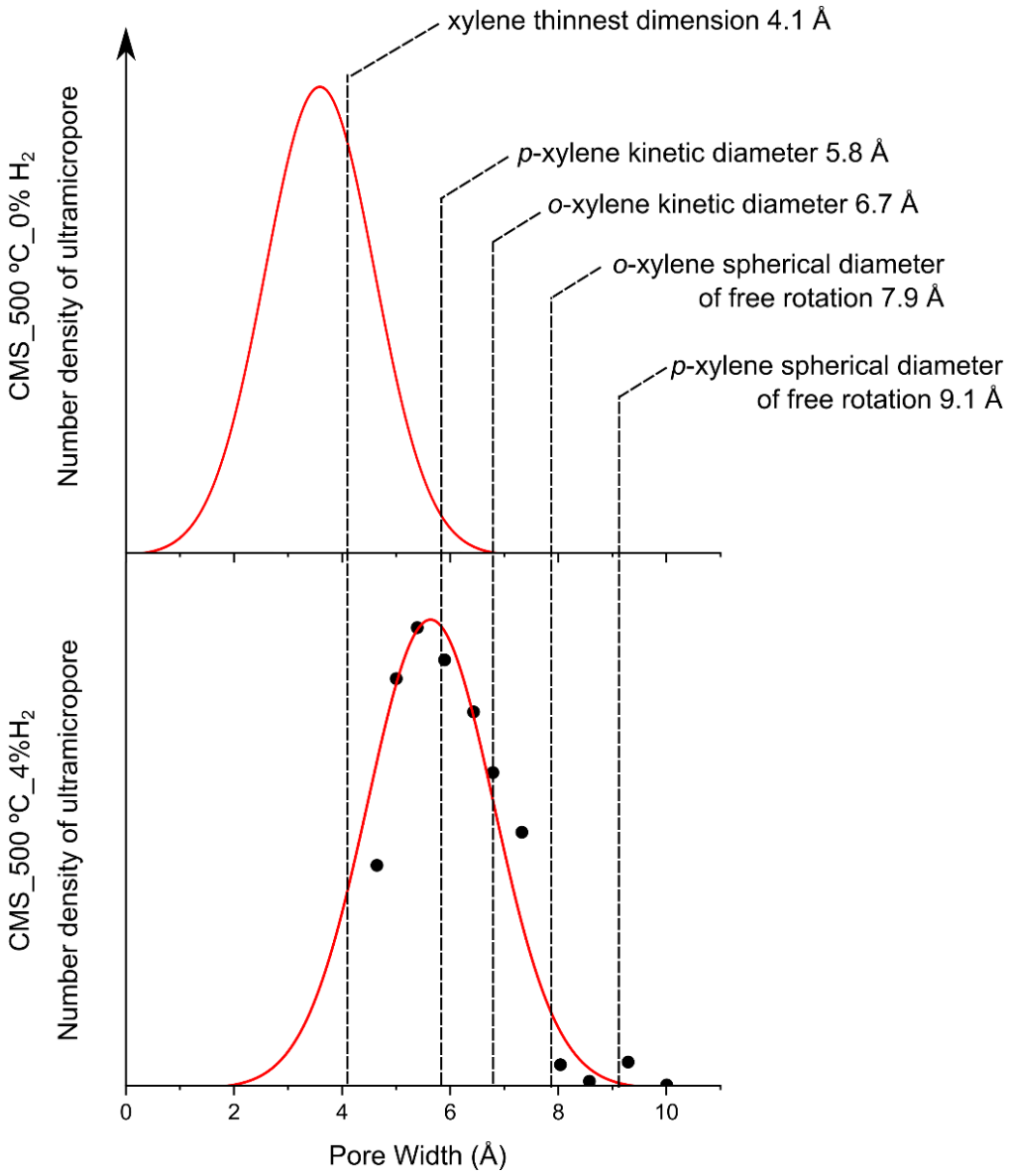

Figure 5.29 The hypothetic ultramicropore size distribution of CMS_500 °C_0% H_2 and ultramicropore size distribution of CMS_500 °C_4% H_2 measured with N_2 physisorption at 77K [38] with the comparison of xylene isomer dimensions.

The xylene isomers each possess thicknesses of around 4.1 Å. As a result, ultramicropores below 4.1 Å will molecularly exclude both *p*-xylene and *o*-xylene, which

suggests that most ultramicropores in CMS_500 °C_0% H_2 do not contribute to the xylene transport. That hypothesis is supported by the low permeability of CMS_500 °C_0% H_2 membranes [1]. However, most ultramicropores of CMS_500 °C_4% H_2 are accessible to xylene transport, resulting in a significant enhancement in xylene permeability [38].

The largest diameters of freely rotating *p*-xylenes and *o*-xylene molecules are 9.1 Å and 7.9 Å, respectively. Within ultramicropores smaller than 9.1 Å, the xylene molecules cannot freely rotate without collision with the wall of the ultramicropores. Considering this, we hypothesize that ultramicropores ranging from 4.1 Å to 9.1 Å will limit – to varying degrees – the conformations available to *p*-xylene and *o*-xylene in the activated state of diffusion. Both CMS_500 °C_0% H_2 and CMS_500 °C_4% H_2 possess ultramicropores within 4.1 Å to 9.1 Å, which enables entropically-moderated selective xylene transportation in both membranes although the entropic diffusion selectivity is found to decrease in the larger ultramicropore case (14.3 vs. 12.8 as shown in Table 5.6). Since the ultramicropores of CMS_500 °C_0% H_2 are much smaller than those of CMS_500 °C_4% H_2, CMS_500 °C_0% H_2 exhibits a stronger conformation restriction for the xylene isomers compared with CMS_500 °C_4% H_2 and thus results in a higher selectivity. Micropores larger than 9.1 Å will exert negligible conformational restrictions to the xylene molecules and are not expected to contribute to the selective xylene transport significantly. Micropores formed by the CMS_500 °C_4% H_2 carbon plates range from 9.1 Å to 20 Å. Xylene transport within these pores – when gated by ultramicroporous windows – can be described by classical sorption-diffusion mechanism without any conformational restrictions. Pores with even larger width will result in pore flow of xylene fluids, which will significantly impair the separation performance.

Table 5.7 summarized the effects of pores with different sizes relevant to the selective transport of xylene isomers. A successful CMS membrane for xylene separation should possess two features: (1) narrow and intensive distribution of ultramicropores ranging from 4 Å to 9 Å for high xylene isomer selectivity; (2) significant amount of micropores ranging from 9 Å to 20 Å for enhancement in xylene permeability.

Table 5.7 Xylene transportation in different micropores.

Pore Width (Å)	Transport mechanism	Conformation restriction to xylene isomers
0 ~ 4	Inaccessible to xylene isomers	N/A, molecular exclusion
4 ~ 9	Conformation-controlled sorption-diffusion transport	Significant
9 ~ 15	Sorption-diffusion transport	Negligible

5.8 Summary and Conclusions

In summary, the microstructure of PIM-1-derived CMS membranes is facilely tuned by the pyrolysis of polymer precursors in the presence of H_2. During the pyrolysis process, the introduction of H_2 inhibits the aromatization of the decomposing polymer network. The size of the ultramicropores inside pure Ar pyrolyzed CMS is quite similar to N_2 while the CMS pyrolyzed under an H_2-included environment shows ultramicropores ranging from 5-7 Å, which are highly similar to the size of methyl-substituted benzene

derivatives (5.3-8.0 Å). The increase of H_2 concentration in the pyrolysis environment or the decrease of pyrolysis temperature results in an increase in ultramicropore size and sp^3/sp^2 carbon ratio, which we hypothesize is a fundamental property related to the transport properties of guest molecules in the CMS membrane. The H_2-assisted CMS membranes reveal good *p*-xylene/*o*-xylene separation with a significant increase in *p*-xylene permeability of $6.0\times10^{-14}\ mol\ m/m^2\ s\ Pa$) and a *p*-xylene/*o*-xylene selectivity of 14.7 for equimolar mixture tests. Moreover, the hollow fiber CMS membranes, fabricated under 4% H_2/Ar show a *p*-xylene permeance of $5.2\times10^{-10}\ mol/m^2\ s\ Pa$ and a high activity vapor mixture permselectivity of 8.9 based on WK measurements and a *p*-xylene hydraulic permeance of $2.6\times10^{-10}\ mol/m^2\ s\ Pa$ and a separation factor of 3.7 based on OSRO tests. In general, this relatively rapid and straightforward pyrolysis method is expected to be further extended for the fabrication of CMS derived from other kinds of polymeric precursors and open up new opportunities for the membrane-based applications of CMS materials.

5.9 References

1. Y. Ma, F. Zhang, S. Yang, R. P. Lively. Evidence for entropic diffusion selection of xylene isomers in carbon molecular sieve membranes. *Journal of Membrane Science* **2018**;564:404-414.

2. J. Jang, B. Lim. Selective Fabrication of Carbon Nanocapsules and Mesocellular Foams by Surface‐Modified Colloidal Silica Templating. *Advanced Materials* **2002**;14(19):1390-1393.

3. R. Ryoo, S. H. Joo, M. Kruk, M. Jaroniec. Ordered mesoporous carbons. *Advanced Materials* **2001**;13(9):677-681.

4. J. Lee, S. Han, T. Hyeon. Synthesis of new nanoporous carbon materials using nanostructured silica materials as templates. *Journal of Materials Chemistry* **2004**;14(4):478-486.

5. X. Ning, W. J. Koros. Carbon molecular sieve membranes derived from Matrimid® polyimide for nitrogen/methane separation. *Carbon* **2014**;66:511-522.

6. S. Fu, E. S. Sanders, S. S. Kulkarni, W. J. Koros. Carbon molecular sieve membrane structure–property relationships for four novel 6FDA based polyimide precursors. *Journal of Membrane Science* **2015**;487:60-73.

7. H. J. Kim, D.-G. Kim, K. Lee, Y. Baek, Y. Yoo, Y. S. Kim, B. G. Kim, J.-C. Lee. A carbonaceous membrane based on a polymer of intrinsic microporosity (PIM-1) for water treatment. *Scientific reports* **2016**;6:36078.

8. A. S. Gasse. *Experimentelle Bestimmung und Simulation von Explosionsgrenzen, untersucht an wasserstoffhaltigen Brenngasgemischen*: Shaker; **1992**.

9. M. Rungta, L. Xu, W. J. Koros. Carbon molecular sieve dense film membranes derived from Matrimid® for ethylene/ethane separation. *Carbon* **2012**;50(4):1488-1502.

10. D. Q. Vu, W. J. Koros, S. J. Miller. High pressure CO2/CH4 separation using carbon molecular sieve hollow fiber membranes. *Industrial & Engineering Chemistry Research* **2002**;41(3):367-380.

11. A. Wollbrink, K. Volgmann, J. Koch, K. Kanthasamy, C. Tegenkamp, Y. Li, H. Richter, S. Kämnitz, F. Steinbach, A. Feldhoff. Amorphous, turbostratic and crystalline carbon membranes with hydrogen selectivity. *Carbon* **2016**;106:93-105.

12. H. Richter, H. Voss, N. Kaltenborn, S. Kämnitz, A. Wollbrink, A. Feldhoff, J. Caro, S. Roitsch, I. Voigt. High‐flux carbon molecular sieve membranes for gas separation. *Angewandte Chemie International Edition* **2017**;56(27):7760-7763.

13. P. Merel, M. Tabbal, M. Chaker, S. Moisa, J. Margot. Direct evaluation of the sp3 content in diamond-like-carbon films by XPS. *Applied Surface Science* **1998**;136(1-2):105-110.

14. D. B. G. Beamson. *High resolution XPS of organic polymers: The Scienta ESCA 300 database.* : Wiley Online Library; **1992**.

15. Y. K. Kim, H. B. Park, Y. M. Lee. Preparation and characterization of carbon molecular sieve membranes derived from BTDA–ODA polyimide and their gas separation properties. *Journal of Membrane Science* **2005**;255(1):265-273.

16. G. Jenkins, K. Kawamura. *Polymeric carbons- carbon fibre, glass and char***1976**.

17. O. Salinas, X. Ma, E. Litwiller, I. Pinnau. Ethylene/ethane permeation, diffusion and gas sorption properties of carbon molecular sieve membranes derived from the prototype ladder polymer of intrinsic microporosity (PIM-1). *Journal of Membrane Science* **2016**;504:133-140.

18. L. Hao, K.-S. Liao, T.-S. Chung. Photo-oxidative PIM-1 based mixed matrix membranes with superior gas separation performance. *Journal of Materials Chemistry A* **2015**;3(33):17273-17281.

19. S. A. El-Khodary, G. M. El-Enany, M. El-Okr, M. Ibrahim. Preparation and characterization of microwave reduced graphite oxide for high-performance supercapacitors. *Electrochimica Acta* **2014**;150:269-278.

20. M. Rungta, G. B. Wenz, C. Zhang, L. Xu, W. Qiu, J. S. Adams, W. J. Koros. Carbon molecular sieve structure development and membrane performance relationships. *Carbon* **2017**;115:237-248.

21. J. S. Adams, A. K. Itta, C. Zhang, G. B. Wenz, O. Sanyal, W. J. Koros. New insights into structural evolution in carbon molecular sieve membranes during pyrolysis. *Carbon* **2019**;141:238-246.

22. P. J. Flory. Molecular theory of liquid crystals. *Liquid Crystal Polymers I*: Springer; 1984:1-36.

23. G. van Anders, D. Klotsa, N. K. Ahmed, M. Engel, S. C. Glotzer. Understanding shape entropy through local dense packing. *Proceedings of the National Academy of Sciences* **2014**;111(45):E4812-E4821.

24. D. Frenkel. Entropy-driven phase transitions. *Physica A: statistical mechanics and its applications* **1999**;263(1-4):26-38.

25. L. Xu, M. Rungta, J. Hessler, W. Qiu, M. Brayden, M. Martinez, G. Barbay, W. J. Koros. Physical aging in carbon molecular sieve membranes. *Carbon* **2014**;80:155-166.

26. Y. M. Melinda L. Jue, Ryan P. Lively. Streamlined Fabrication of Asymmetric Carbon Molecular Sieve Hollow Fiber Membranes. *Journal of Membrane Science* **2019**.

27. Z. Lai, G. Bonilla, I. Diaz, J. G. Nery, K. Sujaoti, M. A. Amat, E. Kokkoli, O. Terasaki, R. W. Thompson, M. Tsapatsis. Microstructural optimization of a zeolite membrane for organic vapor separation. *Science* **2003**;300(5618):456-460.

28. D. Kim, M. Y. Jeon, B. L. Stottrup, M. Tsapatsis. para ‐ Xylene Ultra ‐ selective Zeolite MFI Membranes Fabricated from Nanosheet Monolayers at the Air – Water Interface. *Angewandte Chemie International Edition* **2018**;57(2):480-485.

29. M. L. Jue, Y. Ma, R. P. Lively. Streamlined Fabrication of Asymmetric Carbon Molecular Sieve Hollow Fiber Membranes. *ACS Applied Polymer Materials* **2019**;1(8):1960-1964.

30. J. Hedlund, J. Sterte, M. Anthonis, A.-J. Bons, B. Carstensen, N. Corcoran, D. Cox, H. Deckman, W. De Gijnst, P.-P. de Moor. High-flux MFI membranes. *Microporous and Mesoporous Materials* **2002**;52(3):179-189.

31. G. Xomeritakis, Z. Lai, M. Tsapatsis. Separation of xylene isomer vapors with oriented MFI membranes made by seeded growth. *Industrial & Engineering Chemistry Research* **2001**;40(2):544-552.

32. T. C. T. Pham, T. H. Nguyen, K. B. Yoon. Gel ‐ free secondary growth of uniformly oriented silica MFI zeolite films and application for xylene separation. *Angewandte Chemie* **2013**;125(33):8855-8860.

33. K. V. Agrawal, B. Topuz, T. C. T. Pham, T. H. Nguyen, N. Sauer, N. Rangnekar, H. Zhang, K. Narasimharao, S. N. Basahel, L. F. Francis. Oriented MFI membranes by gel ‐ less secondary growth of sub ‐ 100 nm MFI ‐ nanosheet seed layers. *Advanced Materials* **2015**;27(21):3243-3249.

34. W. Yuan, Y. Lin, W. Yang. Molecular sieving MFI-type zeolite membranes for pervaporation separation of xylene isomers. *Journal of the American Chemical Society* **2004**;126(15):4776-4777.

35. D.-Y. Koh, B. A. McCool, H. W. Deckman, R. P. Lively. Reverse osmosis molecular differentiation of organic liquids using carbon molecular sieve membranes. *Science* **2016**;353(6301):804-807.

36. S. Glasstone, K. J. Laidler, H. Eyring. *The theory of rate processes; the kinetics of chemical reactions, viscosity, diffusion and electrochemical phenomena*: McGraw-Hill Book Company;1941.

37. Y. Ma, F. Zhang, H. W. Deckman, W. J. Koros, R. P. Lively. Flux Equations for Osmotically Moderated Sorption–Diffusion Transport in Rigid Microporous Membranes. *Industrial & Engineering Chemistry Research* **2019**.

38. Y. Ma, M. L. Jue, F. Zhang, R. Mathias, H. Y. Jang, R. Lively. Creation of well‐defined “mid‐sized” micropores in carbon molecular sieve membranes. *Angewandte Chemie International Edition*.

CHAPTER 6. **PIM-SBF DERIVED CMS MEMBRANES FOR XYLENE ISOMER SEPARATIONS**[§]

6.1 Introduction

As noted in earlier chapters, carbon molecule sieve (CMS) membranes are fabricated via the pyrolysis of polymeric precursors. Under a high-temperature inert atmosphere, the polymer backbone is activated and rearranged. During the rearrangement, the polymer chains are transferred into stable highly carbonized structures driven by entropy. By manipulating the formation of carbon strands and the packing of carbon cages, a porous CMS membrane with a bimodal pore size distribution is fabricated. By engineering the pore size distribution of the CMS membrane, differentiation of certain molecular pairs can be achieved.

The pore size distribution of the resulting CMS membrane is significantly affected by the type of polymer precursor chosen [1]. The polymer structure determines the spatial distribution of the carbon atoms. A polymer with high free volume or interconnected micropores tends to form highly porous CMS. As demonstrated in previous chapters, PIM-1 has been proven a successful precursor for the fabrication of highly porous CMS membranes for organic solvent separations. PIM-1 uses a fused-ring structure to increase chain rigidity in addition to a spirocenter in the repeat unit. These two factors result in high free volume within the membrane by inhibiting effective chain packing [2-6]. However, a

[§] The polymer precursor in this chapter, spirobifluorene-based polymer of intrinsic microporosity (PIM-SBF), was synthesized and provided by Dr. Nicholas Bruno from the Finn Group in the School of Chemistry and Biochemistry at Georgia Institute of Technology.

decrease of pore size and porosity was observed for the PIM-1-derived CMS after the pyrolysis compared with the polymer precursors [7,8], as indicated in Table 5.2 and Figure 5.6. Such undesired pore collapsing is hypothetically attributed to the destruction of the spirocarbon, which resulting in the flattening of the polymer backbone (Figure 5.15). It has been suggested that a more rigid polymer chain will result in a better performance of the polymeric membranes (i.e., enhanced permeability of gas molecules) [9,10]. In this context, we believe that a more rigid polymer precursor and perhaps a more thermally stable spirocenter may also prevent the polymer chain flattening and pore collapsing to some degree during pyrolysis and lead to the formation of CMS membranes with a better separation performance.

Heuchel et al. has provided evidence that the spirocentre of the spirobisindane unit inside PIM-1 has a certain degree of conformational flexibility using molecular dynamic modeling methods [11]. However, it has been suggested that the spirobifluorene unit, because of the introduction of the fused benzene rings, can effectively limit the movement of the spirocentre and result in a more rigid structure [12]. In this chapter, a spirobifluorene-based polymer of intrinsic microporosity (PIM-SBF, the structure of which is shown in Figure 6.1) is used as the new polymer precursor for CMS membrane fabrication. It is expected that the rearrangement of spirobifluorene tends to form contorted, carbonized chains and results in inefficient packing of the carbon strands.

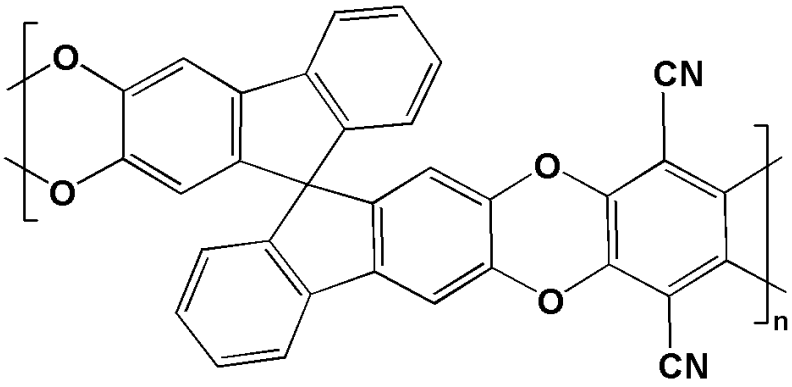

Figure 6.1 Molecular structures of PIM-SBF.

6.2 Synthesis of Polymer Precursor PIM-SBF

As noted earlier, the PIM-SBF was synthesized and provided by Dr. Nicholas Bruno from the Finn Group in the School of Chemistry and Biochemistry at Georgia Institute of Technology. For completeness, Dr. Nicholas Bruno's synthetic procedure is reproduced here.

6.2.1 Materials

Anhydrous THF was purchased from Sigma Aldrich and vigorously purged with nitrogen for 2 h. The solvents were further purified by passing them under nitrogen pressure through two packed columns of neutral alumina. All reagents and solvents were purchased and used as received unless otherwise noted. 2-Aminobiphenyl palladium methanesulfonate precatalyst (SPhos-Pd-G3) was synthesized according to the literature procedure [13]. SPhos, phenylboronic acid, and 4-bromoveratrole were purchased from Oakwood (Estill, South Carolina, USA). Tetrafluoroterphthalonitrile, potassium phosphate

tribasic, n-butyl lithium, and boron tribromide were purchased from Aldrich Chemical Company (St. Louis, Missouri, USA).

6.2.2 Synthesis of 3,4-dimethoxy-1,1'-biphenyl

A 1 L round-bottomed flask equipped with a magnetic stir bar and rubber septum was charged with 4-bromoveratrole (43.4 g, 200 mmol, 1.0 equiv.), phenylboronic acid (29 g, 240 mmol, 1.2 equiv.), potassium carbonate (69 g, 500 mmol, 2.5 equiv.), and toluene (300 mL). The flask was capped with a rubber septum and sparged with nitrogen for 15 min. Under nitrogen, SPhos-Pd-G3 precatalyst (78 mg, 0.1 mmol, 0.05 mol %) was added in one portion, the flask capped and the reaction mixture was stirred at 110 °C for 6 h. After completion, the reaction mixture was cooled to room temperature, diluted with dichloromethane (200 mL), and filtered through a plug of celite on top of a plug of silica gel, eluting with dichloromethane. The resulting solution was concentrated via rotary evaporation and further dried on a Schlenk line to provide the title compound as an off-white solid. The molecular structures of 3,4-dimethoxy-1,1'-biphenyl and other chemicals involved during the synthesis of PIM-SBF were shown in Table 6.1.

Table 6.1 Molecular structures of chemicals involved during the synthesis of PIM-SBF.

Chemical	Molecular structure
3,4-dimethoxy-1,1'-biphenyl	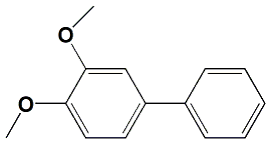
2-bromo-4,5-dimethoxy-1,1'-biphenyl	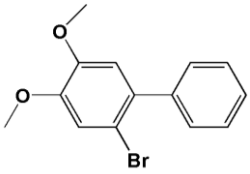
2,3-dimethoxy-9H-fluoren-9-one	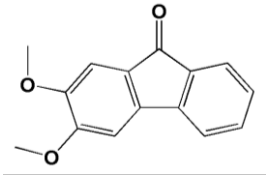
2,2’,3,3’-tetramethoxy-9,9'-spirobifluorene	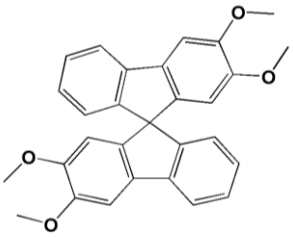
2,2’,3,3’-tetrahydroxy-9,9'-spirobifluorene	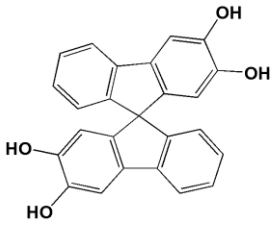

6.2.3 Synthesis of 2-bromo-4,5-dimethoxy-1,1'-biphenyl

A 500 mL round-bottomed flask equipped with a magnetic stir bar was charged with 3,4-dimethoxy-1,1’-biphenyl (42.8 g, 200 mmol, 1 equiv.) followed by the addition of dichloromethane (300 mL). With stirring, bromine (11.4 mL, 220 mmol, 1.1 equiv.) was added dropwise and after the addition was complete, the resulting solution was stirred at room temperature for 1 h. The reaction mixture was then quenched with saturated, aqueous sodium bicarbonate and sodium sulfite. The layers were separated and the organic fraction was washed with water then brine. The organic layer was dried over magnesium sulfate, filtered through a pad of silica gel, and concentrated via rotary evaporation. The crude product was triturated with methanol, filtered, and dried under vacuum to provide the title compound as a white solid.

6.2.4 Synthesis of 2,3-dimethoxy-9H-fluoren-9-one

A flame-dried 1 L round-bottomed Schlenk flask equipped with a magnetic stir bar and rubber septum was charged with 2-bromo-4,5-dimethoxy-1,1’-biphenyl (22 g, 75 mmol, 1 equiv.). The flask was evacuated and backfilled with nitrogen (this sequence was repeated a total of three times). THF (400 mL) was added via cannula and the mixture was cooled to -78 °C in a dry ice/acetone bath under argon. A solution of nBuLi in hexanes (30 mL, 2.5 M, 75 mmol, 1 equiv.) was added slowly and after addition the reaction mixture was stirred for 2 h at -78 °C. Dry carbon dioxide was then bubbled through the reaction mixture until the deep yellow color dissipated to a pale yellow and the mixture was allowed to warm to room temperature overnight (a thin-gauge vent needle was inserted into the septum to prevent the build-up of pressure). The solvent was removed via rotory

evaporation until a solid was obtained, after which diethyl ether (200 mL) and water (400 mL) were added. The layers were separated and the aqueous layer was acidified with HCl (1 M, 100 mL), precipitating the carboxylic acid. The solid was filtered, dried, added to 150 mL methanesulfonic acid, and stirred at room temperature overnight. The resulting deep emerald green solution was then poured onto ice, resulting in the precipitation of an orange solid. The solid was isolated via vacuum filtration, washed with water, triturated with methanol, and dried under vacuum to provide the title compound as a vibrant orange solid.

6.2.5 Synthesis of 2,2',3,3'-tetramethoxy-9,9'-spirobifluorene

A flame-dried 500 mL round-bottomed flask equipped with a rubber septum and magnetic stir bar was charged with 2-bromo-4,5-dimethoxy-1,1'-biphenyl (8.3 g, 28.3 mmol, 1.13 equiv.). The flask was evacuated and backfilled with nitrogen (this procedure was performed a total of three times). Dry THF (200 mL) was added and the flask cooled to -78 °C under nitrogen in a dry ice/acetone bath. n-butyl lithium (2.5 M in hexanes, 11.3 mL, 28.3 mmol, 1.13 equiv.) was added dropwise and after the addition was complete, the reaction mixture was stirred at -78 °C for 2 hours. 3,4-dimethoxyfluorenone (6 g, 25 mmol, 1 equiv.) was then added in one portion and the mixture was stirred overnight, warming to room temperature. The reaction was then quenched with the addition of saturated aqueous ammonium chloride (10 mL). The mixture was filtered and concentrated and the resulting solid was triturated with methanol, filtered, and dried under vacuum. It was then suspended in nitromethane and anhydrous iron trichloride (20 mg, 5 mol %) was added. The mixture was stirred at room temperature for 10 minutes, 90% of the solvent removed via rotary

evaporation, and the residue triturated with methanol and filtered to provide the title compound as a white solid.

6.2.6 Synthesis of 2,2',3,3'-tetrahydroxy-9,9'-spirobifluorene

A 500 mL round-bottomed flask equipped with a magnetic stir bar and rubber septum was charged with 2,2',3,3'-tetramethoxy-9,9'-spirobifluorene (6 g, 13.7 mmol, 1 equiv.). The flask was evacuated and backfilled with nitrogen (this sequence was performed a total of three times) and dry dichloromethane was added (150 mL) [14]. The mixture was cooled under nitrogen in an ice bath and boron tribromide (3.9 mL, 41.1 mmol, 3 equiv.) was added by syringe and the reaction mixture was stirred overnight. The mixture was then poured into water (500 mL), stirred at room temperature for 30 min, filtered, washed with water and dichloromethane, and dried under vacuum to provide the title compound as an off-white solid.

6.2.7 Synthesis of PIM-SBF

PIM-SBF was synthesized using the standard PIM-forming aromatic nucleophilic substitution polymerization reaction, as shown in Figure 6.2 [4,12]. A flame-dried, 250 mL round-bottomed flask equipped with a magnetic stir bar and rubber septum was charged with 2,2',3,3'-tetrahydroxy-9,9'-spirobifluorene (4.18 g, 11 mmol, 1 equiv.) and tetrafluoroterphthalonitrile (2.2 g, 11 mmol, 1 equiv.). Dry DMF (55 mL) was added by syringe and the reaction mixture was stirred under nitrogen at room temperature until the complete dissolution of both monomers. Potassium carbonate (12.1 g, 88 mmol, 8 equiv.) was added in one portion and the reaction mixture was stirred at 65 °C for 92 hours. After completion, the reaction mixture was poured into water, filtered, and washed with water,

methanol, and acetone. The crude material was redissolved in chloroform, precipitated into 2:1 methanol:acetone, filtered, and dried in a vacuum oven at 100 °C to provide the title compound as a vibrant, yellow powder. The molecular weight as determined by GPC in THF was Mw = 54,000.

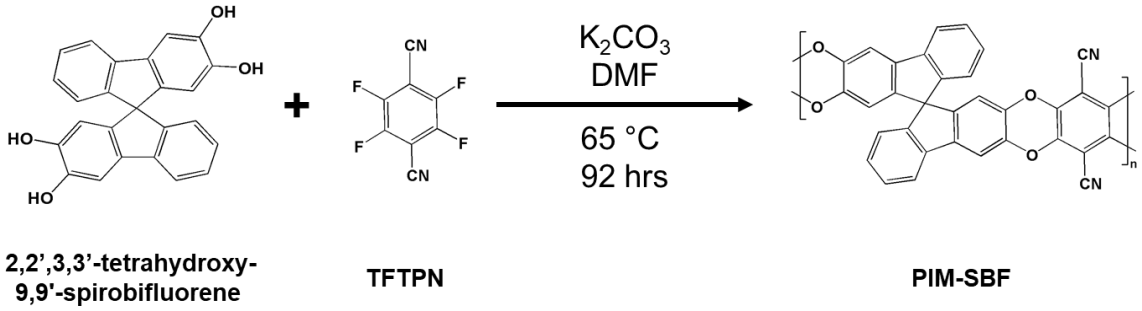

Figure 6.2 Reaction scheme for the synthesis of PIM-SBF.

6.3 Characterization of PIM-SBF-derived CMS

6.3.1 Nitrogen physisorption

The pore structure of PIM-SBF polymer precursors and the corresponding PIM-SBF-derived CMS membranes under different fabrication conditions were characterized by nitrogen physisorption experiments performed at 77 K. As shown in Figure 6.3, the final pyrolysis temperatures (i.e., 500, 800, and 1100 °C) was investigated under a hydrogen volume fraction of 4 vol% H_2, while two hydrogen volume fractions (i.e., 0 and 4 vol% H_2) were studied under a final pyrolysis temperature of 500 °C. As illustrated in Figure 6.3a, PIM-SBF precursors displayed a sharp rise in the low pressure range, followed by a more

linear rise as a result of polymer swelling [15-17]. The absence of swelling region in the PIM-SBF-derived CMS samples (Figure 6.3b) indicates that the CMS samples possess more rigid structures compared with the polymer precursor.

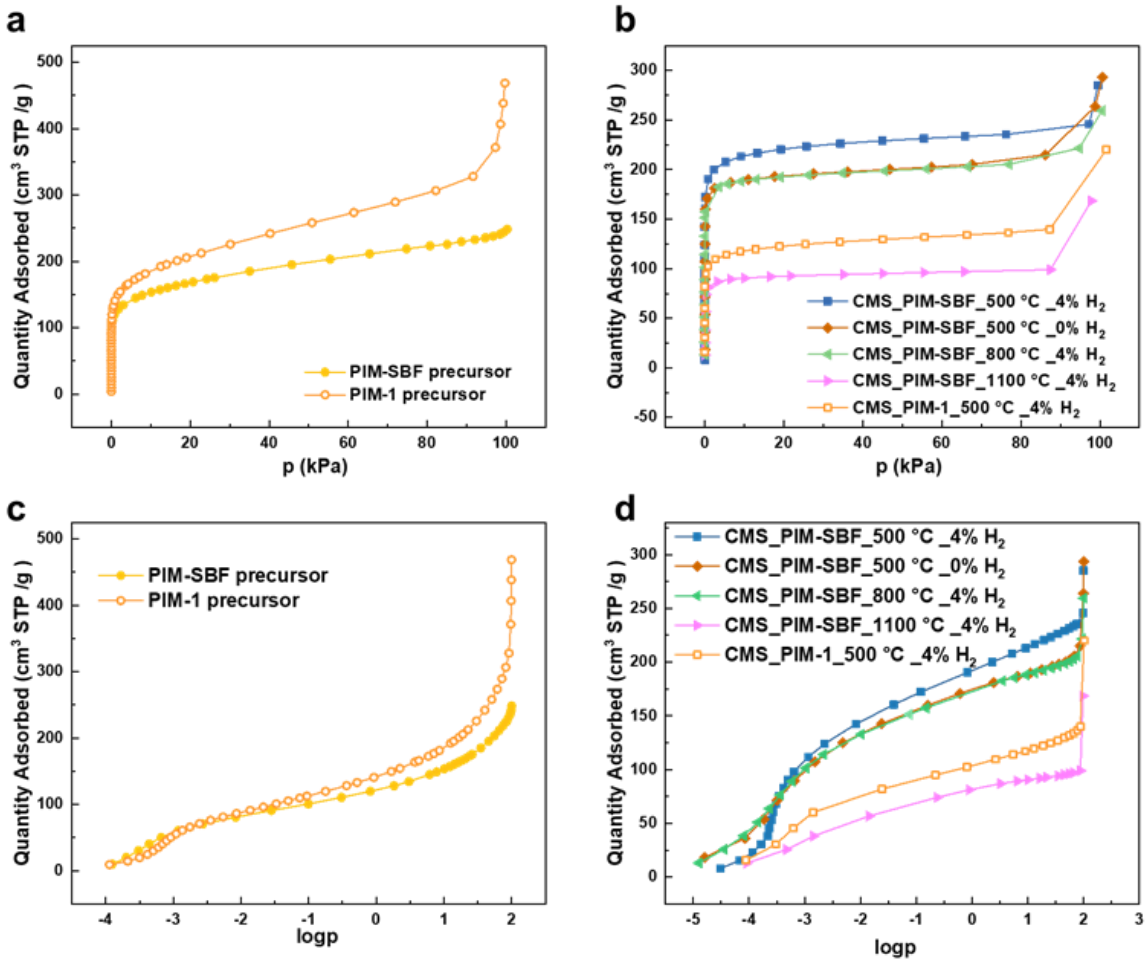

Figure 6.3 Nitrogen physisorption at 77 K for PIM-SBF and PIM-1 polymer precursors (a, c) and PIM-SBF-derived CMS fabricated under different conditions (b, d) as a function of p (a, b) and log p (c, d) compared with CMS_ PIM-1 _500 °C_4% H_2.

As indicated in Table 6.2, the PIM-SBF derived CMS membranes possess high surface areas (366-855 m^2/g) and large pore volumes (0.153-0.380 cm^3/g). It is worth noting that some of the PIM-SBF derived CMS membranes (i.e., CMS_ PIM-SBF _500 °C_4% H_2) were characterized by an increase of the surface area and pore volume compared with the precursor. These results agree with our hypothesis that a more rigid polymer precursor may prevent the polymer chain flattening and pore collapsing to some degree during pyrolysis. Moreover, by comparing Table 6.2 and Table 5.2, one can conclude that both the BET surface area and pore volume are larger for PIM-SBF derived CMS relative to the values for PIM-1 derived CMS fabricated under same pyrolysis conditions. These higher pore volumes are advantageous in contributing to the high permeability (i.e., flux or throughput) of the CMS membranes.

Table 6.2 Pore volume and surface area for PIM-SBF precursor and CMS formed under different conditions.

Sample	Pore volume (cm^3/g)	Surface area (m^2/g)
PIM-SBF precursor	0.360	601
CMS_ PIM-SBF _500 °C_4% H_2	0.380	855
CMS_ PIM-SBF _500 °C_0% H_2	0.343	748
CMS_ PIM-SBF _800 °C_4% H_2	0.331	692
CMS_ PIM-SBF _1100 °C_4% H_2	0.153	366

The pore size distribution of the PIM-SBF polymer precursors and the corresponding PIM-SBF-derived CMS membranes under different fabrication conditions was derived from the nitrogen isotherms at 77 K using the 2D-NLDFT method. The pore size distribution curves are illustrated using two different y axis scale in order to make both the ultramicorpores and micropores visible. As illustrated in Figure 6.4, PIM-SBF has ultramicropores ranging from 5-8 Å. After the pyrolysis (under the pure argon or 4% H_2/Ar environment), the "mid-sized" ultramicropores (i.e., 5-7 Å) were still maintained inside the CMS membranes, which will result in effective molecular sieving between organic solvents molecules (e.g., xylene isomers). It is worth noting that reasonable nitrogen physisorption isotherms at 77 K for CMS_ PIM-1 _500 °C_0% H_2 cannot be obtained, which indicates that the size of ultramicropores within this CMS is quite similar to N_2 (3.64 Å) thus resulting in extremely slow N_2 diffusion [8]. In contrast, the CMS_ PIM-SBF _500 °C_0% H_2 revealed ultramicropores ranging from 5-7 Å, which means it is feasible to fabricate CMS membranes with "mid-sized" micropores using the polymer of intrinsic microporosity (PIMs) as precursors under the pure argon pyrolysis environment. The avoidance of hydrogen species in the pyrolysis environment will make the pyrolysis process safer and reduce the complexity of the overall fabrication process.

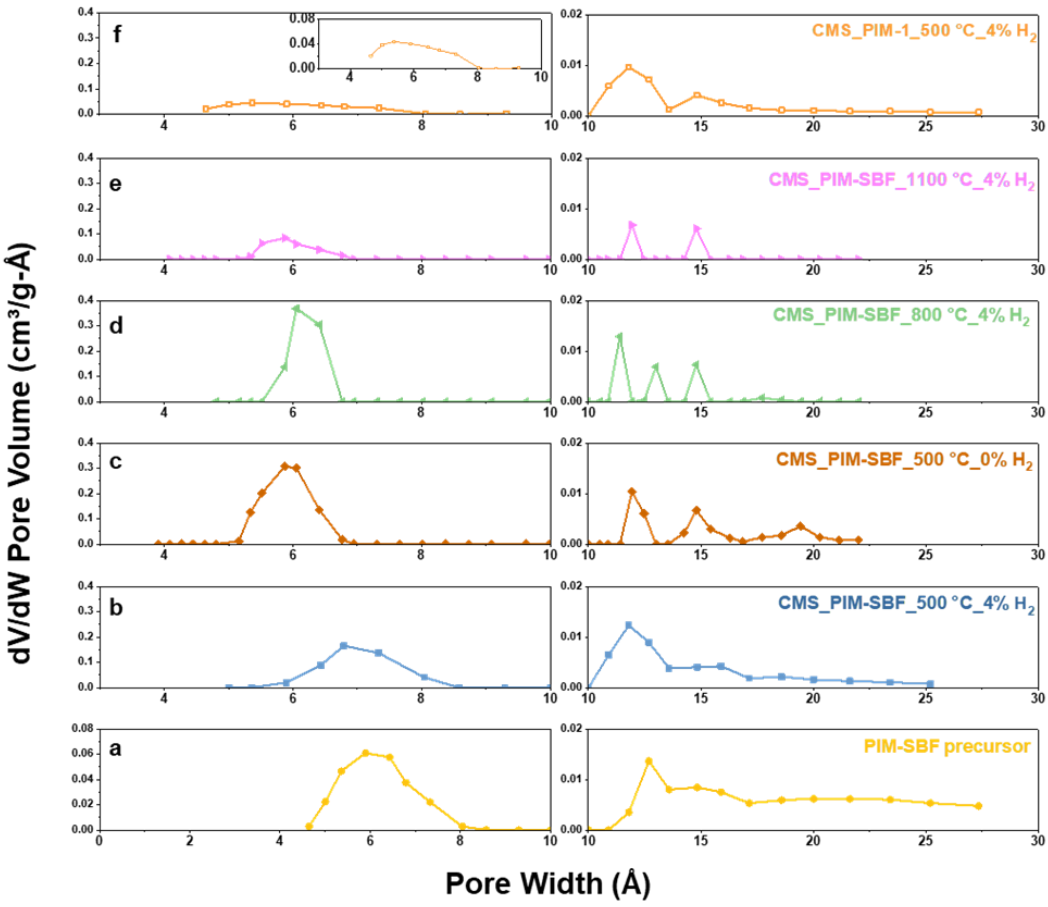

Figure 6.4 Pore size distributions measured by nitrogen physisorption at 77 K for (a)PIM-SBF and (b-e) PIM-SBF-derived CMS fabricated under different conditions compared with (f) CMS_ PIM-1 _500 °C_4% H_2.

The full width at half maximum, the average pore size and the micropore and ultramicropore volumes for PIM-SBF-derived CMS formed under different conditions were summarized in Table 6.3. The distributions of ultramicropores were narrower, and the average ultramicropore size was smaller as the hydrogen content decreased from 4 vol% to 0 vol%. By comparing the pore size distributions for PIM-SBF derived CMS samples pyrolyzed under 500, 800, and 1100 °C, it can be summarized that the average

size of the ultramicropores decreased with the increase of the pyrolysis temperature indicating the tightening of CMS matrix under a higher pyrolysis temperature. The micropore volumes inside the PIM-SBF derived CMS membranes increased with the decrease of the pyrolysis temperature or the increase of the hydrogen content. As shown in Table 6.3, the pyrolysis of PIM-SBF under relatively low temperatures (≤ 800 °C) will lead to the fabrication of CMS membranes with large ultramicropore volumes (0.230-0.280 cm^3/g). However, very high pyrolysis temperatures (e.g., 1100 °C) will induce a decrease of both the micropore and ultramicropore volumes. The above analysis showed that both hydrogen concentration in the pyrolysis atmosphere and the final pyrolysis temperature are effective tuning methods to manipulate the pore structure of the CMS membranes.

It is worth noting that CMS_PIM-SBF_500 °C_4% H_2 has a narrow distribution of ultramicropores (an FWHM of 1.30 Å vs. 2.69 Å), but a slightly larger average ultramicropore size (7.1 Å vs. 5.6 Å) relative to CMS_PIM-1_500 °C_4% H_2. These two effects compete against each other (i.e., larger pore size will result in a decrease in selectivity, but a tighter pore size distribution will increase selectivity), and so it is difficult to estimate *a priori* how the membrane performance will change based on the change in the precursor. As will be shown later, the selectivity is largely maintained while the permeability increases dramatically.

Table 6.3 Full width at half maximum, average pore size, micropore and ultramicropore volumes for PIM-SBF-derived CMS formed under different conditions compared with CMS_ PIM-1 _500 °C_4% H_2.

Sample	Full width at half maximum (Å)	Average ultramicropore size (Å)	Micropore volume (cm^3/g)	Ultramicropore Volume (cm^3/g)
CMS_ PIM-SBF _500 °C_4% H_2	1.30	7.1	0.043	0.230
CMS_ PIM-1 _500 °C_4% H_2	2.69	5.6	0.034	0.113
CMS_ PIM-SBF _500 °C_0% H_2	0.93	6.0	0.023	0.280
CMS_ PIM-SBF _800 °C_4% H_2	0.69	6.1	0.016	0.276
CMS_ PIM-SBF _1100 °C_4% H_2	0.77	5.8	0.007	0.133

6.3.2 FTIR

The chemical evolution of the PIM-SBF precursor and the carbonized PIM-SBF as a function of pyrolysis temperature and H_2 concentration was shown in FTIR spectra (Figure 6.5). The PIM-SBF spectrum shows characteristic absorbance bands at 2238 cm^{-1} (C≡N), 1607 cm^{-1} (aromatic C=C bending), 1470-1430 cm^{-1} (-C-H bending within -CH_2- and -C-CH_3 groups) and 1300-1000 cm^{-1} (-C-O- stretching) [18]. As shown in Figure 5.11, for CMS_ PIM-SBF _500 °C_4% H_2, even though the peak intensities of several bands reduce significantly compared to the PIM-SBF precursor, there are still obvious absorbance bands, which means CMS samples pyrolyzed at relatively low temperatures retain some

degree of polymeric characteristics to some degree. However, the absorbance bands disappear as the pyrolysis temperature further increased to 800 °C or 1100 °C. XRD results show that CMS formed at higher pyrolysis temperatures are more graphite-like [19,20]. It is worth noting that there are no functional groups presenting in the FTIR spectrum for ideal graphite [21].

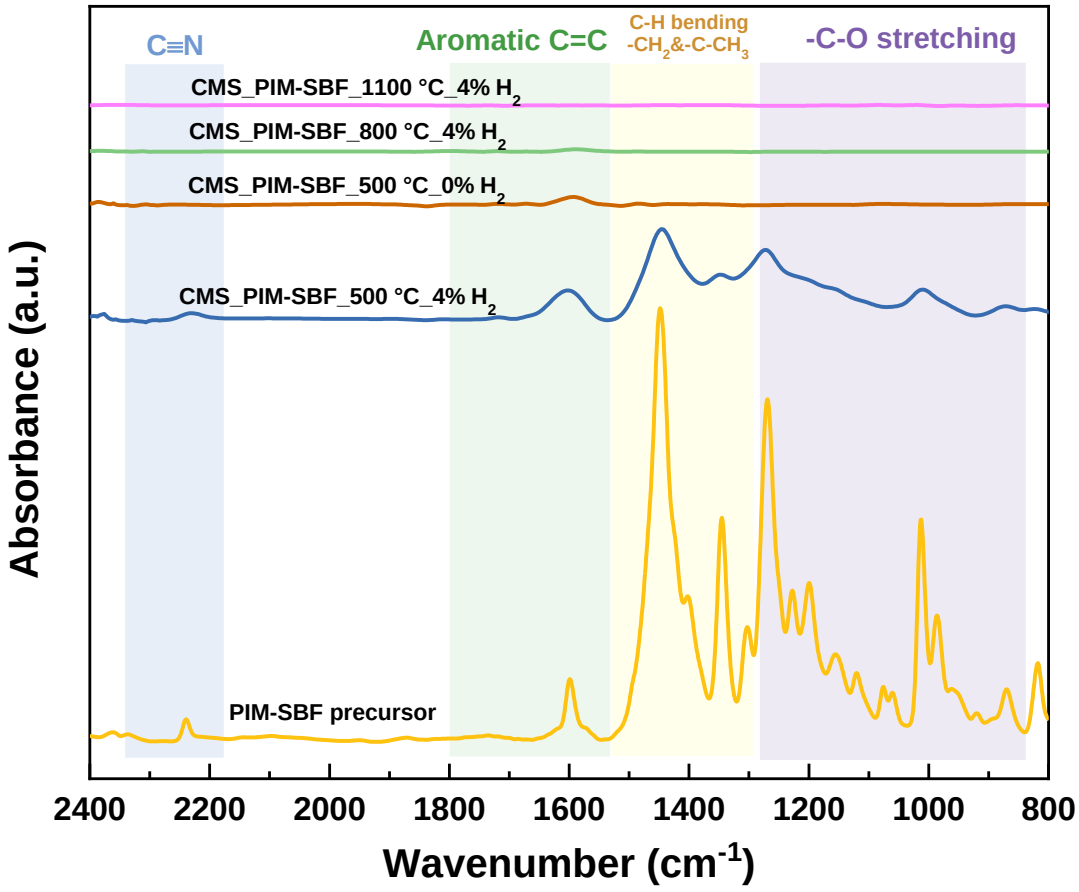

Figure 6.5 FTIR spectra of PIM-SBF and PIM-SBF-derived CMS fabricated under different conditions.

6.4 Diffusion and Sorption Property of PIM-SBF-derived CMS

6.4.1 Sorption property

The sorption isotherms of *p*-xylene and *o*-xylene for CMS_PIM-SBF_500 °C_4% H_2 and CMS_PIM-1_500 °C_4% H_2 are collected at 55 °C. As shown in Figure 6.6, all isotherms display a sharp increase in adsorption capacity in the low saturation region and then plateau at higher saturation values. As expected, for the same type of CMS membranes, the sorption uptake for *p*-xylene at each pressure condition is quite similar to that of the *o*-xylene (uptake differences are within 5 wt%) because of their similar chemical and physical properties, which indicates the absence of a sorption-selective separation mechanism within CMS membranes. It is worth noting that sorption uptakes of the CMS_PIM-SBF_500 °C_4% H_2 membranes for *p*-xylene and *o*-xylene are both a little bit higher (i.e., ~1.2 times higher) than that of the CMS_PIM-1_500 °C_4% H_2 at all relative pressures, indicating a much more porous structure in CMS_PIM-SBF_500 °C_4% H_2. This observation agrees well with the nitrogen physisorption measurements (Figure 5.6 and Figure 6.4), which illustrate a higher micropore volume value for CMS_PIM-SBF_500 °C_4% H_2 (0.043 cm^3/g vs. 0.038 cm^3/g) relative to CMS_PIM-1_500 °C_4% H_2.

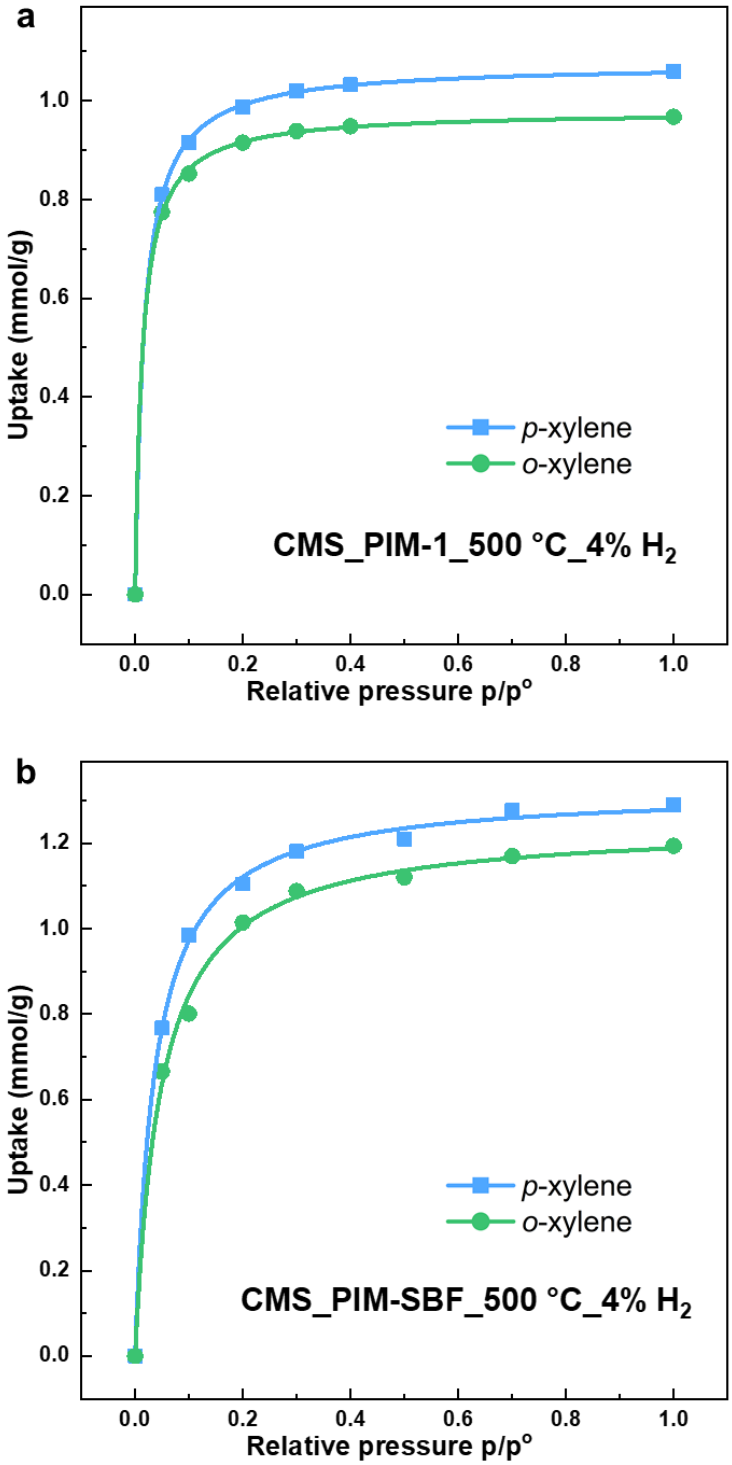

Figure 6.6 Single component sorption isotherms of *p*-xylene and *o*-xylene in (a) CMS_PIM-1_500 °C_4% H_2 and (b) CMS_PIM-SBF_500 °C_4% H_2 measured at 55 °C.

6.4.2 Diffusivity estimation

Even though *p*-xylene and *o*-xylene possess similar sorption properties within the PIM-SBF CMS, the "mid-sized" ultramicropores (i.e., 5-7 Å) inside the rigid CMS membranes enable molecular sieving of the xylene isomers. The single component kinetic uptake curves were determined by the dynamic vapor sorption analysis method and were utilized to estimate the transport diffusivities, D of xylene isomers in different CMS samples.

The transport diffusion coefficients for xylene isomers in CMS_PIM-1_500 °C_4% H_2 and CMS_PIM-SBF_500 °C_4% H_2 and the transport diffusion selectivity between *p*-xylene and *o*-xylene for these two kinds of CMS materials were illustrated in Figure 6.7. As shown in Figure 6.7, the transport diffusion coefficients for both *p*-xylene and *o*-xylene in the PIM-SBF derived CMS increase obviously relative to the PIM-1 derived CMS samples in the same pyrolysis environment (3.9×10^{-9} vs. 1.0×10^{-9} cm^2/s for *p*-xylene, 2.3×10^{-10} vs. 4.0×10^{-11} cm^2/s for *o*-xylene). Consistent with our observations from the nitrogen physisorption measurements, CMS_PIM-SBF_500 °C_4% H_2 has a much higher pore volume (0.161 cm^3/g vs. 0.380 cm^3/g as shown in Table 5.2 and Table 6.2) relative to that of CMS_PIM-1_500 °C_4% H_2, which will result in a more rapid diffusion of guest molecules through PIM-SBF-derived CMS. Moreover, CMS_PIM-SBF_500 °C_4% H_2 exhibits a smaller diffusion selectivity (17 vs. 25) relative to that of CMS_PIM-1_500 °C_4% H_2 which is mainly contributed by the larger average ultramicropore size (7.1 Å vs. 5.6 Å). The larger diffusion coefficients (~ 4 times) of *p*-xylene and little sacrifice of

the diffusion selectivity indicate that the PIM-SBF derived CMS can act as promising membranes for xylene isomer separations.

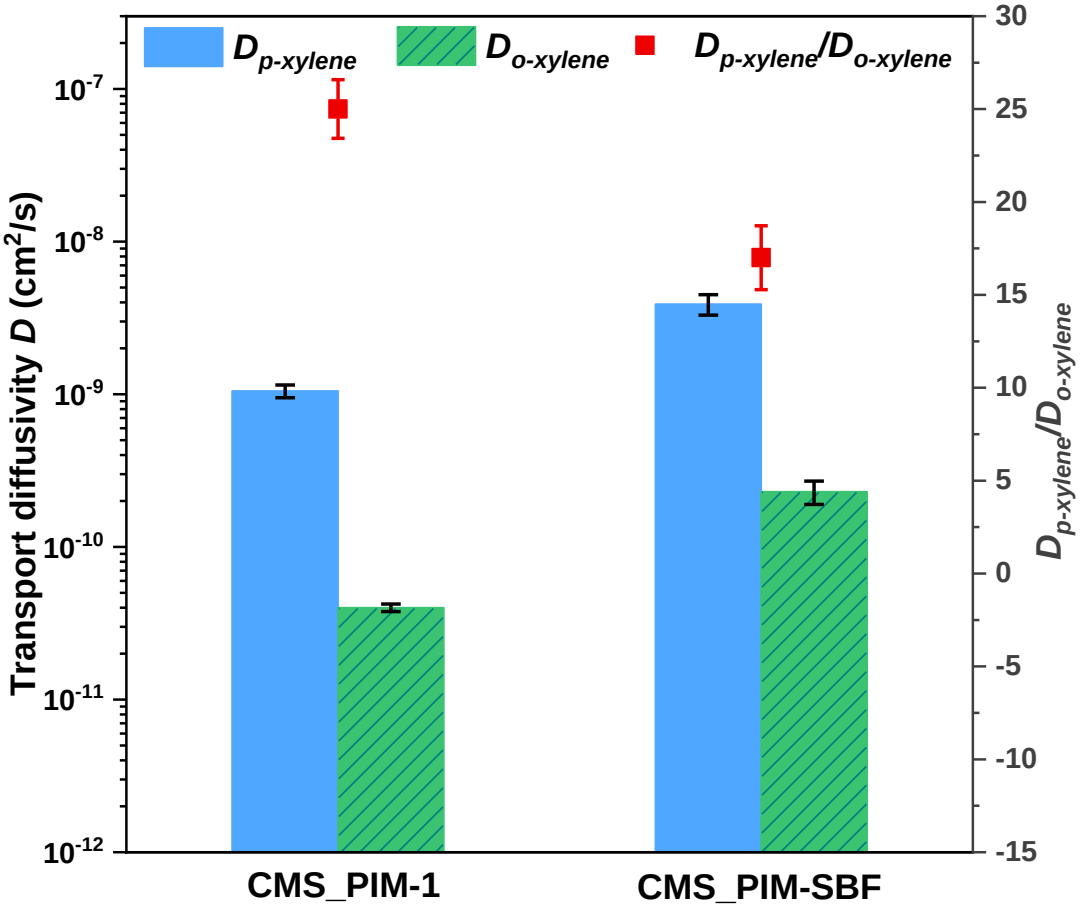

Figure 6.7 The transport diffusion coefficients for xylene isomers in CMS_PIM-1_500 °C_4% H_2 and CMS_PIM-SBF_500 °C_4% H_2.

6.5 Separation Performance of PIM-SBF-derived CMS Membranes

6.5.1 Separation performance measured by Wicke-Kallenbach tests

The separation performance of PIM-SBF-derived CMS Membranes was tested using a Wicke-Kallenbach permeation setup, where the total pressure difference across the membrane is maintained at zero. The feed, an equimolar *p*-xylene/*o*-xylene mixture vapor carried by nitrogen, flushes the upstream while a nitrogen sweep carries the permeate to a gas chromatograph to determine the xylene flux across the membrane (experimental details in Section 3.8). The influence of polymer precursor on the permeation performance of CMS membranes for the xylene isomers is illustrated in Figure 6.8. As shown in Figure 6.8, the membranes derived from PIM-SBF gain around 4 times higher *p*-xylene permeability than the membranes derived from PIM-1. This is consistent with our characterization results that the pore volume for PIM-SBF derived CMS are larger relative to the values for PIM-1 derived CMS fabricated under same pyrolysis conditions (0.380 cm^3/g for CMS_PIM-SBF_500 °C_4% H_2 vs. 0.161 cm^3/g for CMS_PIM-1_500 °C_4% H_2 as shown in Table 6.2 and Table 5.2). The larger pore volume inside the CMS membranes will create more diffusion pathways for guest molecules to pass through and lead to an increased diffusivity, which benefits permeability. Unlike the permeability, the *p*-xylene/ *o*-xylene permselectivity exhibits a much smaller change. This is likely owing to the fact that permselectivity is mainly dominated by the ultramicropores inside the CMS membranes. The size of the ultramicropores inside both the CMS_PIM-SBF_500 °C_4% H_2 and CMS_PIM-1_500 °C_4% H_2 is around 5-7 Å, (note that the xylene isomers to be separated, *p*-xylene and *o*-xylene, have kinetic diameters of 5.8 Å and 6.8 Å, respectively). As a result,

the rigid ultramicropores with the appropriate size can effectively distinguish between *p*-xylene and *o*-xylene.

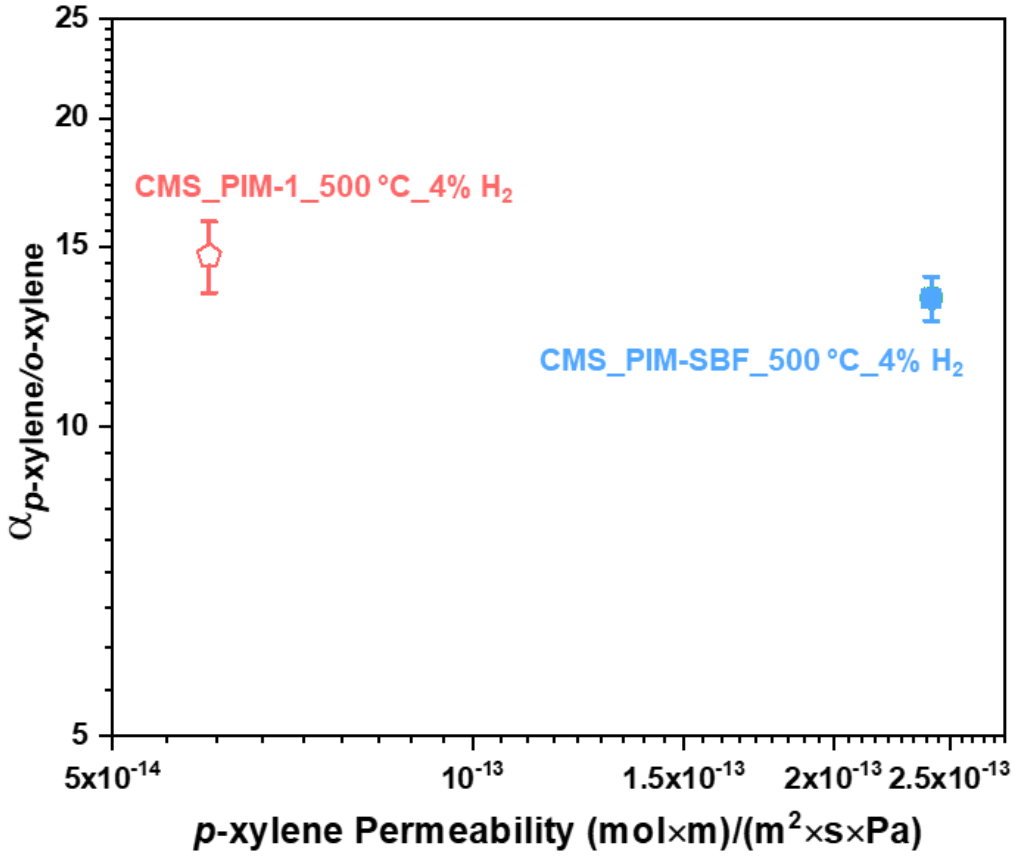

Figure 6.8 The *p*-xylene/*o*-xylene separation performance of CMS_PIM-SBF_500 °C_4% H_2 (square marker) compared to CMS_PIM-1_500 °C_4% H_2 (pentagon marker). Experimental data from the equimolar xylene vapor mixture Wicke-Kallenbach tests.

The effect of the final pyrolysis temperatures and the hydrogen concentration in the pyrolysis environment on the separation performance of PIM-SBF derived CMS membranes is shown in Figure 6.9. It is shown that a higher *p*-xylene permeability and a similar permselectivity was observed when the hydrogen concentration in the pyrolysis

environment was increased from 0 to 4 vol%. This result agrees with the nitrogen physisorption measurements that hydrogen will help to create CMS membranes with a higher BET surface area and a larger pore volume. In addition, as expected, a lower *p*-xylene permeability and a higher permselectivity were observed when the final pyrolysis temperature was increased from 500 to 800 °C.

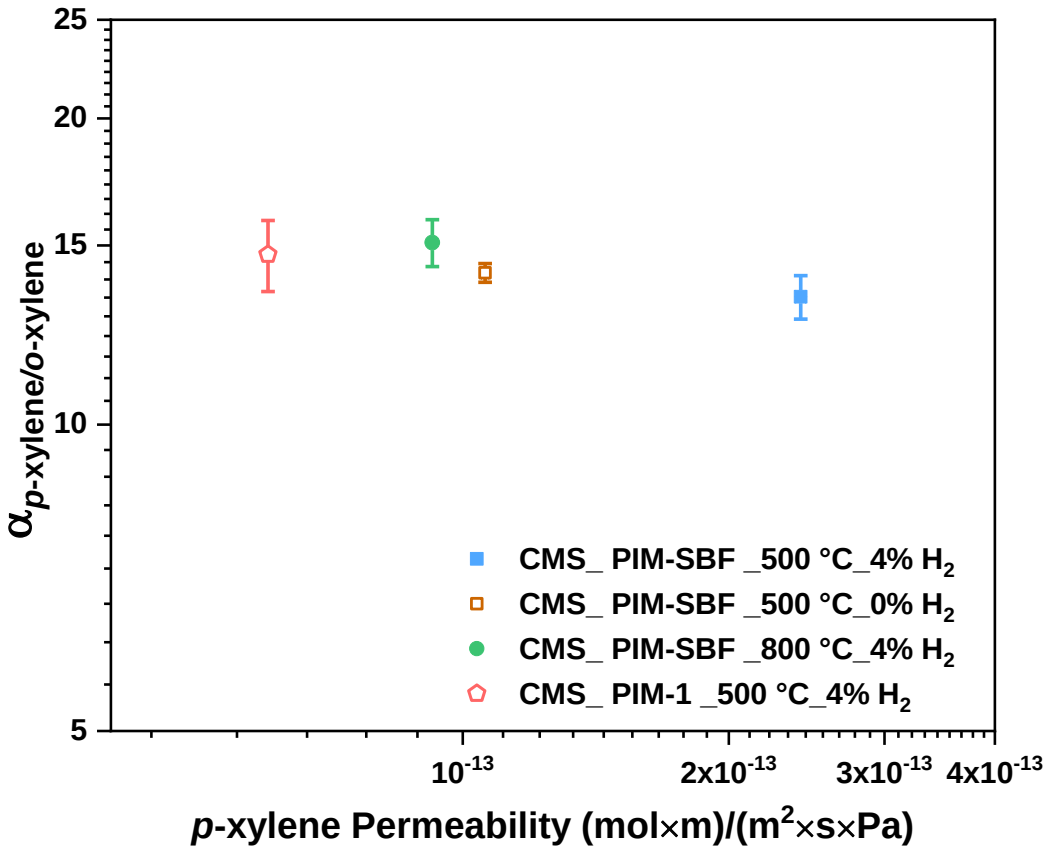

Figure 6.9 The *p*-xylene/*o*-xylene separation performance of PIM-SBF derived CMS membranes fabricated under different hydrogen concentration and final pyrolysis temperature based on equimolar xylene vapor mixture Wicke-Kallenbach tests.

6.5.2 Maxwell-Stefan model predicted separation performance

The single component sorption and diffusion data were utilized as inputs into the Maxwell-Stefan model to predict the mixture permeabilities with and without frictional coupling effects. The previous study has shown that CMS_PIM-1_500 °C_4% H_2 sample can be described by the Maxwell-Stefan formulation for "weak confinement" case considering the loading dependence of single-component Maxwell-Stefan diffusivity [22]. The nitrogen physisorption measurements indicated that CMS_PIM-SBF_500 °C_4% H_2 has a similar pore structure relative to CMS_PIM-1_500 °C_4% H_2. Hence, it is reasonable to utilize the Maxwell-Stefan formulation for the "weak confinement" case to predict the mixture separation performance of CMS_PIM-SBF_500 °C_4% H_2. Here, the frictional coupling effects between xylene isomers were estimated using a Vignes-type correlation [23,24].

Figure 6.10 shows the comparison of experimental results of an equimolar *p*-xylene/*o*-xylene vapor mixture separated by dense CMS_PIM-SBF_500 °C_4% H_2 membranes measured at 55 °C by Wicke-Kallenbach tests and predictions by the Maxwell-Stefan model for the "weak confinement" case (detailed modeling parameters can be found in Table 6.4).

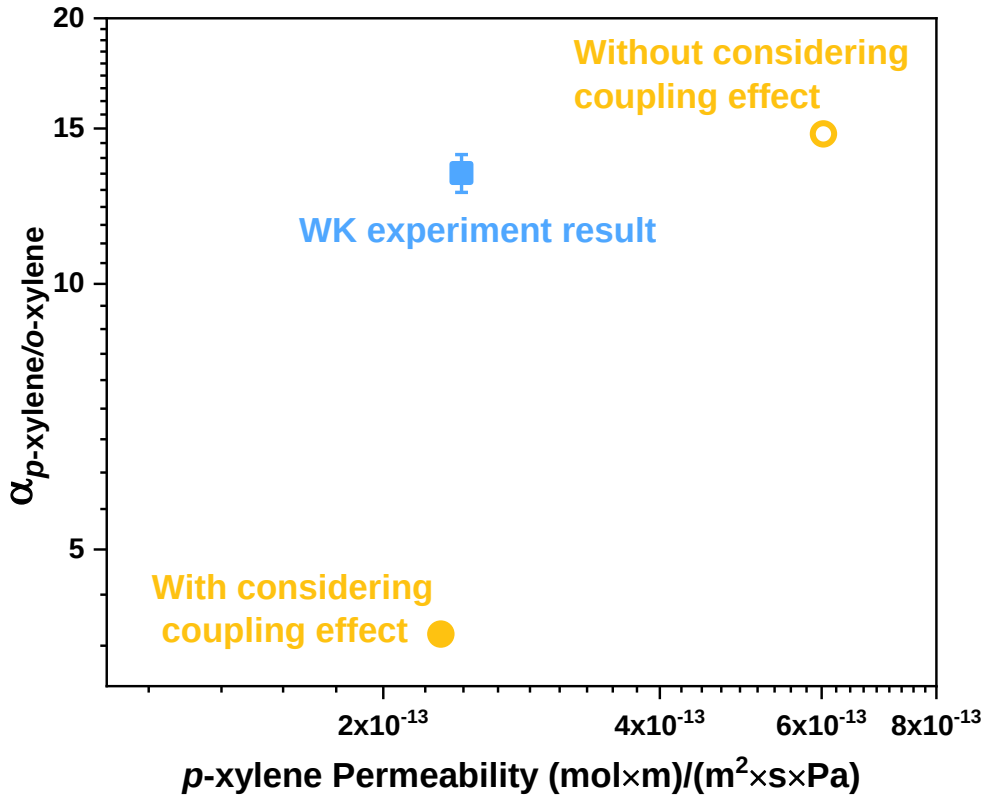

Figure 6.10 The comparison of Maxwell-Stefan predictions of *p*-xylene/*o*-xylene permselectivity and *p*-xylene permeability with experimental results. Model: Maxwell-Stefan model for "weak confinement" case with and without considering frictional coupling effects, Experimental: equimolar *p*-xylene : *o*-xylene mixture separated by dense CMS_PIM-SBF_500 °C_4% H_2 membranes measured at 55 °C by Wicke-Kallenbach test.

The experimental *p*-xylene permeability is slightly higher (1.05 times) than the Maxwell-Stefan model predicted value using frictional coupling effects and is observed to be 59.6 % lower than the result predicted by the MS model without coupling effects. In this work, the maximum loading of the xylene isomers in the CMS materials was estimated by utilizing the total pore volume of the membrane (measured by nitrogen physisorption

tests at 77 K) and the molar volume of the xylene isomers. However, this assumption may overestimate the amount of xylene isomer sorption for Wicke-Kallenbach tests. It is the micropore volume that mainly contributes to the sorption of xylene molecules while the ultramicropore volume contributes little. Such an overestimation would lead to an overestimation of the model predicted permeability. With that as background, the real membranes, which may have some small leaking pathways, do not show a higher permeability value compared with the model-predicted value. The permeability predicted by the MS model with coupling effects is instead observed to be 61.7 % *lower* than the result predicted by the MS model without coupling effects. That is expected within the generalized Maxwell-Stefan framework, where the frictional coupling effects between rapidly and slowly transporting components are known to reduce the transport rates of the rapidly transporting components (*p*-xylene here). The experimental *p*-xylene/*o*-xylene selectivity falls between the selectivity predicted by the Maxwell-Stefan model with and without considering the coupling effect. The result suggests that selectivity losses in the membrane were not as severe as predicted by the MS mixture case with frictional coupling effects considered. This indicated that the Vignes-type correlation, which was used to estimate the frictional coupling effects here, is not accurately capturing the extent of the frictional coupling. Alternatively, there could be a gradient of frictional coupling effects, which are not considered here (a constant "cross coupling" diffusivity, $Đ_{12}$, was used in these estimates). Such a gradient would indicate that the xylene isomers are highly coupled on the high activity side of the membrane yet relatively uncoupled on the low activity side, which plausibly explains the difference between the two models and the experiment.

Table 6.4. Parameters for estimation of permeability and permselectivity in Figure 6.10 using the Maxwell-Stefan equation for "weak confinement" case.

Item	Value
Feed mixture	50:50 (mol/mol) vapor mixture of *p*-xylene/*o*-xylene
Testing temperature T	328.15 K
Molar volume of *p*-xylene V_{mi}	123.3 cm^3/mol
Molar volume of *o*-xyleneV_{mj}	120.6 cm^3/mol
Saturation loading q_i^{sat}	$V_p\,/V_m = 0.380\ \frac{cm^3}{g}/123.3\ \frac{cm^3}{mol} = 3.0819\ mmol/g$
Saturation loading q_j^{sat}	$V_p\,/V_m = 0.380\ \frac{cm^3}{g}/120.6\ \frac{cm^3}{mol} = 3.1509\ mmol/g$
Langmuir affinity constant b_i	5.0251 kPa^{-1}
Langmuir affinity constant b_j	4.8675 kPa^{-1}
p-xylene feed pressure p_i^{up}	2.42 kPa
o-xylene feed pressure p_j^{up}	2.42 kPa
p-xylene permeate pressurep_i^{down}	0 kPa
o-xylene permeate pressure p_j^{down}	0 kPa
Density of CMS membrane ρ	2 g/cm^3
Thickness of the membrane ℓ	32.8 μm
Saturation pressure of *p*-xylene	$p_{p-xylene}^{sat}\,(328K) = 5.4757\ kPa$

Saturation pressure of *o*-xylene	$p_{0-xylene}^{sat}\ (328K) = 4.3182\ kPa$
p-xylene Maxwell-Stefan coefficients at infinite dilution $Đ_{i0}$	1.64×10^{-9} cm^2/s
o-xylene Maxwell-Stefan coefficients at infinite dilution $Đ_{j0}$	1.12×10^{-10} cm^2/s

6.6 Summary and Conclusions

In summary, PIM-SBF was synthesized and fabricated into CMS membranes for xylene isomer separations. The pore structure of the resulting CMS membrane was characterized using nitrogen physisorption. Both BET surface area and pore volume were found to be larger for PIM-SBF derived CMS relative to the values for PIM-1 derived CMS fabricated under the same pyrolysis conditions. These higher pore volumes are thought to be the main contributor to the high permeability (i.e., flux or throughput) of the CMS membranes. The hydrogen concentration in the pyrolysis atmosphere and the final pyrolysis temperature were found to be effective tuning methods to manipulate the pore structure of the CMS membranes. The sorption isotherms of *p*-xylene of *o*-xylene illustrated that there is no sorption-selective separation between xylene isomers within PIM-SBF derived CMS membranes. However, high diffusion selectivity (~17) between *p*-xylene of *o*-xylene was found within PIM-SBF derived CMS. The transport diffusion coefficients for both *p*-xylene and *o*-xylene in the PIM-SBF derived CMS increase relative to the PIM-1 derived CMS samples in the same pyrolysis environment. Finally, Wicke-Kallenbach permeation experiments indicated significant improvement in the xylene

permeability for PIM-SBF derived CMS compared with CMS derived from PIM-1. Moreover, this work suggests that it is feasible to fabricate CMS membranes with suitable micropore structure for xylene isomer separations using the PIM-SBF as precursors under the pure argon pyrolysis environment, which avoids the use of combustible gases and simplifies the overall membrane fabrication process.

6.7 References

1. O. Sanyal, C. Zhang, G. B. Wenz, S. Fu, N. Bhuwania, L. Xu, M. Rungta, W. J. Koros. Next generation membranes—using tailored carbon. *Carbon* **2018**;127:688-698.

2. N. B. McKeown, P. M. Budd. Polymers of intrinsic microporosity (PIMs): organic materials for membrane separations, heterogeneous catalysis and hydrogen storage. *Chemical Society Reviews* **2006**;35(8):675-683.

3. P. M. Budd, B. S. Ghanem, S. Makhseed, N. B. McKeown, K. J. Msayib, C. E. Tattershall. Polymers of intrinsic microporosity (PIMs): robust, solution-processable, organic nanoporous materials. *Chemical Communications* **2004**(2):230-231.

4. P. M. Budd, E. S. Elabas, B. S. Ghanem, S. Makhseed, N. B. McKeown, K. J. Msayib, C. E. Tattershall, D. Wang. Solution‐processed, organophilic membrane derived from a polymer of intrinsic microporosity. *Advanced Materials* **2004**;16(5):456-459.

5. P. M. Budd, K. J. Msayib, C. E. Tattershall, B. S. Ghanem, K. J. Reynolds, N. B. McKeown, D. Fritsch. Gas separation membranes from polymers of intrinsic microporosity. *Journal of Membrane Science* **2005**;251(1-2):263-269.

6. P. M. Budd, N. B. McKeown, B. S. Ghanem, K. J. Msayib, D. Fritsch, L. Starannikova, N. Belov, O. Sanfirova, Y. Yampolskii, V. Shantarovich. Gas permeation parameters and other physicochemical properties of a polymer of intrinsic microporosity: Polybenzodioxane PIM-1. *Journal of Membrane Science* **2008**;325(2):851-860.

7. Y. Ma, M. L. Jue, F. Zhang, R. Mathias, H. Y. Jang, R. P. Lively. Creation of well‐defined “mid‐sized” micropores in carbon molecular sieve membranes. *Angewandte Chemie* **2019**;131(38):13393-13399.

8. Y. Ma, F. Zhang, S. Yang, R. P. Lively. Evidence for entropic diffusion selection of xylene isomers in carbon molecular sieve membranes. *Journal of Membrane Science* **2018**;564:404-414.

9. L. Robeson, B. D. Freeman, D. R. Paul, B. Rowe. An empirical correlation of gas permeability and permselectivity in polymers and its theoretical basis. *Journal of Membrane Science* **2009**;341(1-2):178-185.

10. B. D. Freeman. Basis of permeability/selectivity tradeoff relations in polymeric gas separation membranes. *Macromolecules* **1999**;32(2):375-380.

11. M. Heuchel, D. Fritsch, P. M. Budd, N. B. McKeown, D. Hofmann. Atomistic packing model and free volume distribution of a polymer with intrinsic microporosity (PIM-1). *Journal of Membrane Science* **2008**;318(1-2):84-99.

12. C. G. Bezzu, M. Carta, A. Tonkins, J. C. Jansen, P. Bernardo, F. Bazzarelli, N. B. McKeown. A spirobifluorene - based polymer of intrinsic microporosity with improved performance for gas separation. *Advanced Materials* **2012**;24(44):5930-5933.

13. N. C. Bruno, M. T. Tudge, S. L. Buchwald. Design and preparation of new palladium precatalysts for C–C and C–N cross-coupling reactions. *Chemical science* **2013**;4(3):916-920.

14. R. G. Clarkson, M. Gomberg. Spirans with four aromatic radicals on the spiro carbon atom1. *Journal of the American Chemical Society* **1930**;52(7):2881-2891.

15. M. Thommes, K. Kaneko, A. V. Neimark, J. P. Olivier, F. Rodriguez-Reinoso, J. Rouquerol, K. S. Sing. Physisorption of gases, with special reference to the evaluation of surface area and pore size distribution (IUPAC Technical Report). *Pure and Applied Chemistry* **2015**;87(9-10):1051-1069.

16. P. M. Budd, A. Butler, J. Selbie, K. Mahmood, N. B. McKeown, B. Ghanem, K. Msayib, D. Book, A. Walton. The potential of organic polymer-based hydrogen storage materials. *Physical Chemistry Chemical Physics* **2007**;9(15):1802-1808.

17. M. Minelli, B. R. Pimentel, M. L. Jue, R. P. Lively, G. C. Sarti. Analysis and utilization of cryogenic sorption isotherms for high free volume glassy polymers. *Polymer* **2019**;170:157-167.

18. L. Hao, K.-S. Liao, T.-S. Chung. Photo-oxidative PIM-1 based mixed matrix membranes with superior gas separation performance. *Journal of Materials Chemistry A* **2015**;3(33):17273-17281.

19. O. Salinas, X. Ma, E. Litwiller, I. Pinnau. High-performance carbon molecular sieve membranes for ethylene/ethane separation derived from an intrinsically microporous polyimide. *Journal of Membrane Science* **2016**;500:115-123.

20. X. Ma, R. Swaidan, B. Teng, H. Tan, O. Salinas, E. Litwiller, Y. Han, I. Pinnau. Carbon molecular sieve gas separation membranes based on an intrinsically microporous polyimide precursor. *Carbon* **2013**;62:88-96.

21. S. A. El-Khodary, G. M. El-Enany, M. El-Okr, M. Ibrahim. Preparation and characterization of microwave reduced graphite oxide for high-performance supercapacitors. *Electrochimica Acta* **2014**;150:269-278.

22. Y. Ma, F. Zhang, H. W. Deckman, W. J. Koros, R. P. Lively. Flux Equations for Osmotically Moderated Sorption–Diffusion Transport in Rigid Microporous Membranes. *Industrial & Engineering Chemistry Research* **2019**.

23. R. Krishna, J. Wesselingh. The Maxwell-Stefan approach to mass transfer. *Chemical Engineering Science* **1997**;52(6):861-911.

24. R. Krishna, R. Baur. Analytic solution of the Maxwell–Stefan equations for multicomponent permeation across a zeolite membrane. *Chemical Engineering Journal* **2004**;97(1):37-45.

CHAPTER 7. FLUX EQUATIONS FOR OSMOTICALLY-MODERATED SORPTION-DIFFUSION TRANSPORT IN RIGID MICROPOROUS MEMBRANES[**]

7.1 Introduction

The development of the correct driving force and flux equations for osmotically-moderated, pressure-induced solution-diffusion transport in swollen polymeric membranes was a major debate that occurred during the nascent stages of membrane research [1-6]. The key outcome of this debate was that a hydraulic pressure applied on the upstream side of the polymeric membrane generates an activity gradient driving force for penetrant transport within the membrane, which is perhaps best understood in a physical sense as a gradient in the volume fraction of the penetrant (from high to low) between the upstream and downstream faces of the membrane. This interpretation requires that the pressure throughout the membrane be constant and equivalent to the upstream hydraulic pressure; subsequent experiments have suggested that this is indeed the case or, at the very least, is a useful approach for capturing the complex swelling mechanics of polymeric membranes in a simplified way. The resulting flux equations derived using this approach have been successfully utilized by the reverse osmosis community ever since.

[**] This chapter has been published on *Industrial & Engineering Chemistry Research* as Flux Equations for Osmotically Moderated Sorption–Diffusion Transport in Rigid Microporous Membranes, **2020**, Doi: 10.1021/acs.iecr.9b05199.

Recently, rigid microporous materials such as carbon molecular sieves have been shown to separate alkyl aromatics via an organic solvent reverse osmosis modality [7]. Microporous materials such as carbons and zeolites (and to a lesser extent, metal-organic frameworks) swell only negligibly or not at all upon sorption of the solvent molecules, and thus the driving force for solvent transport through these membranes must be reconsidered. Moreover, the combined existence of permanent and interconnected molecule-sized pores (e.g., ~0.6 nm) and large cavities (e.g., ~1 nm) that support fluid-like phases of the solvent complicates the analysis relative to that of the solvent-polymer "solid solution" physical image utilized in earlier work on polymer membranes. The goal of this work is to define the driving force in an OSRO separation system and to provide phenomological expressions for solvent flux as a function of pressure for systems that exhibit different types of separation mechanisms.

In this chapter, we utilize both Fickian and Maxwell-Stefan formulations for solvent transport in microporous membranes. It is well-established that the Fickian diffusion coefficient (D_i) can strongly depend on the loading of guest molecules in the materials. However, the Maxwell-Stefan (M-S) diffusivity ($Đ_i$), or "corrected" diffusivity of species i, conceptually removes the confounding effect of sorption interactions between the sorbed species i and the framework of the microporous medium. Indeed, in several classic publications on the subject of guest diffusion within zeolites, it has been common to assume (and sometimes observed) that $Đ_i$ is independent of the guest loading [8,9]. Not all systems behave as ideally as these. There has been increasing evidence, both from quasielastic neutron scattering (QENS) experiments [10-13] and from molecular dynamics simulations [14-17], that $Đ_i$ can be strongly dependent on the loadings within microporous materials.

Here, we will consider the effects of solvent loading dependence of the Maxwell-Stefan diffusivity when applied to osmotically-moderated, steady-state membrane flux equations. We will begin with an examination of the Maxwell-Stefan diffusion loading dependence in bimodal microporous systems before moving onto the derivation of the flux equations for the different diffusion regimes and comparison to experimental data.

7.2 The Driving Force for Solvent Transport Through Microporous Materials

To unambiguously describe the driving force for solvent transport across a rigid microporous membrane, we will first consider three types of microporous material architectures. The first and second cases are architectures in which every penetrant molecule is affected by the force field exerted by the microporous material (Figure 7.1, cases I and II, respectively). The first case highlights a situation where the solvent molecules never reach densities similar to those found in their bulk, liquid counterparts. This case is most analogous to the "solid solution" found in the solvent-polymer system. The second case illustrates a very common situation in microporous materials, wherein both ultramicropores (e.g., the "aperture" in a carbon molecular sieve, or the "window" in a zeolite or MOF) and micropores (e.g., the "gallery" in a CMS or the "cage" in a zeolite or MOF) exist. Solvent molecules contained within micropores less than ~1-1.3 nm in diameter can reasonably be considered to be affected by the force field exerted by the micropore surface, and thus, they can still be considered as 'solid solutions' similar to the first case. However, systems with sufficiently large micropores (>1.5 nm) will allow fluid phases of the solvent to exist within the pores of the membrane, with a large fraction of these solvent molecules not being influenced by the field from the pore wall. This last case

is case III in Figure 7.1, and this case clearly describes the situation for “pore flow” transport, which will not be discussed in this chapter, as materials with this pore architecture are unable to separate similarly-shaped solvent molecules that are substantially smaller than the pore diameter. We hypothesize that the pore size required to transition between cases II and III is dependent on the size of the solvent molecules relative to the size of the microporous cavity. Spherical micropores with diameters of 1.5 nm could accommodate three xylene molecules with relatively high rotational and vibrational degrees of freedom (vide infra, Section 7.4), at which point we hypothesize that a transition from sorption-diffusion transport to Darcy-type transport begins to occur if there is not ultramicroporous window between the spherical micropores. In our illustrative case III example, it is clear that two phases exist in the membrane: the solid phase of the porous membrane and the continuous liquid phase of the solvents in the microporous channel. It is clear that case II is more complex than case I (and this complexity will be discussed later), but as all solvent molecules interact with the pore wall, these two cases will both be considered as ‘solid solutions’ operating in sorption-diffusion transport modality and subsequently utilized to identify the driving force for permeation.

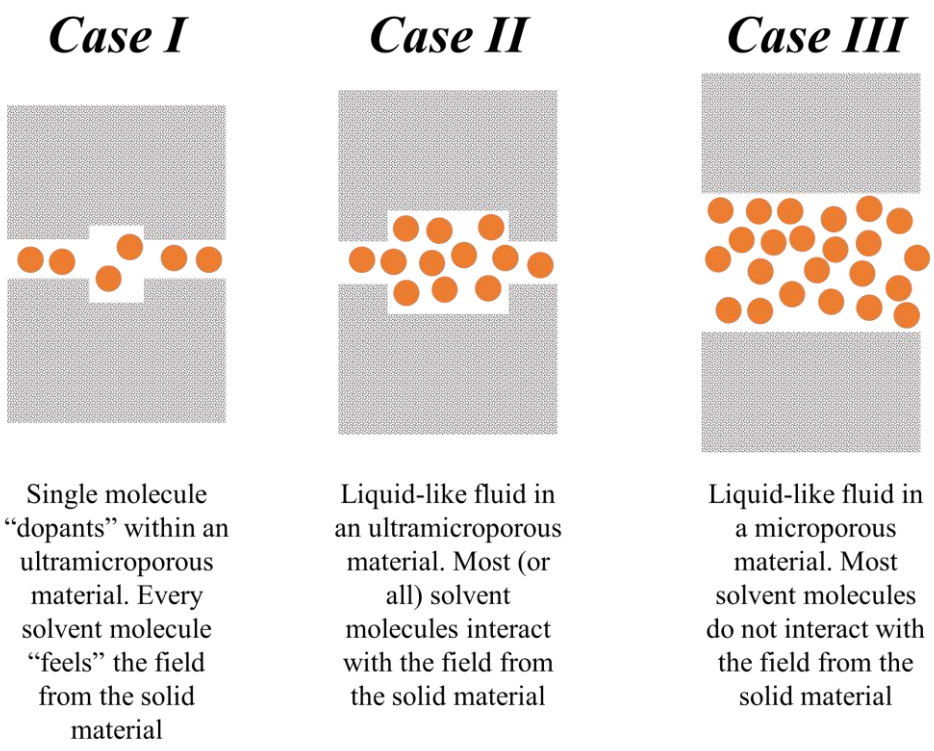

Figure 7.1. Three kinds of microporous material architectures.

In the conditions posed in cases I and II, the solvent transport through the membrane occurs most fundamentally via a chemical potential driving force. Using a Maxwell expansion, we can describe the chemical potential gradient across the membrane based on three intensive variables: pressure, temperature, and composition ($\theta_i^m = q_i/q_i^{sat}$, the fractional molecular loading of species i within the membrane), viz., Eq. 7.1

$$d\mu^m = \left(\frac{\partial \mu^m}{\partial \theta_i^m}\right)_{p,T} d\theta_i^m + \left(\frac{\partial \mu^m}{\partial T}\right)_{p,\theta_i^m} dT + \left(\frac{\partial \mu^m}{\partial p}\right)_{\theta_i^m,T} dp \qquad \textbf{Eq. 7.1}$$

The middle term in Eq. 7.1 is zero under essentially isothermal operation typically found in RO and OSRO separations. The partial derivative of the chemical potential of the membrane with respect to pressure at constant composition and temperature is the definition of the partial molar volume of the membrane (i.e., $\left(\frac{\partial \mu^m}{\partial p}\right)_{\theta_i^m,T} = \bar{V}^m$). A nonswelling, inorganic, and microporous material does not exhibit volume additivity; in fact, the total volume of the membrane is ideally constant with additional input of solvent molecules i so the partial molar volume of the membrane is essentially 0 (i.e., $\bar{V}^m = \left(\frac{\partial V_{total}}{\partial n_i}\right)_{p,T,n_j} = 0$) [18], so the term on the far right of Eq. 7.1 is also 0. Thus the change in chemical potential of the membrane is driven solely by compositional changes, which is consistent with classical sorption-diffusion theory, viz.,

$$d\mu^m = \left(\frac{\partial \mu^m}{\partial \theta_i^m}\right)_{p,T} d\theta_i^m \qquad \textbf{Eq. 7.2}$$

On the basis of this conclusion, we can derive the flux equations based only on compositional changes within the membrane without concerning ourselves with the status of the pressure within the membrane.

7.3 Guest-Loading-Dependent Maxwell-Stefan Diffusivity

Although widely used in characterizing the performance of microporous membranes [19-21], it is possible for transport diffusion coefficients to be highly dependent on concentration, as noted earlier [22]. The Fickian diffusion coefficient D_i can be written in terms of the "thermodynamically corrected" diffusion coefficient (equivalent to the

Maxwell-Stefan diffusivity $Đ_i$ in the case of single component transport), which is a mobility factor that accounts for guest-membrane interactions. The Fickian diffusion coefficient can be estimated from the Maxwell-Stefan diffusivity (and vice-versa) with detailed guest-host sorption information (e.g., sorption isotherms), viz.,

$$D_i \equiv Đ_i \frac{dlnf_i^m}{dln\theta_i^m} = Đ_i \frac{dlnf_i^{fl}}{dln\theta_i^m} \qquad \textbf{Eq. 7.3}$$

where f_i^{fl} is the fugacity of component i in the fluid phase. The thermodynamic correction can be applied throughout the membrane as a result of the assumption of local equilibrium between a fluid phase and the sorbed phase within the membrane. This thermodynamic factor can be visualized most easily using a simple Langmuir isotherm:

$$\theta_i^m = \frac{q(f_i^{fl})}{q_i^{sat}} = \frac{b_i f_i^{fl}}{1 + b_i f_i^{fl}} \qquad \textbf{Eq. 7.4}$$

where θ_i^m is the fractional occupancy of the guest molecule i, b_i is the Langmuir affinity constant, and q_i^{sat} is the saturation loading of guest species within the membrane. In this work, we have assumed that a Langmuir isotherm relationship holds at all pressures (it is important to note that we experimentally observe Langmuir isotherms during vapor sorption measurements of the xylene isomers). Unlike crystalline materials in which guest capacities at saturation can be readily calculated, in amorphous materials (such as CMS), it is difficult to estimate the true saturation capacity of guest molecules. In our work, we utilize the pore volume (as determined by N_2 physisorption at 77 K) and the molar volume

of the solvent molecules to estimate the saturation capacity of the xylene isomers at high pressures.

In the case of a Langmuir isotherm, the thermodynamic correction can thus be simplified to $\frac{dlnf_i^{fl}}{dln\theta_i^m} = \frac{1}{1-\theta_i^m}$, allowing the following relationship between the Maxwell-Stefan diffusivity $Đ_i$ and the Fickian diffusivity D_i:

$$Đ_i = D_i(1 - \theta_i^m) \qquad \textbf{Eq. 7.5}$$

7.3.1 General guest-loading-dependent Maxwell-Stefan diffusivity

Krishna, Sholl, and other researchers in the area of diffusion in microporous materials have posited that the Maxwell-Stefan diffusivity itself can be a function of guest loading in the material [22,23], and this dependency (or lack thereof) is typically separated into two ideal regimes: a so-called "weakly confined" diffusion and a "strongly confined" diffusion regime.

"Weakly confined" diffusion is often applied to small guest molecules diffusing in channels that do not restrict guest conformations and also allow for guest molecules to "rearrange" within a pore. Common examples include diffusion of methane, helium, and argon in MFI zeolite [24-28]. In these cases, the Maxwell-Stefan diffusivity is found to be independent of the fractional occupancy, i.e.,

$$Đ_i = Đ_{i,0} \qquad \textbf{Eq. 7.6}$$

where $Đ_{i,0}$ is the Maxwell-Stefan diffusivity of component i at infinite dilution.

The “strongly confined” case is defined as having a nonconstant Maxwell-Stefan diffusivity. The “strongly confined” case is typically applied to large guest molecules in small channels in which guest rearrangement within the pore is difficult. Common examples are the diffusion of tetrafluoromethane, sulfur hexafluoride and 2-methylhexane in MFI [28]. In the simplest “strongly confined” case, the Maxwell-Stefan diffusivity decreases with increasing guest loadings and approaches zero upon pore saturation. For example, in the system studied by Chempath et al. [15], simulations indicated that the Maxwell-Stefan diffusivity decreased linearly with increasing fractional occupancy. This so-called site occupancy “strongly confined” model [15] can be applied to describe this loading dependence, viz.,

$$Đ_i = Đ_{i,0}(1 - \theta_i^m) = Đ_{i,0}\theta_V^m \qquad \textbf{Eq. 7.7}$$

where θ_i^m is the fractional occupancy of component i inside the membrane and θ_V^m is the vacancy-occupancy in the membrane. Vacancy-occupancy θ_V^m directly reflects the fractional occupancy conditions in the multicomponent permeation case and will be used for the subsequent analysis in this chapter, as it is convenient to think in terms of “vacancies” when multiple components are transporting through the membrane.

As shown in Figure 7.2a and Figure 7.2b, molecular dynamic calculations from Skoulidas and Sholl of CH_4 and CF_4 transport in zeolite MFI reveal that the Maxwell-Stefan coefficient has a $(1 - \theta_i^m)$ dependence for the larger, more constrained CF_4 molecule, whereas CH_4 is predicted to have an essentially constant Maxwell-Stefan diffusivity [22]. These calculations highlight the importance of considering the loading

dependence on the Maxwell-Stefan diffusivity when formulating flux equations for microporous membrane materials that can potentially operate under a wide range of guest fractional occupancies.

These two classical scenarios are illustrated in Figure 7.2c and Figure 7.2d. CH_4 and CF_4 can be viewed as spheres, which completely occupy the adsorption site and block the transportation of adjacent molecules through the occupied sites. For the "weak confinement" case illustrated in Figure 7.2c, the force fields of the channel wall do not equivalently influence the void space. Therefore, even at full loading, the molecules can still diffuse through spaces that have weak guest-host interactions. For the "strong confinement" case illustrated in Figure 7.2d, the entire micropore is nearly uniformly influenced by the force field of the solid. At full guest molecule loading (i.e., a fractional occupancy of 1), the entire pore volume is occupied, and guest molecule diffusion is prohibited.

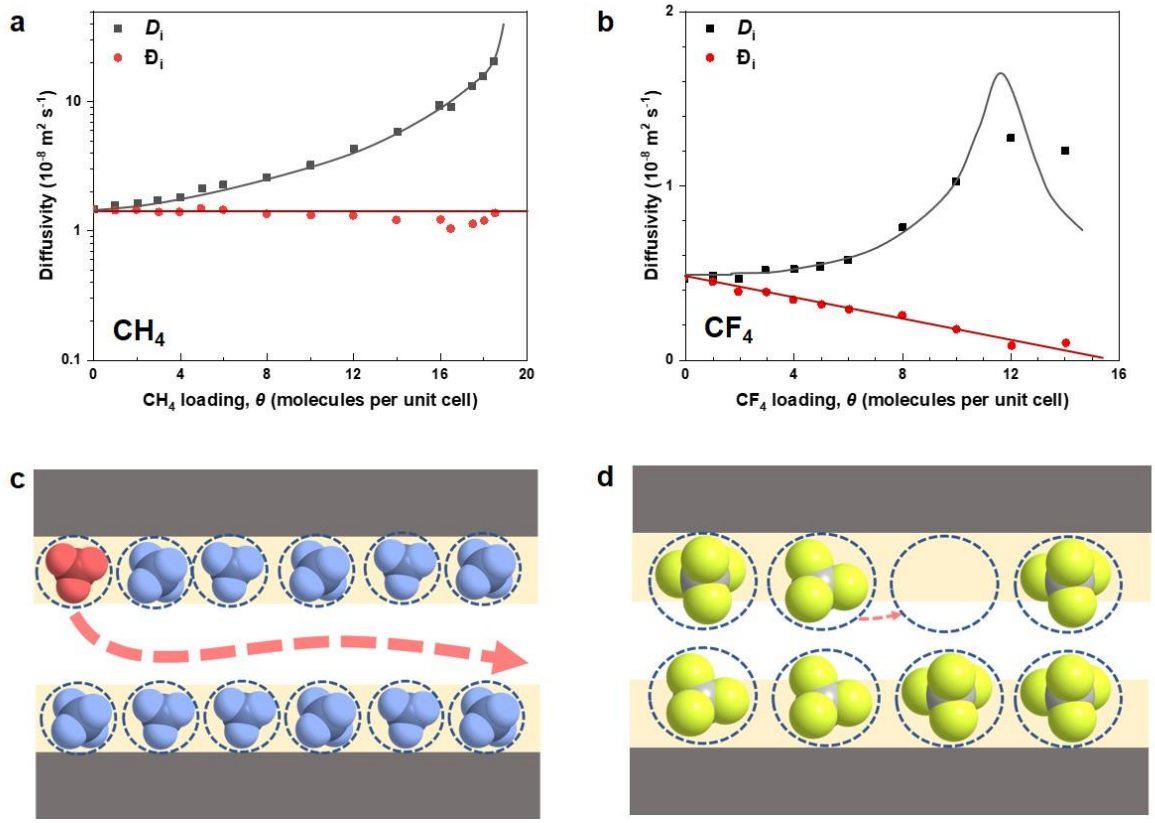

Figure 7.2 Molecular dynamics simulations (symbols) of M-S diffusivities and Fick diffusivities of (a) CH_4 and (b) CF_4, in MFI at 298 K as a function of molecular loading θ. (data from Ref.[22]) The classical physical view of micropores fully occupied by (c) CH_4 and (d) CF_4. The yellow shade denotes the region strongly influenced by the force field of the molecule sieve walls, which provide adsorption sites capturing guest molecules from the gas phase.

7.3.2 Guest-loading-dependent Maxwell-Stefan diffusivity of xylene molecules in CMS

Here, we measured the diffusion coefficients for xylene molecules in rigid microporous CMS materials as a function of fractional loadings. Two different kinds of rigid microporous carbon materials were fabricated by the pyrolysis of polymer precursors in different environments. CMS membranes were fabricated from the polymer of intrinsic

microporosity-1 (PIM-1) in a pyrolysis set-up located inside a fume hood [29,30]. The final pyrolysis temperature (500 °C) was controlled via a three-zone tube furnace. Different H_2 concentrations (4 vol% or 0 vol%) in an argon environment were utilized to fabricate CMS membranes with different pore structures. The resulting membrane samples were named with the final pyrolysis temperature and H_2 concentration. "CMS_PIM-1_500°C _4% H_2" indicates PIM-1-derived CMS membranes fabricated at 500°C in a 4 vol% H_2 atmosphere, while "CMS_PIM-1_500°C _0% H_2" indicates CMS membranes fabricated at 500°C in a pure argon atmosphere. The detailed experimental method can be found in Chapter 3.

Single component diffusion studies revealed significant differences in the kinetic uptakes (Figure 7.3 and Figure 7.4) of *p*-xylene under different relative pressure conditions, with more rapid *p*-xylene diffusion observed with increasing relative pressure, a common observation for the transport of vapors in microporous materials. These experiments were utilized to estimate the Fickian transport diffusivities, D_i and Maxwell-Stefan diffusivities, $Đ_i$.

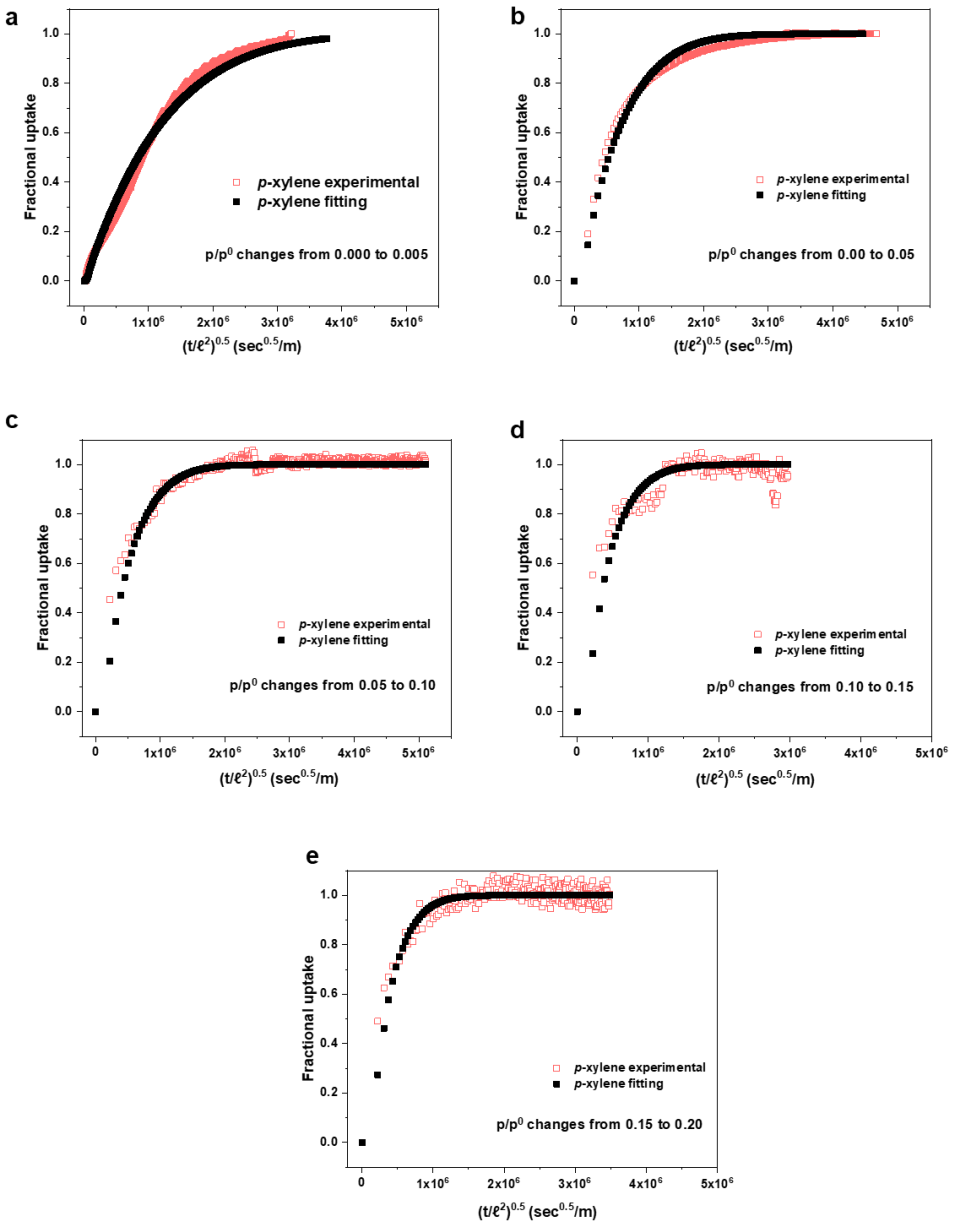

Figure 7.3 Kinetic uptake curves of *p*-xylene in CMS_PIM-1_500 °C_4% H_2 performed at 55 °C with a a) 0.000-0.005, b) 0.00-0.05, c) 0.05-0.10, d) 0.10-0.15 and e) 0.15-0.20 change in relative pressure measured with a VTI-SA+ automated vapor sorption analyzer (b, c, d and e) and DVS (a).

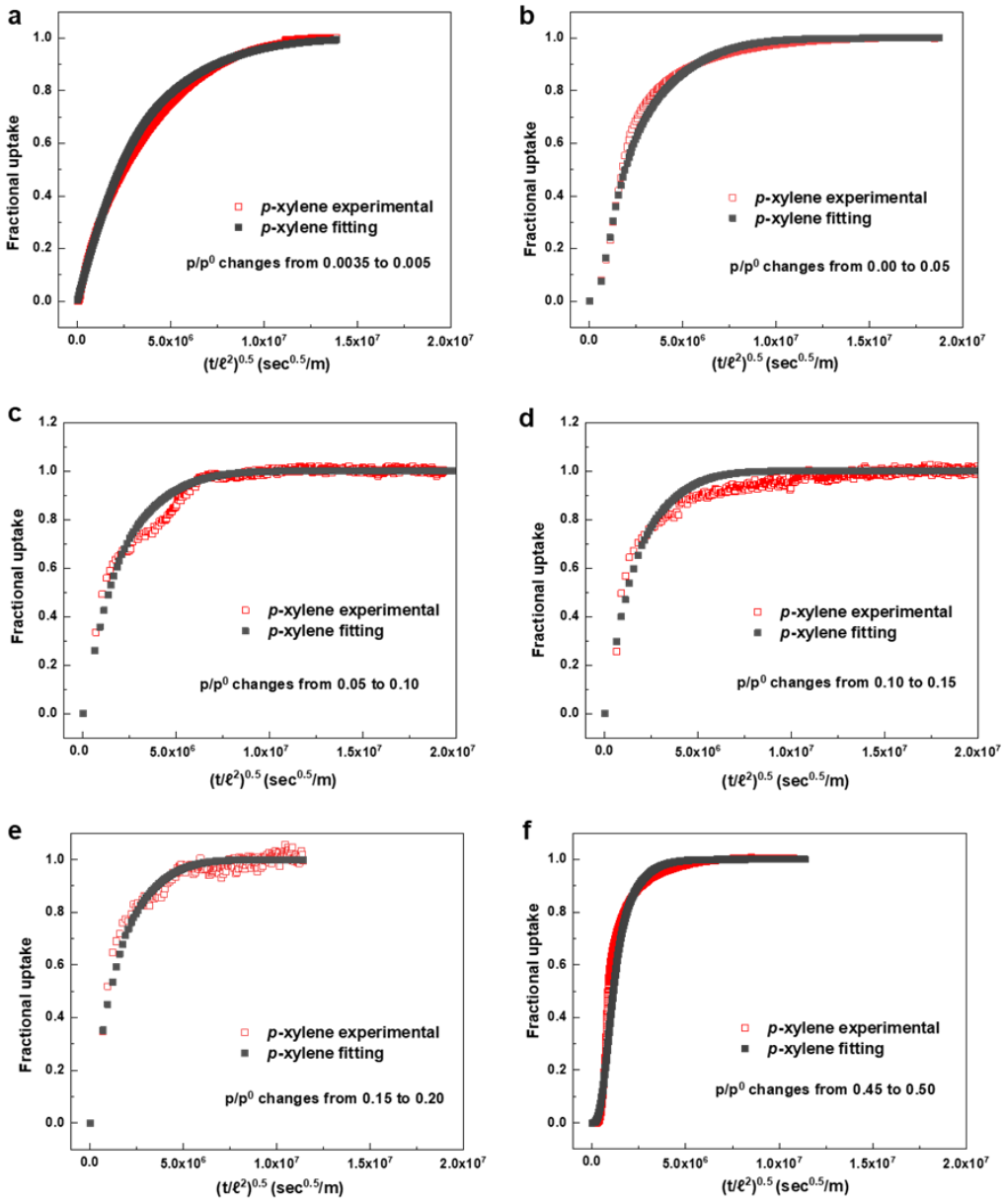

Figure 7.4 Kinetic uptake curves of *p*-xylene in CMS_PIM-1_500 °C_0% H_2 performed at 55 °C with a a) 0.0035-0.005, b) 0.00-0.05, c) 0.05-0.10, d) 0.10-0.15, e) 0.15-0.20 and f) 0.45-0.50 change in relative pressure measured with a VTI-SA+ automated vapor sorption analyzer (b, c, d and e) and DVS (a and f) .

Figure 7.5 shows the change of Maxwell-Stefan diffusivities and transport diffusivities of *p*-xylene within CMS_PIM-1_500 °C_0% H_2 and CMS_PIM-1_500 °C_4% H_2 under different *p*-xylene fractional occupancy conditions. As stated in our previous study [29], CMS_PIM-1_500 °C_4% H_2 has much larger ultramicropores compared with CMS_PIM-1_500 °C_0% H_2 (approximately 5.5 Å for the former and approximately 3.6 Å for the latter). As expected, the transport diffusivities of *p*-xylene in these two CMS materials increase with fractional occupancy. However, the CMS_PIM-1_500°C_4% H_2 sample with larger ultramicropores exhibited a constant Maxwell-Stefan diffusivity (Figure 7.5a) as fractional occupancy approaches 1.0. On the other hand, the CMS_PIM-1_500°C_0% H_2 sample with small micropores gave a decreasing Maxwell-Stefan diffusivity with increasing fractional occupancy (Figure 7.5b). Importantly, the Maxwell-Stefan diffusivity clearly approaches a minimum *nonzero* diffusivity value at conditions that are close to the vapor pressure of *p*-xylene (we estimate that this is a fractional occupancy of approximately 80%). As these materials contain a bimodal micropore structure (i.e., a microporous "cage" and an ultramicroporous "window"), it is reasonable to suspect that neither of the classical "weak" or "strong" confinement cases will necessarily apply since the xylenes possess nonspherical geometries and the pore structure of the carbon molecular sieve is much more complex than MFI zeolite. We believe this special situation can be thought of as a "hybrid confinement" case in which the diffusivity is dependent on the loading yet maintains some minimum ability for molecular exchange (and thus a nonzero diffusivity at unit fractional occupancy). We tentatively describe this situation using the following ad hoc expression:

$$Đ_i = Đ_{i,\infty} + Đ_{i,0}\theta_V^m = (a + \theta_V^m)Đ_{i,0} \qquad \textbf{Eq. 7.8}$$

where $Đ_{i,0}$ is the Maxwell-Stefan diffusivity of component i at infinite dilution while $Đ_{i,\infty}$ is the Maxwell-Stefan diffusivity of component i at a saturated loading condition and a is the ratio of $Đ_{i,\infty}/Đ_{i,0}$. Alternatively, Eq. 7.8 can be viewed as the apparent Maxwell-Stefan diffusivity for two parallel diffusion processes: $Đ_i = d^{weak}Đ_i^{weak} + d^{strong}Đ_{i,0}^{strong}\theta_V^m$, where d^{weak} and d^{strong} are the fraction of the pore volume that operates in the weak and strong confinement region, respectively [31]. By considering: $d^{weak} + d^{strong} = 1$, $Đ_i$ can be expressed as $Đ_i = d^{weak}Đ_i^{weak} + (1 - d^{weak})Đ_{i,0}^{strong}\theta_V^m$, which is mathematically equivalent to Eq. 7.8. This equation provides a possible alternative view of the hybrid confinement mode.

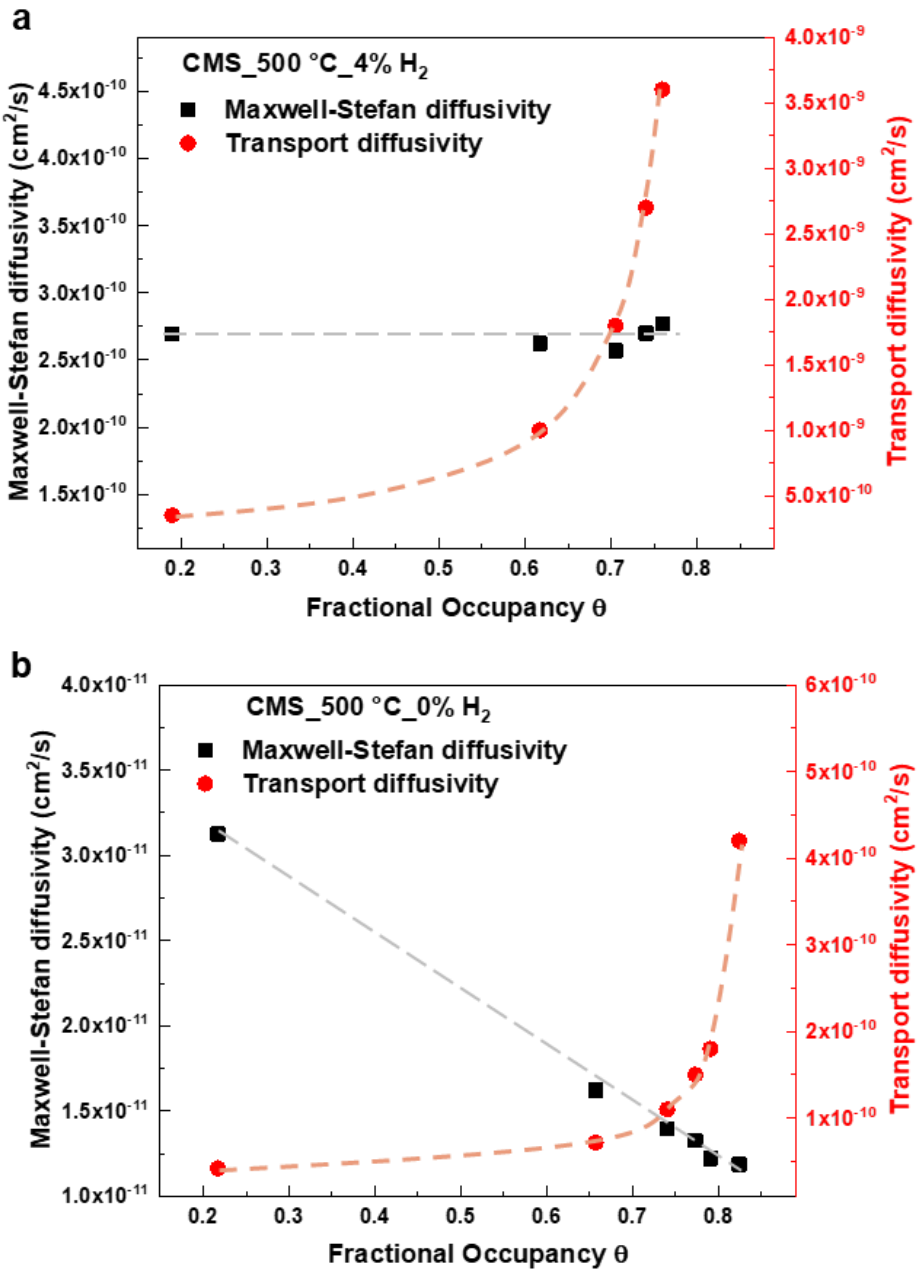

Figure 7.5. Transport and Maxwell-Stefan diffusivities of *p*-xylene in a) CMS_PIM-1_500 °C_4% H_2 and b) CMS_PIM-1_500 °C_0% at 55 °C under different fractional occupancy conditions. Lines are drawn to guide the eye.

Clearly, the "hybrid confinement" situation is a combination of the "weak confinement" cases (which we believe would be observed in a uniform of micropore 7 Å ~ 20 Å) and "strong confinement" cases (which we believe would be observed in a uniform ultramicropore of (3.8 Å ~ 7Å). It is worth considering a physical picture of the hybrid confinement case and how it differs from the classical depictions of loading-dependent diffusion. There are at least two factors that need to be captured in this physical picture: (i) the nonzero diffusivity at unit fractional occupancy and (ii) the loading dependence of the diffusivity.

One interpretation for this hybrid confinement case focuses on the special situation of nonspherical solvents diffusing in a microporous solid (Figure 7.6). If we imagine a lattice site model system filled with spherical solvents, it is clear that molecular exchange between sites is difficult at unit fractional occupancy (Figure 7.6a). However, if the lattice is filled with nonspherical solvents (e.g., xylene isomers), the various rotations of the solvent molecule in each site will create microstates that have free volume available for molecular exchange and thus enable a minimum diffusivity of solvents within the microporous system (Figure 7.6b). Current experimental data do not allow us to draw a definitive conclusion regarding the correctness of this picture; however, it is clear that the classic site-occupancy-based "strong confinement" factor of $(1-\theta_i^m)$ is not applicable to xylene diffusion in CMS membranes. This loading dependence is crucial in the derivation of flux equations for liquid systems, which is described at the end of this chapter.

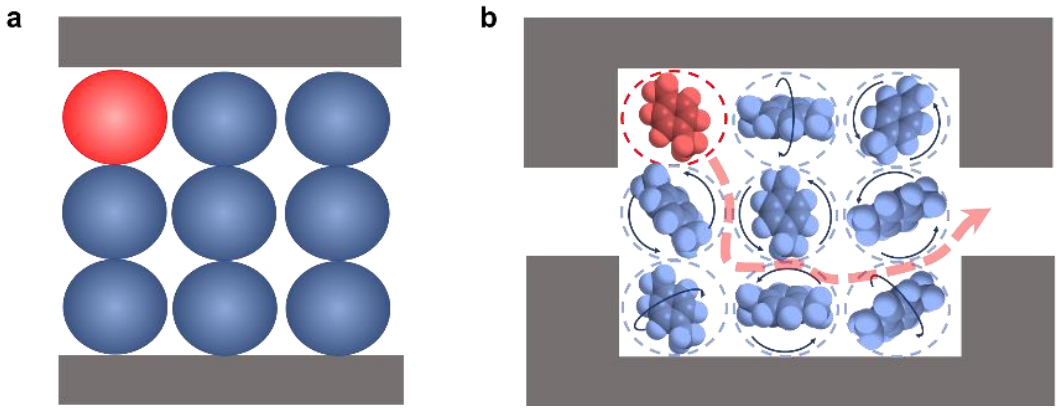

Figure 7.6 Physical illustration of "hybrid confinement" cases at full loading: (a) CMS filled with classical spherical molecules exhibit no space for diffusion, and (b) the space between adjacent nonspherical molecules allows diffusion.

We hypothesize that the distinct loading dependencies in the two chemically-similar yet structurally-distinct CMS materials can be explained by the bimodal distribution of the micropores and ultramicropores (Figure 7.7). As shown in Figure 7.7a and Figure 7.7d, the diffusion process at high fractional occupancies can be deconvoluted into 5 states: (i) normal state 1 of the tracked molecule at the high chemical potential side, (ii) transition state 1 of the tracked molecule between existing adsorbed molecules at the high chemical potential side, (iii) the transition state of the tracked molecule in the ultramicropores, (iv) transition state 2 of the tracked molecule between existing adsorbed molecules at the low chemical potential side, and (v) normal state 2 of the tracked molecule at the low chemical potential side. The transition states in the micropores are related to the diffusion through the temporary voids that arise during normal movement of adsorbed molecules, similar to the case of a liquid. With this in mind, the Gibbs free energies of the tracked molecule between existing adsorbed molecules are therefore functions of vacancy occupancy, θ_V^m. Higher xylene molecule loading (lower θ_V^m) will increase the Gibbs free energy of the

energetically-unfavorable transition states of the tracked molecule between existing adsorbed molecules in the micropores. On the other hand, the transition states of xylene molecules in the ultramicropores are essentially unrelated to the vacancy occupancy since the ultramicropores are not expected to be occupied at any xylene loading. Owing to the different pore size distributions, xylene molecules in CMS_PIM-1_500 °C_4% H_2 (Figure 7.7a-Figure 7.7c) and CMS_PIM-1_500 °C_0% H_2 (Figure 7.7d-Figure 7.7f) are hypothesized to exhibit different transition states. The Gibbs free energy difference between the transition state at ultramicropores and the initial normal state in CMS_PIM-1_500 °C_0% H_2 is higher than that in CMS_PIM-1_500 °C_4% H_2. For CMS_PIM-1_500 °C_4% H_2, the Gibbs free energy of the transition states of the tracked molecule between existing adsorbed molecules is always smaller than the transition state in the ultramicropores. If this interpretation is correct, the overall Maxwell-Stefan diffusivity will be independent of the vacancy occupancy. For CMS_PIM-1_500 °C_0% H_2, the Gibbs free energy of the transition states of the tracked molecule between existing adsorbed molecules is larger than the transition state in the ultramicropores at high loading (in essence, the system becomes “micropore-limited”, despite having a smaller ultramicropore than the CMS_PIM-1_500°C_4%H_2 material). As a result, the overall Maxwell-Stefan diffusivity is a function of the vacancy occupancy.

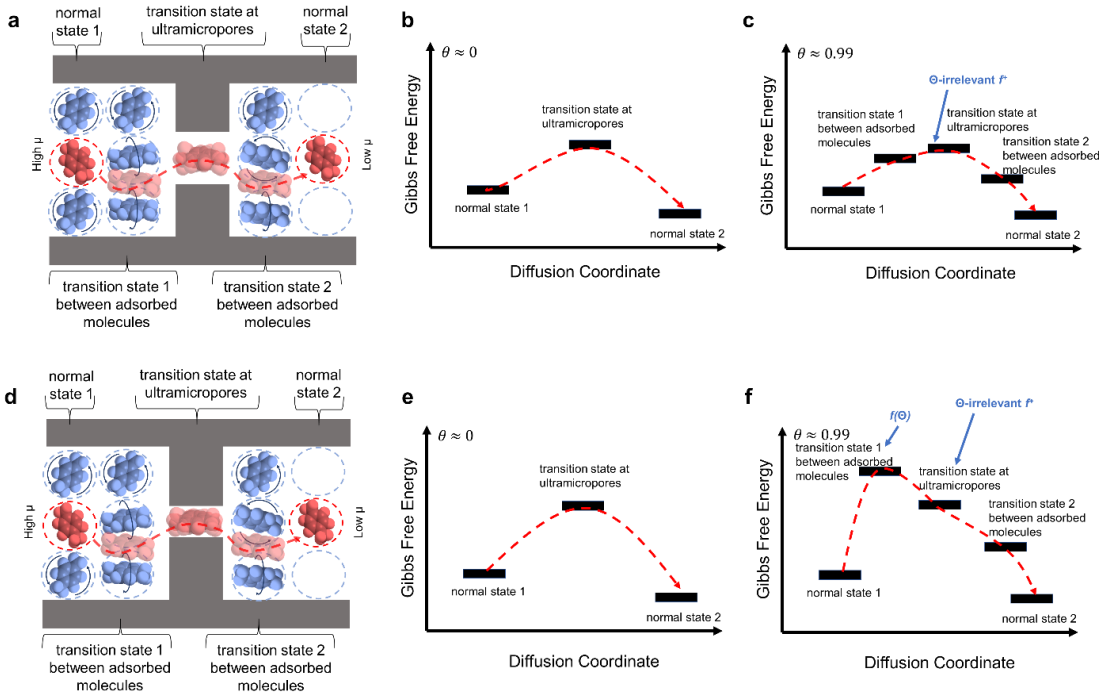

Figure 7.7 Hypothetical physical illustration of the loading dependency of Maxwell−Stefan diffusivity for the "weak confinement" case (a-c) and the "hybrid confinement" cases (d−f). (a-c): Material: CMS_PIM-1_500 °C_4% H_2. The diffusion of the red *p*-xylene molecule is tracked (a), and the hypothetical Gibbs free energy at each diffusion coordinate is shown in the low loading (b) and high loading (c) conditions. (d−f) Material: CMS_PIM-1_500 °C_0% H_2. The diffusion of the red *p*-xylene molecule is tracked (d) and the hypothetical Gibbs free energy at each diffusion coordinate is shown in the low loading (e) and high loading (f) conditions. f^+ is the partition function for a xylene molecule in the ultramicropores. The Gibbs free energy of transition state 1 is hypothesized to be a function of xylene molecule loading, which is denoted as "f(θ)" in the figure.

The temperature dependence of the diffusion coefficient was also assessed at low loadings (i.e., p/p^0 stepped from 0 to 0.05) where the transport and Maxwell-Stefan diffusion coefficients are alike. Transient kinetic uptake curves of *p*-xylene and *o*-xylene taken at different temperatures (35, 45 and 55°C) in both CMS_PIM-1_500 °C_0% H_2 and CMS_PIM-1_500 °C_4% H_2 samples were used to evaluate the temperature dependence

of the transport diffusivities and assess the separation mechanism of xylenes in these two rigid bimodally microporous membranes (details can be found in Section 5.7).

7.4 Single Component Flux Expressions

These loading-dependent Maxwell-Stefan diffusivities and selection mechanisms provide a basis for deriving flux equations for situations in which the CMS membranes are confronted with high solvent loadings (i.e., fractional occupancies near 1.0). This can be visualized by applying a hydraulically pressurized liquid on one side of the membrane while leaving the other side of the membrane in contact with a liquid at atmospheric pressure. This changes the chemical potential of species in the pressurized compartment relative to those in the non-pressurized compartment separated via the microporous membrane (Figure 2.4).

In this chapter, we will utilize fugacity to describe the chemical potential, as the flux equations derived using fugacity can be unambiguously utilized to describe both liquid and vapor transport, and the fugacity avoids mathematical inconveniencies such as the chemical potential approaching an infinite negative value as pressure approaches zero (which would complicate analysis of pervaporation systems). This change in fugacity on the pressurized side results in an increased loading of solvent molecules on this side of the membrane relative to the non-pressurized side of the membrane (referred to as “upstream” and “downstream”, respectively, for the rest of the chapter), thus providing the driving force for permeation according to Eq. 7.2. Considering this, it is useful to illustrate how the flux of solvents changes as a function of upstream hydraulic pressure, and we will first illustrate this using the simplifying case of single-component transport before moving onto

the more complex case of OSRO and mixture transport. Assuming no convection of solvents through the membrane, local chemical equilibrium between the upstream/downstream fluid and face of the membrane, negligible bulk flow or frame of reference terms exist (which is implicit in the Maxwell-Stefan formulation), and the Langmuir isotherm can relate the fluid phase fugacity to the concentration of the solvent in the membrane, we find the following single component flux equations for the various cases.

Fick's first law can be written in terms of the solvent loading in the membrane using $C_i^m = \theta_i^m q_i^{sat}$ viz.,

$$dN_i = -D_i q_i^{sat} \frac{\partial \theta_i^m}{\partial z} \qquad \textbf{Eq. 7.9}$$

where D_i is the transport or Fickian diffusion coefficient of the solvent molecule "i" in the rigid microporous membrane, and q_i^{sat} is the Langmuir saturation constant. Combining this with Eq. 7.3 and Eq. 7.5 results in a form of Fick's first law that is easily integrated:

$$N_i = \frac{-Đ_i q_i^{sat}}{1 - \theta_i^m} \cdot \frac{\partial \theta_i^m}{\partial z} \qquad \textbf{Eq. 7.10}$$

In the "weak confinement" case ($Đ_i = Đ_{i,0}$), the flux equation after the integration of Eq. 7.10 from the upstream and downstream loadings at the membrane faces becomes:

$$N_i = \frac{Đ_{i,0} q_i^{sat}}{\ell} ln\left(\frac{1-\theta_i^{m,down}}{1-\theta_i^{m,up}}\right) \qquad \textbf{Eq. 7.11}$$

where ℓ is the membrane thickness.

In the "strong confinement" case ($Đ_i = Đ_{i,0}(1-\theta_i^m)$), after the integration of Eq. 7.10 becomes:

$$N_i = \frac{Đ_{i,0} q_i^{sat}}{\ell}\left(\theta_i^{m,up} - \theta_i^{m,down}\right) \qquad \textbf{Eq. 7.12}$$

In the "hybrid confinement" case, we define $Đ_i$ in a semi ad hoc fashion ($Đ_i = Đ_{i,\infty} + Đ_{i,0}(1-\theta_i^m) = aĐ_{i,0} + (1-\theta_i^m)Đ_{i,0}$). The flux equation after the integration of Eq. 7.10 from the upstream and downstream loadings at the membrane faces becomes:

$$N_i = \frac{aĐ_{i,0} q_i^{sat}}{\ell} ln\left(\frac{1-\theta_i^{m,down}}{1-\theta_i^{m,up}}\right) + \frac{Đ_{i,0} q_i^{sat}}{\ell}\left(\theta_i^{m,up} - \theta_i^{m,down}\right) \qquad \textbf{Eq. 7.13}$$

The weak confinement result reveals that the solvent flux is expected to increase almost linearly as pressure increases and apparently goes to infinity as the upstream hydraulic pressure keeps increasing, whereas the strong confinement analysis suggests that there is an upper limit to the flux through the membrane. With the flux equations available (Eq. 7.11-Eq. 7.13), we can derive the relationship between flux N_i and upstream hydraulic pressure p^{up} for the weak confinement and strong confinement cases. The detailed derivation process is shown below:

For pure component diffusion process:

$$f_i = p_i^{sat} \exp\left[\frac{\hat{V}_i}{\mathrm{RT}}(p - p_i^{sat})\right] \quad \textbf{Eq. 7.14}$$

$$\theta_i^{m,up} = \frac{b_i f_i^{up}}{1+b_i f_i^{up}} \text{ and } \theta_i^{m,down} = \frac{b_i f_i^{down}}{1+b_i f_i^{down}} \quad \textbf{Eq. 7.15}$$

$\theta_i^{m,down} = \frac{b_i f_i^{down}}{1+b_i f_i^{down}}$ =constant, if p^{down} is a constant

In the "weak confinement" case

$$N_i = \frac{Đ_{i,0} q_i^{sat}}{\ell} ln\left(\frac{1-\theta_i^{m,down}}{1-\theta_i^{m,up}}\right) = \frac{Đ_{i,0} q_i^{sat}}{\ell} ln\left(1-\theta_i^{m,down}\right) - \frac{Đ_{i,0} q_i^{sat}}{\ell} ln\left(1-\theta_i^{m,up}\right) \quad \textbf{Eq. 7.16}$$

By putting Eq. 7.15 into Eq. 7.16, we can obtain:

$$N_i = \frac{Đ_{i,0} q_i^{sat}}{\ell} ln\left(1-\theta_i^{m,down}\right) - \frac{Đ_{i,0} q_i^{sat}}{\ell} ln\left(1-\frac{b_i f_i^{up}}{1+b_i f_i^{up}}\right)$$

$$N_i = \frac{Đ_{i,0} q_i^{sat}}{\ell} ln\left(1-\theta_i^{m,down}\right) - \frac{Đ_{i,0} q_i^{sat}}{\ell} ln\left(\frac{1}{1+b_i f_i^{up}}\right)$$

$$N_i = \frac{Đ_{i,0} q_i^{sat}}{\ell} ln\left(1-\theta_i^{m,down}\right) - \frac{Đ_{i,0} q_i^{sat}}{\ell} \left[l\,n(1) - \ln\left(1+b_i f_i^{up}\right)\right]$$

$$N_i = \frac{Đ_{i,0} q_i^{sat}}{\ell} ln\left(1-\theta_i^{m,down}\right) + \frac{Đ_{i,0} q_i^{sat}}{\ell} ln\left(1+b_i f_i^{up}\right)$$

$$N_i = \frac{Đ_{i,0} q_i^{sat}}{\ell} ln\left(1 - \theta_i^{m,down}\right) + \frac{Đ_{i,0} q_i^{sat}}{\ell} ln\left\{1 + b_i p_i^{sat} \exp\left[\frac{\hat{V}_i}{\mathrm{RT}}(p^{up} - p_i^{sat})\right]\right\} \quad \textbf{Eq. 7.17}$$

where $\frac{Đ_{i,0} q_i^{sat}}{\ell}$ and $\frac{Đ_{i,0} q_i^{sat}}{\ell} ln\left(1 - \theta_i^{m,down}\right)$ are constants

In the "strong confinement" case

$$N_i = \frac{Đ_{i,0} q_i^{sat}}{\ell}\left(\theta_i^{m,up} - \theta_i^{m,down}\right) = \frac{Đ_{i,0} q_i^{sat}}{\ell}\theta_i^{m,up} - \frac{Đ_{i,0} q_i^{sat}}{\ell}\theta_i^{m,down} \quad \textbf{Eq. 7.18}$$

By putting Eq. 7.15 into Eq. 7.18, we can obtain:

$$N_i = \frac{Đ_{i,0} q_i^{sat}}{\ell}\frac{b_i f_i^{up}}{1 + b_i f_i^{up}} - \frac{Đ_{i,0} q_i^{sat}}{\ell}\theta_i^{m,down}$$

$$N_i = \frac{Đ_{i,0} q_i^{sat}}{\ell}\frac{b_i p_i^{sat} \exp\left[\frac{\hat{V}_i}{\mathrm{RT}}(p^{up} - p_i^{sat})\right]}{1 + b_i p_i^{sat} \exp\left[\frac{\hat{V}_i}{\mathrm{RT}}(p^{up} - p_i^{sat})\right]} - \frac{Đ_{i,0} q_i^{sat}}{\ell}\theta_i^{m,down} \quad \textbf{Eq. 7.19}$$

where $\frac{Đ_{i,0} q_i^{sat}}{\ell}$ and $\frac{Đ_{i,0} q_i^{sat}}{\ell}\theta_i^{m,down}$ are constants

Eq. 7.17 and Eq. 7.19 are the relationship between flux N_i and upstream hydraulic pressure $p^{up}$for the weak confinement and strong confinement cases, respectively. With all the parameters available for *p*-xylene transport through CMS membranes as an example, we can draw the figures of flux N_i v.s upstream hydraulic pressure p^{up} .As shown in Figure 7.8 **(**All the parameters in the Eq. 7.17 and Eq. 7.19 prediction can be found in Table 7.1.**)**, the flux increases almost linearly as pressure increase and apparently goes to infinity as the upstream hydraulic pressure keep increasing for weak confinement case, whereas

the strong confinement analysis suggests that there is an upper limit to the flux through the membrane.

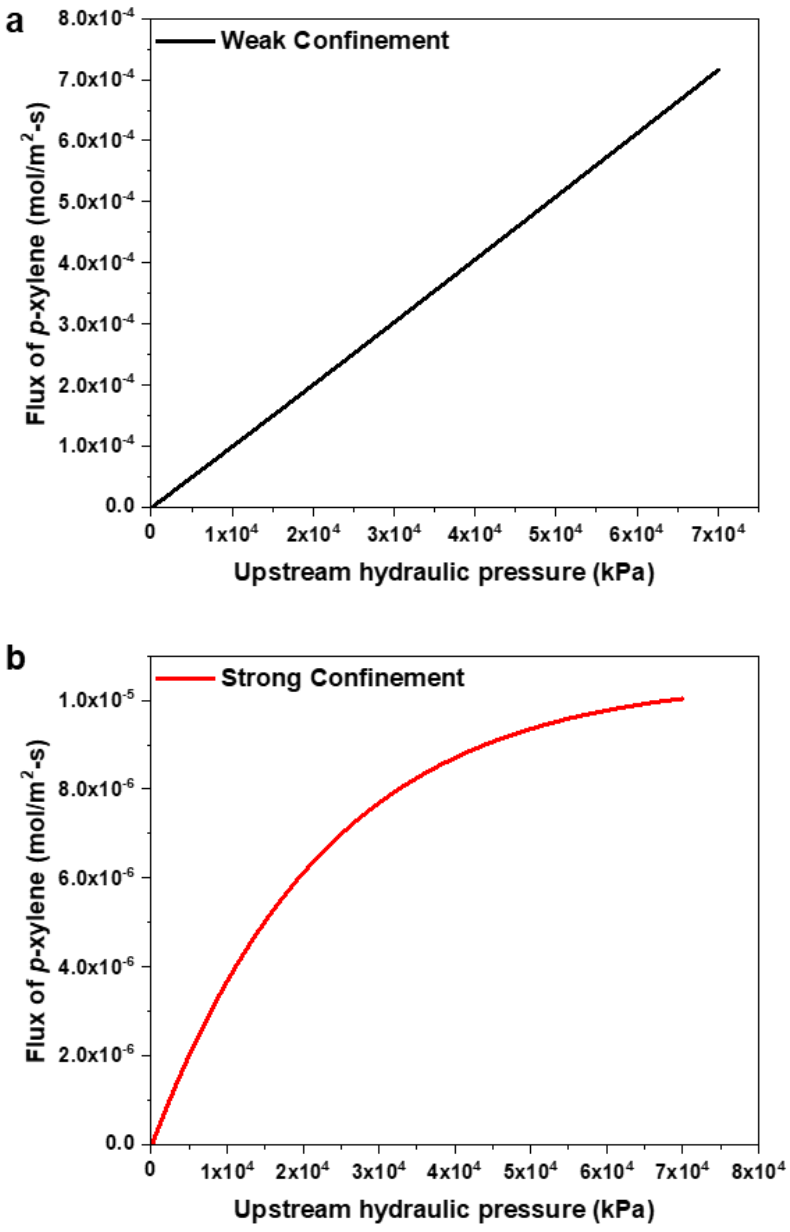

Figure 7.8 Fickian model predictions for flux changes with upstream hydraulic pressure for a) "weak confinement" case and b) "strong confinement" case.

Table 7.1 Parameters for estimation of flux in Figure 7.8 using the Fickian approach.

Item	Value
p-xylene Maxwell-Stefan coefficients at infinite dilution $Đ_{i0}$	2.67×10^{-10} cm^2/s=2.67×10^{-14} m^2/s
Saturation loading q_i^{sat}	$1.3057\frac{mmol}{g} = 1.3057\frac{mmol}{g}\frac{2g}{cm^3} = 2.6114\frac{mmol}{cm^3} = 2611.4\ \frac{mol}{m^3}$
Thickness of the membrane ℓ	300 nm=3×10^{-7} m
Permeate side pressure p^{down}	1 bar, abs=101 kPa
Langmuir affinity constant b_i	3.7957 kPa-1
Testing temperature T	328.15 K
Molar volume of *p*-xylene $\hat{V}_i$	123.3 cm^3/mol=1.233×10^{-4} m^3/mol
Saturation pressure of *p*-xylene p_i^{sat}	5.4757 kPa
Feed side pressure p^{up}	101kPa~70000 kPa

In polymer membranes, a phenomenological "fingerprint" of sorption-diffusion permeation is an apparent asymptote in the flux with increasing upstream fluid pressure, whereas a fingerprint for pore flow permeation is an apparent linear increase in solvent flux with increasing upstream fluid pressure. Our analysis suggests that in the case of rigid (i.e., not swellable) microporous membranes, both phenomenological responses are possible within a sorption-diffusion regime and thus, other methods are needed to unambiguously describe the transport modality.

7.5 Flux Expressions for Binary OSRO Transport

The Maxwell-Stefan formulation describes flux by considering both the driving force for diffusion and the frictional coupling effects of molecules passing each other and the membrane surface. Krishna et al. have derived a Maxwell-Stefan formulation for a two-component transport case in which the membrane loading is described with a competitive Langmuir isotherm [25,32]. We utilize this analysis as our starting point and utilize liquid phase fugacities on the upstream and downstream sides of the membrane as our boundary conditions (Figure 2.4).

If membrane loading can be described with a competitive Langmuir isotherm:[25,32]

$$\theta_i^m = \frac{q(f_i^{fl})}{q_i^{sat}} = \frac{b_i f_i^{fl}}{1 + \sum_{i=1}^{n} b_i f_i^{fl}} = \frac{b_i f_i^{fl}}{1 + b_i f_i^{fl} + b_j f_j^{fl}} \qquad \textbf{Eq. 7.20}$$

For liquids, the fugacity can be approximated by:

$$\hat{f}_i^{fl} = x_i \gamma_i p_i^{sat} \exp\left[\frac{\hat{V}_i}{\mathrm{RT}}(p - p_i^{sat})\right] \qquad \textbf{Eq. 7.21}$$

where γ_i is an activity coefficient, x_i is the mole fraction of the component i, $\hat{V}_i$ is the molar volume, p is the liquid phase pressure, p_i^{sat} is the saturated vapor pressure of the component i.

The vacancy occupancy is defined as following to quantify the vacant sites left in the membrane:

$$\theta_V^m \equiv 1 - \sum_{i=1}^{n} \theta_i^m = 1 - \theta_i^m - \theta_j^m = \frac{1}{1 + \sum_{i=1}^{n} F_i} \qquad \textbf{Eq. 7.22}$$

Where F is dimensionless fugacity $F_i = b_i f_i$. For a membrane of thickness ℓ, a model is established for its equilibrium state. z is defined as a distance coordinate along the membrane. Two boundary conditions can be obtained:

- At the upstream,

$$z = 0\text{: } q_i = q_i^{up}, \quad \theta_i^m = \theta_i^{m,up}, \quad \theta_V^m = \theta_V^{m,up}, \quad f_i = f_i^{up} \qquad \textbf{Eq. 7.23}$$

- At the downstream,

$$z = \ell\text{: } q_i = q_i^{down},\ \theta_i^m = \theta_i^{m,down},\ \theta_V^m = \theta_V^{m,down},\ f_i = f_i^{down} \qquad \textbf{Eq. 7.24}$$

f_i^{up} and f_i^{down} are the fugacities within the membrane on the feed and permeate sides, respectively. Local thermodynamic equilibrium makes the fugacity within the membrane (f_i^{up} *or* f_i^{down}) equal to that of either the feed or permeate (f_i^{feed} *or* f_i^{permeate}), which are determined by fluid thermodynamics.

After the rearrangement of Maxwell-Stefan formulation, the relationship between chemical potential gradients and the transmembrane flux can be described as follow:[25,33]

$$-\frac{\rho\theta_i^m}{RT}\frac{\partial\mu_i}{\partial z}=\sum_{j=1,j\neq i}^{n}\frac{q_jN_i-q_iN_j}{q_i^{sat}q_j^{sat}Đ_{ij}}+\frac{N_i}{q_i^{sat}Đ_i},\qquad i=1,2 \qquad \textbf{Eq. 7.25}$$

Where ρ is the density of the membrane and can be treated as 2.0 g/cm^3 for CMS membranes. As derived by R. Krishna and R. Baur,[25] the generalized Maxwell-Stefan flux expression for similarly-sized molecules through a microporous membrane can be explicitly expressed as follow: [25,32]

$$(\boldsymbol{N})=-\frac{\rho}{\ell}[\boldsymbol{q^{sat}}][\boldsymbol{B}]^{-1}\theta_V^m\frac{\partial(\boldsymbol{F})}{\partial\eta} \qquad \textbf{Eq. 7.26}$$

ℓ is the thickness of the membrane. η is a dimensionless position through the membrane $\eta=\frac{z}{\ell}$. and z is defined as a distance coordinate across the membrane.

$$(\boldsymbol{N})=\begin{pmatrix}N_1\\N_2\end{pmatrix} \qquad \textbf{Eq. 7.27}$$

$$[\boldsymbol{q^{sat}}]=\begin{bmatrix}q_1^{sat} & o\\ o & q_2^{sat}\end{bmatrix} \qquad \textbf{Eq. 7.28}$$

$$(\boldsymbol{F})=\begin{pmatrix}F_1\\F_2\end{pmatrix} \qquad \textbf{Eq. 7.29}$$

The 2×2 matrix, [$\boldsymbol{B}$], is the inverse diffusion matrix and is defined as the following:

$$B_{ii}=\frac{1}{Đ_i}+\sum_{j=1,j\neq i}^{n}\frac{\theta_j^m}{Đ_{ij}},\ \ i=1,2\ ;\ B_{ij}=-\frac{\theta_i^m}{Đ_{ij}},\ \ i\neq j=1,2 \qquad \textbf{Eq. 7.30}$$

We have utilized Vignes-type assumptions to estimate the frictional coupling effects.

$$Đ_{ij} = Đ_{ji} = Đ_i^{\frac{\theta_i^m}{\theta_i^m+\theta_j^m}} \times Đ_j^{\frac{\theta_j^m}{\theta_i^m+\theta_j^m}} \quad \textbf{Eq. 7.31}$$

7.5.1 "Weak Confinement" Case

For the "weakly confined" case, the Maxwell-Stefan diffusivity matrix is independent of solvent loading. In this case, the inverse diffusion matrix $[\boldsymbol{B}]$ is defined as $[\boldsymbol{B}(\mathbf{0})]$ to signify the evaluation of the inverse diffusion matrix using the infinite dilution diffusion coefficients.

$$[\boldsymbol{B}] = [\boldsymbol{B}(\mathbf{0})] \quad \textbf{Eq. 7.32}$$

$$B_{ii}(0) = \frac{1}{Đ_{i,0}} + \sum_{j=1,j\neq i}^{n} \frac{\theta_j^m}{Đ_{ij,0}}, \;\; i = 1,2; \; B_{ij}(0) = -\frac{\theta_i^m}{Đ_{ij,0}}, \;\; i \neq j = 1,2 \quad \textbf{Eq. 7.33}$$

$$Đ_{ij,0} = Đ_{ji,0} = Đ_{i,0}^{\frac{\theta_i^m}{\theta_i^m+\theta_j^m}} \times Đ_{j,0}^{\frac{\theta_j^m}{\theta_i^m+\theta_j^m}} \quad \textbf{Eq. 7.34}$$

Therefore, after the re-arrangement of Eq. 7.26, the differentiation of F_i over η can be expressed as:

$$\frac{\partial F_i}{\partial \eta} = -\frac{1}{\theta_V^m}\sum_{j=1}^{n} B_{ij}\frac{N_j\ell}{\rho q_j^{sat}} = -\frac{1}{\theta_V^m}\sum_{j=1}^{n} B_{ij}(0)\frac{N_j\ell}{\rho q_j^{sat}} \quad \textbf{Eq. 7.35}$$

For the ease of calculation, dimensionless molar flux, ϕ_i is defined as follows:

$$\phi_i \equiv \sum_{j=1}^{n} B_{ij}(0) \frac{N_j \ell}{\rho q_j^{sat}} \qquad \textbf{Eq. 7.36}$$

Flux vector in the weak confinement case can be expressed in terms of dimensionless flux after putting Eq. 7.35 and Eq. 7.36 into Eq. 7.26:

$$(\boldsymbol{N}) = -\frac{\rho}{\ell}[\boldsymbol{q^{sat}}][\boldsymbol{B}]^{-1}\theta_V^m \frac{\partial(\boldsymbol{F})}{\partial \eta} = \frac{\rho}{\ell}[\boldsymbol{q^{sat}}][\boldsymbol{B}(\boldsymbol{0})]^{-1}(\boldsymbol{\phi}) \qquad \textbf{Eq. 7.37}$$

Summing Eq. 7.35 over the species by introducing Eq. 7.22, one can obtain:

$$\frac{\partial(\frac{1}{\theta_V^m})}{\partial \eta} = -\frac{1}{\theta_V^m}\sum_{i=1}^{n}\sum_{j=1}^{n} B_{ij}\frac{N_j \ell}{\rho q_j^{sat}} = -\frac{1}{\theta_V^m}\sum_{i=1}^{n}\sum_{j=1}^{n} B_{ij}(0)\frac{N_j \ell}{\rho q_j^{sat}} \qquad \textbf{Eq. 7.38}$$

For the ease of calculation dimensionless total molar flux, ϕ_t is defined as follows:

$$\phi_t \equiv \sum_{i=1}^{n} \phi_i = \sum_{i=1}^{n}\sum_{j=1}^{n} B_{ij}(0)\frac{N_j \ell}{\rho q_j^{sat}} = \sum_{i=1}^{n} \frac{N_i \ell}{\rho q_i^{sat} Đ_{i,0}} \qquad \textbf{Eq. 7.39}$$

We notice that $B_{ij}(0)$ does not contribute to ϕ_t. As a result, ϕ_t is independent of the loading and dimensionless position η. By putting Eq. 7.39 into Eq. 7.38, one can obtain:

$$\frac{\partial(\frac{1}{\theta_V^m})}{\partial \eta} = -\frac{\phi_t}{\theta_V^m} \quad \textbf{Eq. 7.40}$$

After the definite integration of Eq. 7.40 with the boundary conditions at upstream and downstream. The dimensionless total flux can be expressed as:

$$\phi_t = \ln(\frac{\theta_V^{m,down}}{\theta_V^{m,up}}) \quad \textbf{Eq. 7.41}$$

Indefinite integration of Eq. 7.40 will result in:

$$\eta\phi_t = \ln(\frac{\theta_V^{m,\eta}}{\theta_V^{m,up}}) \quad \textbf{Eq. 7.42}$$

The differentiation of η over θ_V^m can be expressed as:

$$\frac{d\eta}{d\theta_V^m} = \frac{1}{\phi_t \theta_V^{m,\eta}} \quad \textbf{Eq. 7.43}$$

By putting Eq. 7.36 into Eq. 7.35, one can obtain:

$$\frac{\partial F_i}{\partial \eta} = -\frac{\phi_i}{\theta_V^{m,\eta}} \quad \textbf{Eq. 7.44}$$

Combing Eq. 7.43 and Eq. 7.44, the differentiation of F_i over θ_V^m can be expressed as:

$$\frac{\partial F_i}{\partial \theta_V^m} = \frac{\partial F_i}{\partial \eta}\frac{d\eta}{d\theta_V^m} = -\frac{\phi_i}{\phi_t \theta_V^{m,\eta^2}} \qquad \textbf{Eq. 7.45}$$

After definite integration of Eq. 7.45 by assuming that ϕ_i is independent of η,[25,32] dimensionless flux of component i can be expressed as:

$$\phi_i = \frac{\ln\left(\frac{\theta_V^{m,down}}{\theta_V^{m,up}}\right)(F_i^{up} - F_i^{down})}{\left(\frac{1}{\theta_V^{m,up}} - \frac{1}{\theta_V^{m,down}}\right)} \qquad \textbf{Eq. 7.46}$$

Therefore, the flux vector in the case of weak confinement can be expressed as:

$$(\boldsymbol{N}) = \frac{\rho}{\ell}\frac{\ln\left(\frac{\theta_V^{m,down}}{\theta_V^{m,up}}\right)}{\left(\frac{1}{\theta_V^{m,up}} - \frac{1}{\theta_V^{m,down}}\right)}[\boldsymbol{q^{sat}}][\boldsymbol{B}(\boldsymbol{0})]^{-1}(\boldsymbol{F^{up}} - \boldsymbol{F^{down}}) \qquad \textbf{Eq. 7.47}$$

This generalized Maxwell-Stefan weak confinement model agrees with the literature [24,25,34] and can be used to predict the mixture permeation of *p*-xylene (component 1) and *o*-xylene (component 2) through CMS membranes that were created using hydrogen pyrolysis (i.e., CMS_PIM-1_500°C_4% H_2).

7.5.2 "Strong Confinement" Case

A similar approach can be utilized to derive the flux expressions for the "strong confinement" case by noting that $Đ_i = Đ_{i,0}\theta_V^m$ (θ_V^m is the vacancy-occupancy that

quantifies the vacant sites left in the membrane). The inverse diffusion matrix [$\boldsymbol{B}$] is defined as:

$$[\boldsymbol{B}] = \frac{1}{\theta_V^m}[\boldsymbol{B}(\boldsymbol{0})] \qquad \textbf{Eq. 7.48}$$

Therefore, after the re-arrangement of Eq. 7.26, the differentiation of F_i and $\frac{1}{\theta_V^m}$ over η can be expressed as:

$$\frac{\partial F_i}{\partial \eta} = -\frac{1}{\theta_V^m}\sum_{j=1}^{n} B_{ij}\frac{N_j \ell}{\rho q_j^{sat}} = -\frac{1}{\theta_V^{m2}}\sum_{j=1}^{n} B_{ij}(0)\frac{N_j \ell}{\rho q_j^{sat}} = -\frac{\phi_i}{\theta_V^{m2}} \qquad \textbf{Eq. 7.49}$$

$$\begin{aligned}\frac{\partial(\frac{1}{\theta_V^m})}{\partial \eta} &= -\frac{1}{\theta_V^m}\sum_{i=1}^{n}\sum_{j=1}^{n} B_{ij}\frac{N_j \ell}{\rho q_j^{sat}} = -\frac{1}{\theta_V^{m2}}\sum_{i=1}^{n}\sum_{j=1}^{n} B_{ij}(0)\frac{N_j \ell}{\rho q_j^{sat}} \\ &= -\frac{\phi_t}{\theta_V^{m2}}\end{aligned} \qquad \textbf{Eq. 7.50}$$

Flux vector in the strong confinement case can be expressed in terms of dimensionless flux:

$$(\boldsymbol{N}) = -\frac{\rho}{\ell}[\boldsymbol{q^{sat}}][\boldsymbol{B}]^{-1}\theta_V^m\frac{\partial(\boldsymbol{F})}{\partial \eta} = \frac{\rho}{\ell}[\boldsymbol{q^{sat}}][\boldsymbol{B}(\boldsymbol{0})]^{-1}(\boldsymbol{\phi}) \qquad \textbf{Eq. 7.51}$$

After definite integration of Eq. 7.50:

$$\phi_t = \theta_V^{m,down} - \theta_V^{m,up} \qquad \textbf{Eq. 7.52}$$

Indefinite integration of Eq. 7.50 will result in:

$$\eta\phi_t = \theta_V^{m,\eta} - \theta_V^{m,up} \qquad \textbf{Eq. 7.53}$$

The differentiation of η over θ_V^m can be expressed as:

$$\frac{d\eta}{d\theta_V^m} = \frac{1}{\phi_t} \qquad \textbf{Eq. 7.54}$$

Therefore, the differentiation of F_i over θ_V^m can be expressed as:

$$\frac{\partial F_i}{\partial \theta_V^m} = \frac{\partial F_i}{\partial \eta}\frac{d\eta}{d\theta_V^m} = -\frac{\phi_i}{\phi_t \theta_V^{m,\eta 2}} \qquad \textbf{Eq. 7.55}$$

After definite integration, the dimensionless flux of component i can be expressed as:

$$\phi_i = \frac{(\theta_V^{m,down} - \theta_V^{m,up})(F_i^{m,up} - F_i^{m,down})}{\left(\frac{1}{\theta_V^{m,up}} - \frac{1}{\theta_V^{m,down}}\right)} = \theta_V^{m,up}\theta_V^{m,down}(F_i^{up} - F_i^{down}) \qquad \textbf{Eq. 7.56}$$

Therefore, the flux vector in the case of strong confinement can be expressed as:

$$(\boldsymbol{N}) = \frac{\rho}{\ell}\theta_V^{m,up}\theta_V^{m,down}[\boldsymbol{q^{sat}}][\boldsymbol{B}(\boldsymbol{0})]^{-1}(\boldsymbol{F^{up}} - \boldsymbol{F^{down}}) \qquad \textbf{Eq. 7.57}$$

7.5.3 "Hybrid Confinement" Case

Finally, we consider the special "hybrid confinement" case. Here, we assume that the Maxwell-Stefan diffusivity varies with fractional occupancy via $Đ_i = Đ_{i,\infty} +$

$Đ_{i,0}\theta_V^m = (a + \theta_V^m)Đ_{i,0}$, such that the Maxwell-Stefan inverse diffusivity matrix can be expressed as:

$$[\boldsymbol{B}] = \frac{[\boldsymbol{B}(\mathbf{0})]}{a + \theta_V^m} \qquad \textbf{Eq. 7.58}$$

After the re-arrangement of Eq. 7.26, the dimensionless fugacity gradient can be expressed as:

$$\begin{aligned} \frac{\partial F_i}{\partial \eta} &= -\frac{1}{\theta_V^m}\sum_{j=1}^{n} B_{ij}\frac{N_j \ell}{\rho q_j^{sat}} = -\frac{1}{\theta_V^m[a + \theta_V^m]}\sum_{j=1}^{n} B_{ij}(0)\frac{N_j \ell}{\rho q_j^{sat}} \\ &= -\frac{\phi_i}{\theta_V^m[a + \theta_V^m]} \end{aligned} \qquad \textbf{Eq. 7.59}$$

According to the definition of vacancy occupancy and Langmuir isotherm, the equation above can be summed:

$$\begin{aligned} \frac{\partial(\frac{1}{\theta_V^m})}{\partial \eta} &= -\frac{1}{\theta_V^m}\sum_{i=1}^{n}\sum_{j=1}^{n} B_{ij}\frac{N_j \ell}{\rho q_j^{sat}} \\ &= -\frac{1}{\theta_V^m[a + \theta_V^m]}\sum_{i=1}^{n}\sum_{j=1}^{n} B_{ij}(0)\frac{N_j \ell}{\rho q_j^{sat}} \\ &= -\frac{\phi_t}{\theta_V^m[a + \theta_V^m]} \end{aligned} \qquad \textbf{Eq. 7.60}$$

Combining Eq. 7.26 and Eq. 7.59, the flux vector $\boldsymbol{N}$ can be expressed as:

$$(\boldsymbol{N}) = \frac{\rho}{\ell}[\boldsymbol{q^{sat}}][\boldsymbol{B}(\boldsymbol{0})]^{-1}(\boldsymbol{\phi}) \qquad \textbf{Eq. 7.61}$$

After the integration of Eq. 7.60, the dimensionless total flux can be expressed as:

$$[\phi_t = aln\left(\frac{\theta_V^{m,down}}{\theta_V^{m,up}}\right) + (\theta_V^{m,down} - \theta_V^{m,up}) \qquad \textbf{Eq. 7.62}$$

$$\eta\phi_t = aln\left(\frac{\theta_V^{m,\eta}}{\theta_V^{m,up}}\right) + (\theta_V^{m,\eta} - \theta_V^{m,up}) \qquad \textbf{Eq. 7.63}$$

The differentiation of η over θ_V^m can be expressed as:

$$\frac{d\eta}{d\theta_V^m} = \frac{a}{\phi_t\theta_V^{m,\eta}} + \frac{1}{\phi_t} \qquad \textbf{Eq. 7.64}$$

Combining Eq. 7.59 and Eq. 7.64, the differentiation of dimensionless fugacity over dimensionless membrane thickness can be converted to differentiation over vacancy occupancy:

$$\frac{\partial F_i}{\partial\theta_V^m} = \frac{\partial F_i}{\partial\eta}\frac{d\eta}{d\theta_V^m} = -\left(\frac{a}{\phi_t\theta_V^{m,\eta}} + \frac{1}{\phi_t}\right)\frac{\phi_i}{\theta_V^{m,\eta}[a + \theta_V^{m,\eta}]} \qquad \textbf{Eq. 7.65}$$

After rearrangement:

$$-\frac{\phi_t}{\phi_i}dF_i = \left(\frac{a}{a\theta_V^{m,\eta^2} + \theta_V^{m,\eta^3}} + \frac{1}{a\theta_V^{m,\eta} + \theta_V^{m,\eta^2}}\right)d\theta_V^m \qquad \textbf{Eq. 7.66}$$

After integration and applying the boundary condition at upstream and downstream, the dimensionless flux of component i can be expressed as:

$$-\frac{\phi_t}{\phi_i}\left(F_i^{up}-F_i^{down}\right)=-\left(\frac{1}{\theta_V^{m,up}}-\frac{1}{\theta_V^{m,down}}\right) \quad \textbf{Eq. 7.67}$$

$$\phi_i=\frac{[aln\left(\frac{\theta_V^{m,down}}{\theta_V^{m,up}}\right)+(\theta_V^{m,down}-\theta_V^{m,up})]\left(F_i^{up}-F_i^{down}\right)}{\left(\frac{1}{\theta_V^{m,up}}-\frac{1}{\theta_V^{m,down}}\right)} \quad \textbf{Eq. 7.68}$$

By introducing Eq. 7.68 into Eq. 7.61, the final expression of flux is:

$$(\boldsymbol{N})=\frac{\rho}{\ell}\frac{[aln\left(\frac{\theta_V^{m,down}}{\theta_V^{m,up}}\right)+(\theta_V^{m,down}-\theta_V^{m,up})]}{\left(\frac{1}{\theta_V^{m,up}}-\frac{1}{\theta_V^{m,down}}\right)}[\boldsymbol{q^{sat}}][\boldsymbol{B}(\boldsymbol{0})]^{-1}\left(\boldsymbol{F^{up}}-\boldsymbol{F^{down}}\right) \quad \textbf{Eq. 7.69}$$

It is interesting to note that the analytical expression for the transmembrane flux of the "hybrid confinement" case is the superposition of the "strong" and "weak" confinement cases ($(\boldsymbol{N})_{\text{hybrid}}$ ranges from $(\boldsymbol{N})_{\text{weak}}$ to $(\boldsymbol{N})_{\text{strong}}$ depending on the pore dimensions).

7.5.4 Summary

In all three cases, the flux expressions without frictional coupling effects between solvent molecules can also be expressed by setting the off-diagonal terms of the inverse diffusivity matrix to 0. As shown later, we will evaluate the severity of frictional effects in CMS membranes separating xylene isomers.

It is important to point out that the flux response in the binary system of equations is phenomenologically consistent with those found in the single-component permeation case. That is, as the transmembrane fugacity increases for the weak and hybrid confinement cases, the fluxes of both components are expected to continue without limit (although practically this will not be observed due to mechanical issues associated with the membrane). Moreover, the binary strong confinement case also suggests that an asymptotic flux with increasing transmembrane fugacity will be observed (i.e., in Eq. 7.4, as the upstream fugacity increases, the fraction of the void spaces in the membrane will decrease).

7.6 Binary OSRO Flux Predictions

The analytical solutions of the Maxwell-Stefan equation can be used in combination with our experimental sorption and diffusion data to predict the flux for osmotically-moderated sorption-diffusion permeation in rigid microporous membranes for the three confinement cases, and these can be compared to experimental flux and separation factor values. To simulate OSRO conditions that have been investigated previously by Ma et al.[29], Figure 7.9 shows the predicted flux of *p*-xylene for xylene isomers mixture (a 90:10 (mol/mol) liquid mixture of *p*-xylene/*o*-xylene feed) with reverse osmosis under different hydraulic feed pressures and 55 °C. “Weak confinement”, “strong confinement” and “hybrid confinement” cases are described by the Maxwell-Stefan-based mathematical expression shown in Eq. 7.47, Eq. 7.57 and Eq. 7.69 respectively. All the parameters for the model prediction can be found in Table 7.2. In all cases, positive flux through the membrane is predicted once the osmotic pressure of the mixture has been overcome (~17 bar).

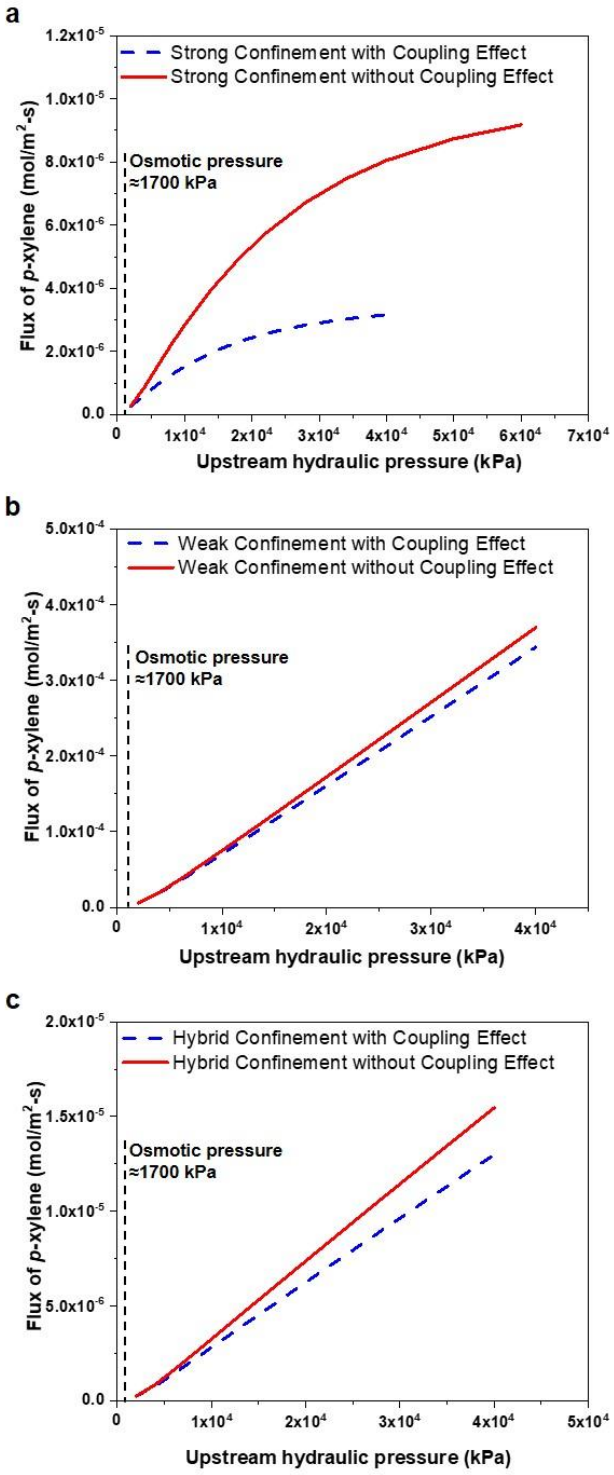

Figure 7.9 Maxwell-Stefan model predictions for *p*-xylene flux with varying upstream with upstream hydraulic pressure for a) "strong confinement" case, b) "weak confinement" case and c) "hybrid confinement" case.

Table 7.2 Parameters for estimation of flux in Figure 7.9 using the Maxwell-Stefan equation for three confinement cases.

Item	Value
Feed mixture	90:10 (mol/mol) liquid mixture of *p*-xylene/*o*-xylene
Testing temperature T	328.15 K
Feed side pressure p^{up}	2000kPa~70000 kPa
Permeate side pressure p^{down}	1 bar, abs=101 kPa
Molar volume of *p*-xylene V_{mi}	123.3 cm^3/mol
Molar volume of *o*-xyleneV_{mj}	120.6 cm^3/mol
Saturation loading q_i^{sat}	$V_p\ /V_m = 0.161\ \frac{cm^3}{g}/123.3\ \frac{cm^3}{mol} = 1.3057\ mmol/g$
Saturation loading q_j^{sat}	$V_p\ /V_m = 0.161\ \frac{cm^3}{g}/120.6\ \frac{cm^3}{mol} = 1.3345\ mmol/g$
Langmuir affinity constant b_i	3.7957 kPa^{-1}
Langmuir affinity constant b_j	3.1919 kPa^{-1}
p-xylene feed compositionx_i^{up}	0.9 mol/mol
o-xylene feed composition x_j^{up}	0.1 mol/mol
Density of CMS membrane ρ	2 g/cm^3
Thickness of the membrane ℓ	300 nm
Saturation pressure of *p*-xylene	$p_{p-xylene}^{sat}\ (328K) = 5.4757\ kPa$
Saturation pressure of *o*-xylene	$p_{0-xylene}^{sat}\ (328K) = 4.3182\ kPa$
"Strong confinement" and "weak confinement" case	
p-xylene Maxwell-Stefan coefficients at infinite dilution $Đ_{i0}$	2.67×10^{-10} cm^2/s
o-xylene Maxwell-Stefan coefficients at infinite dilution $Đ_{j0}$	8.74×10^{-12} cm^2/s
"Hybrid confinement" case	

p-xylene Maxwell-Stefan coefficients at infinite dilution $Đ_{i0}$	2.76×10^{-11} cm^2/s
o-xylene Maxwell-Stefan coefficients at infinite dilution $Đ_{j0}$	7.12×10^{-13} cm^2/s
a	0.383

As shown in Figure 7.9a, in the "strong confinement" case without solvent-solvent coupling effects between *p*-xylene and *o*-xylene molecules, the *p*-xylene flux is expected to increase to an asymptotic value as pressure increases. Although the increase of the feed pressure results in the enhancement of the diffusion driving force (i.e., the fugacity gradient), it also results in a severe decrease of the Maxwell-Stefan diffusivity by decreasing the available vacancies within the membrane. The decrease of the Maxwell-Stefan diffusivity inhibits the further increase of flux under high pressure. When the coupling effect between *p*-xylene and *o*-xylene is considered, the inhibition of the flux increase at high pressure is even more severe.

In both the "weak confinement" and "hybrid confinement" cases (Figure 7.9b and Figure 7.9c, respectively) without solvent-solvent coupling effects between *p*-xylene and *o*-xylene, the *p*-xylene flux increases almost linearly as pressure increases, which is reminiscent of pore-flow-type permeation. However, it is important to note that the expressions derived here are strictly based on loading gradients within the membrane and with sorption-diffusion permeation transport equations.

The predictions from the Maxwell-Stefan model for the *p*-xylene/*o*-xylene separation factors and fluxes were also compared with experimental results as shown in

Figure 7.10-Figure 7.12**,** which illustrates the utility of these flux expressions for predicting both "simple" vapor permeation and osmotically-moderated permeation.

Figure 7.10 shows the comparison of experimental results of an equimolar *p*-xylene/*o*-xylene *vapor* mixture separated by dense CMS_PIM-1_500 °C_4% H_2 membranes measured at 55 °C by a Wicke-Kallenbach test [29] and the results predicted by the Maxwell-Stefan model for the "weak confinement" case (detailed modeling parameters can be found in Table 7.3). The experimental *p*-xylene flux is slightly higher (1.5 times higher in MS mixture case without frictional coupling effects, 3.1 times higher in MS mixture case with frictional coupling effects) than the Maxwell-Stefan model predicted values. It is reasonable to conclude that small, nonselective leak pathways in the permeation system (or in the membrane) are contributing to the experimental flux. The flux predicted by the MS model with coupling effects is observed to be 63.5 % lower than the result predicted by the MS model without coupling effects. That is expected within the generalized Maxwell-Stefan framework, where the frictional coupling effects between rapidly and slowly transporting components are known to reduce the transport rates of the rapidly transporting components (*p*-xylene here). The experimental *p*-xylene/*o*-xylene selectivity falls between the selectivity predicted by the Maxwell-Stefan model with and without considering the coupling effect. The result suggests that selectivity losses in the membrane were not as severe as predicted by the MS mixture case with frictional coupling effects considered. This indicated that the Vignes-type correlation, which was used to estimate the frictional coupling effects here, is not accurately capturing the extent of the frictional coupling.

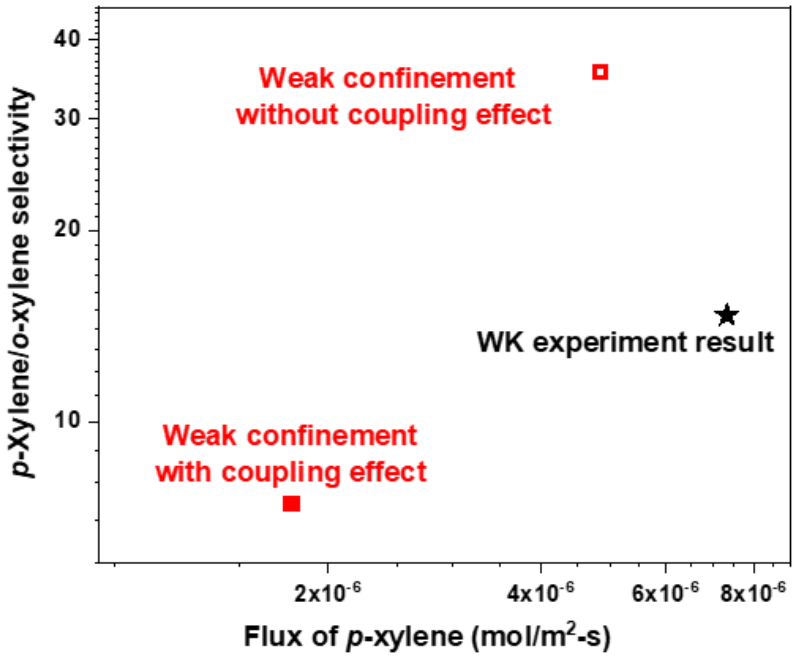

Figure 7.10 The comparison of Maxwell-Stefan predictions of *p*-xylene/*o*-xylene separation factors and flux with experimental results. a) Model: Maxwell-Stefan model for "weak confinement" case with and without frictional coupling effects, Experimental: equimolar *p*-xylene : *o*-xylene mixture separated by dense CMS_PIM-1_500 °C_4% H_2 membranes measured at 55 °C by Wicke-Kallenbach test [29].

Table 7.3. Parameters for estimation of flux and separation factor in Figure 7.10 using the Maxwell-Stefan equation for "weak confinement" case.

Item	Value
Feed mixture	50:50 (mol/mol) vapor mixture of *p*-xylene/*o*-xylene
Testing temperature T	328.15 K
Molar volume of *p*-xylene V_{mi}	123.3 cm^3/mol
Molar volume of *o*-xyleneV_{mj}	120.6 cm^3/mol
Saturation loading q_i^{sat}	$V_p\,/V_m = 0.161\ \frac{cm^3}{g}/123.3\ \frac{cm^3}{mol} = 1.3057\ mmol/g$
Saturation loading q_j^{sat}	$V_p\,/V_m = 0.161\ \frac{cm^3}{g}/120.6\ \frac{cm^3}{mol} = 1.3345\ mmol/g$
Langmuir affinity constant b_i	3.7957 kPa^{-1}
Langmuir affinity constant b_j	3.1919 kPa^{-1}
p-xylene feed pressure p_i^{up}	2.42 kPa
o-xylene feed pressure p_j^{up}	2.42 kPa
p-xylene permeate pressurep_i^{down}	0 kPa
o-xylene permeate pressure p_j^{down}	0 kPa
Density of CMS membrane ρ	2 g/cm^3
Thickness of the membrane ℓ	22.5 μm
Saturation pressure of *p*-xylene	$p_{p-xylene}^{sat}\,(328K) = 5.4757\ kPa$

Saturation pressure of *o*-xylene	$p_{0-xylene}^{sat}\ (328K) = 4.3182\ kPa$
p-xylene Maxwell-Stefan coefficients at infinite dilution $Đ_{i0}$	2.67×10^{-10} cm^2/s
o-xylene Maxwell-Stefan coefficients at infinite dilution $Đ_{j0}$	8.74×10^{-12} cm^2/s

Figure 7.11 shows the comparison of experimental results of equimolar *p*-xylene/*o*-xylene mixtures separated by dense CMS_PIM-1_500 °C_4% H_2 membranes measured at 55 °C by a Wicke-Kallenbach test [30] and the Maxwell-Stefan predictions for the "hybrid confinement" case (detailed modeling parameters can be found in Table 7.4). Similar to the results for dense CMS_PIM-1_500 °C_4% H_2 membranes, dense CMS_PIM-1_500 °C_0% H_2 membranes apparently are affected by small, nonselective leak pathways contributing to the experimental flux. The frictional coupling effects between xylene molecules are not as severe as the prediction by the Vignes-type correlation used in the Maxwell-Stefan model. An alternative explanation of the discrepancy between the Maxwell-Stefan model and the experimental observations is given later in this chapter.

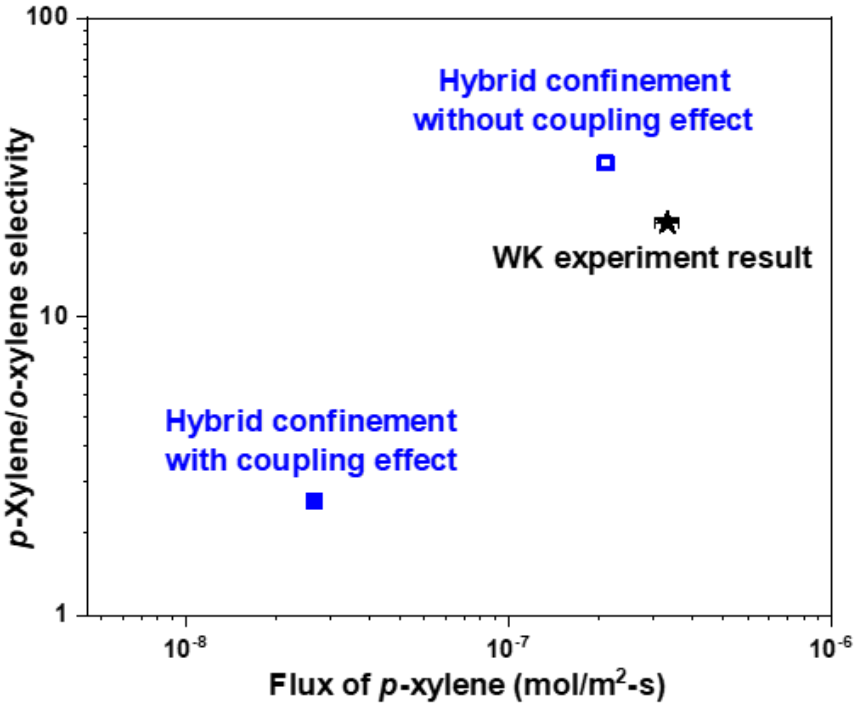

Figure 7.11 The comparison of Maxwell-Stefan predictions of *p*-xylene/*o*-xylene separation factors and flux with experimental results. Model: Maxwell-Stefan model for "hybrid confinement" case with and without frictional coupling effect, Experimental: equimolar *p*-xylene : *o*-xylene mixture separated by dense CMS_PIM-1_500 °C_0% H_2 membranes measured at 55 °C by the Wicke-Kallenbach test.[30]

Table 7.4 Parameters for estimation of flux and separation factor in Figure 7.11 using the Maxwell-Stefan equation for "hybrid confinement" case.

Item	Value
Feed mixture	50:50 (mol/mol) vapor mixture of *p*-xylene/*o*-xylene
Testing temperature T	328.15 K
Molar volume of *p*-xylene V_{mi}	123.3 cm^3/mol
Molar volume of *o*-xyleneV_{mj}	120.6 cm^3/mol
Saturation loading q_i^{sat}	1.1856 mmol/g
Saturation loading q_j^{sat}	1.1056 mmol/g
Langmuir affinity constant b_i	14.1999 kPa^{-1}
Langmuir affinity constant b_j	18.0351 kPa^{-1}
p-xylene feed pressure p_i^{up}	2.42 kPa
o-xylene feed pressure p_j^{up}	2.42 kPa
p-xylene permeate pressurep_i^{down}	0 kPa
o-xylene permeate pressure p_j^{down}	0 kPa
Density of CMS membrane ρ	2 g/cm^3
Thickness of the membrane ℓ	38.2 μm
Saturation pressure of *p*-xylene	$p_{p-xylene}^{sat}\ (328K) = 5.4757\ kPa$
Saturation pressure of *o*-xylene	$p_{0-xylene}^{sat}\ (328K) = 4.3182\ kPa$

p-xylene Maxwell-Stefan coefficients at infinite dilution $Đ_{i0}$	2.76×10^{-11} cm^2/s
o-xylene Maxwell-Stefan coefficients at infinite dilution $Đ_{j0}$	7.12×10^{-13} cm^2/s
a	0.383

Figure 7.12 shows the comparison of experimental OSRO results of a 90:10 (mol/mol) *liquid* mixture of *p*-xylene/*o*-xylene separated by hollow fiber CMS_PIM-1_500 °C_4% H_2 membranes measured at 22 °C [29] and the results predicted by the Maxwell-Stefan model for the "weak confinement" case (detailed modeling parameters can be found in Table 7.5). The experimental *p*-xylene flux is almost 2 orders of magnitude higher than the predicted values from the two models. Moreover, the experimental *p*-xylene/*o*-xylene separation factor is smaller than the predicted one, even with the frictional coupling effect. Both of these factors initially suggest the existence of defects penetrating the thin selective layer (~300 nm). Unlike the essentially isobaric Wicke-Kallenbach system, the OSRO system is also placed under a severe pressure gradient, which can result in substantial flux contributions from nonselective transport pathways; it is difficult to imagine the membranes having any selectivity at all if such pressure-driven defect pathways existed. An alternative explanation for the anomalously high flux centers around the accurate determination of the saturation loading of xylene isomers in the membrane and the diffusion coefficients at these conditions. In this work, we utilized the pore volume of the membrane (determined by N_2 physisorption at 77 K) and the molar volume of the xylene

isomers to estimate the maximum loading of these solvents in the CMS material. However, this assumption may underestimate the amount of xylene isomer sorption at the high pressures experienced during the OSRO separation. Such an underestimation would then lead to an underestimation of the flux. Our current data set and experimental capabilities prevent us from providing a more definitive explanation of the anomalously high flux. Moreover, the diffusion coefficients may change dramatically as the fractional occupancy approaches 1.0 at these high pressure conditions. It is interesting to note that for the same membrane, the vapor permeation separation modality is predicted to achieve much higher separation factors (~35) than the OSRO case (~7), while the OSRO case is expected to have 10-30 times higher flux.

The separation performance of the CMS_PIM-SBF_500 °C_4% H_2 membranes in the OSRO mode is also predicted using the Maxwell-Stefan model for the "weak confinement" case as shown in Figure 7.12 (detailed modeling parameters can be found in Table 7.6). The model predicted *p*-xylene flux for CMS_PIM-SBF_500 °C_4% H_2 is roughly 15 times higher than the model predicted value for CMS_PIM-1_500 °C_4% H_2, assuming that these two kinds of hollow fiber membranes share the same selective layer thickness (300 nm) and the OSRO tests are conducted under the same upstream (6100 kPa), downstream pressure (101 kPa) and a 90:10 (mol/mol) liquid mixture of p-xylene/o-xylene feed. The significant increase of flux is contributed by the increased diffusivity and sorption factor. The model predicted separation factor between *p*-xylene and *o*-xylene for CMS_PIM-SBF_500 °C_4% H_2 is lower than the model predicted separation factor for CMS_PIM-1_500 °C_4% H_2 (5.2 vs .8.2 for the model without considering coupling effect, 4.4 vs. 6.9 for the model without considering coupling effect). This result suggests the

trade-off between flux and separation factor for the CMS type materials. However, conducting experimental OSRO measurements with real CMS_PIM-SBF_500 °C_4% H_2 hollow fiber membranes is recommended for future work.

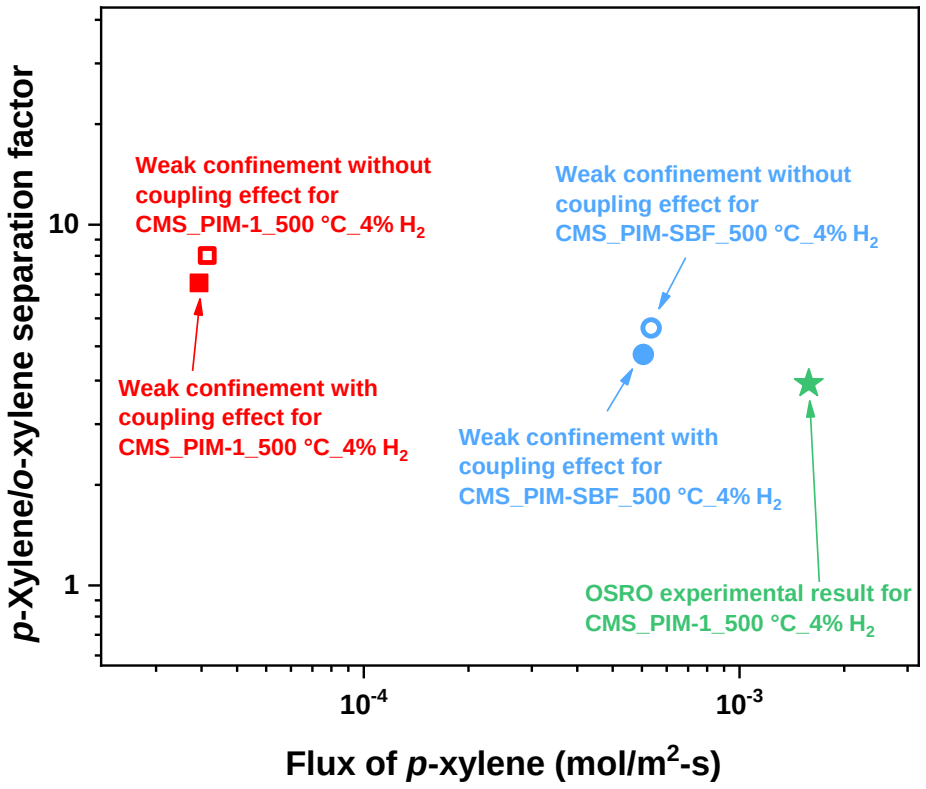

Figure 7.12 The comparison of Maxwell-Stefan predictions of *p*-xylene/*o*-xylene separation factors and flux with experimental results. Model: Maxwell-Stefan model for "weak confinement" case with and without considering frictional coupling effect, Experimental: a 90:10 (mol/mol) liquid mixture of *p*-xylene : *o*-xylene separated by hollow fiber CMS_500 °C_4% H_2 membranes measured at 22 °C by OSRO test [29] Model (square): Maxwell-Stefan model for "weak confinement" case with and without considering frictional coupling effect using single component sorption and diffusion data for CMS_PIM-1_500 °C_4% H_2 sample, Model (circle): Maxwell-Stefan model for "weak confinement" case with and without considering frictional coupling effect using single component sorption and diffusion data for CMS_PIM-SBF_500 °C_4% H_2 sample.

Table 7.5 Parameters for estimation of flux and separation factor through CMS_PIM-1_500 °C_4% H_2 membranes in Figure 7.12 using the Maxwell-Stefan equation for "weak confinement" case.

Item	Value
Feed mixture	90:10 (mol/mol) liquid mixture of *p*-xylene/*o*-xylene
Testing temperature T	328.15 K
Feed side pressure pup	6100 kPa
Permeate side pressure pdown	1 bar, abs=101 kPa
Molar volume of *p*-xylene V_{mi}	123.3 cm^3/mol
Molar volume of *o*-xyleneV_{mj}	120.6 cm^3/mol
Saturation loading q_i^{sat}	$V_p\ /V_m = 0.161\ \frac{cm^3}{g} / 123.3\ \frac{cm^3}{mol} = 1.3057\ mmol/g$
Saturation loading q_j^{sat}	$V_p\ /V_m = 0.161\ \frac{cm^3}{g} / 120.6\ \frac{cm^3}{mol} = 1.3345\ mmol/g$
Langmuir affinity constant b_i	3.7957 kPa^{-1}
Langmuir affinity constant b_j	3.1919 kPa^{-1}
p-xylene feed compositionx_i^{up}	0.9 mol/mol
o-xylene feed composition x_j^{up}	0.1 mol/mol
Density of CMS membrane ρ	2 g/cm^3
Thickness of the membrane ℓ	300 nm
Saturation pressure of *p*-xylene	$p_{p-xylene}^{sat}\ (328K) = 5.4757\ kPa$

Saturation pressure of *o*-xylene	$p_{0-xylene}^{sat}\ (328K) = 4.3182\ kPa$
p-xylene Maxwell-Stefan coefficients at infinite dilution $Đ_{i0}$	2.67×10^{-10} cm^2/s
o-xylene Maxwell-Stefan coefficients at infinite dilution $Đ_{j0}$	8.74×10^{-12} cm^2/s

Table 7.6. Parameters for estimation of flux and separation factor through CMS_PIM-SBF_500 °C_4% H_2 membranes in Figure 7.12 using the Maxwell-Stefan equation for "weak confinement" case.

Item	Value
Feed mixture	90:10 (mol/mol) liquid mixture of *p*-xylene/*o*-xylene
Testing temperature T	328.15 K
Feed side pressure pup	6100 kPa
Permeate side pressure pdown	1 bar, abs=101 kPa
Molar volume of *p*-xylene V_{mi}	123.3 cm^3/mol
Molar volume of *o*-xyleneV_{mj}	120.6 cm^3/mol
Saturation loading q_i^{sat}	$V_p\ /V_m = 0.380\ \frac{cm^3}{g}/123.3\ \frac{cm^3}{mol} = 3.0819\ mmol/g$
Saturation loading q_j^{sat}	$V_p\ /V_m = 0.380\ \frac{cm^3}{g}/120.6\ \frac{cm^3}{mol} = 3.1509\ mmol/g$
Langmuir affinity constant b_i	5.0251 kPa^{-1}

Langmuir affinity constant b_j	4.8675 kPa^{-1}
p-xylene feed compositionx_i^{up}	0.9 mol/mol
o-xylene feed composition x_j^{up}	0.1 mol/mol
Density of CMS membrane ρ	2 g/cm^3
Thickness of the membrane ℓ	300 nm
Saturation pressure of *p*-xylene	$p_{p-xylene}^{sat}\ (328K) = 5.4757\ kPa$
Saturation pressure of *o*-xylene	$p_{0-xylene}^{sat}\ (328K) = 4.3182\ kPa$
p-xylene Maxwell-Stefan coefficients at infinite dilution $Đ_{i0}$	1.64×10^{-9} cm^2/s
o-xylene Maxwell-Stefan coefficients at infinite dilution $Đ_{j0}$	1.12×10^{-10} cm^2/s

7.7 Summary and Conclusions

In summary, the fractional occupancy gradient of penetrant molecules within the micropores of the membrane is considered as the driving force for permeation without requiring knowledge regarding the pressure within the membrane. We discuss a new "hybrid confinement" diffusion regime, which captures the special case of xylene isomers diffusing in bimodal microporous systems. The origin of this hybrid confinement is hypothesized to derive from the nonspheroidal nature of the xylene isomers; however, our current experiments are unable to definitively support this physical picture. Moreover, our current formulation for the loading dependence of the "hybrid confinement" is somewhat ad hoc, and this formulation can certainly be improved upon. Interestingly, we find that

entropic diffusion selectivities can exist even in cases where the Maxwell-Stefan diffusion coefficients are not strongly dependent on the loading. The analytical solutions of the Fickian equations and Maxwell-Stefan equations were developed to predict the flux for osmotically-moderated sorption-diffusion transport in rigid microporous membranes for the three confinement cases. The derived analytical solutions enable the estimation of the membrane performance operated in an osmotically-moderated manner and can be easily incorporated into the design procedures for membrane separation devices in both liquid and vapor systems. In general, these expressions are not only practically important, but also fundamentally valuable in understanding the osmotically-moderated sorption-diffusion transport of solvent molecules through rigid microporous membranes.

7.8 Nomenclature

Subscripts or Superscripts

$i, j, 1, 2$	Component $i, j, 1$ or 2
V	Vacancy
up	Upstream face of the membrane
$down$	Downstream face of the membrane
m	Membrane
fl	Liquid phase

Nomenclature

a	Ratio of $Đ_{i,\infty}$ / $Đ_{i,0}$.	-
b_i	Langmuir affinity constant	kPa^{-1}
$[\boldsymbol{B}]$	Square matrix of inverse Maxwell-Stefan diffusivity	$m^{-2}\,s$
$[\boldsymbol{B}(\boldsymbol{0})]$	Square matrix of inverse Maxwell-Stefan diffusivity at	$m^{-2}\,s$
d^{weak}	Fraction of the pore volume that operates in the weak	-
d^{strong}	Fraction of the pore volume that operates in the strong	-
D_i	Transport diffusivity	m^2/s
$Đ_i$	Maxwell-Stefan diffusivity	m^2/s
$Đ_{i,0}$	Maxwell-Stefan diffusivity at infinite dilution	m^2/s
$Đ_{i,\infty}$	Maxwell-Stefan diffusivity at saturated loading conditions	m^2/s
$Đ_{ij}$	Maxwell-Stefan diffusivity describing interchange	m^2/s
D_{0i}	Pre-exponential factor of diffusion	m^2/s

$E_{D,i}$	Activation energy for diffusion	*J/mol*
f_i^{fl}	Fugacity of component i in the pure liquid phase	*Pa*
f_i^m	Fugacity of component i in the membrane	*Pa*
$\hat{f}_i^{fl}$	Fugacity of component i in the mixture liquid phase	*Pa*
F_i	Dimensionless fugacity	-
f^+	Partition function for a molecule in the ultramicropores	-
$H_{D,i}$	Activation enthalpy for diffusion	*J/mol*
N_i	Flux of component i through membrane	*mol/m^2-s*
p	Pressure	*Pa*
$q(f_i^{fl})$	Loading of guest species under specific fugacity	*mmol/g*
q_i^{sat}	Saturation loading of guest species	*mmol/g*
R	Gas constant	*J/mol-K*
$S_{D,i}$	Activation entropy for diffusion	*J/mol-K*
T	Absolute temperature	*K*
$\bar{V}^m$	Partial mole volume of guest molecule	*cm^3/mol*
x_i	Mol concentration of component i	-
z	Distance coordinate along membrane	*m*

Greek Letters

θ_i	Fractional occupancy of component i	-
θ_V	Fractional vacancy	-
ρ	Density of the membrane	*g/cm^3*

ℓ	Thickness of the membrane	*m*
η	Dimensionless position along membrane	-
F_i	Dimensionless fugacity	-
μ_i	Chemical potential	*J/mol*

7.9 References

1. H. Yasuda, A. Peterlin. Diffusive and bulk flow transport in polymers. *Journal of Applied Polymer Science* **1973**;17(2):433-442.

2. A. Peterlin, H. Yasuda. Comments on the relation between hydraulic permeability and diffusion in homogeneous swollen membranes. *Journal of Polymer Science: Polymer Physics Edition* **1974**;12(6):1215-1220.

3. D. R. Paul, O. Ebra‐Lima. Pressure‐induced diffusion of organic liquids through highly swollen polymer membranes. *Journal of Applied Polymer Science* **1970**;14(9):2201-2224.

4. D. Paul. Diffusive transport in swollen polymer membranes. *Permeability of plastic films and coatings*: Springer; 1974:35-48.

5. D. Paul. Further comments on the relation between hydraulic permeation and diffusion. *Journal of Polymer Science: Polymer Physics Edition* **1974**;12(6):1221-1230.

6. J. G. Wijmans, R. W. Baker. The solution-diffusion model: a review. *Journal of Membrane Science* **1995**;107(1-2):1-21.

7. Y. Ma, F. Zhang, R. P. Lively. Manufacturing Nanoporous Materials for Energy-Efficient Separations: Application and Challenges. *Sustainable Nanoscale Engineering*: Elsevier; 2020:33-81.

8. S. Li, J. G. Martinek, J. L. Falconer, R. D. Noble, T. Q. Gardner. High-pressure CO2/CH4 separation using SAPO-34 membranes. *Industrial & Engineering Chemistry Research* **2005**;44(9):3220-3228.

9. W. Zhu, P. Hrabanek, L. Gora, F. Kapteijn, J. A. Moulijn. Role of adsorption in the permeation of CH4 and CO2 through a silicalite-1 membrane. *Industrial & Engineering Chemistry Research* **2006**;45(2):767-776.

10. H. Jobic, N. Laloué, C. Laroche, J. Van Baten, R. Krishna. Influence of isotherm inflection on the loading dependence of the diffusivities of n-hexane and n-heptane in MFI zeolite. Quasi-elastic neutron scattering experiments supplemented by molecular simulations. *The Journal of Physical Chemistry B* **2006**;110(5):2195-2201.

11. G. K. Papadopoulos, H. Jobic, D. N. Theodorou. Transport diffusivity of N2 and CO2 in silicalite: coherent quasielastic neutron scattering measurements and molecular dynamics simulations. *The Journal of Physical Chemistry B* **2004**;108(34):12748-12756.

12. S.-S. Chong, H. Jobic, M. Plazanet, D. S. Sholl. Concentration dependence of transport diffusion of ethane in silicalite: A comparison between neutron scattering experiments and atomically detailed simulations. *Chemical Physics Letters* **2005**;408(1-3):157-161.

13. H. Jobic, J. Kärger, M. Bee. Simultaneous measurement of self-and transport diffusivities in zeolites. *Physical Review Letters* **1999**;82(21):4260.

14. A. I. Skoulidas, D. S. Sholl. Molecular dynamics simulations of self-diffusivities, corrected diffusivities, and transport diffusivities of light gases in four silica zeolites to assess influences of pore shape and connectivity. *The Journal of Physical Chemistry A* **2003**;107(47):10132-10141.

15. S. Chempath, R. Krishna, R. Q. Snurr. Nonequilibrium molecular dynamics simulations of diffusion of binary mixtures containing short n-alkanes in faujasite. *The Journal of Physical Chemistry B* **2004**;108(35):13481-13491.

16. R. Krishna, J. Van Baten. Diffusion of alkane mixtures in zeolites: Validating the Maxwell− Stefan formulation using MD simulations. *The Journal of Physical Chemistry B* **2005**;109(13):6386-6396.

17. J. Van Baten, R. Krishna. Entropy effects in adsorption and diffusion of alkane isomers in mordenite: An investigation using CBMC and MD simulations. *Microporous and Mesoporous Materials* **2005**;84(1-3):179-191.

18. J. Wijmans. The role of permeant molar volume in the solution-diffusion model transport equations. *Journal of Membrane Science* **2004**;237(1-2):39-50.

19. S. Lagorsse, F. Magalhaes, A. Mendes. Carbon molecular sieve membranes: Sorption, kinetic and structural characterization. *Journal of Membrane Science* **2004**;241(2):275-287.

20. X. Ning, W. J. Koros. Carbon molecular sieve membranes derived from Matrimid® polyimide for nitrogen/methane separation. *Carbon* **2014**;66:511-522.

21. J. Adams, N. Bighane, W. J. Koros. Pore morphology and temperature dependence of gas transport properties of silica membranes derived from oxidative thermolysis of polydimethylsiloxane. *Journal of Membrane Science* **2017**;524:585-595.

22. A. I. Skoulidas, D. S. Sholl, R. Krishna. Correlation effects in diffusion of CH4/CF4 mixtures in MFI zeolite. A study linking MD simulations with the Maxwell− Stefan formulation. *Langmuir* **2003**;19(19):7977-7988.

23. S. Keskin. Adsorption, diffusion, and separation of CH4/H2 mixtures in covalent organic frameworks: molecular simulations and theoretical predictions. *The Journal of Physical Chemistry C* **2012**;116(2):1772-1779.

24. R. Krishna, R. Baur. Modelling issues in zeolite based separation processes. *Separation and Purification Technology* **2003**;33(3):213-254.

25. R. Krishna, R. Baur. Analytic solution of the Maxwell–Stefan equations for multicomponent permeation across a zeolite membrane. *Chemical Engineering Journal* **2004**;97(1):37-45.

26. A. I. Skoulidas, D. S. Sholl. Direct tests of the Darken approximation for molecular diffusion in zeolites using equilibrium molecular dynamics. *The Journal of Physical Chemistry B* **2001**;105(16):3151-3154.

27. A. I. Skoulidas, D. S. Sholl. Transport diffusivities of CH4, CF4, He, Ne, Ar, Xe, and SF6 in silicalite from atomistic simulations. *The Journal of Physical Chemistry B* **2002**;106(19):5058-5067.

28. D. Paschek, R. Krishna. Monte Carlo simulations of self-and transport-diffusivities of 2-methylhexane in silicalite. *Physical Chemistry Chemical Physics* **2000**;2(10):2389-2394.

29. Y. Ma, M. L. Jue, F. Zhang, R. Mathias, H. Y. Jang, R. Lively. Creation of well‐defined “mid‐sized” micropores in carbon molecular sieve membranes. *Angewandte Chemie International Edition*.

30. Y. Ma, F. Zhang, S. Yang, R. P. Lively. Evidence for entropic diffusion selection of xylene isomers in carbon molecular sieve membranes. *Journal of Membrane Science* **2018**;564:404-414.

31. C. Ma, J. J. Urban. Polymers of Intrinsic Microporosity (PIMs) Gas Separation Membranes: A mini Review.

32. R. Krishna. Using the Maxwell-Stefan formulation for highlighting the influence of interspecies (1− 2) friction on binary mixture permeation across microporous and polymeric membranes. *Journal of Membrane Science* **2017**;540:261-276.

33. R. B. Bird, W. E. Stewart, E. N. Lightfoot. *Transport phenomena*: John Wiley & Sons; **2006**.

34. F. Kapteijn, J. Moulijn, R. Krishna. The generalized Maxwell–Stefan model for diffusion in zeolites:: sorbate molecules with different saturation loadings. *Chemical Engineering Science* **2000**;55(15):2923-2930.

CHAPTER 8. CONCLUSIONS AND FUTURE DIRECTIONS

8.1 Dissertation Overview

This dissertation focused on the creation of CMS membranes for xylene isomer separations. Polymers of intrinsic microporosity were synthesized and fabricated into membranes of different morphologies and then pyrolyzed into carbon molecular sieve membranes. These CMS membranes exhibited outstanding xylene isomer separation performance. Mass transfer and thermodynamic analysis reveal that the entropic diffusion selection of xylene isomers contributes to the outstanding molecular sieving performance. Besides, this thesis also thoroughly investigated the influence of the pyrolysis atmosphere on the CMS formation and the flux equations for osmotically-moderated sorption-diffusion transport in rigid microporous membranes [1,2].

8.2 Summary and Conclusions

8.2.1 Chapter summaries

Xylene isomers are important chemical feedstocks for the modern chemical industry. Owing to similar physical properties, xylene isomers are difficult to separate. Membrane-based organic solvent reverse osmosis differentiates xylene molecules based on their sub-Angstrom size difference, which provides an energy-efficient approach to xylene isomer separations. Successful OSRO relies on high-performance membranes, the development of which is challenging and important.

This thesis starts with the background introduction in Chapter 1, which includes the importance of organic separation, xylene separation techniques, and alternative membrane-based xylene separation techniques. In Chapter 2, the background knowledge about xylene separation membrane materials and mass transfer theory in the membrane were discussed in detail. The materials and experimental methods were included in Chapter 3.

In Chapter 4, CMS membranes derived from PIM-1 membranes were utilized for xylene isomer separation. The fundamental sorption and diffusion data were obtained via organic vapor sorption experiments. The thermodynamic analysis was conducted to explain the high *p*/*o*-xylene selectivity. Significant entropic diffusion selectivity was observed in favor of *p*-xylene over *o*-xylene, and this is attributed to the relatively tight "slit-shaped" micropore structure in the carbon membrane, which effectively limits more conformational states of the less symmetric *o*-xylene during its diffusive jump through an ultramicropores when compared to the more symmetric *p*-xylene [3]. For the first time, this study provides solid evidence for the significance of entropic diffusion selectivity of non-gaseous molecules in carbon membranes.

In Chapter 5, hydrogen was introduced into the pyrolysis atmosphere to manipulate the CMS formation process. The introduction of hydrogen significantly enlarged the ultramicropores in the resulting CMS. CMS membranes with well-defined "mid-sized" micropores were successfully created. The H_2-assisted CMS membranes reveal good *p*-xylene/*o*-xylene separation with a significant increase in *p*-xylene permeability of $6.0\times10^{-14}\ mol\ m/m^2\ s\ Pa$) and a *p*-xylene/*o*-xylene selectivity of 14.7 for equimolar mixture tests. Moreover, the hollow fiber CMS membranes, fabricated under 4% H_2/Ar show a *p*-

xylene permeance of $5.2\times10^{-10}\ mol/m^2\ s\ Pa$ and a high activity vapor mixture permselectivity of 8.9 based on WK measurements and a *p*-xylene hydraulic permeance of $2.6\times10^{-10}\ mol/m^2\ s\ Pa$ and a separation factor of 3.7 based on OSRO tests. Continued refinements of the pyrolysis atmosphere, protocol, and polymer precursors have the potential to make CMS membranes perform comparably with MFI for high activity solvent vapor separations [4,5]. Moreover, the hollow fiber CMS materials enable energy-efficient liquid phase osmotically-moderated separations that generally have much higher product fluxes and lower separation factors than MFI operating in vapor separation modalities.

In Chapter 6, PIM-SBF was used as the polymeric precursor for CMS membrane fabrication. Owing to the special polymer backbones, the resulting CMS membranes contain more "mid-sized" ultramicropores compared with PIM-1 derived CMS membranes. Permeation experiments reveal that the CMS membranes derived from PIM-SBF exhibit significantly increased xylene permeability with an acceptable sacrifice of selectivity. Moreover, it is feasible to fabricate CMS membranes with suitable micropore structure for xylene isomer separations using the PIM-SBF as precursors under the pure argon pyrolysis environment, which avoids the use of combustible gases (e.g., H_2) and simplifies the overall membrane fabrication process.

In Chapter 7, the fractional occupancy gradient of penetrant molecules within the micropores of the membrane is considered as the driving force for permeation without requiring knowledge regarding the pressure within the membrane. Depending on the pore structure of the CMS membranes, the interaction between the guest molecules and CMS membrane can be significantly influenced. Molecular modeling results available in the

literature and experimental data obtained from CMS membranes showcase that these loading-dependent changes in the Maxwell-Stefan diffusivity are possible. This loading dependence is separated into three regimes: so-called “weak confinement” diffusion and “strong confinement” diffusion, both of which have been discussed at length in the literature, and a new “hybrid confinement” diffusion [6]. The analytical solutions of the Fickian equations and Maxwell-Stefan equations were developed to predict the flux for osmotically-moderated sorption-diffusion transport in rigid microporous membranes for the three confinement cases. The derived analytical solutions enable the estimation of the membrane performance operated in an osmotically-moderated manner and can be easily incorporated into the design procedures for membrane separation devices in both liquid and vapor systems.

8.2.2 Conclusions and Impacts

Carbon molecular sieve membranes are derived from polymers of intrinsic microporosity. The pore size distributions of the CMS membranes were manipulated to separate xylene isomers. The resulting CMS membranes exhibited good separation performance when both permeability and separation factors are considered. The guest molecule diffusion process was analyzed. It is shown that the entropy difference of the transition states of different xylene molecules results in the high xylene isomer selectivity. This thesis investigated the influence of reactive components in the pyrolysis atmosphere to the resulting CMS structure, which provides a general strategy for the creation of “mid-sized” CMS materials. The flux equations for the osmotically-moderated sorption-

diffusion model also provides insights into the mass transfer within CMS and a reliable tool for process optimization.

8.3 Future Directions

8.3.1 CMS membranes derived from new PIM polymers

Separation of xylene isomers requires well-defined "mid-size" micropores (e.g., 5-9 Å). By introducing intrinsic ultramicropores into the polymer precursor and conducting pyrolysis under a hydrogen environment, PIM-1-derived-CMS with "mid-size" micropores can be created. Classical PIMs consists of the twisted and conjugated polymer backbone, which spatially disperses the organic components and resulting in porous CMS structures during pyrolysis. The twisted and conjugated polymer backbone significantly impacts the processability of PIM-1.

PIM-Duckys (synthesized and provided by Dr. Nicholas Bruno from the Finn Group in the School of Chemistry and Biochemistry at Georgia Institute of Technology) refer to a series of polymers with linear twisted backbones with relatively flexible linkage (e.g., PIM-Ducky-9, as shown in Figure 8.1). Compared with classical PIMs (e.g., PIM-1), PIM-Duckys feature flexible polymer backbones, which significantly improve their processability. While the conjugated spirobisindane are spatially dispersed, PIM-Duckys do not contain a high population of interconnected micropores owing to the free rotation of the flexible linkage. However, PIM-Duckys can be excellent polymer precursors for CMS membranes. During pyrolysis, the unstable, flexible linkage degrades and the rearrangement of the spatially separated spirobisindane units results in porous CMS.

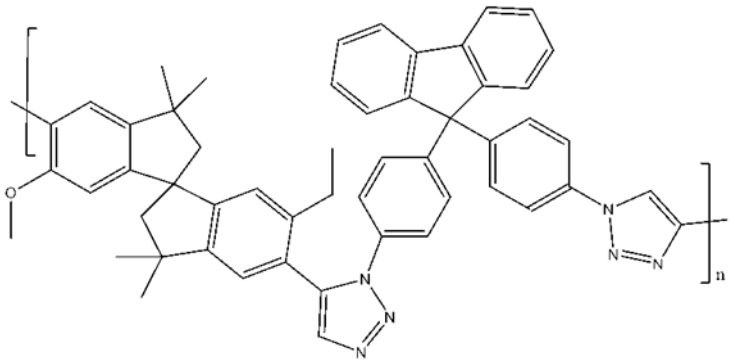

Figure 8.1 Chemical structure of PIM-Ducky-9 polymer precursor.

PIM-Ducky-9 was pyrolyzed into CMS under a hydrogen-included atmosphere. After pyrolysis, the CMS derived from PIM-Ducky-9 exhibits a BET surface area of 239 m^2/g and a pore volume of 0.110 cm^3/g. By applying the 2D-NLDFT model, the pore size distribution is obtained, as shown in Figure 8.2. The abundant micropores suggest promising organic solvent separation performance. Preliminary results are encouraging, and it is speculated that the impact of pyrolysis conditions and the separation performance of PIM-Ducky-derived CMS membranes are all important areas for future investigations.

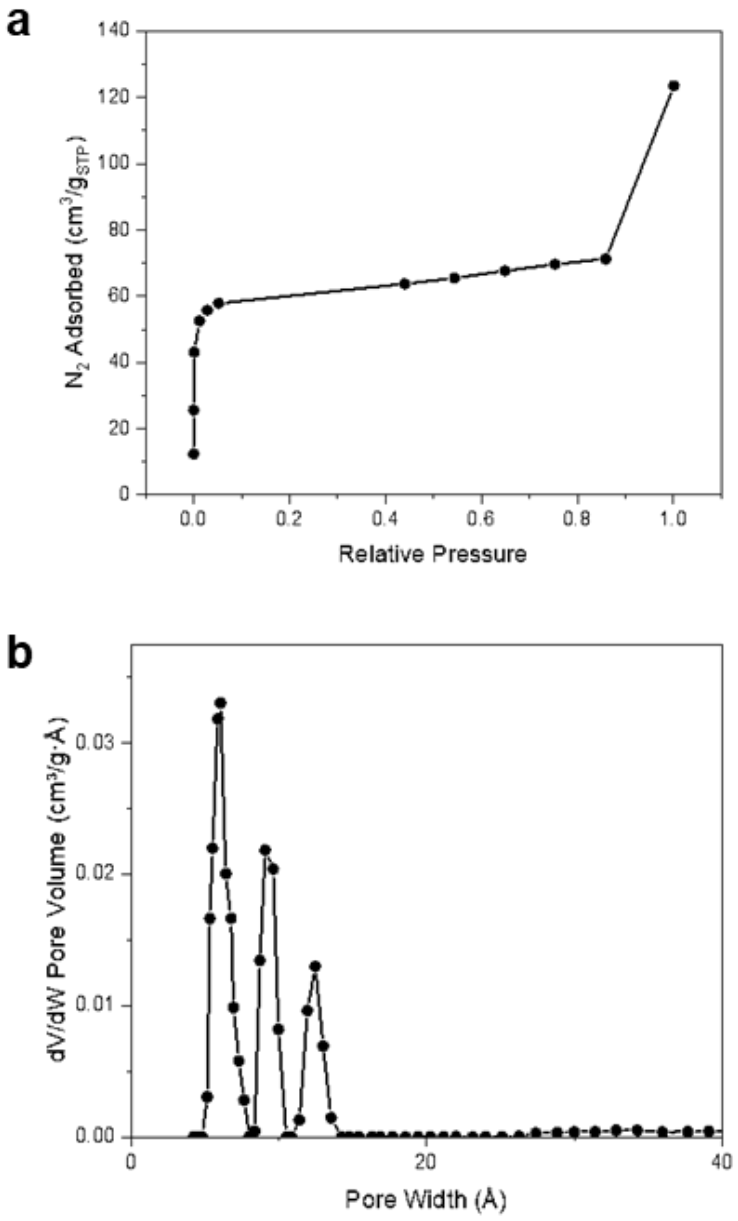

Figure 8.2 CMS derived from PIM-Ducky-9. (a) Nitrogen physisorption at 77 K for PIM-Ducky-9-derived CMS fabricated at 500 °C and 4 % H_2/Ar. (b) Pore size distribution measured by nitrogen physisorption at 77 K for PIM-Ducky-9-derived CMS fabricated at 500 °C and 4 % H_2/Ar.

8.3.2 CMS membranes derived from organic-inorganic hybrid films

Vapor phase infiltration is a technique that can be used to stabilize microporous polymers. By infiltrating the microporous polymer with nanoporous inorganic strands, the stability of the composite material can be significantly improved. It has been demonstrated that the AlO_x/PIM-1 hybrid membrane fabricated via vapor phase infiltration exhibits outstanding organic solvent separation performance [7]. The infiltrated AlO_x networks successfully reinforced the pore structures of PIM-1. Inspired by that, AlO_x/PIM-1 can be used as the precursor for CMS membrane fabrication. During the pyrolysis, the infiltrated AlOx network is expected to retain the pore structure of PIM-1.

As shown in Figure 8.3, the CMS membranes derived from AlO_x/PIM-1 possess abundant micropores even after the pyrolysis under a pure Ar environment and a very high temperature (e.g., 1100 ℃). As a comparison, CMS derived from pristine PIM-1 exhibits no detectable porosity after 500 ℃ pyrolysis (see Chapter 4). In addition to the above promising preliminary results, the pyrolysis mechanism and the permeation behaviors are all interesting research directions.

It is worth noting that Pinnau and coworkers have also infiltrated with PIM-polyimide precursors with Al_2O_3 prior to pyrolysis [8]. According to the gas permeation result, the infiltrated Al_2O_3 occupies the pores within the resulting CMS membrane instead of enlarging the pores. The different phenomena may be attributed to the difference in Al_2O_3 contents. The relatively low Al_2O_3 content (7.7%) suggests that the Al_2O_3 reside in the polymer as isolated oligomers instead of interconnected networks, which is necessary to prevent the collapse of micropores during pyrolysis.

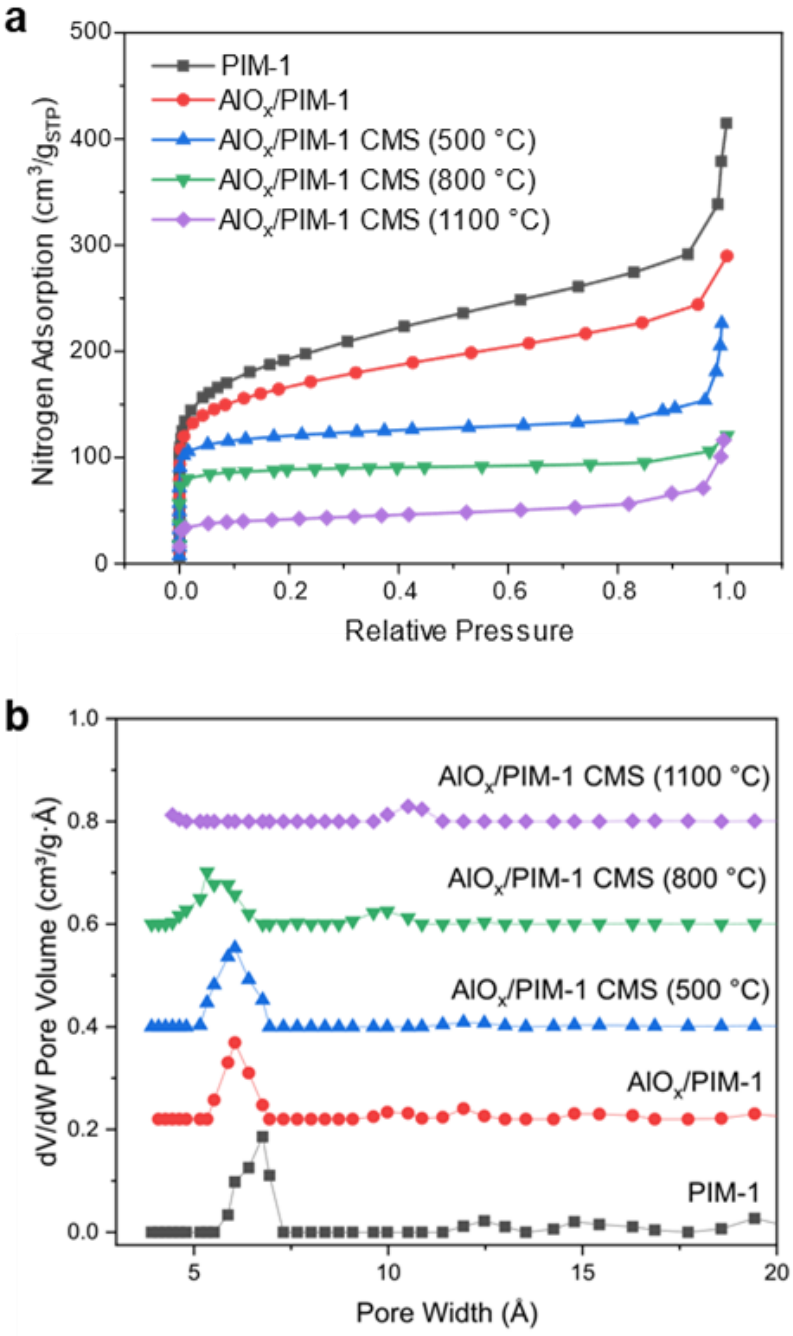

Figure 8.3 Nitrogen physisorption at 77 K (a) and the corresponding pore size distribution (b) for PIM-1, AlOx/PIM-1, and AlOx/PIM-1 derived CMS fabricated at a pure argon environment and different pyrolysis temperature.

8.3.3 Investigation of the physical aging in CMS membranes

Although carbon molecular sieves are inert to most chemicals except oxygen, the packing structure of carbon sheets can still be altered in different conditions. Like most disordered materials, carbon molecular sieve membranes can undergo the problem of physical aging or chemical aging. The latter case may be caused by either chemisorption of oxygen, or physical adsorption of water and organics in the pore structures [9-12]. The former case can occur due to slow rearrangements of imperfectly stacked carbon plates seeking thermodynamically more stable states, which result in the loss of micropores and the decrease of the permeability through CMS membranes. Fortunately, the physical aging problem of the CMS membrane can be effectively inhibited. For example, the performance of the CMS membrane for CO_2/CH_4 separation remains stable if the membranes are can be stored under a 100 psig CO_2 environment [13].

While the physical aging of CMS in gaseous and moisture environment has been investigated, the. microvoids inside CMS structure are generally hydrophobic [9], which means that they tend to adsorb organics. Investigating and controlling the physical aging of CMS membranes in different environment is required to maintain their outstanding separation performance.

8.3.4 Scale-up pf CMS membranes fabrication

For materials prepared by special routes, equipment investment should also be considered. For instance, CMS hollow fiber membranes derived from polymers can be handled without expensive substrates; however, pyrolysis furnaces with inert gas purging or vacuum are required [14,15]. Compared with polymeric membranes, the cost of CMS

membranes per unit area is likely to be 2 to 3 times higher due to the difficulty of scaling up to rapid production rates for modules [16,17]. This high investment cost makes CMS membranes more attractive only when they can achieve a much better performance than polymeric membranes.

A new continuous CMS membrane fabrication strategy is proposed, as shown in Figure 8.4. The CMS fabrication starts with a hollow fiber spinning process. The polymeric hollow fiber membrane precursor is firstly fabricated via dry-wet hollow fiber spinning. The multicomponent polymer solution is transformed into hollow fiber membranes with an integrated selective layer of nanometer thickness. After the solvent exchange process, the fresh hollow fiber membranes are pyrolyzed by a continuously running furnace. The resulting CMS membranes can then be assembled into membrane modules.

In this optimized CMS fabrication process, the efficiency improvement results from the elimination of the polymer crosslinking and the replacement of the batch pyrolysis process with a continuous one. First, the polymer precursor is specially designed with a rigid polymer backbone such that the glass transition temperature (~442 °C) of PIM-1 exceeds the pyrolytic decomposition temperature (~400 °C) [18], which suggests that PIM-1 should be resistant to morphological collapse during thermal treatments. Second, the multi-section furnace can be modified to conduct roll-to-roll hollow fiber membrane pyrolysis in an isolated environment, although special attention will need to be given to the inlets and outlets of the furnace to ensure that oxygen does not leak into the system. In the future, more research is required to develop suitable polymer precursor materials and safe, scalable pyrolysis equipment.

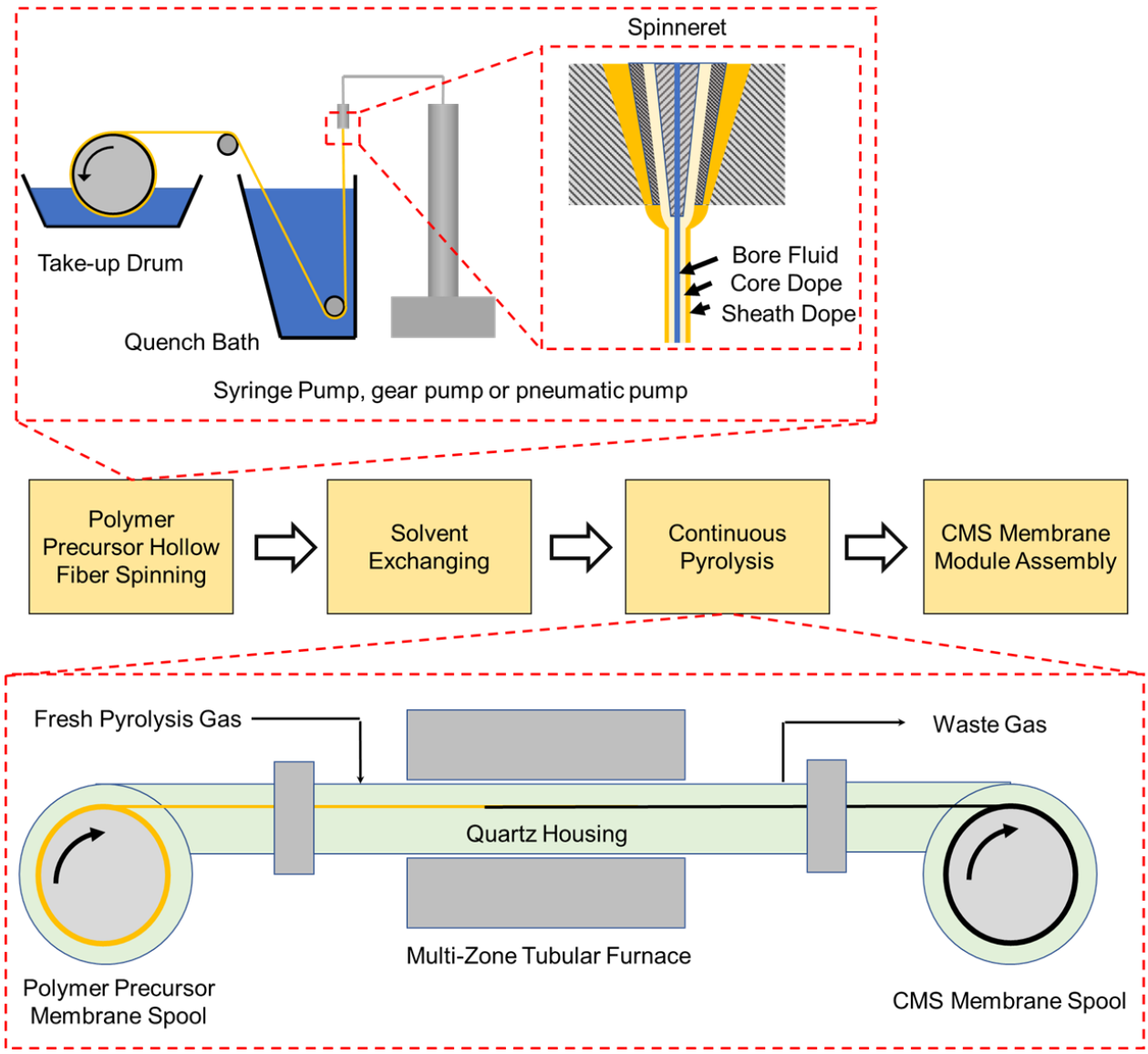

Figure 8.4 The proposed continuous CMS membrane fabrication strategy.

8.4 References

1. Y. Ma, F. Zhang, H. W. Deckman, W. J. Koros, R. P. Lively. Flux equations for osmotically-moderated sorption-diffusion transport in rigid microporous membranes. *Industrial & Engineering Chemistry Research* **2019**.

2. Y. Ma, M. L. Jue, F. Zhang, R. Mathias, H. Y. Jang, R. P. Lively. Creation of well‐defined "mid‐sized" micropores in carbon molecular sieve membranes. *Angewandte Chemie* **2019**;131(38):13393-13399.

3. Y. Ma, F. Zhang, S. Yang, R. P. Lively. Evidence for entropic diffusion selection of xylene isomers in carbon molecular sieve membranes. *Journal of Membrane Science* **2018**;564:404-414.

4. J. Hedlund, J. Sterte, M. Anthonis, A.-J. Bons, B. Carstensen, N. Corcoran, D. Cox, H. Deckman, W. De Gijnst, P.-P. de Moor. High-flux MFI membranes. *Microporous and Mesoporous Materials* **2002**;52(3):179-189.

5. Z. Lai, G. Bonilla, I. Diaz, J. G. Nery, K. Sujaoti, M. A. Amat, E. Kokkoli, O. Terasaki, R. W. Thompson, M. Tsapatsis. Microstructural optimization of a zeolite membrane for organic vapor separation. *Science* **2003**;300(5618):456-460.

6. Y. Ma, F. Zhang, H. W. Deckman, W. J. Koros, R. P. Lively. Flux Equations for Osmotically Moderated Sorption–Diffusion Transport in Rigid Microporous Membranes. *Industrial & Engineering Chemistry Research* **2019**.

7. E. K. McGuinness, F. Zhang, Y. Ma, R. P. Lively, M. D. Losego. Vapor phase infiltration of metal oxides into nanoporous polymers for organic solvent separation membranes. *Chemistry of Materials* **2019**;31(15):5509-5518.

8. W. Ogieglo, T. Puspasari, M. K. Hota, N. Wehbe, H. N. Alshareef, I. Pinnau. Nanohybrid thin-film composite carbon molecular sieve membranes. *Materials Today Nano* **2020**;9:100065.

9. L. Xu, M. Rungta, J. Hessler, W. Qiu, M. Brayden, M. Martinez, G. Barbay, W. J. Koros. Physical aging in carbon molecular sieve membranes. *Carbon* **2014**;80:155-166.

10. S. Lagorsse, F. Magalhaes, A. Mendes. Aging study of carbon molecular sieve membranes. *Journal of Membrane Science* **2008**;310(1-2):494-502.

11. M. G. Kamath, S. Fu, A. K. Itta, W. Qiu, G. Liu, R. Swaidan, W. J. Koros. 6FDA-DETDA: DABE polyimide-derived carbon molecular sieve hollow fiber membranes: Circumventing unusual aging phenomena. *Journal of Membrane Science* **2018**;546:197-205.

12. S. S. Hays, O. Sanyal, N. E. León, P. Arab, W. J. Koros. Envisioned role of slit bypass pores in physical aging of carbon molecular sieve membranes. *Carbon* **2020**;157:385-394.

13. G. B. Wenz. *Tuning Carbon Molecular Sieve Membrane Performance for Challenging Gas Separations*, Georgia Institute of Technology; **2017**.

14. D.-Y. Koh, B. A. McCool, H. W. Deckman, R. P. Lively. Reverse osmosis molecular differentiation of organic liquids using carbon molecular sieve membranes. *Science* **2016**;353(6301):804-807.

15. O. Karvan, J. R. Johnson, P. J. Williams, W. J. Koros. A pilot‐scale system for carbon molecular sieve hollow fiber membrane manufacturing. *Chemical Engineering & Technology* **2013**;36(1):53-61.

16. N. W. Ockwig, T. M. Nenoff. Membranes for hydrogen separation. *Chemical Reviews* **2007**;107(10):4078-4110.

17. P. J. Williams, W. J. Koros. Gas separation by carbon membranes. *Advanced membrane technology and applications* **2008**:599-631.

18. H. Yin, Y. Z. Chua, B. Yang, C. Schick, W. J. Harrison, P. M. Budd, M. Böhning, A. Schönhals. First Clear-Cut Experimental Evidence of a Glass Transition in a Polymer with Intrinsic Microporosity: PIM-1. *The journal of physical chemistry letters* **2018**;9(8):2003-2008.

APPENDIX A. MAXWELL-STEFAN MODELING CODE FOR WK TESTS

A.1 "Weak Confinement" Case

A.1.1 No frictional coupling effects

```
function [Nflux] = WeaknoCoupling(thickness, pPXSat, pOXSat, Vpx, Vox,
qpxSat, qoxSat, bpx, box, fPxUp, fOxUp, DpxMS, DoxMS)
%This is used to estimate Flux through membrane using Maxwell-Stefan
model for the "weak confinement" case
%No frictional coupling effects
%2-component, A~p-xylene, B~o-xylene
%Input pressure is a column of target (kPa)
%---------------------------Parameters Below-----------------
%N is the flux (mmol/sqcm/s))
%R is R (J/mol/K)
R=8.314;
%The temperature is 55C
T=328.15;
%rou is membrane density (g/cucm)
rou=2;
%l is mem thickness (cm)
l=thickness;
%pASAT is the saturation pressure for A (kPa)
pASAT = pPXSat;
pBSAT = pOXSat;

%VA is molar volume of A (cucm/mol)
VA=Vpx;
VB=Vox;
%bA, bB are the Langmuir Model parameters (kPa^-1)
```

```
bA=bpx;
bB=box;

%qSAT is the diagonal matrix of saturation capacities
%unit of each entry is mmol/g;
qSAT=[qpxSat, 0;0,qoxSat];

%pUp and pDo are the upstream and downstream hydraulic pressure (kPa)
pDo=101.325;
%--------------------Calculation Below---------------------------
%Set up Iteration
L=1;
%First column Nflux is pressure
Nflux=ones(L,3);
Nflux(:,1)=101;
for i = 1:L

%fAUp, fADo are the fugacity of A at upstream and downstream (kPa)
%Unit conversion for R is required!!!
fAUp=fPxUp;
fADo=0;
fBUp=fOxUp;
fBDo=0;

%piAUp, piADo are the dimensionless fugacity
piAUp=bA*fAUp;
piADo=bA*fADo;
piBUp=bB*fBUp;
piBDo=bB*fBDo;
%piUp, piDo are the vector forms
piUp=[piAUp;piBUp];
piDo=[piADo;piBDo];
```

```
%thetaAUp is fractional occupancy of A at upstream
thetaAUp=bA*fAUp/(1+bA*fAUp+bB*fBUp);
thetaBUp=bB*fBUp/(1+bA*fAUp+bB*fBUp);
%thetaADo is fractional occupancy of A at Downstream
thetaADo=0;
thetaBDo=0;

%DAMS, DBMS Maxwell-Stefan Diffusivity (sqcm/s)
DAMS=DpxMS;
DBMS=DoxMS;
DABMS=10000000000;
DBAMS=DABMS;

%Bup0 is Square matrix of inverse MS coefficients at zero loading
Bup0=[(1/DAMS+thetaBUp/DABMS),(-thetaAUp/DABMS);(-thetaBUp/DBAMS),
(1/DBMS+thetaAUp/DBAMS)];
Binv=inv(Bup0);

%calculate flux vector
%ln=log((1-thetaADo-thetaBDo)/(1-thetaAUp-thetaBUp));
Nweak=rou/l*log((1-thetaADo-thetaBDo)/(1-thetaAUp-thetaBUp))/((1/(1-
thetaAUp-thetaBUp))-(1/(1-thetaADo-thetaBDo)))*qSAT*Binv*(piUp-piDo);

%Column 1 is pressure (kPa), column 2 is flux of p-xylene
(mmol/sqcm/s), column 3 is flux of o-xylene (mmol/sqcm/s)
Nflux(i,2)=Nweak(1,1);
Nflux(i,3)=Nweak(2,1);

end
end
```

A.1.2 Frictional coupling effects considered

```
function [Nflux] = WeakCoupling(thickness, pPXSat, pOXSat, Vpx, Vox,
qpxSat, qoxSat, bpx, box, fPxUp, fOxUp, DpxMS, DoxMS)
%This is used to estimate Flux through membrane using Maxwell-Stefan
model for the "weak confinement" case
%with frictional coupling effect is considered
%2-component, A~p-xylene, B~o-xylene
%Input pressure is a column of target (kPa)
%----------------------------Parameters Below-----------------


%N is the flux (mmol/sqcm/s))
%R is R (J/mol/K)
R=8.314;
%The temperature is 55C
T=328.15;
%rou is membrane density (g/cucm)
rou=2;
%l is mem thickness (cm)
l=thickness;
%pASAT is the saturation pressure for A (kPa)
pASAT = pPXSat;
pBSAT = pOXSat;

%VA is molar volume of A (cucm/mol)
VA=Vpx;
VB=Vox;
%bA, bB are the Langmuir Model parameters (kPa^-1)
bA=bpx;
bB=box;

%qSAT is the diagonal matrix of saturation capacities
%unit of each entry is mmol/g;
```

```
qSAT=[qpxSat, 0;0,qoxSat];

%pUp and pDo are the upstream and downstream hydraulic pressure (kPa)
pDo=101.325;

%--------------------Calculation Below----------------------------

%Set up Iteration
L=1;
%First column Nflux is pressure
Nflux=ones(L,3);
Nflux(:,1)=101;
for i = 1:L

%fAUp, fADo are the fugacity of A at upstream and downstream (kPa)
%Unit conversion for R is required!!!
fAUp=fPxUp;
fADo=0;
fBUp=fOxUp;
fBDo=0;

%piAUp, piADo are the dimensionless fugacity
piAUp=bA*fAUp;
piADo=bA*fADo;
piBUp=bB*fBUp;
piBDo=bB*fBDo;
%piUp, piDo are the vector forms
piUp=[piAUp;piBUp];
piDo=[piADo;piBDo];

%thetaAUp is fractional occupancy of A at upstream
thetaAUp=bA*fAUp/(1+bA*fAUp+bB*fBUp);
```

```
thetaBUp=bB*fBUp/(1+bA*fAUp+bB*fBUp);
%thetaADo is fractional occupancy of A at Downstream
thetaADo=0;
thetaBDo=0;

%DAMS, DBMS Maxwell-Stefan Diffusivity (sqcm/s)
DAMS=DpxMS;
DBMS=DoxMS;
DABMS=DAMS^(thetaAUp/(thetaAUp+thetaBUp))*DBMS^(thetaBUp/(thetaAUp+thet
aBUp));
DBAMS=DABMS;

%Bup0 is Square matrix of inverse MS coefficients at zero loading
Bup0=[(1/DAMS+thetaBUp/DABMS),(-thetaAUp/DABMS);(-thetaBUp/DBAMS),
(1/DBMS+thetaAUp/DBAMS)];
Binv=inv(Bup0);

%calculate flux vector
%ln=log((1-thetaADo-thetaBDo)/(1-thetaAUp-thetaBUp));
Nweak=rou/l*log((1-thetaADo-thetaBDo)/(1-thetaAUp-thetaBUp))/((1/(1-
thetaAUp-thetaBUp))-(1/(1-thetaADo-thetaBDo)))*qSAT*Binv*(piUp-piDo);

%Column 1 is pressure (kPa), column 2 is flux of p-xylene
(mmol/sqcm/s), column 3 is flux of o-xylene (mmol/sqcm/s)
Nflux(i,2)=Nweak(1,1);
Nflux(i,3)=Nweak(2,1);

end
end
```

A.2 "Strong Confinement" Case

A.2.1 No frictional coupling effects

```
function [Nflux] = StrongnoCoupling(thickness, pPXSat, pOXSat, Vpx,
Vox, qpxSat, qoxSat, bpx, box, fPxUp, fOxUp, DpxMS, DoxMS)
%This is used to estimate Flux through membrane using Maxwell-Stefan
model for the "strong confinement" case
%No frictional coupling effects
%2-component, A~p-xylene, B~o-xylene
%Input pressure is a column of target (kPa)
%--------------------------Parameters Below----------------


%N is the flux (mmol/sqcm/s))
%R is R (J/mol/K)
R=8.314;
%The temperature is 55C
T=328.15;
%rou is membrane density (g/cucm)
rou=2;
%l is mem thickness (cm)
l=thickness;
%pASAT is the saturation pressure for A (kPa)
pASAT = pPXSat;
pBSAT = pOXSat;


%VA is molar volume of A (cucm/mol)
VA=Vpx;
VB=Vox;
%bA, bB are the Langmuir Model parameters (kPa^-1)
bA=bpx;
bB=box;
```

```
%qSAT is the diagonal matrix of saturation capacities
%unit of each entry is mmol/g;
qSAT=[qpxSat, 0;0,qoxSat];

%pUp and pDo are the upstream and downstream hydraulic pressure (kPa)
pDo=101.325;

%--------------------Calculation Below----------------------------

%Set up Iteration
L=size(pressure,1);
%First column Nflux is pressure
Nflux=ones(L,3);
Nflux(:,1)=pressure;
for i = 1:L
pUp=pressure(i);
%fAUp, fADo are the fugacity of A at upstream and downstream (kPa)
%Unit conversion for R is required!!!
fAUp=fPxUp;
fADo=0;
fBUp=fOxUp;
fBDo=0;



%piAUp, piADo are the dimensionless fugacity
piAUp=bA*fAUp;
piADo=bA*fADo;
piBUp=bB*fBUp;
piBDo=bB*fBDo;
%piUp, piDo are the vector forms
piUp=[piAUp;piBUp];
piDo=[piADo;piBDo];
```

```
%thetaAUp is fractional occupancy of A at upstream
thetaAUp=bA*fAUp/(1+bA*fAUp+bB*fBUp);
thetaBUp=bB*fBUp/(1+bA*fAUp+bB*fBUp);
%thetaADo is fractional occupancy of A at Downstream
thetaADo=bA*fADo/(1+bA*fADo+bB*fBDo);
thetaBDo=bB*fBDo/(1+bA*fADo+bB*fBDo);

%DAMS, DBMS Maxwell-Stefan Diffusivity (sqcm/s)
DAMS=DpxMS;
DBMS=DoxMS;
DABMS=100000000;
DBAMS=DABMS;

%Bup0 is Square matrix of inverse MS coefficients at zero loading
Bup0=[(1/DAMS+thetaBUp/DABMS),(-thetaAUp/DABMS);(-thetaBUp/DBAMS),
(1/DBMS+thetaAUp/DBAMS)];
Binv=inv(Bup0);

%calculate flux vector
%ln=log((1-thetaADo-thetaBDo)/(1-thetaAUp-thetaBUp));
Nstrong=rou/l*(1-thetaAUp-thetaBUp)*(1-thetaADo-
thetaBDo)*qSAT*Binv*(piUp-piDo);

%Column 1 is pressure (kPa), column 2 is flux of p-xylene
(mmol/sqcm/s), column 3 is flux of o-xylene (mmol/sqcm/s)
Nflux(i,2)=Nweak(1,1);
Nflux(i,3)=Nweak(2,1);

end
end
```

A.2.2 Frictional coupling effects considered

```
function [Nflux] = StrongCoupling(thickness, pPXSat, pOXSat, Vpx, Vox,
qpxSat, qoxSat, bpx, box, fPxUp, fOxUp, DpxMS, DoxMS)
%This is used to estimate Flux through membrane using Maxwell-Stefan
model for the "strong confinement" case
%with frictional coupling effect is considered
%2-component, A~p-xylene, B~o-xylene
%Input pressure is a column of target (kPa)
%----------------------------Parameters Below-----------------


%N is the flux (mmol/sqcm/s))
%R is R (J/mol/K)
R=8.314;
%The temperature is 55C
T=328.15;
%rou is membrane density (g/cucm)
rou=2;
%l is mem thickness (cm)
l=thickness;
%pASAT is the saturation pressure for A (kPa)
pASAT = pPXSat;
pBSAT = pOXSat;

%VA is molar volume of A (cucm/mol)
VA=Vpx;
VB=Vox;
%bA, bB are the Langmuir Model parameters (kPa^-1)
bA=bpx;
bB=box;

%qSAT is the diagonal matrix of saturation capacities
%unit of each entry is mmol/g;
```

```
qSAT=[qpxSat, 0;0,qoxSat];

%pUp and pDo are the upstream and downstream hydraulic pressure (kPa)
pDo=101.325;

%--------------------Calculation Below----------------------------

%Set up Iteration
L=size(pressure,1);
%First column Nflux is pressure
Nflux=ones(L,3);
Nflux(:,1)=pressure;
for i = 1:L
pUp=pressure(i);
%fAUp, fADo are the fugacity of A at upstream and downstream (kPa)
%Unit conversion for R is required!!!
fAUp=fPxUp;
fADo=0;
fBUp=fOxUp;
fBDo=0;

%piAUp, piADo are the dimensionless fugacity
piAUp=bA*fAUp;
piADo=bA*fADo;
piBUp=bB*fBUp;
piBDo=bB*fBDo;
%piUp, piDo are the vector forms
piUp=[piAUp;piBUp];
piDo=[piADo;piBDo];

%thetaAUp is fractional occupancy of A at upstream
thetaAUp=bA*fAUp/(1+bA*fAUp+bB*fBUp);
```

```
thetaBUp=bB*fBUp/(1+bA*fAUp+bB*fBUp);
%thetaADo is fractional occupancy of A at Downstream
thetaADo=bA*fADo/(1+bA*fADo+bB*fBDo);
thetaBDo=bB*fBDo/(1+bA*fADo+bB*fBDo);

%DAMS, DBMS Maxwell-Stefan Diffusivity (sqcm/s)
DAMS=DpxMS;
DBMS=DoxMS;
DABMS=DAMS^(thetaAUp/(thetaAUp+thetaBUp))*DBMS^(thetaBUp/(thetaAUp+thet
aBUp));
DBAMS=DABMS;

%Bup0 is Square matrix of inverse MS coefficients at zero loading
Bup0=[(1/DAMS+thetaBUp/DABMS),(-thetaAUp/DABMS);(-thetaBUp/DBAMS),
(1/DBMS+thetaAUp/DBAMS)];
Binv=inv(Bup0);

%calculate flux vector
%ln=log((1-thetaADo-thetaBDo)/(1-thetaAUp-thetaBUp));
Nstrong=rou/l*(1-thetaAUp-thetaBUp)*(1-thetaADo-
thetaBDo)*qSAT*Binv*(piUp-piDo);

%Column 1 is pressure (kPa), column 2 is flux of p-xylene
(mmol/sqcm/s), column 3 is flux of o-xylene (mmol/sqcm/s)
Nflux(i,2)=Nweak(1,1);
Nflux(i,3)=Nweak(2,1);

end
end
```

A.3 "Hybrid Confinement" Case

A.3.1 No frictional coupling effects

```
function [Nflux] = HybridnoCoupling(thickness, pPXSat, pOXSat, Vpx,
Vox, qpxSat, qoxSat, bpx, box, fPxUp, fOxUp, ahybrid, DpxMS, DoxMS)
%This is used to estimate Flux through membrane using Maxwell-Stefan
model for the "hybrid confinement" case
%No frictional coupling effects
%2-component, A~p-xylene, B~o-xylene
%Input pressure is a column of target (kPa)
%--------------------------Parameters Below----------------


%N is the flux (mmol/sqcm/s))
%R is R (J/mol/K)
R=8.314;
%The temperature is 55C
T=328.15;
%rou is membrane density (g/cucm)
rou=2;
%l is mem thickness (cm)
l=thickness;
%pASAT is the saturation pressure for A (kPa)
pASAT = pPXSat;
pBSAT = pOXSat;


%VA is molar volume of A (cucm/mol)
VA=Vpx;
VB=Vox;
%bA, bB are the Langmuir Model parameters (kPa^-1)
bA=bpx;
bB=box;
```

```
%qSAT is the diagonal matrix of saturation capacities
%unit of each entry is mmol/g;
qSAT=[qpxSat, 0;0,qoxSat];

%pUp and pDo are the upstream and downstream hydraulic pressure (kPa)
pDo=101.325;
%--------------------Calculation Below---------------------------
%Set up Iteration
L=1;
%First column Nflux is pressure
Nflux=ones(L,3);
Nflux(:,1)=101;
for i = 1:L

%fAUp, fADo are the fugacity of A at upstream and downstream (kPa)
%Unit conversion for R is required!!!
fAUp=fPxUp;
fADo=0;
fBUp=fOxUp;
fBDo=0;

%piAUp, piADo are the dimensionless fugacity
piAUp=bA*fAUp;
piADo=bA*fADo;
piBUp=bB*fBUp;
piBDo=bB*fBDo;
%piUp, piDo are the vector forms
piUp=[piAUp;piBUp];
piDo=[piADo;piBDo];

%thetaAUp is fractional occupancy of A at upstream
thetaAUp=bA*fAUp/(1+bA*fAUp+bB*fBUp);
```

```
thetaBUp=bB*fBUp/(1+bA*fAUp+bB*fBUp);
%thetaADo is fractional occupancy of A at Downstream
thetaADo=bA*fADo/(1+bA*fADo+bB*fBDo);
thetaBDo=bB*fBDo/(1+bA*fADo+bB*fBDo);

%DAMS, DBMS Maxwell-Stefan Diffusivity (sqcm/s)
%a is the ratio of Diinf/Di0
a=ahybrid;
DAMS=DpxMS;
DBMS=DoxMS;
DABMS=10000000;
DBAMS=DABMS;

%Bup0 is Square matrix of inverse MS coefficients at zero loading
Bup0=[(1/DAMS+thetaBUp/DABMS),(-thetaAUp/DABMS);(-thetaBUp/DBAMS),
(1/DBMS+thetaAUp/DBAMS)];
Binv=inv(Bup0);

%calculate flux vector
%ln=log((1-thetaADo-thetaBDo)/(1-thetaAUp-thetaBUp));
Nhc=rou/l*(a*log((1-thetaADo-thetaBDo)/(1-thetaAUp-thetaBUp))+((1-
thetaADo-thetaBDo)-(1-thetaAUp-thetaBUp)))/((1/(1-thetaAUp-thetaBUp))-
(1/(1-thetaADo-thetaBDo)))*qSAT*Binv*(piUp-piDo);

%Column 1 is pressure (kPa), column 2 is flux of p-xylene
(mmol/sqcm/s), column 3 is flux of o-xylene (mmol/sqcm/s)
Nflux(i,2)=Nhc(1,1);
Nflux(i,3)=Nhc(2,1);

end
end
```

A.3.2 Frictional coupling effects considered

```
function [Nflux] = HybridCoupling(thickness, pPXSat, pOXSat, Vpx, Vox,
qpxSat, qoxSat, bpx, box, fPxUp, fOxUp, ahybrid, DpxMS, DoxMS)
%This is used to estimate Flux through membrane using Maxwell-Stefan
model for the "hybrid confinement" case
%with frictional Coupling effect is considered
%2-component, A~p-xylene, B~o-xylene
%Input pressure is a column of target (kPa)
%----------------------------Parameters Below-----------------


%N is the flux (mmol/sqcm/s))
%R is R (J/mol/K)
R=8.314;
%The temperature is 55C
T=328.15;
%rou is membrane density (g/cucm)
rou=2;
%l is mem thickness (cm)
l=thickness;
%pASAT is the saturation pressure for A (kPa)
pASAT = pPXSat;
pBSAT = pOXSat;

%VA is molar volume of A (cucm/mol)
VA=Vpx;
VB=Vox;
%bA, bB are the Langmuir Model parameters (kPa^-1)
bA=bpx;
bB=box;

%qSAT is the diagonal matrix of saturation capacities
%unit of each entry is mmol/g;
```

```
qSAT=[qpxSat, 0;0,qoxSat];

%pUp and pDo are the upstream and downstream hydraulic pressure (kPa)
pDo=101.325;
%--------------------Calculation Below---------------------------
%Set up Iteration
L=1;
%First column Nflux is pressure
Nflux=ones(L,3);
Nflux(:,1)=101;
for i = 1:L

%fAUp, fADo are the fugacity of A at upstream and downstream (kPa)
%Unit conversion for R is required!!!
fAUp=fPxUp;
fADo=0;
fBUp=fOxUp;
fBDo=0;

%piAUp, piADo are the dimensionless fugacity
piAUp=bA*fAUp;
piADo=bA*fADo;
piBUp=bB*fBUp;
piBDo=bB*fBDo;
%piUp, piDo are the vector forms
piUp=[piAUp;piBUp];
piDo=[piADo;piBDo];

%thetaAUp is fractional occupancy of A at upstream
thetaAUp=bA*fAUp/(1+bA*fAUp+bB*fBUp);
thetaBUp=bB*fBUp/(1+bA*fAUp+bB*fBUp);
%thetaADo is fractional occupancy of A at Downstream
```

```
thetaADo=bA*fADo/(1+bA*fADo+bB*fBDo);

thetaBDo=bB*fBDo/(1+bA*fADo+bB*fBDo);


%DAMS, DBMS Maxwell-Stefan Diffusivity (sqcm/s)

%a is the ratio of Diinf/Di0

a=ahybrid;

DAMS=DpxMS;

DBMS=DoxMS;

DABMS=DAMS^(thetaAUp/(thetaAUp+thetaBUp))*DBMS^(thetaBUp/(thetaAUp+thet
aBUp))*(a+1-thetaAUp-thetaBUp);

DBAMS=DABMS;


%Bup0 is Square matrix of inverse MS coefficients at zero loading

Bup0=[(1/DAMS+thetaBUp/DABMS),(-thetaAUp/DABMS);(-thetaBUp/DBAMS),
(1/DBMS+thetaAUp/DBAMS)];

Binv=inv(Bup0);


%calculate flux vector

%ln=log((1-thetaADo-thetaBDo)/(1-thetaAUp-thetaBUp));

Nhc=rou/l*(a*log((1-thetaADo-thetaBDo)/(1-thetaAUp-thetaBUp))+((1-
thetaADo-thetaBDo)-(1-thetaAUp-thetaBUp)))/((1/(1-thetaAUp-thetaBUp))-
(1/(1-thetaADo-thetaBDo)))*qSAT*Binv*(piUp-piDo);


%Column 1 is pressure (kPa), column 2 is flux of p-xylene
(mmol/sqcm/s), column 3 is flux of o-xylene (mmol/sqcm/s)

Nflux(i,2)=Nhc(1,1);

Nflux(i,3)=Nhc(2,1);


end

end
```

APPENDIX B. MAXWELL-STEFAN MODELING CODE FOR OSRO

B.1 "Weak Confinement" Case

B.1.1 No frictional coupling effects

```
function [Nflux] = MSFluxWeaknoCoupling(pressure,thickness, xpxUp,
xoxUp, xpxDo,xoxDo,gpxup, goxup, gpxdo,goxdo, bpx, box, qpxsat, qoxsat,
Vpx, Vox, ppxsat, poxsat, DpxMS, DoxMS)
%This is used to estimate Flux through membrane using Maxwell-Stefan
model for the "weak confinement" case
%No frictional coupling effects
%2-component, A~p-xylene, B~o-xylene
%Input pressure is a column of target (kPa)
%---------------------------Parameters Below-----------------


%N is the flux (mmol/sqcm/s))
%R is R (J/mol/K)
R=8.314;
%The temperature is 55C
T=328.15;
%rou is membrane density (g/cucm)
rou=2;
%l is membrane thickness (cm)
l=thickness;
%pASAT is the saturation pressure for A (kPa)
pASAT = ppxsat;
pBSAT = poxsat;


%VA is molar volume of A (cucm/mol)
VA=Vpx;
VB=Vox;
%bA, bB are the Langmuir Model parameters (kPa^-1)
```

```
bA=bpx;
bB=box;



%qSAT is the diagonal matrix of saturation capacities
%unit of each entry is mmol/g;
qSAT=[qpxsat, 0;0,qoxsat];

%xAUp, xADo are the molar fraction of A at upstream and downstream
xAUp=xpxUp;
xBUp=xoxUp;
xADo=xpxDo;
xBDo=xoxDo;
%gammaAUp, gammaADo are the activity coefficients of A at upstream and
downstream
%Peng-Robinson EOS
gammaAUp = gpxup;
gammaADo = gpxdo;
gammaBUp = goxup;
gammaBDo = goxdo;
%pUp and pDo are the upstream and downstream hydraulic pressure (kPa)
pDo=101.325;

%--------------------Calculation Below----------------------------

%Set up Iteration
L=size(pressure,1);
%First column Nflux is pressure
Nflux=ones(L,3);
Nflux(:,1)=pressure;
for i = 1:L
pUp=pressure(i);
%fAUp, fADo are the fugacity of A at upstream and downstream (kPa)
```

```
%Unit conversion for R is required!!!
fAUp=xAUp*gammaAUp*pASAT*exp(VA*1e-3/(R*T)*(pUp-pASAT));
fADo=xADo*gammaADo*pASAT*exp(VA*1e-3/(R*T)*(pDo-pASAT));
fBUp=xBUp*gammaBUp*pBSAT*exp(VB*1e-3/(R*T)*(pUp-pBSAT));
fBDo=xBDo*gammaBDo*pBSAT*exp(VB*1e-3/(R*T)*(pDo-pBSAT));

%piAUp, piADo are the dimensionless fugacity
piAUp=bA*fAUp;
piADo=bA*fADo;
piBUp=bB*fBUp;
piBDo=bB*fBDo;
%piUp, piDo are the vector forms
piUp=[piAUp;piBUp];
piDo=[piADo;piBDo];

%thetaAUp is fractional occupancy of A at upstream
thetaAUp=bA*fAUp/(1+bA*fAUp+bB*fBUp);
thetaBUp=bB*fBUp/(1+bA*fAUp+bB*fBUp);
%thetaADo is fractional occupancy of A at Downstream
thetaADo=bA*fADo/(1+bA*fADo+bB*fBDo);
thetaBDo=bB*fBDo/(1+bA*fADo+bB*fBDo);

%DAMS, DBMS Maxwell-Stefan Diffusivity (sqcm/s)
DAMS=DpxMS;
DBMS=DoxMS;
DABMS=10000000;
DBAMS=DABMS;

%Bup0 is square matrix of inverse Maxwell-Stefan coefficients at zero
loading
Bup0=[(1/DAMS+thetaBUp/DABMS),(-thetaAUp/DABMS);(-thetaBUp/DBAMS),
(1/DBMS+thetaAUp/DBAMS)];
Binv=inv(Bup0);
```

```
%calculate flux vector

%ln=log((1-thetaADo-thetaBDo)/(1-thetaAUp-thetaBUp));

Nweak=rou/l*log((1-thetaADo-thetaBDo)/(1-thetaAUp-thetaBUp))/((1/(1-
thetaAUp-thetaBUp))-(1/(1-thetaADo-thetaBDo)))*qSAT*Binv*(piUp-piDo);


%Column 1 is pressure (kPa), column 2 is flux of p-xylene
(mmol/sqcm/s), column 3 is flux of o-xylene (mmol/sqcm/s)

Nflux(i,2)=Nweak(1,1);

Nflux(i,3)=Nweak(2,1);


end

end
```

B.1.2 Frictional coupling effects considered

```
function [Nflux] = MSFluxWeakCoupling(pressure,thickness, xpxUp, xoxUp,
xpxDo,xoxDo,gpxup, goxup, gpxdo,goxdo, bpx, box, qpxsat, qoxsat, Vpx,
Vox, ppxsat, poxsat, DpxMS, DoxMS)
%This is used to estimate Flux through membrane using Maxwell-Stefan
model for the "weak confinement" case
%with frictional coupling effect is considered
%2-component, A~p-xylene, B~o-xylene
%Input pressure is a column of target (kPa)
%---------------------------Parameters Below-----------------


%N is the flux (mmol/sqcm/s))
%R is R (J/mol/K)
R=8.314;
%The temperature is 55C
T=328.15;
%rou is membrane density (g/cucm)
rou=2;
%l is membrane thickness (cm)
l=thickness;
%pASAT is the saturation pressure for A (kPa)
pASAT = ppxsat;
pBSAT = poxsat;


%VA is molar volume of A (cucm/mol)
VA=Vpx;
VB=Vox;
%bA, bB are the Langmuir Model parameters (kPa^-1)
bA=bpx;
bB=box;



%qSAT is the diagonal matrix of saturation capacities
```

```
%unit of each entry is mmol/g;
qSAT=[qpxsat, 0;0,qoxsat];

%xAUp, xADo are the molar fraction of A at upstream and downstream
xAUp=xpxUp;
xBUp=xoxUp;
xADo=xpxDo;
xBDo=xoxDo;
%gammaAUp, gammaADo are the activity coefficients of A at upstream and
downstream
%Peng-Robinson EOS
gammaAUp = gpxup;
gammaADo = gpxdo;
gammaBUp = goxup;
gammaBDo = goxdo;
%pUp and pDo are the upstream and downstream hydraulic pressure (kPa)
pDo=101.325;



%--------------------Calculation Below----------------------------

%Set up Iteration
L=size(pressure,1);
%First column Nflux is pressure
Nflux=ones(L,3);
Nflux(:,1)=pressure;
for i = 1:L
pUp=pressure(i);
%fAUp, fADo are the fugacity of A at upstream and downstream (kPa)
%Unit conversion for R is required!!!
fAUp=xAUp*gammaAUp*pASAT*exp(VA*1e-3/(R*T)*(pUp-pASAT));
fADo=xADo*gammaADo*pASAT*exp(VA*1e-3/(R*T)*(pDo-pASAT));
fBUp=xBUp*gammaBUp*pBSAT*exp(VB*1e-3/(R*T)*(pUp-pBSAT));
```

```
fBDo=xBDo*gammaBDo*pBSAT*exp(VB*1e-3/(R*T)*(pDo-pBSAT));

%piAUp, piADo are the dimensionless fugacity
piAUp=bA*fAUp;
piADo=bA*fADo;
piBUp=bB*fBUp;
piBDo=bB*fBDo;
%piUp, piDo are the vector forms
piUp=[piAUp;piBUp];
piDo=[piADo;piBDo];

%thetaAUp is fractional occupancy of A at upstream
thetaAUp=bA*fAUp/(1+bA*fAUp+bB*fBUp);
thetaBUp=bB*fBUp/(1+bA*fAUp+bB*fBUp);
%thetaADo is fractional occupancy of A at Downstream
thetaADo=bA*fADo/(1+bA*fADo+bB*fBDo);
thetaBDo=bB*fBDo/(1+bA*fADo+bB*fBDo);

%DAMS, DBMS Maxwell-Stefan Diffusivity (sqcm/s)
DAMS=DpxMS;
DBMS=DoxMS;
DABMS=DAMS^(thetaAUp/(thetaAUp+thetaBUp))*DBMS^(thetaBUp/(thetaAUp+thet
aBUp));
DBAMS=DABMS;

%Bup0 is square matrix of inverse Maxwell-Stefan coefficients at zero
loading
Bup0=[(1/DAMS+thetaBUp/DABMS),(-thetaAUp/DABMS);(-thetaBUp/DBAMS),
(1/DBMS+thetaAUp/DBAMS)];
Binv=inv(Bup0);

%calculate flux vector
%ln=log((1-thetaADo-thetaBDo)/(1-thetaAUp-thetaBUp));
```

```
Nweak=rou/l*log((1-thetaADo-thetaBDo)/(1-thetaAUp-thetaBUp))/((1/(1-
thetaAUp-thetaBUp))-(1/(1-thetaADo-thetaBDo)))*qSAT*Binv*(piUp-piDo);


%Column 1 is pressure (kPa), column 2 is flux of p-xylene
(mmol/sqcm/s), column 3 is flux of o-xylene (mmol/sqcm/s)
Nflux(i,2)=Nweak(1,1);
Nflux(i,3)=Nweak(2,1);


end
end
```

B.2 "Strong Confinement" Case

B.2.1 No frictional coupling effects

```
function [Nflux] = MSFluxStrongnoCoupling(pressure,thickness, xpxUp,
xoxUp, xpxDo,xoxDo,gpxup, goxup, gpxdo,goxdo, bpx, box, qpxsat, qoxsat,
Vpx, Vox, ppxsat, poxsat, DpxMS, DoxMS)
%This is used to estimate Flux through membrane using Maxwell-Stefan
model for the "strong confinement" case
%No frictional coupling effects
%2-component, A~p-xylene, B~o-xylene
%Input pressure is a column of target (kPa)
%----------------------------Parameters Below-----------------


%N is the flux (mmol/sqcm/s))
%R is R (J/mol/K)
R=8.314;
%The temperature is 55C
T=328.15;
%rou is membrane density (g/cucm)
rou=2;
%l is membrane thickness (cm)
l=thickness;
%pASAT is the saturation pressure for A (kPa)
pASAT = ppxsat;
pBSAT = poxsat;


%VA is molar volume of A (cucm/mol)
VA=Vpx;
VB=Vox;
%bA, bB are the Langmuir Model parameters (kPa^-1)
bA=bpx;
bB=box;
```

```
%qSAT is the diagonal matrix of saturation capacities
%unit of each entry is mmol/g;
qSAT=[qpxsat, 0;0,qoxsat];

%xAUp, xADo are the molar fraction of A at upstream and downstream
xAUp=xpxUp;
xBUp=xoxUp;
xADo=xpxDo;
xBDo=xoxDo;
%gammaAUp, gammaADo are the activity coefficients of A at upstream and
downstream
%Peng-Robinson EOS
gammaAUp = gpxup;
gammaADo = gpxdo;
gammaBUp = goxup;
gammaBDo = goxdo;
%pUp and pDo are the upstream and downstream hydraulic pressure (kPa)
pDo=101.325;

%--------------------Calculation Below----------------------------

%Set up Iteration
L=size(pressure,1);
%First column Nflux is pressure
Nflux=ones(L,3);
Nflux(:,1)=pressure;
for i = 1:L
pUp=pressure(i);
%fAUp, fADo are the fugacity of A at upstream and downstream (kPa)
%Unit conversion for R is required!!!
fAUp=xAUp*gammaAUp*pASAT*exp(VA*1e-3/(R*T)*(pUp-pASAT));
fADo=xADo*gammaADo*pASAT*exp(VA*1e-3/(R*T)*(pDo-pASAT));
```

```
fBUp=xBUp*gammaBUp*pBSAT*exp(VB*1e-3/(R*T)*(pUp-pBSAT));
fBDo=xBDo*gammaBDo*pBSAT*exp(VB*1e-3/(R*T)*(pDo-pBSAT));

%piAUp, piADo are the dimensionless fugacity
%Yao-Lively-Langmuir Model
piAUp=bA*fAUp;
piADo=bA*fADo;
piBUp=bB*fBUp;
piBDo=bB*fBDo;
%piUp, piDo are the vector forms
piUp=[piAUp;piBUp];
piDo=[piADo;piBDo];

%thetaAUp is fractional occupancy of A at upstream
thetaAUp=bA*fAUp/(1+bA*fAUp+bB*fBUp);
thetaBUp=bB*fBUp/(1+bA*fAUp+bB*fBUp);
%thetaADo is fractional occupancy of A at Downstream
thetaADo=bA*fADo/(1+bA*fADo+bB*fBDo);
thetaBDo=bB*fBDo/(1+bA*fADo+bB*fBDo);

%DAMS, DBMS Maxwell-Stefan Diffusivity (sqcm/s)
DAMS=DpxMS;
DBMS=DoxMS;
%Strong Confinement for Upstream
DABMS=10000000;
DBAMS=DABMS;

%Bup0 is square matrix of inverse Maxwell-Stefan coefficients at zero
loading
Bup0=[(1/DAMS0+thetaBUp/DABMS),(-thetaAUp/DABMS);(-thetaBUp/DBAMS),
(1/DBMS0+thetaAUp/DBAMS)];
Binv=inv(Bup0);
```

```
%calculate flux vector

Nstrong=rou/l*(1-thetaAUp-thetaBUp)*(1-thetaADo-
thetaBDo)*qSAT*Binv*(piUp-piDo);


%Column 1 is pressure (kPa), column 2 is flux of p-xylene
(mmol/sqcm/s), column 3 is flux of o-xylene (mmol/sqcm/s)

Nflux(i,2)=Nstrong(1,1);

Nflux(i,3)=Nstrong(2,1);


end

end
```

B.2.2 Frictional coupling effects considered

```
function [Nflux] = MSFluxStrongCoupling(pressure,thickness, xpxUp,
xoxUp, xpxDo,xoxDo,gpxup, goxup, gpxdo,goxdo, bpx, box, qpxsat, qoxsat,
Vpx, Vox, ppxsat, poxsat, DpxMS, DoxMS)
%This is used to estimate Flux through membrane using Maxwell-Stefan
model for the "strong confinement" case
%with frictional Coupling effect is considered
%2-component, A~p-xylene, B~o-xylene
%Input pressure is a column of target (kPa)
%---------------------------Parameters Below-----------------


%N is the flux (mmol/sqcm/s))
%R is R (J/mol/K)
R=8.314;
%The temperature is 55C
T=328.15;
%rou is membrane density (g/cucm)
rou=2;
%l is membrane thickness (cm)
l=thickness;
%pASAT is the saturation pressure for A (kPa)
pASAT = ppxsat;
pBSAT = poxsat;


%VA is molar volume of A (cucm/mol)
VA=Vpx;
VB=Vox;
%bA, bB are the Langmuir Model parameters (kPa^-1)
bA=bpx;
bB=box;
```

```
%qSAT is the diagonal matrix of saturation capacities
%unit of each entry is mmol/g;
qSAT=[qpxsat, 0;0,qoxsat];

%xAUp, xADo are the molar fraction of A at upstream and downstream
xAUp=xpxUp;
xBUp=xoxUp;
xADo=xpxDo;
xBDo=xoxDo;
%gammaAUp, gammaADo are the activity coefficients of A at upstream and
downstream
%Peng-Robinson EOS
gammaAUp = gpxup;
gammaADo = gpxdo;
gammaBUp = goxup;
gammaBDo = goxdo;
%pUp and pDo are the upstream and downstream hydraulic pressure (kPa)
pDo=101.325;



%--------------------Calculation Below---------------------------

%Set up Iteration
L=size(pressure,1);
%First column Nflux is pressure
Nflux=ones(L,3);
Nflux(:,1)=pressure;
for i = 1:L
pUp=pressure(i);
%fAUp, fADo are the fugacity of A at upstream and downstream (kPa)
%Unit conversion for R is required!!!
fAUp=xAUp*gammaAUp*pASAT*exp(VA*1e-3/(R*T)*(pUp-pASAT));
fADo=xADo*gammaADo*pASAT*exp(VA*1e-3/(R*T)*(pDo-pASAT));
```

```
fBUp=xBUp*gammaBUp*pBSAT*exp(VB*1e-3/(R*T)*(pUp-pBSAT));
fBDo=xBDo*gammaBDo*pBSAT*exp(VB*1e-3/(R*T)*(pDo-pBSAT));

%piAUp, piADo are the dimensionless fugacity
%Yao-Lively-Langmuir Model
piAUp=bA*fAUp;
piADo=bA*fADo;
piBUp=bB*fBUp;
piBDo=bB*fBDo;
%piUp, piDo are the vector forms
piUp=[piAUp;piBUp];
piDo=[piADo;piBDo];

%thetaAUp is fractional occupancy of A at upstream
thetaAUp=bA*fAUp/(1+bA*fAUp+bB*fBUp);
thetaBUp=bB*fBUp/(1+bA*fAUp+bB*fBUp);
%thetaADo is fractional occupancy of A at Downstream
thetaADo=bA*fADo/(1+bA*fADo+bB*fBDo);
thetaBDo=bB*fBDo/(1+bA*fADo+bB*fBDo);

%DAMS, DBMS Maxwell-Stefan Diffusivity (sqcm/s)
DAMS0=DpxMS;
DBMS0=DoxMS;
%Strong Confinement for Upstream
DABMS=DAMS0^(thetaAUp/(thetaAUp+thetaBUp))*DBMS0^(thetaBUp/(thetaAUp+th
etaBUp))*(1-thetaAUp-thetaBUp);
DBAMS=DABMS;

%Bup0 is square matrix of inverse Maxwell-Stefan coefficients at zero
loading
Bup0=[(1/DAMS0+thetaBUp/DABMS),(-thetaAUp/DABMS);(-thetaBUp/DBAMS),
(1/DBMS0+thetaAUp/DBAMS)];
Binv=inv(Bup0);
```

```
%calculate flux vector

Nstrong=rou/l*(1-thetaAUp-thetaBUp)*(1-thetaADo-
thetaBDo)*qSAT*Binv*(piUp-piDo);


%Column 1 is pressure (kPa), column 2 is flux of p-xylene
(mmol/sqcm/s), column 3 is flux of o-xylene (mmol/sqcm/s)

Nflux(i,2)=Nstrong(1,1);

Nflux(i,3)=Nstrong(2,1);


end

end
```

B.3 "Hybrid Confinement" Case

B.3.1 No frictional coupling effects

```
function [Nflux] = MSFluxHybridnoCoupling(pressure,thickness, xpxUp,
xoxUp, xpxDo,xoxDo,gpxup, goxup, gpxdo,goxdo, bpx, box, qpxsat, qoxsat,
Vpx, Vox, ppxsat, poxsat, ahybrid, DpxMS, DoxMS)
%This is used to estimate Flux through membrane using Maxwell-Stefan
model for the "hybrid confinement" case
%No frictional coupling effects
%2-component, A~p-xylene, B~o-xylene
%Input pressure is a column of target (kPa)
%----------------------------Parameters Below-----------------


%N is the flux (mmol/sqcm/s))
%R is R (J/mol/K)
R=8.314;
%The temperature is 55C
T=328.15;
%rou is membrane density (g/cucm)
rou=2;
%l is membrane thickness (cm)
l=thickness;
%pASAT is the saturation pressure for A (kPa)
pASAT = ppxsat;
pBSAT = poxsat;


%VA is molar volume of A (cucm/mol)
VA=Vpx;
VB=Vox;
%bA, bB are the Langmuir Model parameters (kPa^-1)
bA=bpx;
bB=box;
```

```
%qSAT is the diagonal matrix of saturation capacities
%unit of each entry is mmol/g;
qSAT=[qpxsat, 0;0,qoxsat];

%xAUp, xADo are the molar fraction of A at upstream and downstream
xAUp=xpxUp;
xBUp=xoxUp;
xADo=xpxDo;
xBDo=xoxDo;
%gammaAUp, gammaADo are the activity coefficients of A at upstream and
downstream
%Peng-Robinson EOS
gammaAUp = gpxup;
gammaADo = gpxdo;
gammaBUp = goxup;
gammaBDo = goxdo;
%pUp and pDo are the upstream and downstream hydraulic pressure (kPa)
pDo=101.325;

%--------------------Calculation Below----------------------------

%Set up Iteration
L=size(pressure,1);
%First column Nflux is pressure
Nflux=ones(L,3);
Nflux(:,1)=pressure;
for i = 1:L
pUp=pressure(i);
%fAUp, fADo are the fugacity of A at upstream and downstream (kPa)
%Unit conversion for R is required!!!
fAUp=xAUp*gammaAUp*pASAT*exp(VA*1e-3/(R*T)*(pUp-pASAT));
fADo=xADo*gammaADo*pASAT*exp(VA*1e-3/(R*T)*(pDo-pASAT));
fBUp=xBUp*gammaBUp*pBSAT*exp(VB*1e-3/(R*T)*(pUp-pBSAT));
```

```
fBDo=xBDo*gammaBDo*pBSAT*exp(VB*1e-3/(R*T)*(pDo-pBSAT));

%piAUp, piADo are the dimensionless fugacity
piAUp=bA*fAUp;
piADo=bA*fADo;
piBUp=bB*fBUp;
piBDo=bB*fBDo;
%piUp, piDo are the vector forms
piUp=[piAUp;piBUp];
piDo=[piADo;piBDo];

%thetaAUp is fractional occupancy of A at upstream
thetaAUp=bA*fAUp/(1+bA*fAUp+bB*fBUp);
thetaBUp=bB*fBUp/(1+bA*fAUp+bB*fBUp);
%thetaADo is fractional occupancy of A at Downstream
thetaADo=bA*fADo/(1+bA*fADo+bB*fBDo);
thetaBDo=bB*fBDo/(1+bA*fADo+bB*fBDo);

%DAMS, DBMS Maxwell-Stefan Diffusivity (sqcm/s)
%a is the ratio of Diinf/Di0
a=ahybrid;
DAMS=DpxMS;
DBMS=DoxMS;
DABMS=100000000;
DBAMS=DABMS;

%Bup0 is square matrix of inverse Maxwell-Stefan coefficients at zero
loading
Bup0=[(1/DAMS+thetaBUp/DABMS),(-thetaAUp/DABMS);(-thetaBUp/DBAMS),
(1/DBMS+thetaAUp/DBAMS)];
Binv=inv(Bup0);

%calculate flux vector
```

```
%ln=log((1-thetaADo-thetaBDo)/(1-thetaAUp-thetaBUp));

Nhc=rou/l*(a*log((1-thetaADo-thetaBDo)/(1-thetaAUp-thetaBUp))+((1-
thetaADo-thetaBDo)-(1-thetaAUp-thetaBUp)))/((1/(1-thetaAUp-thetaBUp))-
(1/(1-thetaADo-thetaBDo)))*qSAT*Binv*(piUp-piDo);


%Column 1 is pressure (kPa), column 2 is flux of p-xylene
(mmol/sqcm/s), column 3 is flux of o-xylene (mmol/sqcm/s)

Nflux(i,2)=Nhc(1,1);

Nflux(i,3)=Nhc(2,1);


end

end
```

B.3.2 Frictional coupling effects considered

```
function [Nflux] = MSFluxHybridCoupling(pressure,thickness, xpxUp,
xoxUp, xpxDo,xoxDo,gpxup,goxup, gpxdo,goxdo, bpx, box, qpxsat, qoxsat,
Vpx, Vox, ppxsat, poxsat, ahybrid, DpxMS, DoxMS)
%This is used to estimate Flux through membrane using Maxwell-Stefan
model for the "hybrid confinement" case
%with Coupling effect is considered
%2-component, A~p-xylene, B~o-xylene
%Input pressure is a column of target (kPa)
%---------------------------Parameters Below-----------------


%N is the flux (mmol/sqcm/s))
%R is R (J/mol/K)
R=8.314;
%The temperature is 55C
T=328.15;
%rou is membrane density (g/cucm)
rou=2;
%l is membrane thickness (cm)
l=thickness;
%pASAT is the saturation pressure for A (kPa)
pASAT = ppxsat;
pBSAT = poxsat;


%VA is molar volume of A (cucm/mol)
VA=Vpx;
VB=Vox;
%bA, bB are the Langmuir Model parameters (kPa^-1)
bA=bpx;
bB=box;
```

```
%qSAT is the diagonal matrix of saturation capacities
%unit of each entry is mmol/g;
qSAT=[qpxsat, 0;0,qoxsat];

%xAUp, xADo are the molar fraction of A at upstream and downstream
xAUp=xpxUp;
xBUp=xoxUp;
xADo=xpxDo;
xBDo=xoxDo;
%gammaAUp, gammaADo are the activity coefficients of A at upstream and
downstream
%Peng-Robinson EOS
gammaAUp = gpxup;
gammaADo = gpxdo;
gammaBUp = goxup;
gammaBDo = goxdo;
%pUp and pDo are the upstream and downstream hydraulic pressure (kPa)
pDo=101.325;

%--------------------Calculation Below----------------------------

%Set up Iteration
L=size(pressure,1);
%First column Nflux is pressure
Nflux=ones(L,3);
Nflux(:,1)=pressure;
for i = 1:L
pUp=pressure(i);
%fAUp, fADo are the fugacity of A at upstream and downstream (kPa)
%Unit conversion for R is required!!!
fAUp=xAUp*gammaAUp*pASAT*exp(VA*1e-3/(R*T)*(pUp-pASAT));
fADo=xADo*gammaADo*pASAT*exp(VA*1e-3/(R*T)*(pDo-pASAT));
fBUp=xBUp*gammaBUp*pBSAT*exp(VB*1e-3/(R*T)*(pUp-pBSAT));
```

```
fBDo=xBDo*gammaBDo*pBSAT*exp(VB*1e-3/(R*T)*(pDo-pBSAT));

%piAUp, piADo are the dimensionless fugacity
piAUp=bA*fAUp;
piADo=bA*fADo;
piBUp=bB*fBUp;
piBDo=bB*fBDo;
%piUp, piDo are the vector forms
piUp=[piAUp;piBUp];
piDo=[piADo;piBDo];

%thetaAUp is fractional occupancy of A at upstream
thetaAUp=bA*fAUp/(1+bA*fAUp+bB*fBUp);
thetaBUp=bB*fBUp/(1+bA*fAUp+bB*fBUp);
%thetaADo is fractional occupancy of A at Downstream
thetaADo=bA*fADo/(1+bA*fADo+bB*fBDo);
thetaBDo=bB*fBDo/(1+bA*fADo+bB*fBDo);

%DAMS, DBMS Maxwell-Stefan Diffusivity (sqcm/s)
%a is the ratio of Diinf/Di0
a=ahybrid;
DAMS=DpxMS;
DBMS=DoxMS;
DABMS=DAMS^(thetaAUp/(thetaAUp+thetaBUp))*DBMS^(thetaBUp/(thetaAUp+thet
aBUp))*(a+1-thetaAUp-thetaBUp);
DBAMS=DABMS;

%Bup0 is square matrix of inverse Maxwell-Stefan coefficients at zero
loading
Bup0=[(1/DAMS+thetaBUp/DABMS),(-thetaAUp/DABMS);(-thetaBUp/DBAMS),
(1/DBMS+thetaAUp/DBAMS)];
Binv=inv(Bup0);
```

```
%calculate flux vector
%ln=log((1-thetaADo-thetaBDo)/(1-thetaAUp-thetaBUp));
Nhc=rou/l*(a*log((1-thetaADo-thetaBDo)/(1-thetaAUp-thetaBUp))+((1-
thetaADo-thetaBDo)-(1-thetaAUp-thetaBUp)))/((1/(1-thetaAUp-thetaBUp))-
(1/(1-thetaADo-thetaBDo)))*qSAT*Binv*(piUp-piDo);


%Column 1 is pressure (kPa), column 2 is flux of p-xylene
(mmol/sqcm/s), column 3 is flux of o-xylene (mmol/sqcm/s)
Nflux(i,2)=Nhc(1,1);
Nflux(i,3)=Nhc(2,1);


end
end
```